# Mechanical nonlinear dynamics of a suspended photonic crystal membrane with integrated actuation

Avishek Chowdhury

NNT : 2016SACLS 284

# THESE DE DOCTORAT
DE
L'UNIVERSITE PARIS-SACLAY
PREPAREE A
L'UNIVERSITE PARIS-SUD XI

Ecole Doctorale N° 572
EDOM (Ondes et Matière)

Spécialité de doctorat : Physique

Par

**Avishek Chowdhury**

# Mechanical nonlinear dynamics of a suspended photonic crystal membrane with integrated actuation

**Thèse présentée et soutenue à CNRS-C2N (Marcoussis), le 28 Septembre, 2016:**

**Composition du Jury :**

| | | |
|---|---|---|
| Dr. Philippe Boucaud | CNRS-C2N, Paris-Sud (France) | Président |
| Dr. Francesco Marin | LENS (Florence, Italie) | Rapporteur |
| Prof. Andrea Fiore | TU Eindhoven (Pays-Bas) | Rapporteur |
| Dr. Alfredo de Rossi | Thales Research and Technology (Palaiseau, France) | Examinateur |
| Dr. Rémy Braive | Université Paris 7/CNRS-C2N | Invité |
| Dr. Isabelle Robert-Philip | CNRS-C2N | Directrice de these |

*To my parents*

*“I went into a McDonald's yesterday and said, 'I'd like some fries.' The girl at the counter said, 'Would you like some fries with that?'”*

- Jay Leno

université PARIS-SACLAY | ÉCOLE DOCTORALE Ondes et Matière (EDOM)

**Titre :** Dynamique non linéaire mécanique d'une membrane photonique cristaux suspendu avec actionnement intégrée

**Mots clés :** dynamique non linéaire, cristaux photonique, actionnement intégrée, opto-mecanique

**Résumé :** Dans les résonateurs nano-mécaniques, les non-linéarités peuvent provenir de différents effets tels que des mécanismes de ressort ou d'atténuation dans des éléments de circuits résistif, inductif et capacitif. Au-delà des intérêts fondamentaux pour tester la réponse dynamique de systèmes non-linéaires avec des nombreux degrés de liberté, les non-linéarités dans les systèmes nano-mécaniques ouvrent de nouvelles voies pour la transduction du déplacement, la détection nano-mécanique et le traitement du signal. Dans cette thèse, nous étudions la réponse non-linéaire d'un résonateur nano-mécanique consistant en une membrane suspendue à cristal photonique jouant le rôle d'un miroir déformable. L'actionnement du mouvement de la membrane dans la gamme de fréquence du MHz est rendu possible par l'utilisation d'électrodes inter-digitées placées en dessous de la membrane. L'efficacité d'actionnement dépend fortement de la distance entre la membrane et les électrodes. La force électrostatique appliquée induit des non-linéarités mécaniques. Le cœur de cette thèse est l'étude des phénomènes de dynamiques non-linéaires sur cette plate-forme mécanique. Les expériences comprennent, par exemple, les résonances sub et super-harmoniques, l'amplification paramétrique et la résonance stochastique.

**Title :** Mechanical nonlinear dynamics of a suspended photonic crystal membrane with integrated actuation

**Keywords :** nonlinear dynamics, photonic-crystal, integrated actuation, opto-mechanics

**Abstract :** Nonlinearities in nanomechanical systems can arise from various sources such as spring and damping mechanisms and resistive, inductive, and capacitive circuit elements. Beyond fundamental interests for testing the dynamical response of discrete nonlinear systems with many degrees of freedom, non-linearities in nanomechanical devices, open new routes for motion transduction, nanomechanical sensing, and signal processing. In this thesis report, we investigate the nonlinear response of a nanomechanical resonator consisting in a suspended photonic crystal membrane acting as a deformable mirror. Actuation of the membrane motion in the MHz frequency range is achieved via interdigitated electrodes placed underneath the membrane. The efficiency of actuation is highly dependent on the separation between the membrane and the electrodes underneath. The applied electrostatic force can induce mechanical non-linearities. The focus of this thesis report is to study the nonlinear dynamical phenomenon of the nano-mechanical platform. The experiments include sub/super-harmonic resonance, parametric amplification and stochastic resonance for example.

# Acknowledgment

The transition from masters to doctor is not straight forward. Especially when the transition is made in just about three years. Honestly speaking, I did not imagine the thesis report to contain such a vast spectra of work when I began my thesis. This is solely attributed to the people I have encountered during the course of these three years. Apart from my supervisors, there are many people in the lab, outside the lab I would like to mention who have helped me during the course of my thesis. So I take this opportunity to give a big thanks to these people.

I have to start with my thesis supervisor Isabelle ROBERT-PHILIP, who just hasn't been my thesis supervisor during the course of these three years. Moreover she has been a mentor, an adviser and a friend. Her encouragement, advice and guidance has helped me to make a transition from being a student to a scientist. I would like to thank her for being there whenever I needed her advice. Be it regarding science, personal life or administrative. Especially I would like to thank her keeping me motivated when I was in self-doubt. Even when she had to change the lab during the very end of my thesis, I never felt left alone and I always felt she was just a phone call away. So I would really like to thank her for the profound help and guidance during these three years, without which completion of my thesis would have been impossible.

Another person I need to thank right after is Remy BRAIVE, who was the co-adviser of my thesis. If there is one person without whom I would think this thesis would have been impossible, then that's definitely him. All the work that I have learned in these three years, a major part is from him. Be it inside the clean room, in optical experiments or even regarding simulations. Even from a humane point of view, he has helped me whenever I needed any kind of help from him without any kind of hesitation. I went to he office anytime with any kind of problem and asked him without hesitation as I knew he will always find a solution. Moreover, I knew that he will always listen to my questions with undivided attention and try to answer it with best of his abilities does not matter how stupid it might have been. So I would really like to thank him for being so nice and kind to me for these three years.

I would like to acknowledge the help and advice that I have received from other permanent staffs in the Lab. I would like to thank Fabrice RAINERI for his mentoring during these three years. Specially in the clean room whenever I needed any help, I had no hesitation to approach him. Apart from the clean room, I really enjoyed the scientific or non-scientific discussions we had every time. I will especially remember the fun time we spend in San Francisco during Photonic West. Another person who had a huge contribution to successfully

complete my thesis was Sylvain BARBAY. Although I didn't really had the opportunity to spend too much time with him during my first two years in the lab. But during the last year I really had the honor to collaborate with him and I was able to learn so much. His critical viewing and guidance was essential for the success of my thesis. I would also like to thank Rama RAJ, for being the fellow Indian in the lab and being able to have conversations about various topics starting from science to politics. I would like to acknowledge the contribution of Inah YEO, who stayed as a post doc during her one year stay at the lab. Her contribution was essential especially in order to building up the experimental set-up. Surely without her help the optical set-up wouldn't have been in the position that it is right now. I would like to thank her also for always bringing positive energy in the work and trying to motivate me to perform some new and challenging experiments. I would also like to appreciate the scientific/non-scientific conversations I had all other permanents, post-docs and PhD students that I had the privilege to spend time with.

I am really thankful to Gilgueng HWANG for having those wonderful conversations. I would like to thank Dominique MAILLY for being the head of the laboratory. I want to give a big thanks to the administrative people in LPN with Agnes ROUX-PERRIN, Marina FERREIRA and Sandrine BOUVY. My acknowledgment to the IT team as well with Lorenzo BERNARDI, Alain PEAN and Mehdi IDOUHAMD, for being available all the time and agreeing to solve all my problems with always a good sense of humor. I would also like to thank the reviewers of my thesis Francesco MARIN and Andrea FIORE for their insightful advice and corrections. Along with that I would like to thank members of the juries which included Phillipe BOUCAUD, Alfredo DE ROSSI and Eva WEIG.

Here I would like to thank several colleagues and friends that I had the opportunity to work and spend time with during this three year stay at LPN. I want to start with Victor TSVIRKUN, who although was one year older to me in the lab however few years younger than me in life. I will never forget how he welcomed me in the lab with his open arms and we became friends instantly. I would like to thank him for being there always when I needed help or when I was in self doubt. Thanks so much for being there at my defense, it really meant a lot to me. Special thanks to Rui ZHU, for making the 'supposedly' difficult last year to be one of the most memorable one for me. I will really cherish all the weird and funny discussions we had during the coffee breaks and I am glad that I have found a friend for life in you. It is really amazing how close friends we have become in such a short amount of time. Good luck for your PhD, I know you will definitely do well. I really need to thank all the people that I have worked with in my group at various time periods. This includes Alessandro SURRENTE, Carla SANNA, Saida RIGHI. I would like to congratulate Guilhem MADIOT for being able to obtain a well deserved PhD opportunity in our group. I would like to wish you best of luck for the bright future and just for the records 'A man who sold the world' is still the best cover song of all time. I would like to thank Dorian SANCHEZ for being such a good friend in and out of the lab. I definitely need to thank other mates that I have enjoyed spending time with. Although the list is unending but I would still like to mention few names. Antu GOTARI, I hope I have your name right. Thanks for being such a wonderful friend, can't believe we have become such good friends in a matter of months. However I hope you can improve your skills with drones, to keep up with 'you know who'!!! Next time we meet we

would have a 'drone-off'. Thanks to Guillome CROSNIER for the all the crazy discussions we had. I can't remember ever having a normal (physicist like) discussion with you. Thanks to Foued SELMI for being my neighbor during the first two years of my PhD. I really enjoyed the discussions we had about god and religion. Other than that I would like to thank Zubair, Mounib, Vishnu, Vivek, Vincenzo, Ivens, John, Philip, Nhung, Iryna, Shayma and a bunch of other friends in LPN without whom I could not imagine this memorable journey. I have to thank the bunch of Indian (more precisely Bengali) friends that I had in Paris, the moments I spent with them I will cherish for my entire life. Thanks to Indra, Biswa, Syam, Kaushik, Mitra, Mitanti, Gantu da for being such good friends for all these years.

This list can not end if I don't mention the two most important persons in my life. They are my parents, my father Ramendra Kumar CHOWDHURY and my mother Rita CHOWDHURY. Without their motivation and sacrifice I cannot imagine of being whatever I am today. I would like to take this opportunity to express my gratitude towards them.

During the course of these three years I had the opportunity of being a part of an European project called ITN-CQOM. This for me was a great opportunity to meet people from Europe and other parts of the globe in order to have not only a scientific but also a cultural exchange. I would like to thank all the members for the wonderful meetings that we had in various parts of Europe during these three years. I hope we will cross our paths again somewhere. And of course thanks to ITN-CQOM for funding my research, that was sooooo important.

And finally I would like to thank God, for making me an atheist.

# Contents

# Chapter 1

# Introduction

General motivation of the PhD is the development and nonlinear dynamical study of a NOEMS platform. The system consists of a suspended 2D-membrane with embedded photonic crystal on it. The rectangular shaped membrane has interdigitated electrodes underneath, used to drive these membranes at its eigen-frequencies. The system therefore has both mechanical and electrical properties enabling possibility of an electro-mechanical coupling. The unique features of the nanomechanical membrane leads to high nonlinearity in the system. The existing nonlinearity in the system enabled us to perform studies involving nonlinear dynamic, which includes sub/super-harmonic excitation, stochastic resonance for example. Moreover, the system being a photonic crystal has optical properties at the same time. Therefore it has capabilities to realize a NOEMS platform, where it is possible to realize integration with larger circuitry, coupling resonators or synchronization. In this chapter we discuss state of the art of such system and significance of the work in the domain of nonlinear dynamics and NOEMS systems.

Over last decade we have observed huge advancement in applications with Nano/Micro-Electro-Mechanical Systems or simply MEMS/NEMS. These involves applications in several electronic devices including accelerometers [1], microphones [2], gyroscopes , pressure/mas/gas sensors [3, 4], energy harvesters [5, 6], lab-on-chip [7] devices for biological applications to name a few. Among the most popular applications in sensing the devices there are the ones based on vibratory modes of crystals [8], micro cantilevers [9, 10, 11, 12] and other electromechanical systems [13, 14].

## 1.1 Nano-Electro-Mechanical systems

Most electromechanical systems consist of two elements; a mechanical system and transducers. The mechanical system is under a force field induced by the transducer causing the system to vibrate. The externally induced force and amplitude of displacement are related as: $F = kx$. Where $F$ is the external force, $x$ is the mechanical resonator displacement and $k$ is what is known as the spring constant of the system. A weak spring constant $k$ means small force can induce high motion. Not only such a system is useful for sensors but at the same

time is useful to study several effects in nonlinear regime. The mechanical resonators are traditionally cantilever structures with clamping on one or both sides [15]. Although rectangular structures have also been realized in order to perform electro-mechanical conversions as demonstrated by [16, 17].

### 1.1.1 Advantages of using a NEMS platform

The small size of these systems means, such systems can be fabricated with eigen-frequencies ranging from a few kHz to GHz regime. For a fully clamped beam the expression of the flexural mode eigen-frequency can be simply written as: $\Omega_0 \sim (k_{eff}/m_{eff})^{1/2}$ [18, 19]. Here, $k_{eff}$ is the effective spring constant and $m_{eff}$ is the effective mass of the system (effective mass is a complex set of elasticity equations that govern the mechanical response of the system). This effective mass on the other hand is proportional to cube of the linear dimension $l$ i.e. $m_{eff} \propto l^3$ while at the same time the effective spring constant is proportional directly to the dimension $l$ i.e. $k_{eff} \propto l$. Thus as $l$ decreases there is an increase of the eigen-frequency of the system while on the other hand resonators with fast response can be designed by working with stiffer structures. These structures can be designed either by working high-stress structures or simply by working with structures having higher Young modulus. Devices with high frequencies therefore can be designed with modern technology by working with nanotube or nanowire like NEMS structures.

Another important factor of NEMS devices is what is known as the quality factor or Q-factor. These NEMS systems can have Q-factors ranging from $10^3 - 10^5$. This value greatly exceeds from the available purely electrical devices, thanks to lack of internal dissipation to low operating power levels. For devices used in signal processing high Q-factor implies low insertion loss [20] and low operating bandwidth [21, 22]. Moreover thermomechanical noise is inversely proportional to the Q-factor, thereby making such devices less susceptible to random mechanical fluctuations and hence highly sensitive to external forcing.

These platforms also act as sensitive mass detectors thanks to the low effective mass or inertia (in case of torsional resonators). The small sizes of these devices generate highly localized spatial response and therefore these devices can be tailored in such a manner so that they react to external forces in specific directions. Finally the low operating power makes them integrable with various circuit components and low consumer of electrical power.

At the heart of any NEMS system is a mechanical resonator, where it is interfaced with transducers used for actuating these resonators to detect mechanical displacements. In the upcoming sections we will discuss about various ways in which a mechanical resonator can be actuated and detected.

### 1.1.2 Actuation schemes

In most cases, mechanical resonators are excited in three different manners: magnetomotive, capacitive (electrostatic) and piezoelectric. In case of the former a magnetic field is generated by current, providing the actuation force [23]. Depending on the orientation of the mechanical beam with respect to the static magnetic field, the force can be either in or out of plane.

Simply the force acting on the resonator can be written as: $F(\Omega) = I(\Omega)Bl$, where $I(\Omega)$ is the drive current, $B$ is the strength of the magnetic field and $l$ is the length of the beam. Ming et al. demonstrated magnetomotive actuation for a frequency around $1GHz$ [19].

In capacitive scheme of actuation, two electrodes work like a parallel plate capacitor applying force on the resonator [24]. In order to actuate efficiently, the electrodes need to be at close vicinity to the resonator. The distance between the resonator and electrodes here becomes governing factor on the electromechanical coupling term. However due to existing parasitic capacitance in the circuit they become less efficient at higher frequency of operation. However, Burek et al. have shown that electrostatic actuation can work reliably for a frequency up to $700MHz$ [25].

Recently some of the devices utilize piezoelectric properties in order to actuate the mechanical resonator. The advantage of these platforms is that its integratibility and the possibility of actuation in the $GHz$ regime. Balram et al. showed that actuation of mechanical resonators having piezoelectric properties is possible using interdigitated electrodes [26]. Other schemes of actuation involve magnetostriction or thermal actuation for example.

### 1.1.3 Detection schemes

The detection scheme needs to be highly sensitive, in order to detect small motion of the nanomechanical oscillators. These schemes again can be magnetomotive, capacitive, piezoelectric or optical for example.

In case of magnetomotive detection, it follows the actuation scheme. The resonator is placed inside a static magnetic field, a movement of the resonator generates a time varying flux. This in turn produces an electromotive force in the loop which can be picked up by an external circuit [23, 27].

In case of capacitive displacement detection, motion of the mechanical element changes the capacitance between the electrodes. In order to detect this change in capacitance, one voltage biases the capacitor and looks for a change in the voltage across the capacitor.

In the piezoelectric scheme, the polarization field within the strained piezoelectric material is utilized to detect the mechanical motion. The detection is then realized by very sensitively measuring the potential drop across the strained device [28]. However the high source impedance of the generated piezoelectric signal makes detection challenging at higher frequencies. Cleland et al. have proposed piezoelectric detection in NEMS using single electron transistors (SET) in order to counter this effect [29].

Recent advancements in interferometric techniques in particular Fabry-Perot and Michelson interferometer makes it possible to detect these mechanical motions optically instead. In case of Fabry-Perot (Figure 1.1(a)) there is a optical cavity formed between the resonator and the substrate. As the resonator oscillates, an out of plane motion modulates the resonance of the optical cavity and thus the intensity and phase of a reflected laser coupled to it, allowing to detect the mechanical motion on the optical laser reflection. An extended version of the Fabry-Perot scheme is used in the membrane in the middle set up in field of optomechanics [30]. For a Michelson interferometer (Figure 1.1(b)), the optical signal from the resonator and a local oscillator (LO) generates an interference signal in the detector. When there is an

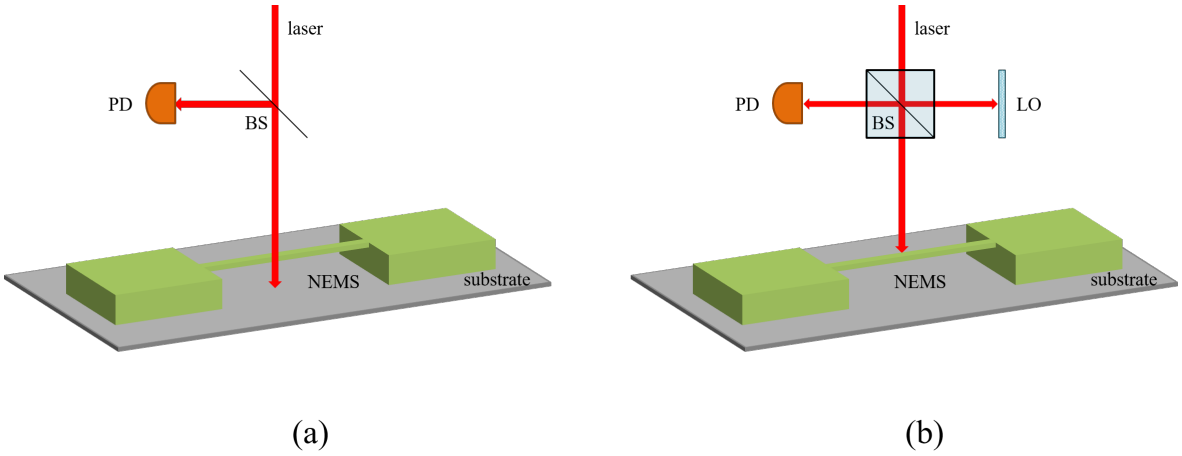


Figure 1.1: Detection of mechanical motion by interferometric technique: (a) uses Fabry-Perot detection scheme where a cavity is formed between the resonator and the substrate and (b) Michelson interferometer, a local oscillator is used to generate an interferometric signal to detect the mechanical motion of the resonator.

out of plane motion of the resonator, a signal related to the displacement of the resonator is detected on the interference pattern. In other kind of optical detection schemes, there is an alternate scheme developed by the group of O.Arcizet [31]. They use a microscope objective with a split photodiode in order to detect the mechanical modes.

## 1.2 Nano-Opto-Electro-Mechanical Systems

Thanks to the integrability of the optical functionalities (cavity,mirrors), it is possible to integrate NEMS/MEMS platforms with optical circuits such as photonic crystal [32] for example in order to design NOEMS devices. Optomechanical systems have found to be quite effective in near quantum limited position read out [33, 34] or the strong back-action effects to cool to its quantum ground state of motion [35].

These NOEMS platforms open up new possibilities where it is possible to realize an interplay between the optic and electronic circuitry. For instance optomechanical devices can be used for shot noise limited detection or back action modification of the mechanical response for MEMS/NEMS sensors. Integrating RF circuit and a system with both optical and mechanical properties gives also opportunity to perform radio frequency to optical conversion via mechanical system [36, 37, 16] and more importantly future application in signal processing [38, 39].

### 1.2.1 State of the art of NEMS/NOEMS devices

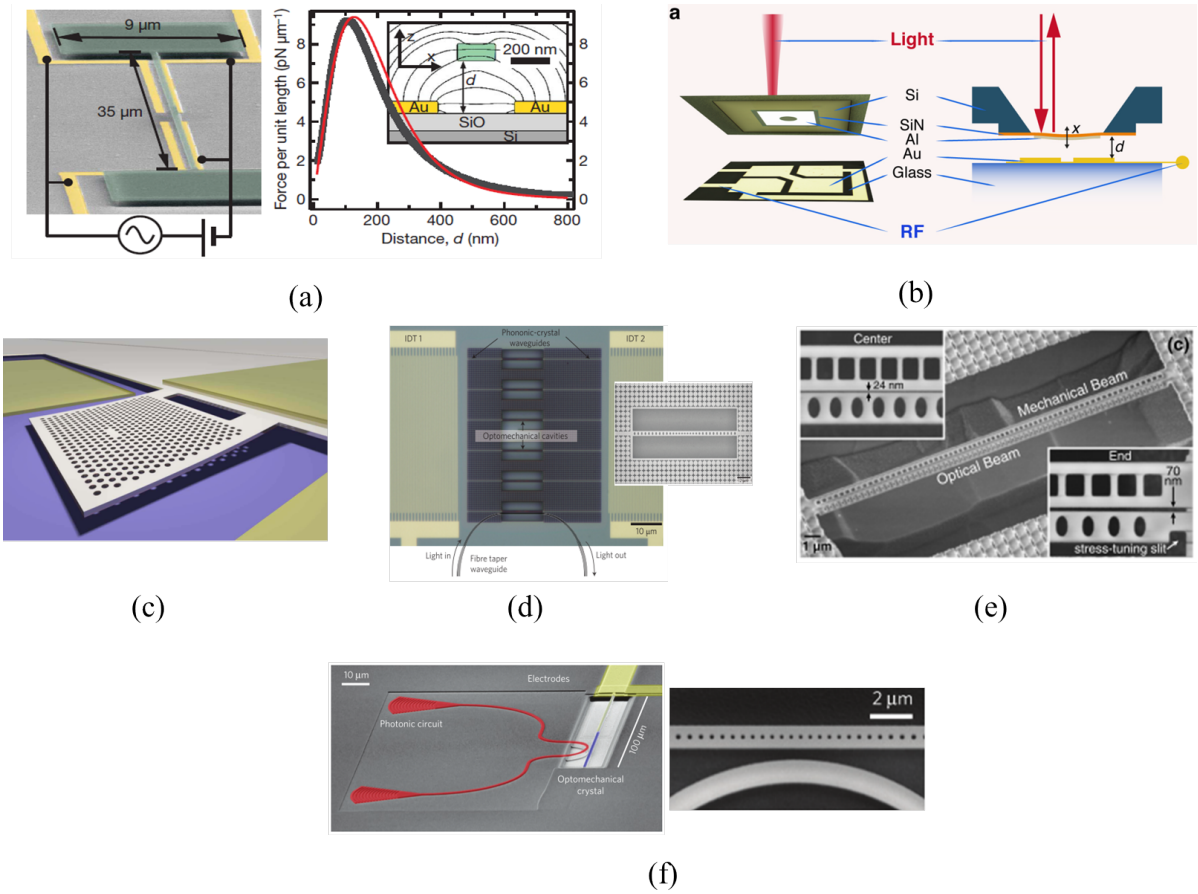


Figure 1.2: (a) Capacitive actuation and detection of a SiN nanobeam [40], (b) capacitive actuation and optical detection of a SiN rectangular membrane realizing microwave to optical conversion [16], (c) electrostatic control of the photonic crystal cavity by application of bias across a p-i-n diode [41] , (d) coupling between radio waves and optical frequency by using 1D GaAs PhC [37], (e) spatially separated photonic and phononic nanobeams separated by a narrow slot providing optomechanical coupling (f) transduction between phonon and photons with strong optomechanical coupling by using a piezoelectric AlN PhC [36].

In past few years there has been a huge development on NOEMS devices actuated by capacitive forces while being probed by optical means. This gives an unique opportunity for microwave to optical frequency conversion. Some of the key results are highlighted in Figure 1.2. The group of E.Weig (Figure 1.2(a)) [40] have successfully demonstrated actuation of a suspended SiN beam by means of capacitive forces. The capacitive force polarizes the material making a force acting on the system which is directly proportional to the amplitude of the a.c. excitation voltage. The eigen-frequency of the system lies in the MHz regime. They were able to show that the eigen-frequency of such systems can be modulated by an external

d.c. voltage. However the detection scheme were completely electrical. The next example is shown in Figure 1.2(b), this system was realized by the group of E.S.Polzik [16]. Here they successfully transduce radio to optical frequency via an intermediate SiN rectangular membrane. The SiN membrane is suspended over electrodes which capacitively actuate it in a sub-MHz frequency regime. The detection is completely optical utilizing the reflectivity of the SiN membrane. They are able to achieve an electromechanical coupling factor of $10.3kV/m$ with such system. The position of the membrane here is controlled via an external piezo.

Another kind of actuation scheme proposed by the group of A.Fiore is shown in Figure 1.2(c). They showed that it is possible to design electromechanically tunable photonic crystal cavities based on double semiconductor slabs [41]. Tuning is achieved by application of a reverse bias on a p-i-n diode. Due to this bias an electrostatic force is generated between the double membranes, resulting in a displacement of the upper slab. The tuning can be reversed by reducing the bias due to restoring elastic forces.

On the other hand Balram et al. [37] used 1D PhC cavity in order to perform coupling between optical and radio waves (Figure 1.2(d)). The used optomechanical cavity supports co-localization of $1550nm$ photons and $2.4GHz$ phonons. The phonons are generated by driving the optomechanical beam via Surface Acoustic Wave (SAW) generated by interdigitated electrodes. The generation utilizes the piezoelectric properties of GaAs, while on the other hand coupling between mechanics and optics utilizes the photonic properties of the PhC. In the same group Grutter et al. [42] realized a NOEMS platform where two nanobeam pairs patterned with photonic and phononic crystals coupled via optomechanical interaction (Figure 1.2(e)).

Similar transduction scheme has been utilized by the group of Cleland [36], here they utilize piezoelectric optomechanical crystal beam to interface optical phonon and microwave signal. The system consists of a suspended AlN beam patterned with photonic crystal (Figure 1.2(f)) designed to support localized phonon modes at $4GHz$ and co-localized optical mode at $196THz$ with strong optomechanical coupling. The device is fully compatible with superconducting quantum circuits, potentially enabling microwave to optical quantum state transfer.

### 1.2.2 Photonic crystals in optomechanics

Among the NOEMS devices presently investigated, a large part of them rely on photonic crystals. These systems are already known for their optical properties. However their low mass allows to use them as mechanical resonators at the same time. Moreover, their planar geometry allows integration of electrical, optical, mechanical components on the same chip. These devices have already been of great interest in the field of optomechanics. In this section therefore we discuss in brief about the state of the art of such systems in field of optomechanics.

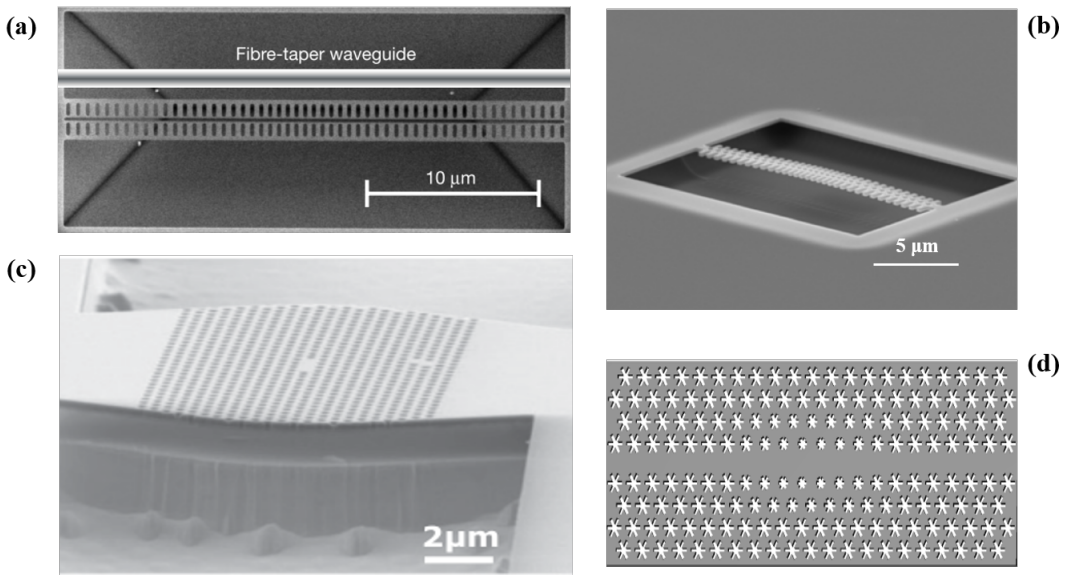


Figure 1.3: Fabricated photonic and phoXonic (photonic and phononic) crystals with 1D and 2D structure (a) 'Zipper cavity' fabricated by two 1D PhC doubly clamped nanobeams [32], (b) 1D phoXonic crystal [43], (c) 2D photonic crystal clamped on both sides [44], (d) 2D phoXonic crystal [45].

Photonic crystals (a.k.a. PhC) are dielectric structures with periodic cylindrical holes engraved in it. These periodic holes generate an optical band gap. The band gap is determined by the hole diameter, their period and thickness of the structure. These cavities can be exploited to implement optical cavities of diffraction-limited volumes. Such PhC can also be designed in order to co-localize optical and mechanical modes, enhancing the optomechanical coupling. Due to their optical properties and low masses, these devices are very interesting candidates for optomechanics. Various kinds of structures from 1-D to 2-D PhC structures are used in the field of optomechanics.

The low mass of 1D-PhC increases the frequency of operation but at the same time these devices come with high Q-factors. The mechanical modes are usually localized at the center of the beam, which decreases the losses due to supports (phonon tunneling for example). These devices at the same time could be coupled to optical field while enhancing the optomechancial coupling strength. The 'zipper cavity' designed by Eichenfield[46] et al. is a combination of two 1D-PhC nanobeams [32] creating a phononic band gap alongside with existing photonic one. In addition to that, a single-beam design of 1D structure, named phoXonic crystal [46], was proposed and implemented experimentally [43].

Another and more usual form of PhC membranes are 2D shaped membranes, suspended by bridges or clamped fully to the substrate. The bridges helps to reduce losses due to supports hence increases the overall quality factor of the system [30]. These structures are sometimes known as the PhC slabs. Cylindrical holes are pattern in 2D manner with a square or a triangular lattice structure. As in 1D devices, a defect can generate cavity within the photonic crystal thereby increasing the optomechanical interaction. These membranes

are able to generate mechanical modes in MHz frequency range by virtue of its drum like mode or at GHz range due to the localized modes [44]. The 2D PhC slabs can not only embed optical cavities of diffraction limited volumes but also can act as reflectors operating at normal incidence. The 2D PhC slabs can not only embed optical cavities of diffraction limited volumes but also can act as reflectors operating at normal incidence. The group of A.Heidmann have worked extensively with such reflective membranes : Makles et al. [47] presented optimization of an optomechanical device based on suspended InP membrane patterned with 2D-near wavelength grating based on 2D PhC geometry. The membrane is used to form a compact microcavity involving the suspended nanomembrane as an end mirror. Whereas the group of J.Lawall developed silicon nitride membrane patterned as a subwavelength grating to demonstrate membrane in the middle optomechanical set-up [48]. With a grating reflectivity of 99.8%, they demonstrated measurements of transmission and refection spectra showing an avoided crossing where the two sub-cavities simultaneously come into resonance, with a frequency splitting of 54 MHz.

### 1.2.3 Concept of the device utilized during this work

In order to design a NOEMS platform, which would include electrical, mechanical and optical platform we decided to use a 2D suspended PhC membrane as the mechanical oscillator and an optical reflector. Since InP has some dielectric properties we decided to utilize this for electrical actuation. The fabricated device is shown in Figure 1.5(a), the system consists of a suspended PhC membrane attached to the substrate by four bridges. The membrane is suspended over interdigitated electrodes used to capacitively actuate the membrane. InP is chosen mainly because of its well known optical properties, as it works really well as an optical reflector. Apart from that the system has dielectric properties which makes it easier to be excited by capacitive actuation.

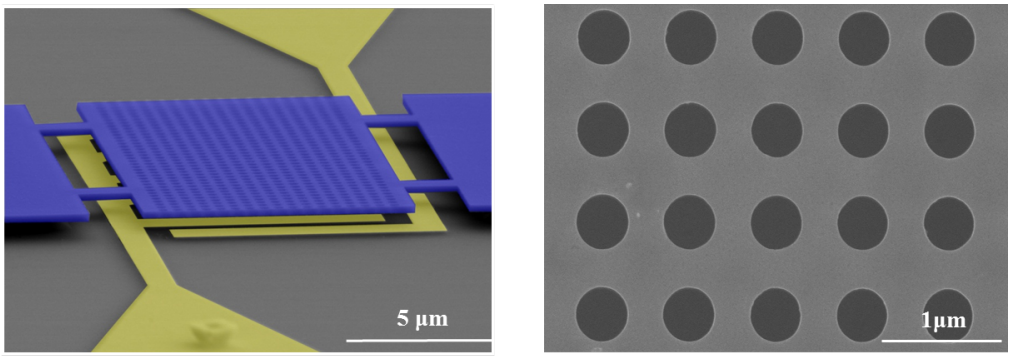


Figure 1.4: (a) Scanning electron micrograph fabricated of electrode-membrane system (b) a zoomed view of the etched cylindrical holes in the PhC membrane.

Voltage is applied externally between these two electrodes and the field lines penetrate and polarize the InP membrane. This induces a capacitive force on the membrane which is

a function of frequency at the same time as well. Therefore when the actuation frequency is close to one of the membrane eigen-frequency, there is a major enhancement of the oscillation amplitude of the membrane. In order to detect the mechanical motion of the membrane, we utilize the optical properties of the InP membrane. A Michelson interferometer like set-up is used to detect the motion of the membrane.

The probed mechanical mode of the membrane called the 'drum mode', corresponds to motion of the entire membrane hence the name. We mainly probe the first order mode of the membrane which has the highest overlap with the incident optical field. This mode due to its high vibrational amplitude also is prone to exhibit nonlinearity. Hence we performed some nonlinear dynamical study on this membrane which is discussed in details on the course of this thesis.

## 1.3 Nonlinear dynamics in NEMS/NOEMS

Micro or nano-scale devices exhibit nonlinear behaviors at a relatively small excitation thanks to their small size. Understanding of nonlinear behavior is important in order to avoid it when it is unwanted and use it where it is needed. Recent advancement in nanofabrication have allowed fabrication of such devices which could be driven into nonlinear regime. These devices usually operates at the RF frequency due to their small size and have relatively high Q-factors ranging from $10^2 - 10^5$. At the beginning of this century, Erbe et al. demonstrated nonlinearity in nanomechanical systems [49]. They presented a methodology to machine nanomechanical resonators out of silicon on insulator wafers having eigen-frequencies in MHz regime. They demonstrated higher order mechanical mixing at radio frequencies, using these nonlinear devices. Furthermore Scheible et al. [50] showed that it was possible to push these systems from linear to nonlinear and then to chaotic regime. Most of these nanomechanical systems are modeled by the famous Duffing equation. Blick et al. [51] in their comprehensive review of NEMS, pointed out that the Duffing equation is best suited to study nanoresonators in the nonlinear regime. One of the most notable groups in the field of nanomechanics is the group of Roukes in Caltech; their work involve from implementing nanoelectromechanical systems [52] to tune the nonlinearity of these devices [53], to sensitive mass detection [14], parametric amplification [54] and recently phase synchronization between oscillators [55].

These devices open new fields of applications including noise reduction, operation in low dissipation regime or amplification of a weak signal. Several coupled resonators can be designed to be operated collectively to reduce the noise level [56]. Reduction of dissipation can be done by operating these systems in the self-oscillation regime [40]. While amplification of a signal in a noisy background can be done by using stochastic [57] or vibrational resonance [58]. During the PhD the main objective was to study two different nonlinear behavior of our NOEMS platform; the first one is called sub/super-harmonic resonance of a nonlinear system while the second one is called as the stochastic resonance. We will discuss briefly about the basic concepts of these experiments. The concept and experimental results are discussed in details in Chapter 4 and Chapter 5.

### 1.3.1 Sub/super-harmonic resonance

A usual manner to excite nonlinear systems is by resonant excitation. However, nonlinear systems may respond to excitation at its sub or super-harmonics as well. As a result they display a resonant tongue like behavior for different harmonics. These excitation schemes also fall under the parametric excitation where a weak signal can be amplified by modulating the spring constant of the system being excited at it harmonics. The idea of sub/super-harmonic resonance has been proposed by Zounes and Rand [59]. The phenomenon in nanomechanical systems has been explored by Shim et al. [60] and also idea of such excitation has been utilized by Mahboob et al. to design parametric resonator array [39]. However phase dynamics of such systems under this regime has not been explored in details, more on this is discussed in Chapter 4.

### 1.3.2 Stochastic resonance

Noise in systems in general are unwanted phenomenon, however Gammaitoni et al. [61] showed that in a nonlinear system this noise can be used in order to amplify weak signals, this is called stochastic resonance. Although in general stochastic resonance applies to mainly white noise, although noises with $1/f^{\alpha}$ spectra also can be used to realize such resonance. This technique therefore can be very useful in order to detect a low frequency signal in a noisy background. Stochastic resonance is observed not only in nanomechanical systems but also has been observed in other systems for example in VCSEL lasers [62]. This resonance has been mainly demonstrated with amplitude noise in nanomechanical systems. Barbay et al. [62] demonstrated that such resonances can be observed with polarization in VCSEL lasers. However we have demonstrated (Chapter 5) that for nanomechanical systems such effects can be observed in phase as well. Till date most of the nanomechanical systems explore such resonance with amplitude noise, Badzey et al. [57] demonstrated such resonance for a nanomechanical beam while Mueller et al. demonstrated for a torsional beam [63]. However such phase stochastic resonance should exist for these nanomechanical systems for phase noise and modulation too, this phenomenon has been explored in Chapter 5.

## 1.4 Organization of the manuscript

Chapter 2 gives a detailed discussion on the detection scheme and basic mechanical measurements on suspended PhC membrane. The optical scheme used in the experiment is called Balanced Homodyne Detection or simply BHD. This is a modified version a simple Michelson interferometer, to reduce the noise level and increase sensitivity. Here we talk in brief about the actuation scheme with an external piezo of fully clamped membranes. As the actuation frequency is swept, mechanical modes are identified with a rise in the detected response. We calculate some fundamental parameters from these experiments, including variation of the eigen-frequency and quality factor with bridge lengths. However in order to efficiently actuate the membrane we go forward to integrated actuation, which is discussed in the next chapter.

In Chapter 3 we begin our discussion with design and optimization of the integrated electrode and membrane platform. This includes optimization of the electromechanical coupling factor, which is mainly governed by the electrode-membrane separation. Then we move forward to the description of the electrode-membrane system fabrication. Here we highlight all the necessary steps of this hybrid heterogeneous integration process of III-V semiconductor with silicon. This includes electron beam lithography, various etching techniques, substrate bonding technique, critical point drying for example. In the context of this we show that how we can control the electrode-membrane separation which ultimately governs the electromechanical coupling factor. Then we discuss the integrated actuation of these membrane in the linear regime. The actuating voltage as it will be shown, has two terms: the first one is ac actuation voltage which is actually responsible for the frequency dependent response of the mechanical oscillator. The second term is a dc term, which provides external stress on the system. We discuss in details influence of both these terms on the nanomechanical membrane. We will see that with this dc excitation, it is possible to tune the eigen-frequency of this membrane. In this chapter we also show the process of calibration of the membrane displacement and from there we were able to measure the electromechanical coupling coefficient.

From Chapter 4 we begin our discussion on nonlinear dynamics. We will show that it is possible to force this nanomechanical membrane into nonlinear regime with external excitation whenever it crosses a certain threshold. Under such a regime the system has access to two stable states instead of just one, this is referred as the bistability. We show that such a bistability exists in amplitude as well as in phase. From here we explore what is known as the sub and super-harmonic excitation regime. In this regime unlike resonant excitation, the nanomechanical system is excited at the sub or super-harmonic of its natural resonance frequency. Therefore this is also sometimes referred as the parametric excitation, as the response is generated by modulating one of its spring constant instead of direct resonant excitation. This phenomenon therefore is a direct consequence of the existing nonlinearity in the system. We go ahead and perform experiments called parametric amplification, where a weak signal is amplified under the sub-harmonic resonance regime. We also discuss about the influence of parametric excitation on the eigen-frequency of the system under such a regime.

In Chapter 5, while discussing still about nonlinear dynamics we move to another kind of experiments called stochastic resonance, the resonant amplification of a weak signal by application of noise. We first discuss the main parameters required in order to observe such resonance. With these parameters we were then able to firstly modulate the double well potential with pure noise or modulation. Finally using all these optimized data we were then able to perform stochastic resonance with phase and amplitude noise.

Chapter 6 is dedicated to conclusions and perspectives. In this chapter we highlight the main results obtained in each chapter and propose future related experiments on these topics. We also propose some new hybrid devices that could be fabricated in order to realize a true electro-opto-mechanical coupling.

# Chapter 2

# Optical detection and external actuation of the NOEMS platform

## 2.1 Introduction

This chapter is dedicated to the detection of the mechanical resonances of our nano-mechanical resonator along with characterization of some parameters like frequency, amplitude, phase, quality factor. The resonator consists of a suspended III-V semiconductor InP membrane, pierced by a two dimensional photonic crystal (or simply PhC) which works as a mirror for normal optical incidence. There are various ways to detect mechanical motion at micro-nano scale, as for example by electrical means which involve capacitive [64]-[65], piezoelectric [66]-[67], electrostatic [68],[69] or resonant frequency shift methods [70]. Optical means can be used in order to detect the mechanical modes [16]-[71]; we decided to choose the later since our system has optical properties thanks to the photonic crystal. The advantage of using such platform is that at the same time the system can act as both mechanical and optical resonator. This shall open the way to the implementation of a true opto-electro-mechanical coupling using such a platform. However, during my thesis I have mainly focused on the mechanical properties of such a resonator although optical properties were highly utilized in order to enhance the detection efficiency.

At the beginning of this chapter we start by discussing about the detection scheme of the mechanical modes of such a platform using Balanced Homodyne Detection method [72]-[73]. After that we will focus on some theoretical discussion and FEM simulations on how the mechanical mode profiles appear and also about their natural resonance. And finally we will discuss about some preliminary actuation scheme and detection of the mechanical modes of the NOEMS resonator.

## 2.2 Optical detection and calibration

The entire optical set-up could be segregated into two main parts; the first part is for the detection of the mechanical modes by interferometric techniques. The other part being

used for calibration which is necessary in order to determine the electromechanical coupling between the electrical actuation and the mechanical motion of the membrane detected by optical means. The calibration procedure is discussed in the next chapter. In this section we will focus on the first part and introduce the technique called Balanced Homodyne Detection or simply BHD used to detect the mechanical modes of the membranes.

Let us first introduce the basic principle of detection and then we describe how this scheme is implemented in our set up in order to perform the measurements. The heart of the optical set-up is basically an interferometer which is famously known as the Michelson interferometer. The Michelson interferometer is a system that produces interference between two different optical beams. The scheme of this process is displayed in Figure 2.1(a); an optical beam is generated from a source which is split into two beams with a beam splitter and sent to two different arms of different lengths $L_1$ and $L_2$. At the end of this two paths are two mirrors $M_1$ and $M_2$. Light reflected from these mirrors recombines and finally produces an interference signal at the detector. If we define the path difference between $L_1$ and $L_2$ to be $\Delta L$, the phase difference can be written as:

$$\Delta\phi = \frac{2\pi}{\lambda + \Delta\lambda}\Delta L \tag{2.1}$$

In case of a basic Michelson interferometer, if $\Delta L$ and $\Delta\lambda$ is fixed, the phase difference $\Delta\phi$ is fixed as well. In this case the interference pattern is static. Fluctuation of wavelength $\Delta\lambda$ results in a fluctuation in $\Delta\phi$, this is taken care of by using a frequency stabilized laser with $\Delta\lambda \simeq 0$. Now if there is a fluctuation in path difference $\delta(\Delta L)$, there would be an equivalent fluctuation in the phase difference $\delta(\Delta\phi)$. This fluctuation in phase will directly reflect on the detected intensity and will therefore be directly related to the fluctuation in the displacement $\delta(\Delta L)$. Also the frequency of phase fluctuation is related to the fluctuation of displacement $\delta(\Delta L)$. Figure 2.1(b) shows scheme of detection with a single photodiode; the photodiode converts incident photons into current ($i_d(t)$), which then can be detected in an oscilloscope.

The scheme of a basic Balanced Homodyne Detector or commonly known as BHD is shown in Figure 2.1(c). It is an extremely useful technique in order to measure amplitude and phase quadratures of the incoming signal. The detected signal with power $I_S(t)$ is mixed with a local oscillator signal of power $I_L(t)$ by means of a beam splitter. The split signal is then fed to two photodetectors $D_1$ and $D_2$ which generate equivalent photocurrents $i_1(t)$ and $i_2(t)$ each of which involves a beat signal and common noise.

The optical signal intensity $I_S$ and the local oscillator intensity $I_L$ can be written as:

$$I_S(t) = I_S + \delta X_S(t) + i\delta P_S(t) \tag{2.2}$$

and

$$I_L(t) = [I_L + \delta X_L(t) + i\delta P_L(t)]e^{i\phi} \tag{2.3}$$

where, $I_L$ and $I_S$ are time independent constants and $\delta X_S(t)$ and $\delta P_S(t)$ ($\delta X_L(t)$ and $\delta P_L(t)$) are the fluctuations in the amplitude and phase quadratures of the signal (LO). The

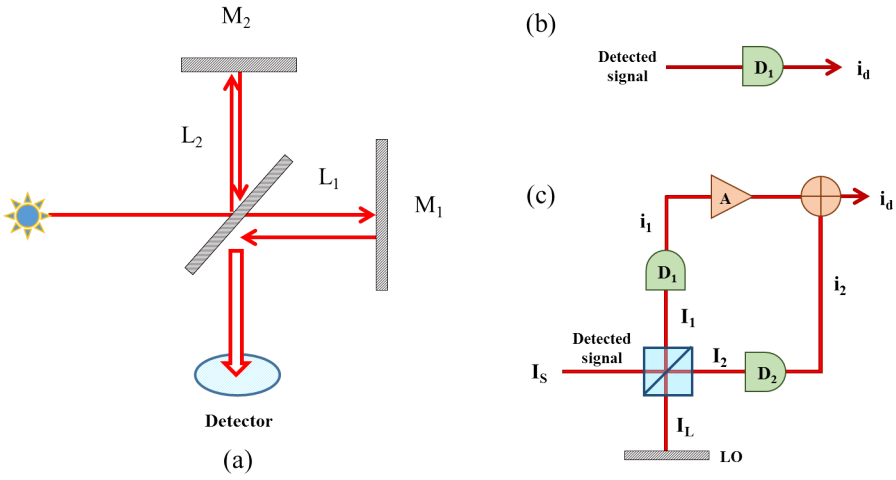


Figure 2.1: (a) A simple Michelson interferoemeter, (b) single detector detection scheme, (c) detection with a Balanced Homodyne Detector.

terms considered here are merely spatial distribution and fast oscillating term $e^{i\omega t}$ is neglected here. The term $\phi$ is the relative phase difference between the signal and the LO field. Under assumption that the LO field is much stronger than the signal i.e. $I_L \gg I_S$ one can write [74]:

$$I_1 = \frac{1}{\sqrt{2}}[I_L + I_S] \tag{2.4}$$

and

$$I_2 = \frac{1}{\sqrt{2}}[I_L - I_S] \tag{2.5}$$

Thus the photocurrents $i_1(t)$ and $i_2(t)$ in detectors $D_1$ and $D_2$ can be written as [74]:

$$i_1(t) \propto \frac{1}{2}[|I_L|^2 + I_L I_S^* + I_L^* I_S + |I_S|^2] \tag{2.6}$$

$$i_2(t) \propto \frac{1}{2}[|I_L|^2 - I_L I_S^* - I_L^* I_S + |I_S|^2] \tag{2.7}$$

Thus the current on the output of the difference amplifier can be written as:

$$i_d(t) = i_1(t) - i_2(t) \propto 2I_L[(I_S + \delta X_S(t))cos\phi + \delta P_S(t)sin\phi] \tag{2.8}$$

$$< i_d^2(t) > \sim 4I_L^2(\delta X_S^2 cos^2\phi + \delta P_S^2 sin^2\phi) \tag{2.9}$$

Equation (2.9) gives the variance of the output current from the difference amplifier. The equation thus shows us that it is now possible to measure the amplitude and phase

quadratures of the signals by means of BHD. Also depending on the value of $\phi$ we can arrive at two separate conditions:

$$< i_d(t)^2 > \propto \begin{cases} 4I_L^2 \delta X_S^2 \quad for\ \phi = 0; \\ 4I_L^2 \delta P_S^2 \quad for\ \phi = \pi/2; \end{cases} \tag{2.10}$$

As it can be seen from equation (2.10) the detected signal in both quadratures is proportional to the LO intensity and thus for a efficient detection of a weak signal field, it is desirable to have a stronger LO field. Thus effect of the BHD is to cancel the common noise that would appear from the local oscillator or any other common source and at the same time providing higher gain for the detected weak signal. However the calculations shown before have been performed by considering the beam splitter to be a perfect 50/50, which unfortunately is not the case for laboratory environment. This requires an additional amplifier A on one of the detector path (for example for $D_1$ in Figure 2.1) in order to compensate for this effect.

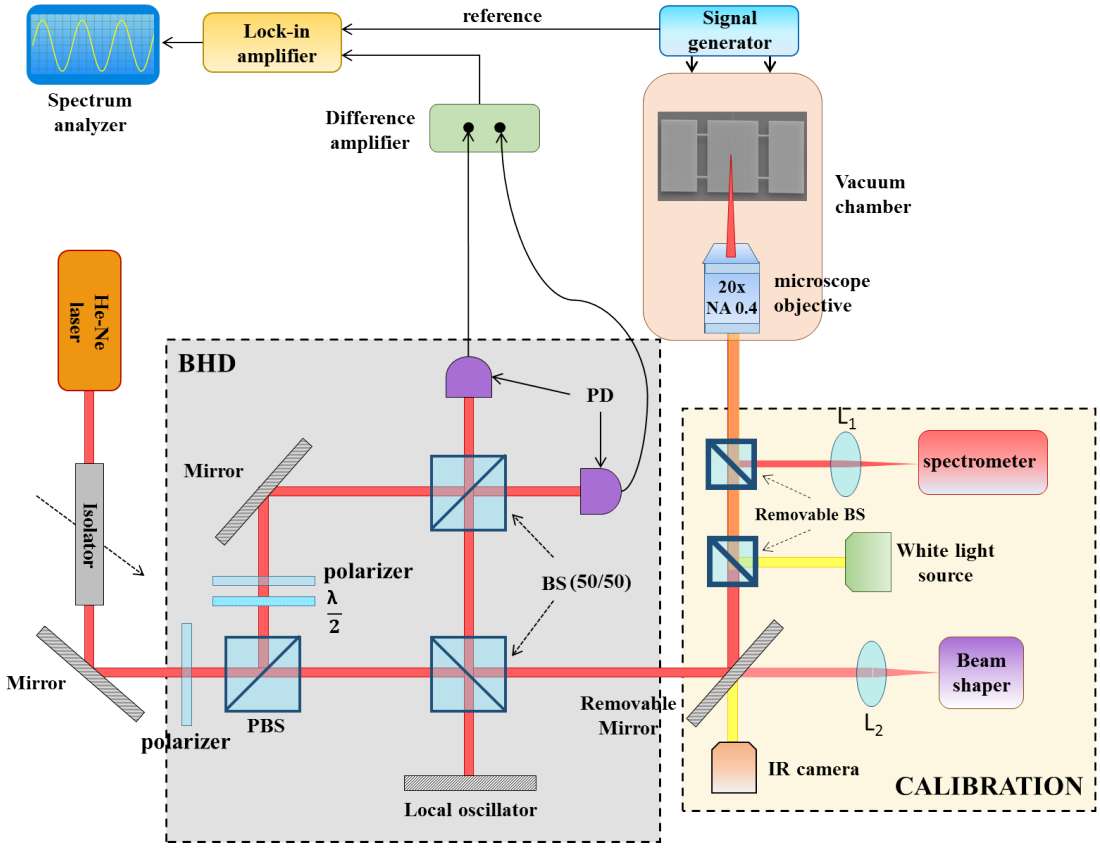


Figure 2.2: Optical detection scheme: Balanced Homodyne Detection.

This scheme was implemented in our system in order to detect the mechanical motion of the PhC membrane. The membrane here acts as a mirror in one arm of the interferometer while the local oscillator is a fixed mirror, thereby any small displacement at the membrane

end will produce an interference at the output. The implemented scheme is displayed in Figure 2.2. A laser signal at around $632nm$ is extracted from a Spectra Physics He-Ne source (in frequency stabilized mode) which is at first passed though an optical isolator in order to prevent reflection from other parts of the set-up. This optical signal is then separated into two parts; one is directed towards the sample and the other one is directed towards the detectors. The splitting of the beam is performed by a Polarizing Beam Splitter (PBS) and the fraction of splitting is controlled by placing a polarizer in front of the PBS. This path gives an extra DC offset to the detected optical beam in order to have a clear detection of the mechanical modes. This path consists of a $\frac{\lambda}{2}$ plate and a polarizer to control the polarization and intensity of the offset. This path is truly crucial in order to obtain a smooth spectra of the mechanical mode. The other optical arm is directed towards the sample which is inside a vacuum chamber. The position of the sample can be controlled externally by virtue of some piezo positioners (Picomotor 8752). A microscope objective is used to focus the laser on the PhC membrane, the objective is 20x with a NA of 0.4 (Mitutoyo) which creates a beam waist of about $0.6\mu m$ on the membrane. At the end of the optical paths, the beams are collected by two different photodetectors (Thorlabs APD 110A/M) with quantum efficiency of $\eta_1$ and $\eta_2$ and finally are fed to a difference amplifier (New Focus LB1005) which subtracts this two electrical signals. The detectors have a quantum efficiency of about 0.4 at the operating laser wavelength. The subtraction gives an enhancement of the detected signals and a reduction of the noise level. The difference amplifier here also can act as a gain medium in one of the paths in order to compensate for the beam splitter effect discussed before.

Another important part of the set-up is the strategy for actuation of the PhC membranes which is purely electrical. The sample mounted on a piezo-electrical stack is driven by an external signal generator which can go up to $50MHz$ and is synchronized with a lock-in amplifier (HF2LI) which demodulates the detected signal at the actuation frequency with the chosen filter parameters (time constant, sampling rate etc). The optimization of the filter parameters are crucial in order to produce a substantially smooth and reliable response. The optimization was done by performing acquisition for various time constants and sampling rates. The value of the chosen time constant and sampling rate were $200\mu s$ and $10^3 samples/sec$ respectively. The sample is placed inside a vacuum chamber with automated mounts which can be controlled via a Lab-View program from outside. The mounts are steppers which are known as picomotors able to translate as small as $30nm$. However the speed of the stepper can be controlled from outside. The vacuum is controlled by one Trivac primary vacuum pump and another Oerlikon turbo pump. The primary pump can go down to about $10^{-1} mbar$ and when the turbo pump takes control, a vacuum of about $10^{-4} mbar$ can be reached. All the experiments discussed from now on were performed under identical vacuum conditions.

## 2.3 Actuation of NOEMS platform

After introducing the detection scheme we now move towards the actuation of the NOEMS platform. We begin discussion with the modal analysis of a rectangular fully clamped un-

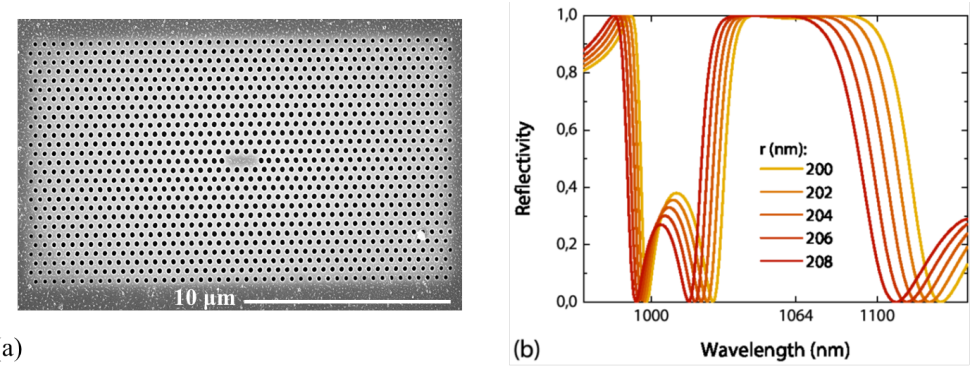


Figure 2.3: (a) Scanning electron micrograph of a PhC mirror, (b) simulated reflectivity profile with the optical wavelength for various PhC hole radius, ranging from $200nm$ to $208nm$.

pierced membrane. The rectangular membrane is a InP photonic crystal membrane which acts as a mechanical resonator and also has optical properties [75][44]. The first step before designing the membrane structures or to perform any experiment was to fully comprehend how different mechanical modes would look like and depending on that we could finally address the actuation scheme. In the first section we will introduce some theoretical modal analysis of a rectangular membrane. This analysis to retrieve the mechanical modes will then be extended, by FEM simulation to the exact structure we will work with. That is a suspended rectangular membrane anchored to the substrate by four bridges still unpierced by PhC as we are not interested in the optical properties but only in the mechanical properties. The theoretical discussion and these simulations give insight on the eigen-modes and the eigen-frequencies of the structure, parameters that will be used in the final section when measuring the mechanical response of the samples.

### 2.3.1 Optical properties of the PhC membrane

The suspended membrane is a rectangular 2D photonic crystal membrane. The photonic crystal is created by etching cylindrical holes inside a 2D membrane (Figure 2.3(a)). The membranes have a dimensions of $10 \times 20\mu m^2$ with thickness around $260nm$. For our case the holes form a square lattice of $196nm$ radius having a period of $725nm$. The hole arrangement, geometries and the slab thickness are chosen in such a way so that the PhC membrane acts as a reflector for normal incidence. FDTD was utilized in order to simulate the reflectivity of this PhC structure with the incident wavelength and the spectra is shown in Figure 2.3(b). We calculated the reflectivity for various hole radius ranging from $r = 200nm$ to $r = 208nm$. The PhC structure showed to have highest reflectivity for a wavelength around $1064nm$, wavelength of emission from Nd-YAG lasers. Although we found that for He-Ne laser i.e. for a wavelength around $633nm$ (laser wavelength used in the experiment) the reflectivity is still

relatively high (about 50%). [1]

### 2.3.2 Modal analysis of a rectangular membrane

Firstly we introduce some basic theoretical background on the mechanical modal shapes of a rectangular membrane. Our system as it was mentioned before consists of a suspended photonic crystal membrane. For simplicity we will consider a simple rectangular 2D membrane which is fully clamped at four sides and solve the wave equation in order to determine the mechanical modes of the membrane. The rectangular membrane has a fully clamped structure with length and width of $a$ and $b$ respectively as shown in Figure 2.4.

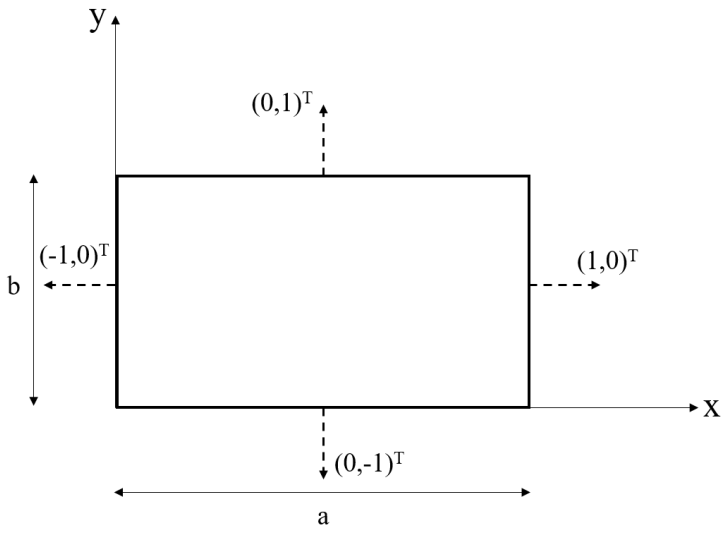


Figure 2.4: A rectangular 2D membrane in Cartesian coordinates being fixed on four sides.

The continuity condition imposes that:

$$w(x,0,t)=0,\quad w(x,b,t)=0,\quad w(0,y,t)=0,\quad w(a,y,t)=0 \tag{2.11}$$

where $w(x,y,t)$ is the transverse displacement of the membrane.
Let's at this stage assume a test solution:

$$w(x,y,t)=W(x,y)exp(j\Omega t) \tag{2.12}$$

where $W(x,y)$ is the eigen-function, $\Omega$ is the angular eigen-frequency. A system under this configuration can described by Helmholtz equation of motion:

$$\nabla^2 W+\frac{\Omega^2}{c^2}W=0\ (c\,being\,the\,wave\,velocity\,in\,a\,given\,material) \tag{2.13}$$

[1] The membranes have indeed been optimized for this wavelength, in the context of our group's collaboration with Laboratoire Kastler Brossel.

Using the modified boundary conditions:

$$W(x,0) = 0, \;\; W(x,b) = 0, \;\; W(0,y) = 0, \;\; W(a,y) = 0 \tag{2.14}$$

Let's use a test solution of the form:

$$W(x,y) = Aexp\{j(k_x x + k_y y)\} \tag{2.15}$$

where $k_x$ and $k_y$ are the wavevectors corresponding to $x$ and $y$ axis respectively. Substituting equation (2.15) in equation (2.13) we can determine the trivial solution as:

$$k_x^2 + k_y^2 = \frac{\Omega^2}{c^2} \tag{2.16}$$

Let us now define $k_x = \pm\alpha$ & $k_y = \pm\beta$ and one can write:

$$\alpha^2 + \beta^2 = \frac{\Omega^2}{c^2} \tag{2.17}$$

and we can redefine solution of $W(x,y)$ as:

$$\begin{aligned} W(x,y) &= (A_1 exp(j\alpha x) + A_2 exp(-j\alpha x)) * (A_3 exp(j\beta y) + A_4 exp(-j\beta y)) \\ &= B_1 cos(\alpha x)cos(\beta y) + B_2 cos(\alpha x)sin(\beta y) + B_3 sin(\alpha x)cos(\beta y) + B_4 sin(\alpha x)sin(\beta y) \end{aligned}$$

Using boundary conditions $W(x,0) = 0$ and $W(0,y) = 0$ we can show:

$$B_1 cos(\alpha x) + B_3 sin(\alpha x) = 0 \tag{2.18}$$

$$and, \;\; B_1 cos(\beta y) + B_2 sin(\beta y) = 0 \tag{2.19}$$

Now by knowing $W(0,0) = 0$ we can conclude:

$$i.e. \;\; B_1 = B_2 = B_3 = 0 \tag{2.20}$$

$$W(x,y) = B_4 sin(\alpha x)sin(\beta y) \tag{2.21}$$

Using boundary conditions $W(a,y) = W(x,b) = 0$:

$$B_4 sin(\alpha a)sin(\beta y) = 0 \;\; and \;\; B_4 sin(\alpha x)sin(\beta b) = 0 \tag{2.22}$$

$$i.e. \;\; \alpha = \frac{m\pi}{a} \; and \; \beta = \frac{n\pi}{b} \tag{2.23}$$

Substituting these values of $\alpha$ and $\beta$ in equation (2.17) we can write:

$$(\frac{m\pi}{a})^2 + (\frac{n\pi}{b})^2 = \frac{\Omega^2}{c^2} \tag{2.24}$$

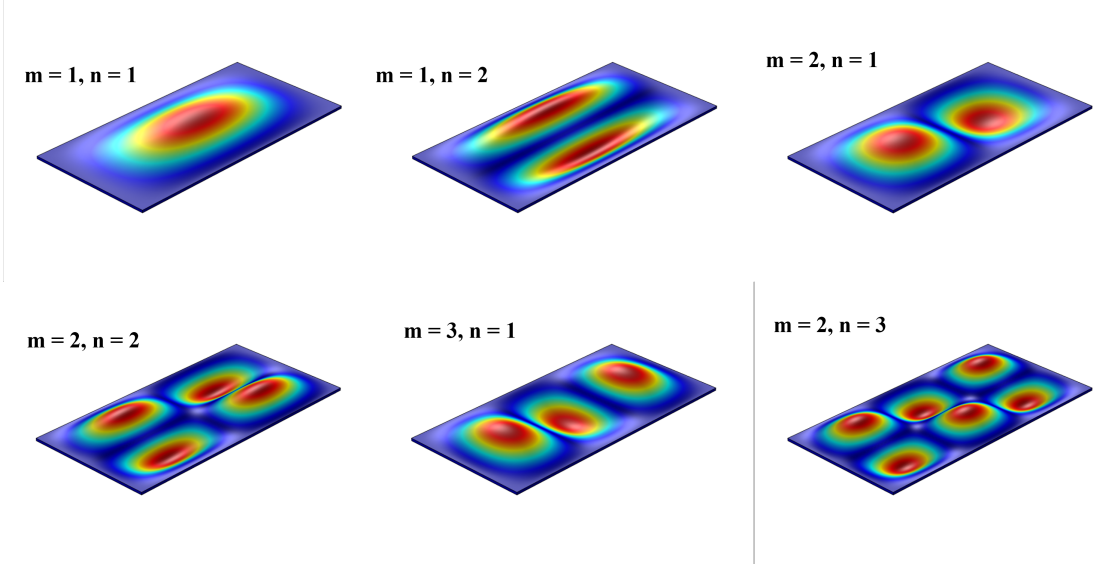


Figure 2.5: First six modes of the rectangular membrane with fixed boundaries.

$$i.e.\ \ \Omega_{mn} = \pi c\sqrt{\frac{m^2}{a^2} + \frac{n^2}{b^2}} \tag{2.25}$$

And the solution of the wave equation can be written as:

$$W(x,y) = B_4 sin(\frac{m\pi x}{a}) sin(\frac{n\pi y}{b}) \tag{2.26}$$

This gives the angular eigen-frequency of the $(m,n)$ mode. However the angular frequency as it can be seen from the equation is not integral multiple of the fundamental frequency (as in the case of 1D string). Determination of the normalization coefficient $B_4$ can be done by:

$$< W^2(x,y) >= 1 \tag{2.27}$$

Using equation (2.28) on equation (2.29) we can write:

$$\int_0^a \int_0^b B_4^2 sin^2(\frac{m\pi x}{a}) sin^2(\frac{n\pi y}{b}) dxdy = 1 \tag{2.28}$$

$$i.e.\ \ B_4 = \sqrt{\frac{4}{ab}} \tag{2.29}$$

Thus the final solution of the wave equation becomes:

$$W(x,y) = \sqrt{\frac{4}{ab}} sin(\frac{m\pi x}{a}) sin(\frac{n\pi y}{b}) \tag{2.30}$$

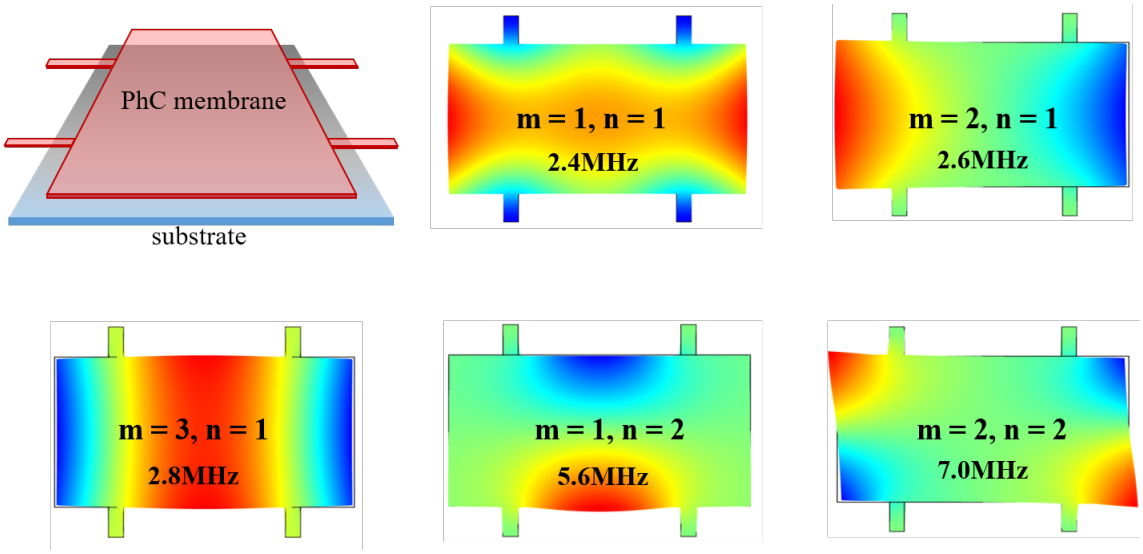


Figure 2.6: Suspended photonic crystal membrane structure with four bridges and the corresponding eigen-modes. Here red color exhibits out of plane vertical displacement while blue color indicates vertical displacement on the other direction.

We can now also check the orthogonality of the mechanical modes, so let us consider two separate modes (m,n) and (p,q):

$$< W^{mn}(x,y), W^{pq}(x,y) >= \int_0^a \int_0^b \frac{4}{ab} sin(\frac{m\pi x}{a}) sin(\frac{n\pi y}{b}) sin(\frac{p\pi x}{a}) sin(\frac{q\pi y}{b}) dxdy \tag{2.31}$$

$$= \delta_{mp}\delta_{nq} \tag{2.32}$$

Thus finally the general solution of the vibrational modes of the rectangular membrane can be written as:

$$w(x,y,t) = \sum_{m=1}^{\infty}\sum_{n=1}^{\infty} sin(\frac{m\pi x}{a}) sin(\frac{n\pi y}{b})[C_{1(mn)} cos(\Omega_{mn} t) + C_{2(mn)} sin(\Omega_{mn} t)] \tag{2.33}$$

### 2.3.3 FEM simulation of the NOEMS platform

We previously discussed the mechanical resonance of a fully clamped membrane. Yet in our experiments, we use membranes which are not exactly fully clamped. In fact the membranes that are used for the experiment are suspended by four bridges. Aspelmeyer et al [30] discussed how clamping may effect the losses encountered by a mechanical oscillator. Following their work we used instead four bridges to support the structure and compensate the loss. The photonic crystal membrane is then suspended with the help of four bridges with width

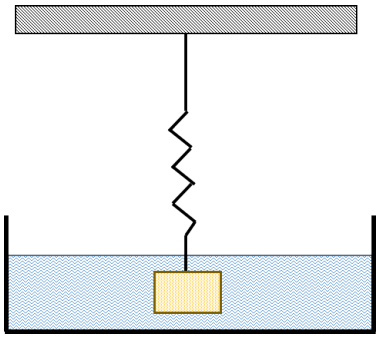

Figure 2.7: Mass spring damped system.

of $1\mu m$ and length which can vary starting from $2\mu m$. The optimization of the design of this particular kind of membranes is discussed in [76].

Knowing these specifications we simulated various mode profiles for these particular kind of membranes (Figure 2.6). The first step was to transfer the design of the suspended membrane system on to a FEM simulator (COMSOL) and then use it to find the eigen-frequencies and the eigen-modes. In Figure 2.5 we show here the first five modes of the suspended structures with eigen-frequencies lying within 2-7 MHz; this range is expected from equation (2.27) as ranges of parameters $a$ and $b$ are within $\mu m$ range. The mode profiles in the figure above also resemble the mode profiles discussed in Figure 2.5.

### 2.3.4 Spectral response under forcing

In our experiments, these modes will be excited by an external force. In this section we introduce some theoretical description of this forced oscillation regime. Let us begin by considering a simple situation where an oscillator of mass $m$ is suspended by some string with spring constant $k$ acting as a restoring force on the oscillator (Figure 2.7). At the same time the mass is suspended inside a damped medium with a damping constant $\Gamma$. Now if the spring is pulled downward with a force of $F'$, the mass starts to oscillate inside the damped medium. Under ideal conditions the system should oscillate forever, although in a more practical scenario after a certain time period the damping and frictional forces would come into play and finally should stop the motion of the oscillator. The dynamics of such a system can be written as:

$$m\ddot{x} + \Gamma\dot{x} + kx = F' \tag{2.34}$$

A modified version of the equation can be written as:

$$\ddot{x} + \Gamma_m\dot{x} + \Omega_{m0}^2 x = F \tag{2.35}$$

where $\Gamma_m = \Gamma/m$ is the damping per unit mass, $\Omega_{m0} = \sqrt{\frac{k}{m}}$ is the undamped natural resonance frequency of the oscillator and $F = F'/m$ is the force acting per unit mass on the oscillator. The idea can be extended to an oscillator under forced excitation. For our system

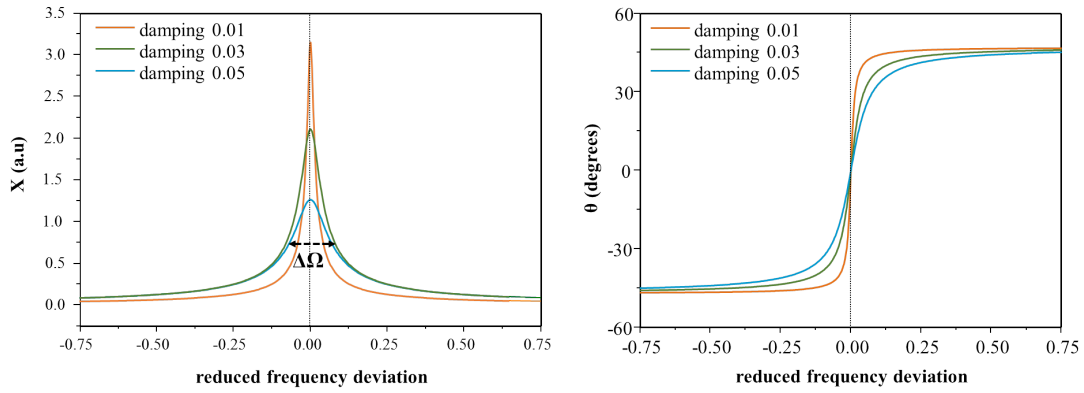


Figure 2.8: (a) Amplitude and (b) phase response of the mechanical oscillator with reduced frequency $\omega$ for three different damping coefficients

formed by a photonic crystal membrane let's focus on one particular mode of eigen-frequency $\Omega_{m0}$.

Solution of equation (2.37) gives what is known as the Mechanical Lorentzian function and if we define Fourier transform of $x(t)$ to be $X(\omega)$, then we can write:

$$X(\omega) = \left[\frac{F^2/4}{\{\omega^2 + (\Gamma_m/2)^2\}}\right]^{1/2} \tag{2.36}$$

and the phase response of the oscillator can be written as:

$$\Theta(\omega) = arctan(\frac{\omega}{\Gamma_m}) \tag{2.37}$$

Here we define $\omega = \Omega - \Omega_{m0}$ as the detuning, while $\Omega$ is the frequency of actuation. The amplitude and the phase response with respect to reduced frequency $\omega$ is shown in Figure 2.8. In an ideal scenario when there is no damping i.e. $\Gamma_m = 0$, the amplitude response $X(\Omega)$ would be a delta function. Whereas due to the presence of damping the amplitude $X(\Omega)$ as well as the phase response $\Theta(\Omega)$ become spread in frequency. As the damping increase so increases the broadening of the response spectra (Figure 2.8). The most common way to quantify the damping acting on the system is by what is known as the Q-factor of a mechanical system. The Q-factor is a dimensionless quantity which is inversely proportional to the damping coefficient $\Gamma_m$ and is measured as $Q = \frac{\Delta\Omega}{\Omega_{m0}}$. $\Delta\Omega$ is known as the FWHM of the response and is quantified as the frequency spread at half of the amplitude maxima.

### 2.3.5 Actuation by an external piezo

The first steps of experiments were performed by doing actuation of the fabricated PhC membranes with an external piezo stack. All the membranes used in these experiments are InP photonic crystal membranes suspended with four bridges (Figure 2.9). All the membranes

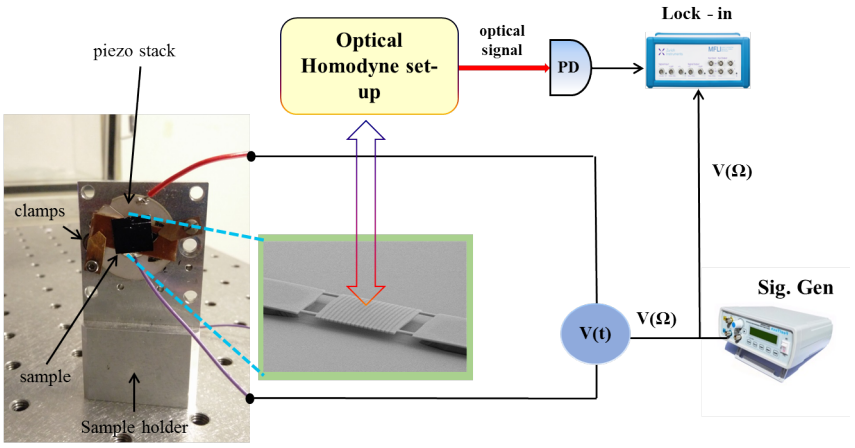


Figure 2.9: Set up for actuation of the PhC membrane with external piezo stack.

have dimension of $10 \times 20\mu m^2$ with different bridge lengths $(2 - 8\mu m)$ and they produce their drum modes in the MHz regime. The piezo stacks that were used for actuation were fabricated by PI ceramic and could produce actuation up to $10MHz$. The set up for this kind of actuation is shown in Figure 2.9; the sample is stuck on the piezo via some sticker and after the piezo is clamped on the sample holder via screws. Contact is made on both sides of the piezo in order to actuate it longitudinally and therefore actuate the photonic crystal membranes indirectly. The piezo was then connected to external signal generator outside the vacuum chamber; a sinusoidal signal is generated by this signal generator which is used to actuate the piezo. Whenever the actuation frequency is close to the eigen-frequency $\Omega_{m0}$ of the mechanical membrane it will excite the corresponding eigenmode. Implementation of such actuation scheme on PhC membrane has already been demonstrated by Antoni et al [77]. The detection then can be performed optically, as discussed in the previous section.

The experimentally detected spectra are shown in Figure 2.10; The mechanical spectra exhibited here is for two different membranes with identical geometry i.e. they have same dimensions $(10 \times 20\mu m^2)$ and also identical bridge lengths $(2\mu m)$. As the piezo actuation is indirect, the efficiency of actuation process is not so high. The response is also a bit noisy and source of this noise can be many fold; firstly it can be purely electrical as there are various connections from outside of the vacuum chamber to inside and finally to the piezo which could introduce many electrical noises. Secondly the piezo itself is a source of noise which makes some noise to appear almost all the time even after optimization. Moreover, for the higher order mechanical modes the spatial overlap between the laser spot and the higher order membrane modes is not high enough to produce a considerably high response in the detector, thereby making a lower contribution to the detected output.

We tried to detect systematically this fundamental mechanical mode for all the available membranes with identical membrane geometry $(10 \times 20\mu m^2)$ but different bridge lengths $(2, 4, 6, 8\mu m)$. And for each case we extracted the eigen-frequency $(\Omega_{m0})$ and the Q-factor. It can be seen from the Figure 2.10 that for a particular bridge length, the eigen-frequencies $(\Omega_{m0})$ follow the same trend with a given dispersion of $\pm 300kHz$ mainly related to the imper-

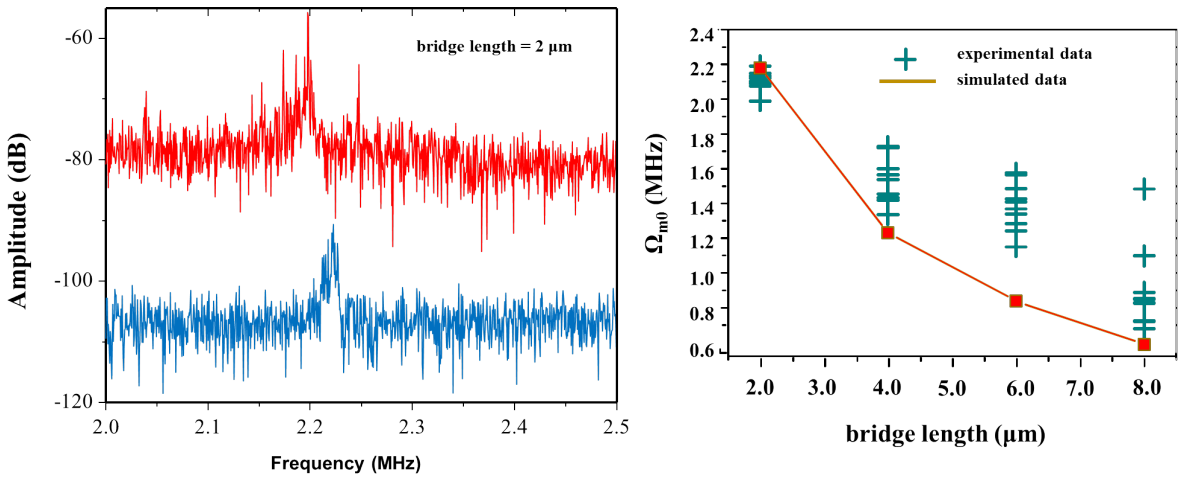


(a) (b)

Figure 2.10: (a) Mechanical noise spectra of two different membranes with identical geometry separated by an offset, (b) plot of experimentally and simulated (FEM simulation) eigen-frequency ($\Omega_{m0}$) .

fection in the membrane geometry (mainly bridge width or length) arising from fabrication imperfections. While with higher bridge lengths there is a gradual decrease of $\Omega_{m0}$. Knowing the geometrical parameters, in the simulations we fix the geometry while playing only with the Young's modulus of the InP membranes. The measured Young's modulus for which we are able to find a fit is around $40GPa$ which is of the same order compared to the bulk Young's modulus of $70GPa$. The simulated values of eigen-frequency found to suit the experimental data quite well (Figure 2.10(b)).

The detection of Q-factor was difficult to perform as proper fitting was difficult to find due to the existing noise in the spectra. Thus we decided to take an alternate approach in order to faithfully recover the Q-factor. The method is known as the ring-down process; the idea is to excite the resonator at the natural resonance $\Omega_{m0}$ and at the same time observe the response signal in time domain. As soon as the excitation is turned off the resonator starts to decay to its rest state. Depending on how many times it oscillates before it reaches the rest state the Q-factor could be determined. In general a resonator excited at natural resonance $\Omega_{m0}$ could be described by a simple harmonic oscillator, with response:

$$x(t) = x_0 e^{-\frac{\Omega_{m0}}{2Q}t} cos(\Omega_{m0} t\sqrt{1 - \frac{1}{4Q^2}} + \phi) \tag{2.38}$$

Where, $x_0$ is the amplitude of displacement and Q is the Q-factor of the resonator. The exponential factor $e^{-\frac{\Omega}{2Q}t}$ mainly determines how many times the resonator oscillates before it arrives at rest state. The decay rate is generally defined as the time when the amplitude of oscillation is 33% of the amplitude maxima. This happens when $\tau_d = 2Q/\Omega_{m0}$, i.e. $Q = \Omega_{m0}\tau_d/2$; which gives a direct measurement of the Q-factor. The experimental method is displayed in Figure 2.11(a); when the resonator decays to its rest state the decay trace

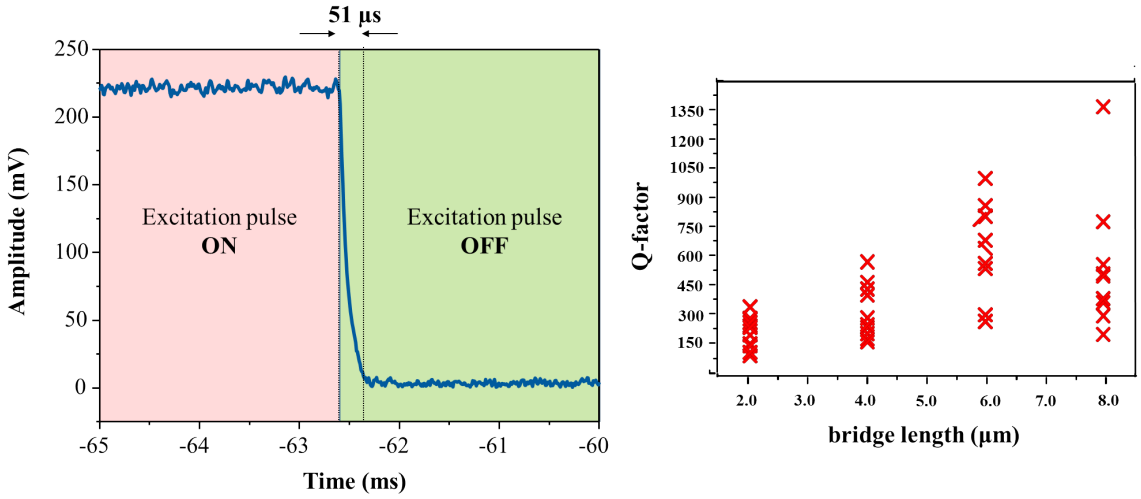


(a) (b)

Figure 2.11: (a) Ring down process in order to determine the Q-factor, (b) extracted Q-factors by ring down process for different membranes with various bridge lengths $(2-8\mu m)$

can be fitted with an exponential decay function and from the fit decay time $\tau_d$ could be extracted. This extracted $\tau_d$ could be then used in order to determine the Q-factor with the method described before. For example in this particular case we extracted a $\tau_d$ of about $51\mu s$ which yields a Q-factor of around 900. This method was repeated several times in order to find an average value of Q-factor. And this process was performed for all other resonators with different geometries and for each case Q-factor was extracted (Figure 2.11(b)). We observe a gradual increase in the Q-factors hence decrease in the mechanical losses with an increase in the bridge length. However, it was difficult to predict the Q-factors with FEM simulations as it was not possible to introduce effect of surrounding losses properly.

Due to the low stress in the InP it was difficult to fabricate InP membranes with bridge lengths as long as described in [30]. However using lattice mismatch between the membrane and the substrate it is possible to increase effective stress in a III-V material. This is achieved for example using GaN/AlN structures (Appendix A.1). Otherwise it can be done by using substrates which have stronger Young's modulus for example diamond (Appendix A.2).

## 2.4 Conclusion

In this chapter we have given a detailed description on the optical set-up in Balanced Homodyne configuration. Then we began discussion on the actuation of first kind of samples via means of an external piezo stack. And finally we observed the mechanical response of the photonic crystal membranes under these indirect actuation regime and performed extraction of some important parameters like resonant frequencies and quality factors. The actuation principle however was via indirect means and hence there is a considerable reduction of the

response amplitude. Also detection of higher order mechanical modes were not possible due to the same problem. The target of our experiment was to explore the nonlinear dynamics of the photonic crystal membrane system, which is not possible under this excitation configuration. To achieve this regime it is now important to increase the actuation efficiency. This can be done by introducing some integrated actuation schemes which can enhance the actuation efficiency of the photonic crystal membrane. Integrated actuation scheme of nanomechanical oscillators have already been implemented [78]-[36]. This kind of actuation can be achieved by utilizing the dielectric properties of InP. Using some electrodes integrated with the photonic crystal structures on the same chip it should be possible to actuate in the desirable frequency range of operation. The requirements here are:

1. Integration of the actuating electrodes and the mechanical resonator on the same chip.

2. Increase the actuation efficiency while not compromising with the mechanical quality factor of the membranes. This can only be achieved if and only if there is a spatial separation between the actuated membrane and the actuating electrodes.

3. This separation between the membrane and the electrode governs the actuation efficiency, thus enhancement of this actuation efficiency can be achieved by decreasing the separation between the electrode and the membrane. This is a purely technological issue and in the next chapter we will show how we were able to achieve a relatively satisfactory amount of electromechanical coupling.

In the next chapter therefore we will introduce such a integrated membrane-electrode structure. We will discuss in details the design, optimization and fabrication of the system. And finally will introduce some preliminary experiments on such a system in the linear regime.

# Chapter 3

# Integrated actuation of NOEMS in linear rsegime

## 3.1 Introduction

This chapter is dedicated to the design, fabrication and excitation of the integrated NOEMS platform. After discussing about the design and optimization, we will discuss in details about the fabrication procedures, challenges and remedies. Finally we will discuss about the actuation of the integrated InP PhC membrane at low power in the linear regime. In chapter 2 we discussed about the actuation via an external piezo and also included a brief discussion on the drawbacks of such an actuation scheme. An improvement on the actuation can be performed if we could replace the piezo stack actuation with some integrated actuation scheme. Common voltage induced actuation schemes include piezo-electrical [39][66][38], capacitive [71][64][17], magnetomotive [79], electrothermal [80], static dipole-based dielectric [81] for example. The latter has less restrictive choice of system and has advantages in term of dissipation, however suffers from problems of integration and high frequency actuation. For our design the goal was integration but at the same time without compromising the quality of the mechanical modes. This could only be attained if we are able to decouple the actuator and the resonator while at the same time being integrated on the same chip. This could be achieved by placing the electrodes beneath the photonic crystal membranes and then actuating the membrane via capacitive force induced due to the dielectric properties of the InP membrane. The integration also allows control of the distance between the electrodes and the membrane, thereby control over the electromechanical coupling. And finally we will also provide a very interesting scheme of experiment where we would see that it is possible to tune the natural eigen-frequency of these micro-resonators by application of a static voltage. These kind of experiments has already been performed where similar schemes were utilized in order to to achieve this goal [16] [17] [15].

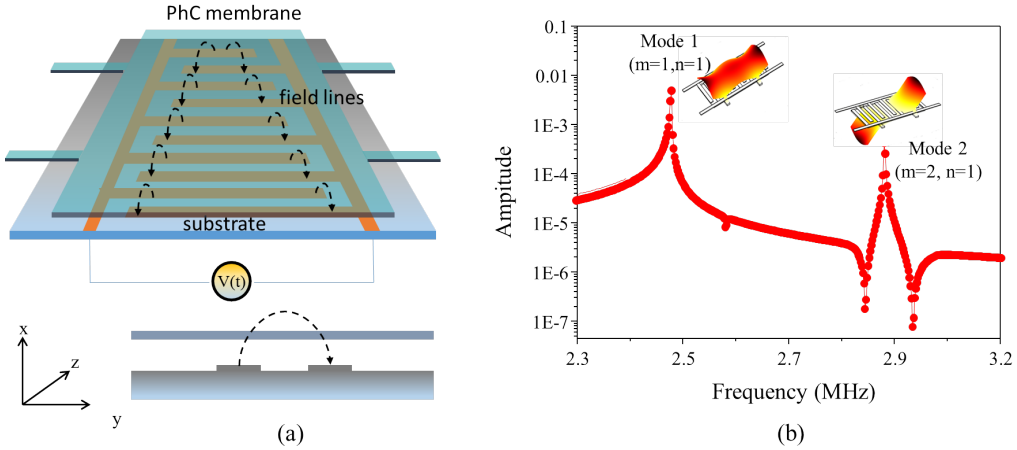


Figure 3.1: (a) Scheme of integrated actuation of the photonic crystal membrane (b) Simulated mechanical spectrum with displacement profile of the first and second mechanical modes.

## 3.2 Design and optimization of the integrated actuation scheme

### 3.2.1 Interdigitated electrodes

In order to achieve efficient actuation, primarily we need to design electrodes which are able to excite properly the mechanical modes. We came up with a design shown in Figure 3.1(a), which is more commonly known as the interdigitated electrodes or IDEs. The choice of the electrode architecture is mainly due to two reasons: firstly these structures are in-plane structures which are able to excite a dielectric medium which is situated above these electrodes. The principle of actuation is shown in Figure 3.1(a), the electric fields penetrate the membrane vertically and thereby inducing a force by means of polarization of the InP membrane. The second reason was effective actuation of the desirable mechanical mode; for the experiments we decided to work with mainly the first mode ($m = 1, n = 1$), since in principle this mode has the highest displacement compared to other modes. This makes actuation and detection much easier compared to other higher order modes. Other reason being that the optical detection scheme is most sensitive to this particular kind of mechanical mode (section 2.2). The shape of this mode as it was discussed in the previous chapter is drum like and the movement of the membrane corresponds to the movement of the entire membrane. These kind of electrodes are very effective in order to actuate these kinds of geometry. Since the electrodes are uniformly distributed along z-axis (Figure 3.1(a)) below the membrane, they are able to homogeneously actuate these planar membranes.

To comprehend how the modes and system would behave, we decided to perform some FEM simulation with this membrane-electrode design. The geometry is a rectangular membrane (Figure 3.1(a)) with dimension $10 \times 20 \mu m^2$ with a thickness of about $260nm$ and the

bridge dimensions were selected to be $2 \times 1\mu m^2$. In order to reduce memory requirement for the simulations we decided to not to draw any holes in the membrane as it mainly alternates the optical properties but not so much the mechanical properties. Amplitude response of the first two simulated mechanical modes are shown in Figure 3.1(b) and we can observe that the modes and the eigen-frequencies lie in the same range as expected from the experimental results with the piezo stack actuation in chapter 2. Here we do not go in detailed discussion on the shape of the eigen-modes as it was discussed in details in the previous chapter.

### 3.2.2 Electromechanical coupling factor

The principal of actuation is the following: when a voltage source $V(t)$ is connected between the external electrodes a potential is applied on the membrane. Field lines penetrate the membrane in a manner shown in Figure 3.1(a), these field lines then polarize the membrane and as a result a dielectric force is applied on the membrane. This force causes the membrane to oscillate at the actuation frequency. The detection principle was discussed in the previous chapter, in short when the actuation frequency is close to the mechanical eigen-frequency, the membrane starts to vibrate profusely and the motion can be detected by the Balanced Homodyne Detection or simply BHD.

The system with electrode-membrane acts mainly as a capacitor; thus the force acting on the membrane is proportional to the square of the applied voltage $V(t)$. Thus the force acting on the membrane is:

$$F = -\frac{d}{dx}E(x) = -\frac{1}{2}\frac{dC(x)}{dx}|_{x=x_0}V^2 \tag{3.1}$$

Where $C(x)$ is the equivalent capacitance of the electrode-membrane system. Now under small signal approximation, the fluctuating actuation force acting on the PhC membrane is:

$$\delta F = \frac{\delta F}{\delta x}|_V \delta x + \frac{\delta F}{\delta V}|_x \delta V \tag{3.2}$$

$$= -\frac{1}{2}\frac{d^2C}{dx^2}|_{x=x_0}V^2\delta x - \frac{1}{2}\frac{dC}{dx}|_{x=x_0}V\delta V \tag{3.3}$$

Where the first term of equation (3.3) represents purely a static voltage acting on the system and the second term represents influence of an alternating voltage acting on the resonator. Where the first term of equation (3.3) represents purely a static (DC) voltage $V$ acting on the system and the second represents influence of an alternating (AC) voltage $\delta V$ actuating the resonator. The first term is interestingly proportional to the displacement of the membrane $\delta x$ which resembles modulation of the spring constant of the nanomechanical resonator. The term $V$ still exist in case of a pre-stressed membrane where we can assume a constant stress acting on the system which can be effectively represented by a static voltage. However when there is no external DC or static voltage acting on the membrane we should be able to neglect the influence of the first term in equation (3.3) as it practically has no

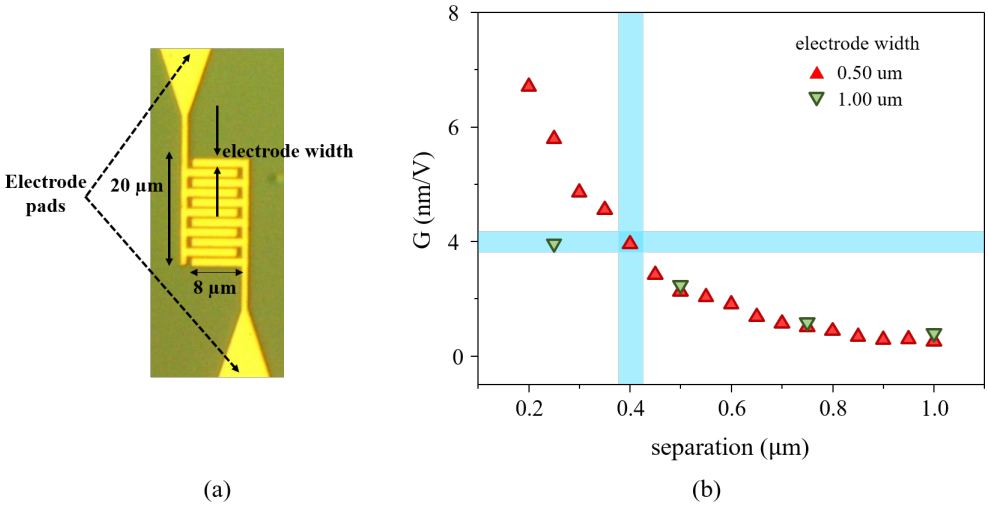


Figure 3.2: (a) Top view of the interdigitated electrodes, the electrode length remains fixed at $8\mu m$ while the electrode widths are varied, (b) variation of the electro-mechanical coupling factor G with the membrane-electrode separation for two electrode widths of $0.50\mu m$ (red) and $1.00\mu m$ (green) with a period of $2.00\mu m$.

effect on the membrane actuation. In that scenario only the second term remains and then the force acting on the system is:

$$\delta F = -\frac{1}{2}\frac{dC(x)}{dx}|_{x=x_0} V\delta V \tag{3.4}$$

Now any oscillator under forced oscillator regime can be described by the equation:

$$\ddot{x} + \Gamma_m \dot{x} + \Omega_{m0}^2 x = F \tag{3.5}$$

Replacing the right hand side of this equation with the expression of the forcing term in equation (3.2), we can write:

$$\ddot{x} + \Gamma_m \dot{x} + \Omega_{m0}^2 x = -\frac{1}{2}\frac{dC(x)}{dx}|_{x=x_0} V\delta V \tag{3.6}$$

The next step was to optimize the design of the IDEs, for the optimization we decided to look at the how the applied electric field couples to the mechanical motion of the membrane. To perform this analysis we referred to Bagci et al. [16] where they provide extended analysis of a similar system (a SiN membrane without photonic crystal) actuated via electrodes underneath by means of capacitive coupling. They proposed the coupling between the applied electric field and the mechanical motion to be governed by a factor G known as the electro-mechanical coupling factor and it is expressed as:

$$G^{-1} = VC(x_0)\frac{\delta}{\delta x}(\frac{1}{C(x)})|_{x=x_0} \tag{3.7}$$

where, $C(x)$ is the capacitance of the electrode-membrane system, $V$ is the applied voltage on the electrodes and $x_0$ is the mean position of the membrane. In general the capacitance $C(x)$ is an exponential function of $x$ which signifies the vertical position of the membrane (Figure 3.1(a)). This makes $G$ automatically an exponential function of membrane position $x$ as well. With increasing membrane-electrode separation therefore there is a gradual decrease in the electro-mechanical coupling factor $G$.

The shape of the electrodes is shown in Figure 3.2(a), the electrodes are teeth-like structures with length of $8\mu m$ which we keep fixed for all simulations, while we vary the electrode widths taking two different values of $0.50\mu m$ and $1.00\mu m$ having a fixed period of $2.00\mu m$ in each case. For each of these electrode widths we change the electrode-membrane separation and for each case we calculate the electro-mechanical coupling by calculating the capacitance $C(x)$ of the system. The resulting plot is shown in Figure 3.2(b). In each case we can observe an exponential decrease of $G$ with $x$. The value of the electromechanical coupling factor G is found to have a higher value for an electrode width of $0.50\mu m$. We did not go beyond width of $1.00\mu m$ for the electrode width as it puts technological restrictions from the point of view of fabrication. When we were in the process of designing the electrodes, due to some technical issues we were restricted to an electrode membrane separation of about $0.4\mu m$, this point is highlighted in Figure 3.2(b) where theoretically we predict an electromechanical coupling factor of about $4nm/V$.

## 3.3 Fabrication Process

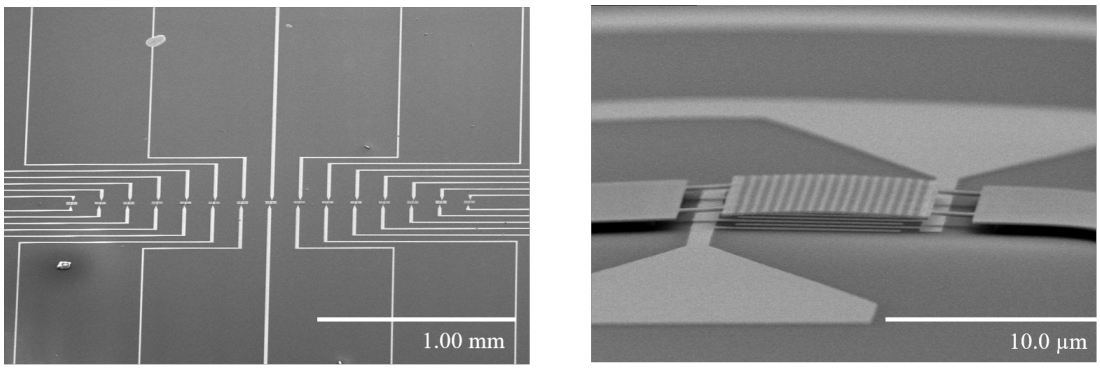


Figure 3.3: Fabricated PhC membrane-electrode structure (a) Top view of the electrode membrane with the extended gold electrodes towards their connecting pads (b) Close view of a fully suspended PhC membrane with interdigitated electrodes underneath.

In the previous sections we introduced the hybrid photonic crystal electrode structure in details and discussed about the optimization of the electrode structure. In this section we will discuss about the fabrication of such a hybrid structure. The photonic crystal membrane

is a rectangular InP structure with a thickness of about 260$nm$ suspended 400$nm$ above the interdigitated electrodes with a typical teeth length of 8.00$\mu m$. Figure 3.3 shows the scanning electron micrograph of fabricated electrode-membrane structure.

The main challenges of the fabrication of such a device is firstly the heterogeneous integration of electrodes with the suspended membrane. Control of the distance between the bottom of the suspended membrane to the top of the electrodes is crucial in order to achieve a satisfactory level of electro-mechanical coupling. Also, in order to have a proper mechanical resonator it is essential to have a fully suspended structure over the electrodes.

### 3.3.1 Fabrication challenges

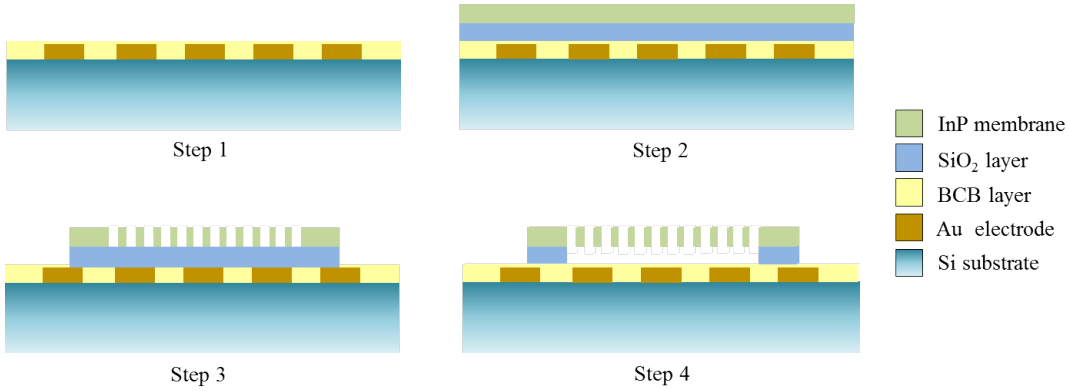


Figure 3.4: Main four fabrication steps in order to create suspended photonic crystal membrane on top of the interdigitated electrodes fabricated on Si substrate. Step 1: electrode patterning, step 2: bonding of electrode and InP substrate, step 3: patterning of PhC, step 4: creation of MESA and membrane release.

The entire procedure of fabrication mainly consists of four main steps (Figure 3.4). The first step involves electrode patterning on top of the Si substrate which has thickness of about few hundred microns (typically around 250$\mu m$). The second step is to bond this interdigitated electrode on Si-substrate with an InP substrate in order to form the electrode-membrane system. The third step is to etch periodic cylindrical holes on the InP membrane to form a photonic crystal structure, this step involves electron beam lithography and various dry etching techniques. The fourth step is to design a MESA to hold the suspended photonic crystal structure, like the earlier step this also involves etching and lithography techniques. This step also involves release the membrane and making it suspended. This step involves wet etching techniques along with a special technique known as the Critical Point Drying or simply CPD. Achieving a suspended membrane structure is very important in order to have a proper mechanical oscillator which generates vibrational mechanical modes in the MHz regime. Also distance between the electrode and the suspended membrane is really important in order to achieve a high electro-mechanical coupling factor (Figure 3.2(b)). All

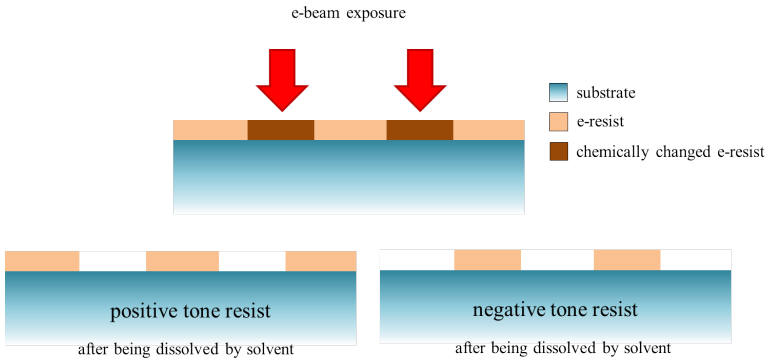


Figure 3.5: Schematic of e-beam lithography with positive/negative tone resist.

these are achieved mainly on the last step which will be discussed later. The four main steps are described in the following sections in details.

### 3.3.2 Various patterning techniques

In this section we will briefly introduce different substrate patterning techniques used for the fabrication of the targeted device. This will mainly consist of two sections: at first we will introduce the basis of electron beam lithography and then the dry etching techniques which are essential in order to pattern and structure the PhC+Mesa structure as well as the electrodes. The entire fabrication process rely on three different electron beam lithography steps and two dry etching steps.

#### 3.3.2.1 Electron beam lithography

Electron beam lithography is a specialized lithography technique for drawing patterns on substrates with a very high resolution. The resist spin coated on the sample is sensitive to the incoming electron beam and thus deposits the incoming electron beam energy in the desired pattern in the resist film. The main advantages of this process is firstly that it is capable of producing patterns with very high resolution and secondly the flexibility of the technique which makes it workable with various kind of materials. The alignment process allows a positioning accuracy which is better than $50nm$. However the technique comes with some drawbacks; for example this technique is relatively expensive and complicated.

The main idea of e-beam lithography is similar to any other lithography techniques, for example like optical lithography. The substrate is coated with thin layer of e-beam resist. Now when this layer is exposed to incident e-beam, depending on whether the resist is positive (or negative) the exposed (or unexposed) layers would be dissolved. This process of using positive or negative mask is shown in Figure 3.5.

For the fabrication procedure we have mainly dealt with structures that have sizes ranging from few hundred of nanometers to few tenths of microns. Thus in each step we have worked exclusively with electron beam lithography. Since each sample in general has roughly only 20

membrane-electrode structures, the writing process although being quite slow doesn't take too long. Fabrication of each sample in general goes through three different electron beam lithography steps; the first one being the design of the interdigitated electrodes. The second step is focused on generation of the photonic crystal on the InP. And finally the last step is the generation of a mesa structure to create a suspended InP membrane-electrode structure. For the first two cases we have used a positive tone resits known as PMMA (PolyMethyl MethAcrylate), this is one of the most popular positive tone resist. For the later we use a negative tone resist known as HSQ (Hydrogen SilsesQuioxane) [82][83], which also acts as a hard mask for dry etching.

#### 3.3.2.2 Dry etching techniques: CCP-RIE and ICP-RIE

A dry etching is a process to remove materials, typically masked pattern of substrates by exposing them to an incoming beam of ions. A typical example of dry etching is what is known as the RIE or Reactive Ion-Etching. RIE works in a low pressure environment with a surrounding of chemically reactive plasma. The plasma is generated under a vacuum by an electromagnetic field (RF field), hence the name.

The principle of operation is displayed in Figure 3.6(a), the plasma is initiated by applying a RF field to the wafer platter. The field typically has a frequency of $13.6MHz$ with a power of few hundreds of Watts. The plasma creates some ions together with some chemical radicals that chemically react to the material one wishes to etch.

An example of RIE process is CCP-RIE (Capacitively Coupled Plasma RIE), this process uses a combination of both physical and chemical etching to have a high level of resolution. The ions are accelerated towards the sample by application of a high voltage between the electrodes, this results in a physical etching of the substrate. While on the other side, the high energy collision between the etchant and the bombarding ions helps to create more reactive species which could react chemically and thus can be removed quickly. Since this process uses a combination of chemical and physical etching technique, it is a much faster process compared to either pure chemical or pure physical etching techniques. The process of CCP-RIE is elaborated in Figure 3.6(b) & (c), the cations are produced from reactive gases which are then accelerated with high energy by the electrodes towards the substrate for reaction. Other than that to achieve a suitable etching condition, factors like applied electrode power, gas flow rate, chamber pressures are also crucial. For different processes each factors need to be optimized in order to have a desired pattern.

The advantage of this process is its directionality; since the process is mainly physical there is a high control over the etched pattern. Also since the process is a little selective between masked and unmasked pattern, use of a hard mask is required to transfer a desired pattern. On the other side compared to wet etching this process is much slower, although with wet etching it's almost impossible to design some structures with high aspect ratio. However, when anisotropic etching is required dry etching process can be really quick and efficient.

The disadvantage of CCP-RIE is that the ion-energy and density can not be controlled independently. However, this comes with an added advantage with a higher selectivity of the

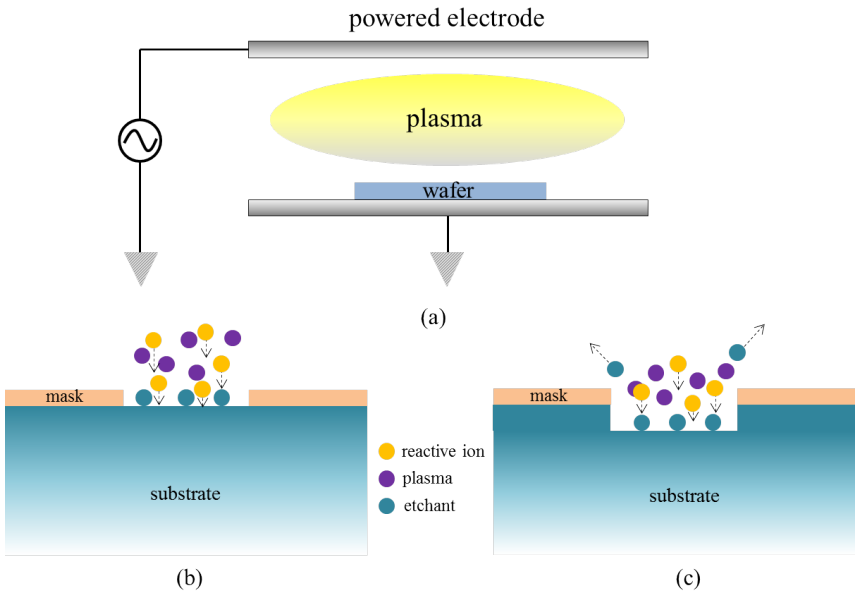


Figure 3.6: (a) Operational principle of CCP-RIE plasma (b) arrival of the accelerated ions on top of the substrate, (c) removal of substrate by a combination of physical and chemical etching;

available materials. Another variation of this technique is known as the Inductively Coupled Plasma RIE or simply ICP-RIE. In this case the density and energy of the incident ions can be controlled independently with the ICP and RF power independently. The ion acceleration is still done by the capacitive coupling, however the control of the ion density gives an added degree of freedom on this process.

### 3.3.3 Electrode patterning and Substrate bonding

In this section we will talk about the first step of generation of the electrode-membrane NOEMS structure. This design is based on what is known as the adhesive bonding of two different substrates. The most well known processes can involve organic and inorganic films deposited on the substrate surfaces. The most popular bonding processes involve SU-8 and BCB (benzocyclobeutene) which are specialized for MEMS/NEMS productions. This heterogeneous integration originally was not developed for optomechanics, but rather for MEMS/NEMS or advanced nanophotonic circuitry in order to integrate active and passive functionalities. There are many advantages of using the substrate bonding techniques; for example this process does not use electric current or voltage and operates at a relatively low temperature. This low temperature operation allows integration of electronic/electrical circuitry or micro structures in the substrate. Secondly, the very nature of the bonding process makes it possible to integrate different substrates like silicon, semiconductor materials, metal and glass for example. Among the drawbacks, the most important one would be the weak control on the dimension of the intermediate bonding layer [84]. Among others the possibility

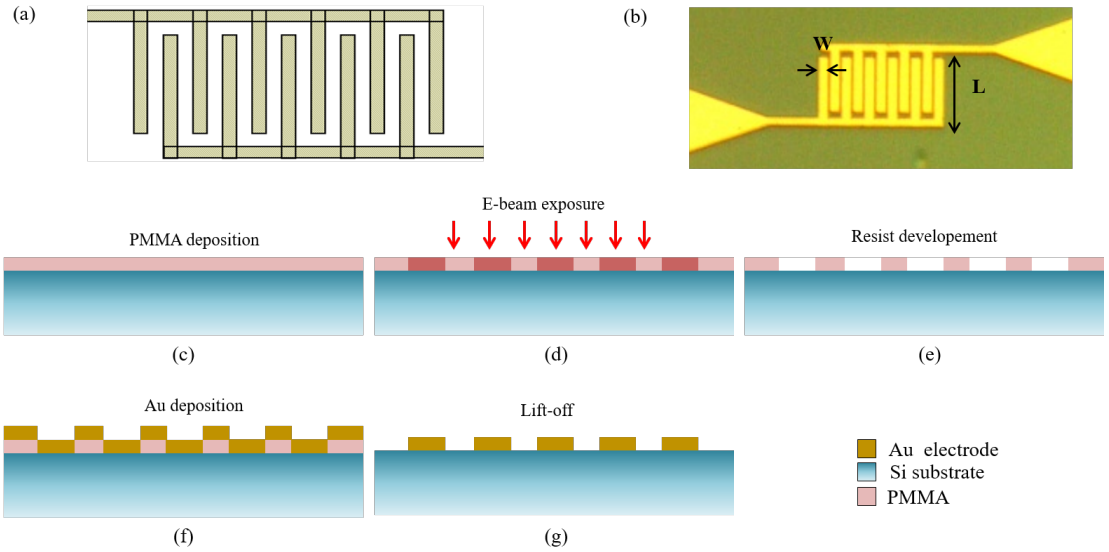


Figure 3.7: (a) Mask used for the IDE patterning, (b) fabricated gold IDE's on top of the Si substrate, (c-f) patterning of the electrodes on top of the Si substrate.

of corrosion due to out-gassed products, thermal instability and penetration of moisture that limits the reliability of bonding process can be crucial [85].

### Electrode patterning and design

The first step of the fabrication process was to pattern interdigitated electrodes (IDEs) on the Si substrate. First of all a mask is prepared with the help of a specialized mask designing software (Tanner L-Edit) which is then transferred to the electron beam lithography (Vistec EBPG 500+) which operates at a working field dimension of $520 \times 520 \mu m^2$ and at a highest available resolution of $0.5nm$. The optimization of the electrode pattern was discussed in the previous section; all the electrodes have a length of $L = 8\mu m$ and with a fixed electrode width which varies between the membrane-electrode structures ranging from $0.5\mu m$ to $1.5\mu m$.

First of all PMMA is deposited on the silicon substrate with help of a spin coater (Figure 3.7(c)). For the coating we choose PMMA A7 with speed of $4000rpm$, acceleration $4000rpm/sec$ and for a duration of $30sec$. This yields a PMMA pattern of $450nm$ of thickness. After that the PMMA is soft baked inside an oven with a temperature of 160°C for around 15'. This is a standard procedure for e-beam lithography for us, from here whenever we use PMMA as a mask for the lithography we would use exact same parameters. Now the sample is ready for e-beam exposure, it is then put inside the lithography chamber where the pattern is written on top of the wafer (Figure 3.7(d)). This process is followed by resist developing by a 1:4 IPA:MIBK (Isopropyle alcohol:Methyl isobutyl ketone) solution for $30sec$, which is followed by $15sec$ IPA rinse in order to clean the obtained openings (Figure 3.7(e)). Such a low concentration of MIBK solution is used in order to preserve the maximal resolution with the PMMA resist.

After the pattern was developed, it was placed into metal deposition chamber. The metallization process works in vacuum where at first the metal is heated over the boiling temperature and then letting condensation deposition on top of the substrate's surface. This yields an uniform coating of metal on top of the electrodes (Figure 3.7(f)). A combination of Ti/Au with thickness $20/200nm$ is deposited on top of the substrate which follows the profile of the substrate governed by lithography. The combination of Ti is used with Au in order to make sure that the metal sticks better with the Si substrate. After the metal deposition is performed, the sample is placed in an ultrasonic bath with Trichloroethylene. The ultrasonic bath now removes the sacrificial material (in this case PMMA) along with the metal that is covering it leaving behind only the metal part directly on the silicon substrate (Figure 3.7(g)). The generated interdigitated pattern is shown in Figure 3.7(b). At the same time marks are drawn on sample that are at known locations with respect to the electrodes. They are used in the following sections in order to precisely position different layers.

**Substrate bonding**

After the metallization is performed the next step is to bond this silicon substrate with electrodes and the InP/InGaAs substrate [82]. The InP/InGaAs substrate consists of three layers: the first layer is the InP membrane layer which is grown by MOCVD with a thickness of $260nm$ (Figure 3.8(b)). The second layer is a thin layer of InGaAs ($1\mu m$ thick) known as the etch-top layer. And finally there is a thick non-epitaxial InP substrate of few hundred microns. At the end of the bonding process only the $260nm$ thick InP membrane would stay on top of the Si substrate. The standard processes for wafer bonding involves either SU-8 or BCB. For fabrication of our system we decided to choose the later due to mainly two reasons. Firstly BCB is widely used in NEMS and MEMS system with electronics [86]. Secondly its optical properties (mainly refractive index) could give us opportunity to add optical components like waveguide in the system. The thickness of the intermediate BCB layer can be chosen to be as low as few nanometers depending on the concentration of the diluting mesitylene solution ($C_9H_{12}$, derivative of benzene). For the adhesive bonding of InP/InGaAs substrate on top of Si substrate we follow the process developed by Roelkens et al. .

To perform the adhesive bonding successfully, deposition of $SiO_2$ layer is required on top of the InP/InGaAs substrate. This acts as an interface between the InP membrane and BCB and its thickness determines the separation of membrane with the electrodes i.e. the electromechanical coupling. In general only a few nanometers of $SiO_2$ is sufficient in order to achieve successful adhesive bonding. However, too thin $SiO_2$ layer can make membrane release difficult, whereas higher thickness of this layer degrades the electromechanical coupling. Thus we arrive at an optimal separation of between $100 - 400nm$ in order to have a satisfactory coupling. For the designed membrane electrode system we use a $SiO_2$ layer with thickness of $400nm$.

In order to have a bonding with high quality and efficiency it is essential to have a clean substrate surface, for that a strict sample cleaning procedure is required. Firstly both substrates are cleaned in an ultrasonic bath with acetone at a frequency of $80Hz$ for 5'. This

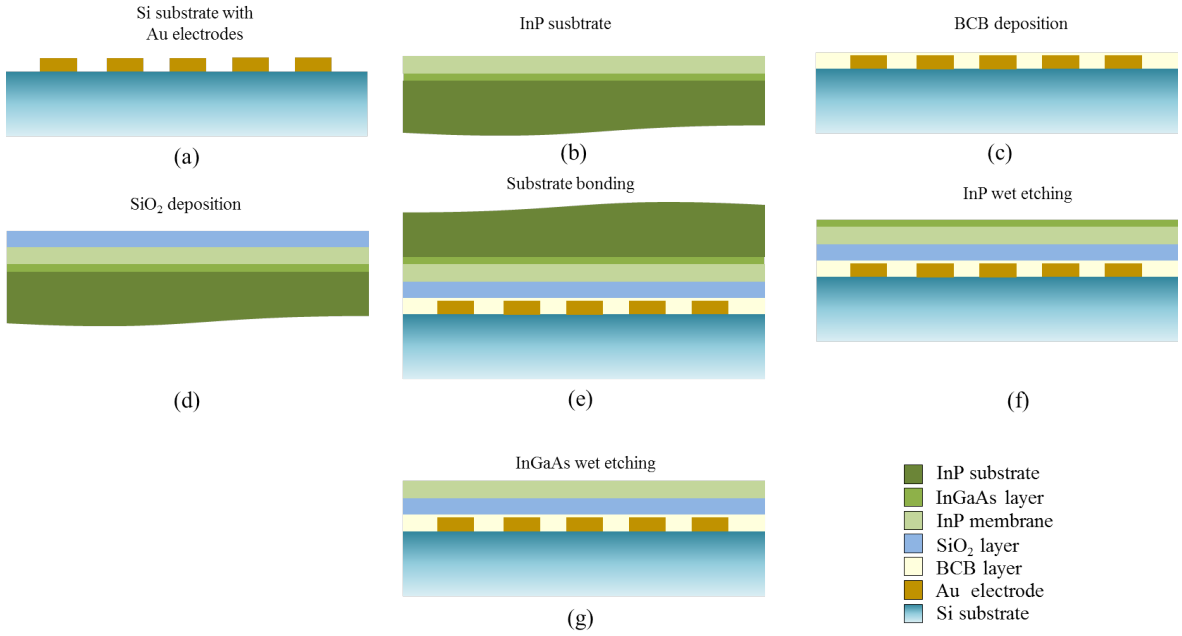


Figure 3.8: Process flow of adhesive bonding between InP substrate and Si substrate with the help of BCB as the intermediate layer.

is followed by a cleaning with IsoPropyl Alcohol (IPA) and $N_2$ drying. This is preceded by an oxygen plasma cleaning for 2'. We used a oxygen flow rate of $50sccm$ and a pressure of $100mTorr$. Whenever oxygen plasma is used from now on, identical parameters will be used. This step is necessary in order to remove the remaining resist on the substrate surface. It also creates a native oxide layer on top of the substrate surface which leads to better adhesion while bonding.

Next step is the deposition of the adhesive BCB layer on top of the Si substrate (Figure 3.8(c)). For this step it is essential to have a smooth and uniform BCB layer on top of the electrodes. This requires immersion of the electrodes inside the BCB layer. Since the thickness of the electrodes is around $200nm$, this limits the thickness of BCB around the same value. For the deposition we use a combination of BCB with Mesitylene at a ratio of 4:3. Use of syringe with filters is necessary in order to block unnecessary particles in the solution. Finally the BCB layer solution is spin coated on top of the silicon substrate with the help of a spin coater. A speed of $5000rpm$, an acceleration of $2000rpm/sec$ and a duration of $30sec$ is chosen for the deposition. This is followed by a soft bake at 80° for about 15'.

On the other hand the cleaned InP/InGaAs substrate is prepared for the $SiO_2$ layer deposition (Figure 3.8(d)). This deposition is achieved in two steps: in the first step a $25nm$ thick layer of $SiO_2$ is deposited on top of the substrate by using PECVD (Plasma Enhanced Chemical Vapor Deposition). This is necessary as this deposition technique does not damage the InP surface as it does not involve ion bombardment. For the next $375nm$ of $SiO_2$ deposition we use sputtering technique to improve adhesion compared to the PECVD deposited silica. This however does not degrade the underlying InP layer as it is now protected

by the thin $SiO_2$ layer created by PECVD. The $SiO_2$ layer with the BCB layer finally defines the electrode-membrane separation of around $400nm$.

Finally when both of these dies are prepared they are ready for the bonding procedure. For this process we use a high precision wafer bonding machine: SUSS MicroTech SB6. The wafer is heated to a temperature around 320°C and a pressure of around $150mbar$ per sample is applied for a duration of around $30'$. This temperature and pressure results in complete polymerization of BCB and finally a layer with uniform surface and thickness. The bonded substrates are displayed in Figure 3.8(e).

After the bonding is performed, the next step is to remove the substrate and etch-top layer in order to expose the thin InP membrane. To achieve this the first step is to clean the InP substrate surface with a $H_2SO_4 : H_2O_2 : H_2O$ solution (3:1:1) for a duration of 1'. Next a chemical etching of the InP substrate is performed by HCL (40%) for a duration about 1 hr (Figure 3.8(f)). Finally the etch top layer is removed by the same $H_2SO_4 : H_2O_2 : H_2O$ solution by etching it for few seconds (Figure 3.8(g)). A change of color of the bonded thin InP layer is a very good indicator of the exposed InP membrane.

### 3.3.4 Patterning photonic crystal: optical component

After adhesive bonding, the thin InP membrane is now on top of the substrate. Thereby the next step is to design the photonic crystal membrane. The alignment between the photonic crystals and the electrodes is done by using alignment marks on four corners of the Si substrate. This procedure confirms that the photonic crystals are drawn correctly on top of the interdigitated electrodes. The method is to etch cylindrical holes in the InP structure, the holes are of $196nm$ radius and with a period of $725nm$. We design a pattern of square lattice structures which generates a band gap around $1\mu m$. Generation of this photonic crystal holes consists of few steps: firstly patterning of holes via electron beam lithography, then dry etching of the cylindrical holes and finally removal of the mask. In order to etch InP membrane ICP-RIE is required, but the positive resist used for e-beam doesn't have enough resist against the bombarding ions. Thus we require an intermediate $Si_3N_4$ 'hard mask' in order to protect the underlying InP layer. Finally the InP photonic crystal will be etched through the patterned $Si_3N_4$ structure. Design of the holes requires high precision as these will finally govern the optical properties of the photonic crystal membrane.

The deposition of $Si_3N_4$ is performed by PECVD at about 280°C which creates a $Si_3N_4$ layer of $300nm$ thickness. This hard mask ensures that the underlying layer is protected while performing ICP-RIE (Figure 3.9(c)). Due to the requirement of high precision we use a positive mask (PMMA). The PMMA is spin coated on top of the substrate (Figure 3.9(c)), the deposition procedure follows identical method described before . Then the substrate is exposed under e-beam with the designed mask and the exposed resist remains undissolved in the resist developer thereby creating the desired pattern (Figure 3.9(d,e)). The electron beam process used electron beam energy of $100keV$, a resolution of $1nm$ and a dose of $1200\mu C/cm^2$. After that the pattern needs to be transferred to the $Si_3N_4$ mask. This is done by etching the hard mask through the holes created in PMMA after resist development. This process is performed with CCP-RIE under a $SF_6$ gas environment with a very low gas flow rate of

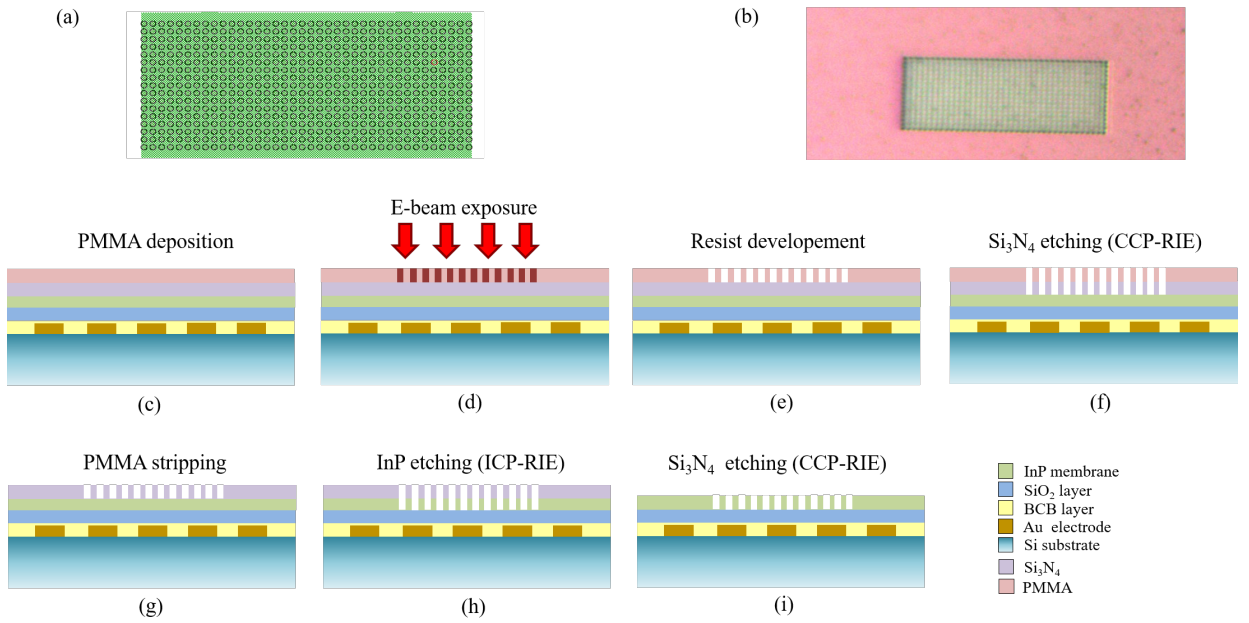


Figure 3.9: (a) The mask used for patterning the photonic crystal, (b) optical image of the fabricated photonic crystal structure, (c-i) process flow of creation of photonic crystal pattern.

$1.4sccm$, low RF power and a pressure of $8mTorr$ (Figure 3.9(f), Figure 3.10(a)). These parameters are necessary in order to create vertical cylindrical holes inside $Si_3N_4$ mask. This step is usually followed by a removal of PMMA resist under an $O_2$ plasma environment (Figure 3.9(g)). The monitoring of PMMA removal is done by an integrated interferometer inside the RIE itself, this helps us to stop the etching as soon as we reach the $Si_3N_4$ layer.

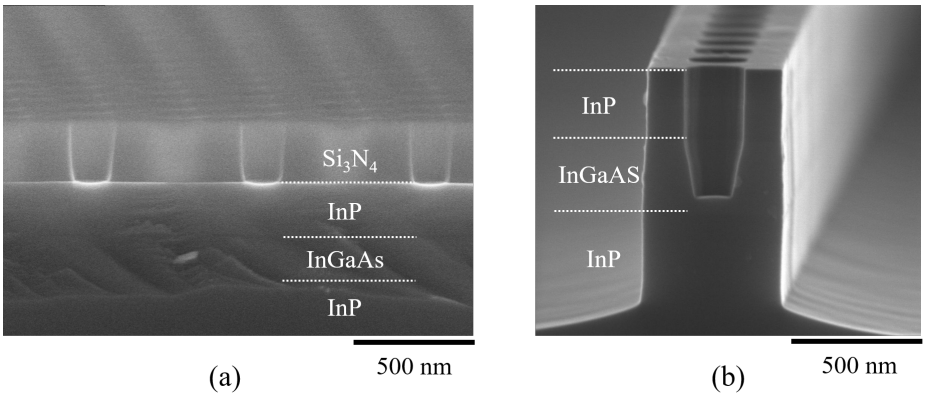


Figure 3.10: SEM picture of a photonic crystal lattice cross-section after its transfer into (a) $Si_3N_4$ mask and (b) into a InP layer.

After the PMMA has been stripped, the next step is to finally draw cylindrical holes

inside the InP layer (Figure 3.9(h), Figure 3.10(b)). This step requires high precision and it is imperative to make sure the drawn holes are perfect cylinders with smooth walls. This ensures high optical quality of the PhC membrane. For this step we use ICP-RIE reactor, mixture of three gases: HBr, $O_2$, He was used at low pressure. This results in a long mean free path of the volatile by products and thereby making it easier to draw them away from the chamber. In general etching of III-V semiconductor family can be performed by halogen gases for example F, Cl and Br. For our process we use Br as the etchant as it provides more energy due to its higher atomic mass. Oxygen is added in the medium in order to achieve sidewall passivation during etching process. For the etching process we use ICP power of $60W$, working pressure of $0.5mTorr$, HBr/$O_2$/He gas ratio: 10/0.6/30. After this etching process the photonic crystal is successfully transferred to the InP layer. This procedure ensures high sidewall quality and thus can be employed for fabrication of photonic components with high optical qualities (Figure 3.10(b)) [87]. This step is followed by removal of $Si_3N_4$ layer by CCP-RIE (Figure 3.9(i)), here again we follow the interferometer signal in order to stop etching as soon as we reach the InP layer. The fabricated PhC structure is shown in Figure 3.9(b).

### 3.3.5 Patterning the mesa: mechanical component

After the PhC holes are patterned the next step is to create the suspended membrane structure what is known as the mesa. The alignment procedure is repeated again with the same marks on the Si substrate in order to make sure the mesa is drawn at correct position. The mesa structure consists of the $10 \times 20\mu m^2$ membrane with the four bridges of dimension $1 \times 2\mu m^2$ and the pads supporting the bridges on the other side having a dimension of $20 \times 20\mu m^2$. Since the dimensions in concern are in the micron range, high resolution is not required. For this reason we switch from the positive tone PMMA mask to the negative tone HSQ mask [88]. Use of a negative mask not only reduces the electron beam exposure time but also avoids use of the hard $Si_3N_4$ mask as HSQ itself is hard enough to resist ICP etching. These factors reduce the extra steps of $Si_3N_4$ layer deposition and removal. The process flow for the creation of the mesa structure is displayed in Figure 3.11(c-g).

The first step involves a InP surface preparation technique. This step involves at first a CCP-RIE with $O_2$ plasma for a duration of 2'. This is followed by a soft baking of 5' at a temperature of 160°C. After the surface is ready, HSQ is deposited by spin-coating (Figure 3.11(c)). The parameters of spin coating are as follows: $1000rpm$ speed, $1000rpm/sec$ velocity and a duration of $30sec$. This results in a deposited HSQ of a thickness around $160nm$. Then the sample is baked on a hotplate at 90°C for a duration of 40'. Now the sample is ready for e-beam exposure (Figure 3.11(d)), the electron beam process used an electron beam energy of $100keV$, a dose of $7000\mu C/cm^2$ and a resolution of $20nm$. After the e-beam exposure the sample is treated for 60" in a $AZ400k : H_2O$ (1:4) solution which dissolves the unexposed part of the HSQ resist (Figure 3.11(e)). This is followed by a ICP-RIE etching (Figure 3.11(f)) with identical parameters as described in the previous section. After this process the mesa and photonic crystal holes are created, however the membranes are not still suspended. Along with the easy mask transfer to the InP layer, HSQ resist also helps to obtain a low

sidewall roughness and good vertical structures.

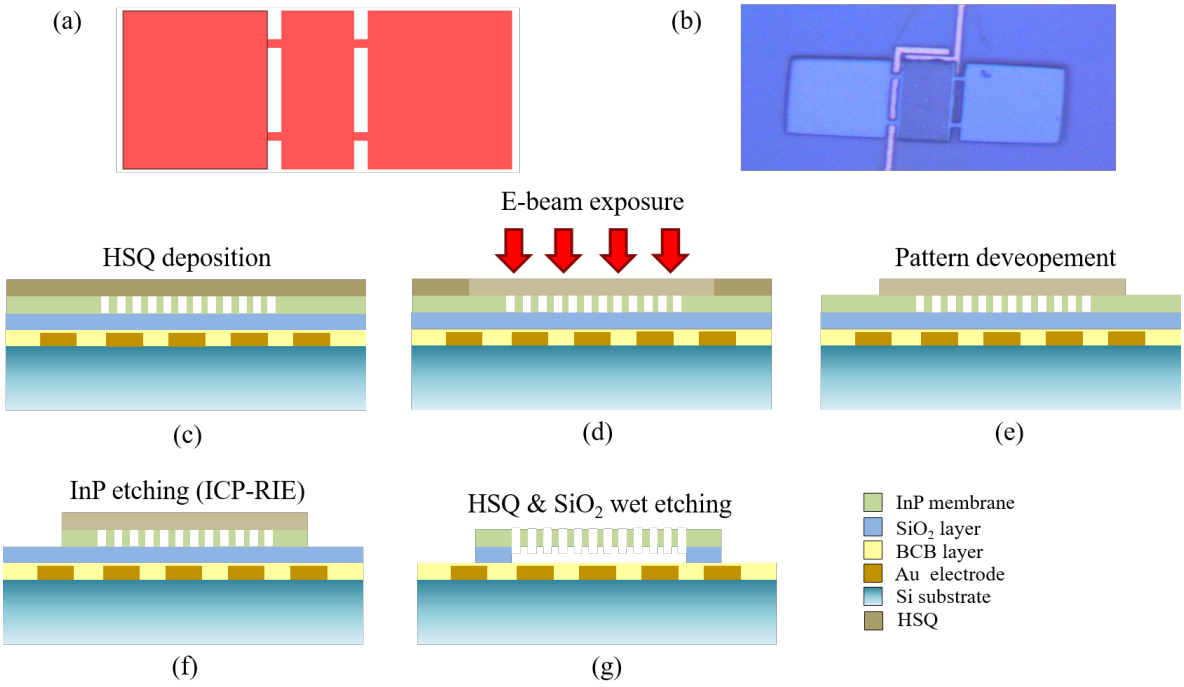


Figure 3.11: (a) Mask for the design of Mesa, (b) optical image of the fabricated PhC membrane with the Mesa (c-g) process flow of creation of mesa structure with suspended PhC membrane.

### 3.3.6 Membrane release and Critical Point Drying

To achieve suspended InP membrane now it is necessary to etch the sacrificial $SiO_2$ layer underneath InP layer. This is done by using a diluted AF solution (10%) for underetching the InP membrane (Figure 3.11(g)). The sample is placed inside the solution for about 15' in order to fully remove the sacrificial layer while also removing the HSQ resist.

The following step after under-etching of the sacrificial layer is to consecutively clean the sample in water and then drying. However, the use of water results in capillary adhesion between the bottom layer of InP and top of the substrate. This makes proper release of suspended membrane very difficult (Figure 3.12(a)).

This problem however could be overcome by using a technique specialized exclusively for this purpose called Critical Point Drying abbreviated as CPD. At the critical point liquid and gaseous phase of a physical system is indistinguishable. Compounds which are at the critical point can be converted into liquid or gaseous phases without going through the interface between the liquid or gaseous phase thereby avoiding the damaging effects discussed before. However, in practical situations application of this method by using water is not feasible as critical point of water lies at 374°C and at 229$bar$, which will destroy any micro-structure. Thus a more practical solution of this problem is to use $CO_2$ as the liquid medium whose

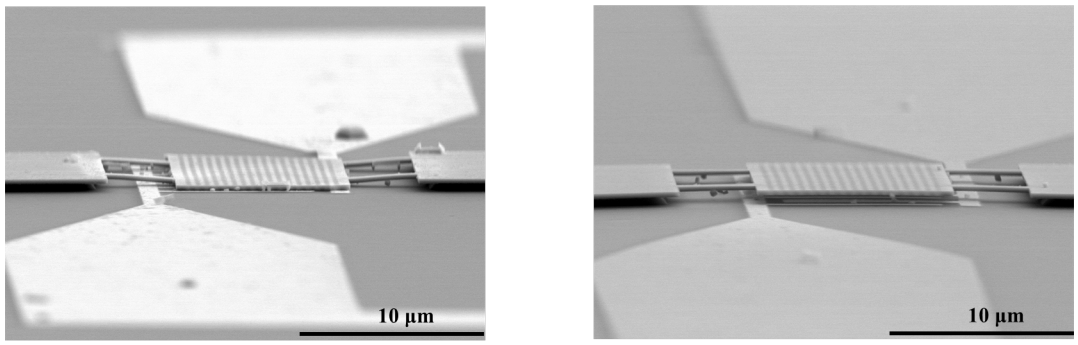


Figure 3.12: Comparison of membrane fabricated (a) without critical point drying (b) with critical point drying.

critical point lies at 31°C and a pressure of around $74bar$ (Figure 3.13). These conditions are more rational for the micro/nano structures and also comparatively easier to maintain. At the same time $CO_2$ is dangerous as a transitional fluid as it is not miscible with water at all. The water thus has to be replaced with another liquid which is miscible in water as well as in $CO_2$ at the same time. This problem is solved by using isopropanol, this exchange fluid will not be used for critical point drying as its critical point is considerably high (241°C, $61bar$). Rather at pre-critical point drying step water is replaced with isopropanol. The transfer of sample from a water bath to isopropanol bath is crucial; it has to be quick and at the same time it is necessary to make sure the liquid adhered to the bottom surface does not roll down which could lead to collapsed membranes even before the CPD process is used. In the chamber then the isopropanol medium is replaced by liquid $CO_2$, which is then brought to the critical point and converted to gaseous phase by decreasing the pressure at a constant critical point temperature (Figure 3.13) [89]. The result of this step is suspended membranes with almost 90% fidelity (Figure 3.12(b)). The collapsing of the remaining 10% of membranes we believe comes from other processing or post-processing steps rather than the capillary adhesion effect.

### 3.3.7 Wire bonding to the external environment

This is the last step of the fabrication of the NOEMS platform. This step is to connect the on-chip electrodes with the external environment. This is necessary as this way the electrodes could be driven by signal generators from outside the vacuum chamber. The process of wire bonding is quite straight forward; the sample is firstly placed on a hot plate at a temperature of around 100°C. Keeping the temperature at this constant value, Au wires of diameters around $50\mu m$ are pressed on top of the on chip electrode pads (Figure 3.14(a)). With optimized conditions (for example; force on the tip, pressure on the wire, length of the wire loop) the wire sticks to the electrode pads on the chip and now this wire can be brought outside to connect to some external medium (Figure 3.14(b)). Even though these

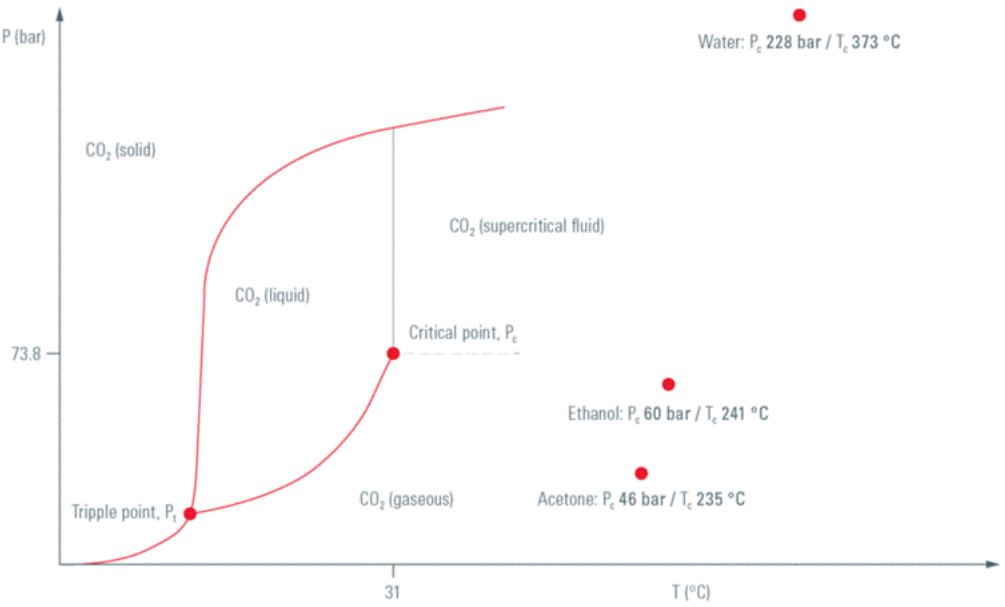


Figure 3.13: Phase diagram showing the supercritical transition of $CO_2$ [89].

wires have low diameters, they are quite robust and can support frequency up to $100GHz$. For our experiments as we mainly focus in the $MHz$ regime thus these wires can be used without any issues. The diameters of the wires however limit the design of the electrode pads on chip. Also the 'ARIES' chip on which the sample is stuck is supplied only with 44 pins which also limits the connections. For these reasons we are limited to fabricate only 20 electrode-membrane systems on a single chip.

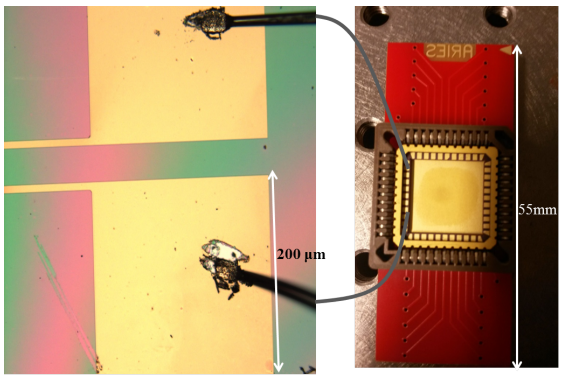


Figure 3.14: Wire bonding: connecting on chip electrode pads (a) to the external medium (b).

## 3.4 Actuation in linear regime

The scheme of actuation is quite simple and it is shown in Figure 3.15: the system consists of a signal generator which is able to excite the membrane electrode system up to $50MHz$. One arm of the signal generator is fed to the electrode and another arm is connected to the lock-in amplifier which locks to the actuation frequency. The detected optical signal is fed to a photodetector which converts the optical signal to an electrical one and this signal is then fed to the receiver on the lock-in amplifier.

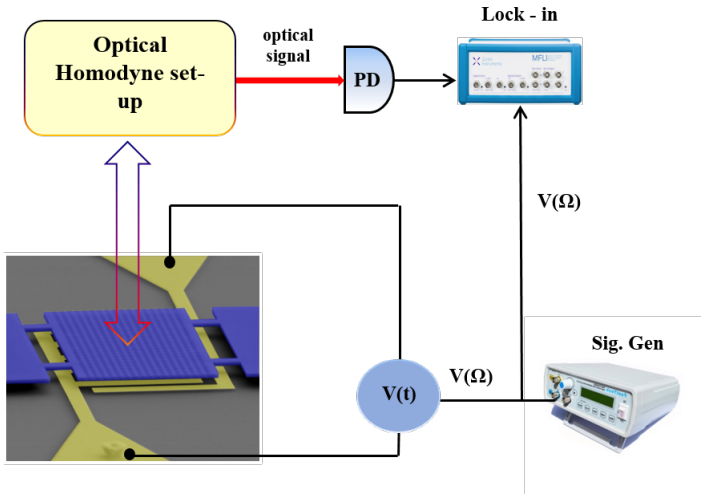


Figure 3.15: Actuation scheme of the integrated electrode-membrane NOEMS system.

### 3.4.1 Measurement of the mechanical response spectra

In this section we will look into the experimental results obtained by actuation of the PhC membrane via the IDEs and the interferometrically detected noise spectrum. In order to fully comprehend the experimental results we will refer to equation (3.6), where we got rid of the second part of the forcing term which is related to the DC stress applied to the system. The AC voltage applied to the system is actually the voltage which is responsible for excitation of the eigenmodes. When the actuating frequency is close to the one of the eigenfrequencies, the oscillator starts to oscillate and thereby producing signal at the receiver end. Thus in general the actuating voltage can be written as:

$$V(t) = V_{ac} cos(\Omega_{drive} t) \tag{3.8}$$

Here, we define $\Omega_{drive}$ as the driving frequency applied to the oscillator externally. When $\Omega_{drive} \sim \Omega_{m0}$ the oscillator starts to oscillate and amplify the motion of the corresponding eigen-mode. In the first experiment we fix $V_{DC} = 0V$ and fix $V_{ac} = 5V$. Then we vary the driving frequency $\Omega_{drive}$, this frequency is varied from $2MHz$ to $17MHz$ and the resulting spectrum is displayed in Figure 3.16. Between $2 - 10MHz$ six mechanical modes are clearly visible (Figure 3.16(b)) and the corresponding simulated modes (FEM) are shown in Figure

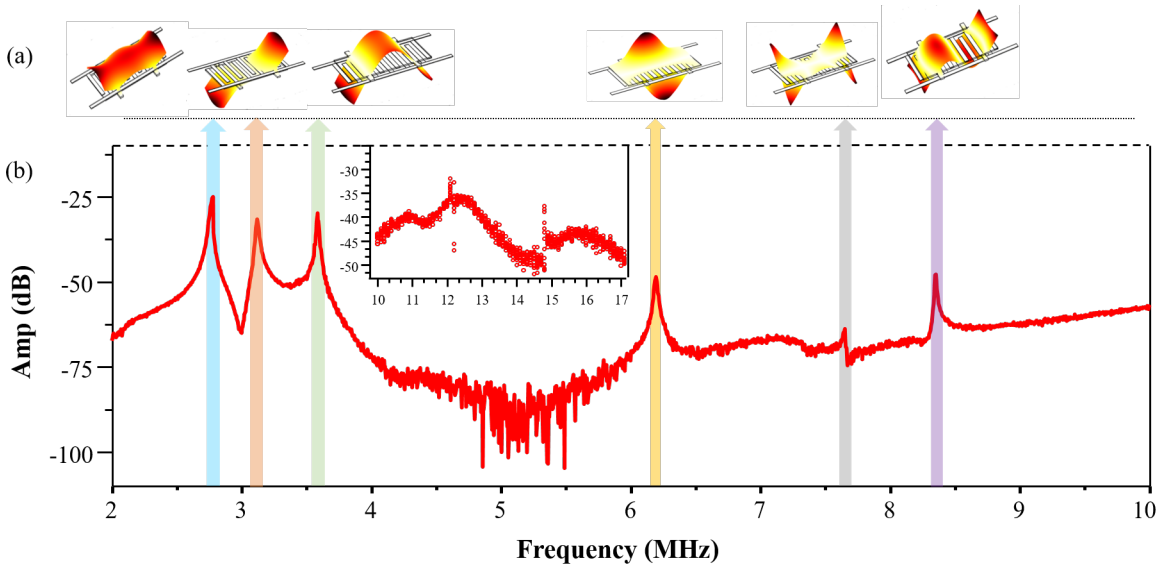


Figure 3.16: (a) FEM simulation of 6 different mechanical modes, (b) observed mechanical spectra while the membrane is actuated externally via interdigitated electrodes; actuation up to 20 MHz was done in this case.

3.16(a). In the inset we show two higher order modes between $10 - 17MHz$. Although here we scan up to $20MHz$ but thanks to the integrated actuation scheme it is possible to scan up to any desirable frequency (no cut-off frequency for applied voltage). Response of the first six modes are quite strong and easily observable while the two higher order modes (between $10 - 17MHz$) are comparatively weak and difficult to detect. The reason can be many fold; firstly the amplitude of displacement is smaller for higher order eigen-modes due to lower Q-factors. Secondly for higher order mechanical modes the overlap between the incident laser spot and the mode profile is smaller, thereby reducing the detected intensity. The third reason can be attributed to the electrical noise present in the system. With higher frequency there is a gradual enhancement in the noise level of the response (Figure 3.16(b)) which degrades the signal to noise ratio (SNR) of the response. Thus even if there is considerably high motion of the membrane for this mode, the response might be buried in the noise itself. And the final reason can be attributed simply to the electrode design. The choice of the electrodes as it was mentioned previously, was mainly due to the fact that it was an efficient design strategy in order to uniformly actuate the first mode i.e. the 'drum mode'. While as we move towards higher order modes it becomes more and more difficult to actuate them with similar efficiency with this kind of electrode design.

In Figure 3.17 we zoomed on the mechanical spectra of the first two modes each for a drive $V_{ac} = 1.0V$. Figure 3.17(a) displays the amplitude as well as the phase response of the mode 1. We are able to retrieve the amplitude as well as the phase response of the system thanks to the BHD scheme. This mode is centered around $2.75MHz$ and a Lorentzian fit yields a $\Gamma_m$ of $0.9kHz$, that is a quality factor of around 1000, which is of the same order compared to the one extracted for piezo stack excitation in the previous chapter. So we are

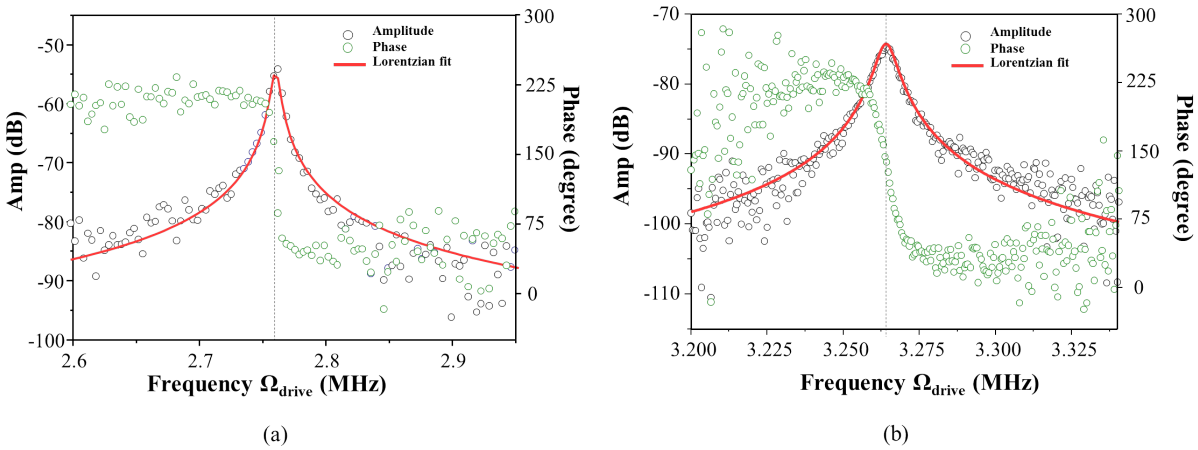


Figure 3.17: (a) Mechanical displacement amplitude as well as phase response of the first drum mode for $V_{ac} = 1.0V$, (b) mechanical displacement amplitude and phase response of the second mode for $V_{ac} = 1.0V$.

able to achieve what was promised in the last chapter i.e. (1) excite the eigen-modes more efficiently, (2) increase the coupling between the electrical field and the mechanics and finally, (3) integration without loosing quality of the mechanical response which is governed by the quality factor of the NOEMS platform. As the frequency of actuation is modulated around the eigenfrequency the phase of the response rotates by 180°. While the second mode is displayed in Figure 3.17(b), this mode has $\Omega_{m0} = 3.2625$MHz and the evaluated $\Gamma_m$ is about $1.3kHz$ for this mode. As the Q-factor is related inversely to the damping factor $\Gamma_m$, one can conclude that this particular mode has a lower value of the Q-factor compared to the first one.

### 3.4.2 Power dependence of the eigen-modes (under AC actuation)

In the next set of experiments we varied the AC actuating voltage $V_{ac}$ and performed a sweep of $\Omega_{drive}$ between $2-10MHz$ for different values of $V_{ac}$ ranging from $0.25V$ to $2.5V$. We made sure that the system is still well below the nonlinear threshold and for each sweep all other conditions like vacuum, filter parameters, sweep range were kept constant. The resulting spectra is shown in Figure 3.18(a). At the lowest voltage $V_{ac} = 0.25V$ only the first order mode is barely visible while the higher order modes do not appear. The 3rd mode starts to appear from $V_{ac} = 0.50V$ while the second mode seems to appear from $V_{ac} = 0.75V$. This mode apparently is less visible because of the optical probing scheme which was discussed in section 3.4.1. At around $V_{ac} = 2.5V$ as many as five modes are visible in the considered spectral range. Response of the first three modes were fitted with the Lorentzian function and the Q-factor was extracted for each case. The extracted values of Q-factor is plotted in Figure 3.18(b) for the first three modes. These three modes exhibit quality factors which are around 1000 inside the linear regime. There is a mild decrease of the Q-factor with $V_{ac}$, this might be due to enhanced dissipation at a higher actuating power.

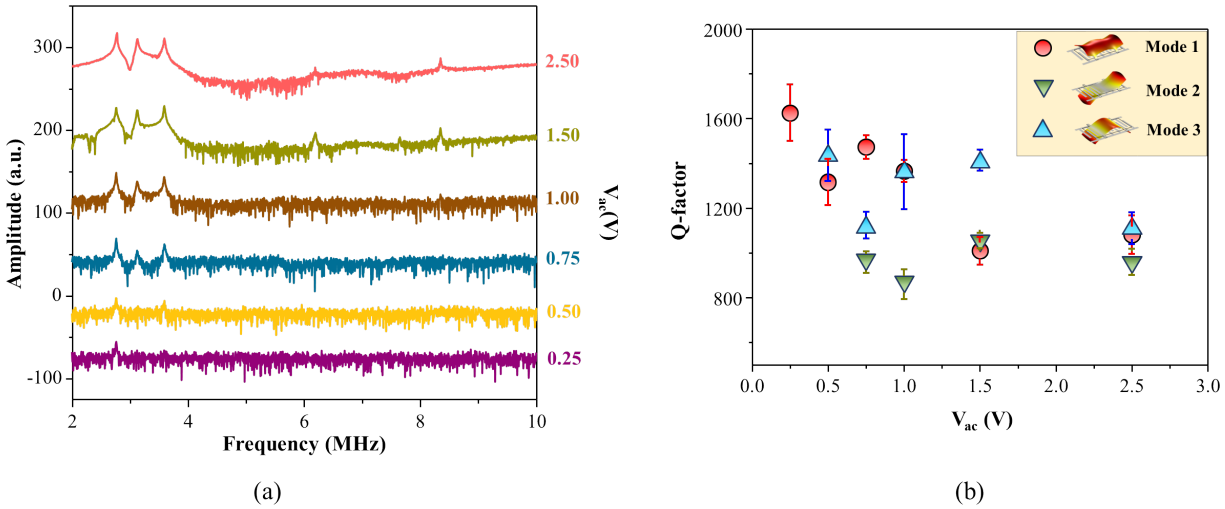


Figure 3.18: (a) Power dependence of the first and second mode within the linear regime (b) Q factor dependence on the applied $V_{ac}(V)$.

### 3.4.3 Calibration of the displacement

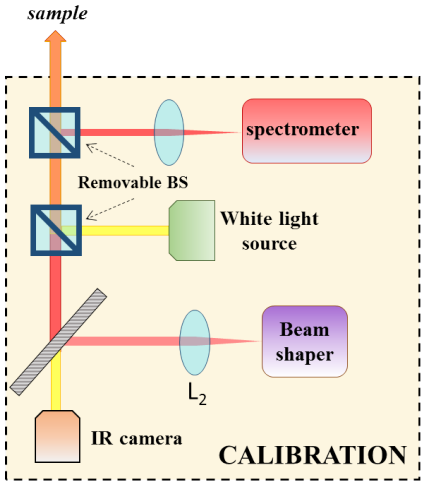


Figure 3.19: Set-up for optical calibration of the membrane displacement.

After we could retrieve the mechanical modes, one of the first objective was to perform proper calibration of the membrane displacement. This process is essential in order to retrieve the electro-mechanical coupling coefficient. The calibration process was based on the method followed by Yeo et al. [31]. The sample is placed on top of a stage which is controlled by three piezomotors called picomotor (Newport), which gives mobility along the three axes. As the picomotors could be controlled externally with an external Lab-View programming it gave us an added advantage. In order to comprehend properly how the calibration works we introduce

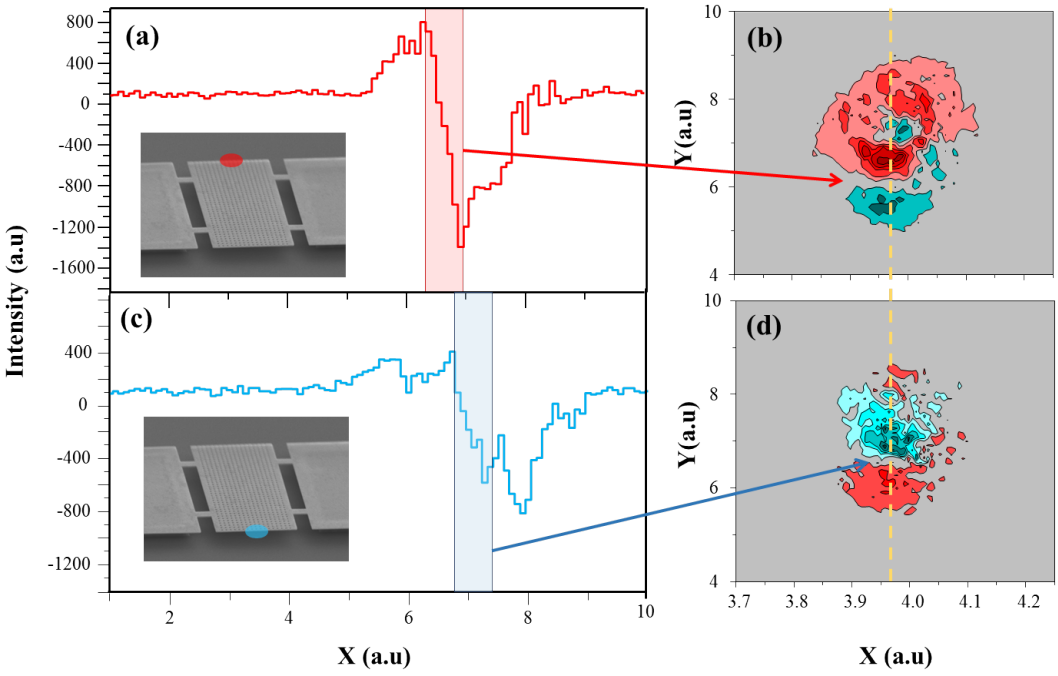


Figure 3.20: (a,b) XY calibration procedure of the membrane displacement; the highlighted regions in both figures shows the region corresponding to the laser spots (at two membrane edges) shown in the SEM image, the diffraction of the laser beam at these edges results in such a slope in the detected intensity (b,d) surface plot of the detected intensities at the corresponding regions.

the part of the optical set up used for calibration in Figure 3.19. The characterization of the membrane displacement requires specific attention to the beam spot on the membrane; the beam spot should be as close to a Gaussian beam shape as possible. This part was taken care of by using a beam shaper to obtain the desired beam profile before beginning the calibration process. It was also imperative to find a good focal spot on the membrane, this was done by observing the reflected optical reading from the membrane at the BHD end. Our plan was to use a two dimensional mapping in order to properly find a calibration:

- **XY map**: To calibrate each step of the picomotor we move the piezomotor stage from one edge of the membrane to another end while going always in one direction to avoid hysteresis. Knowing the distance from one end of the membrane to the other it is easy to calibrate each step of the piezo. The idea is to place the laser spot first on one edge of the membrane (Figure 3.20(a)) which gives a strong gradient on the reflected optical signal (Figure 3.20(b)) on CCD sensor of the spectrometer. Now the membrane is moved (in order to move the laser spot on top of it) by a fixed amount of steps until similar effect is observed on the other end (Figure 3.120(c) & (d)). Then finally knowing the distance traveled to be $20\mu m$ imposed by fabrication, if we divide this by

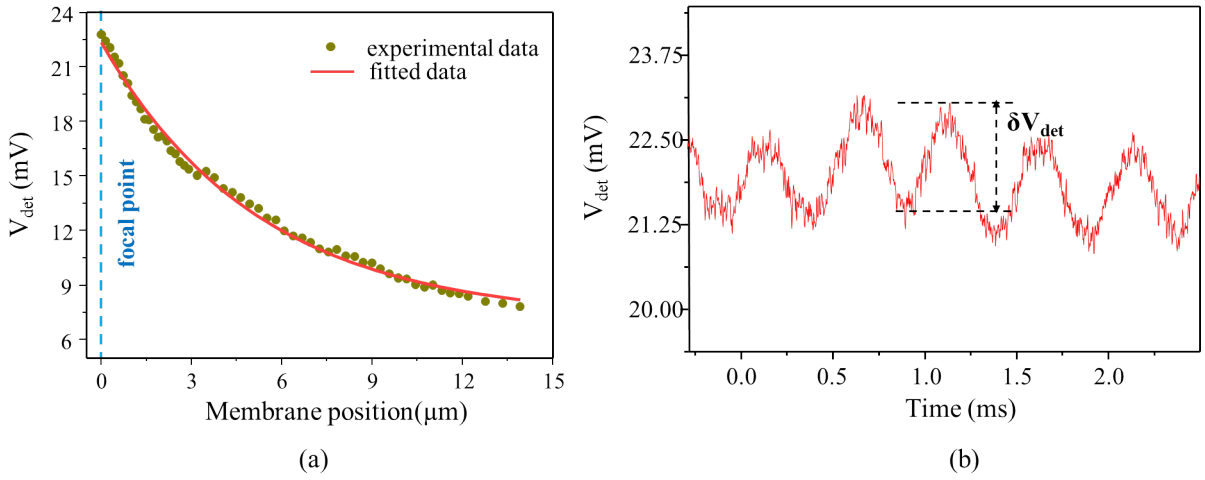


Figure 3.21: (a) Mapping the z-axis: position of the membrane along z-axis vs. detected voltage at the BHD output with no membrane excitation, (b) oscillation of the output voltage while the membrane (placed at the focal point) is resonantly excited, the fluctuation is directly related to the membrane displacement.

the number of steps the piezo traveled we will finally achieve to calibrate the piezo. The process is repeated many times in order to cancel out any error that might appear. The resulting calibrated step of picomotor is about $(29 \pm 1.5)nm$ which agrees quite well with the one specified in the manual: "less than $30nm$".

- **Z-axis map**: This is the second map and the final stage to calibrate the membrane displacement. This could be done by displacing the sample with the piezo stage along the z-axis i.e. along the focal plane. This essentially means that when the membrane is displaced, the beam is not properly focused on the membrane anymore and as a result there is a change in the reflected optical intensity which will be imposed in the detected output voltage. Membrane position of $0\mu m$ signifies that the membrane is at the focal point of the laser spot, now as the membrane is displaced with the help of the piezo we observe an exponential decrease in the detected voltage $V_{det}$(Figure 3.21(a)). An exponential fit with the recorded data gives (here we assume that all the piezo motors traverse same distance at a single step):

$$V_{det} = 0.0071 + 0.0152exp(-0.189x) \tag{3.9}$$

Here we can compute small fluctuations around the focal point by doing derivation of equation (3.9) and putting $x = 0$, this yields:

$$\delta V_{det}(mV) = 0.0152 * (-0.189)\delta x(\mu m) \tag{3.10}$$

Now when the membrane is resonantly excited, the membrane starts to fluctuate about its mean position (which is at the focal point of the laser beam). This situation is represented in Figure 3.21(b), where we observe fluctuation of the detected voltage with time related

to the membrane excitation. Now the fluctuation of the detected voltage is related to the displacement governed by equation (3.10). Hereafter considering first the influence of several mirrors, beam splitters in the path (which divides the optical intensity by several factors) and then knowing the relation between excitation voltage $V_{ac}$ and detected voltage $V_{det}$, we finally conclude:

$$\frac{\delta x}{\delta V_{ac}} = 2.18\ nm/V \tag{3.11}$$

The obtained value of the coupling is in good agreement with the predicted $4nm/V$ by FEM simulation in the previous chapter.

### 3.4.4 Tuning of eigenfrequency by DC polarizing voltage

Up to this section we have not considered the effect of the DC polarizing voltage, in this section we will try to discuss the effect of this voltage on this membrane-electrode system. The effect of such DC voltage on these kind of platform has already been discussed by Unterreithmeier et al. [40] and Bagci [16] et al. on nanomechanical and nano opto mechanical platform. When along with the fluctuating AC power $V_{ac}$ this DC polarizing voltage is also turned on, the effective force acting on the oscillator becomes:

$$\delta F = \frac{1}{2}\frac{d^2C}{dx^2}|_{x=x_0}V^2\delta x + \frac{1}{2}\frac{dC}{dx}|_{x=x_0}V\delta V \tag{3.12}$$

The effect of this $V_{DC}$ on the dielectric InP membrane is to independently control the strength of polarization on the membrane. This polarization results in a dielectric gradient acting across the thickness of the membrane causing it to deform and thereby producing a DC stress on the membrane. This stress is thus independent of frequency and a higher amount of stress can be generated just by applying higher $V_{DC}$. The first term in equation (3.12) represents the DC polarizing force on the membrane. What is notable here is that this component of force is directly proportional to the fluctuation of vertical position of the PhC membrane $\delta x$. This is equivalent to a spring where the force acting on the system is directly proportional to the displacement i.e. $F = k\delta x$. Using this analogy we can conclude that this force acting on the membrane directly affects the spring constant of the system and eventually modifies the equation of motion of the oscillator. Under this changed condition one is able to write:

$$\ddot{x} + \Gamma_m\dot{x} + (\Omega_{m0}^2 - \alpha V_{DC}^2)x = \delta F \ \ where, \delta F = -\frac{1}{2}\frac{dC}{dx}|_{x=x_0}V\delta V \tag{3.13}$$

Where we assume that the factor $\alpha$ takes into account the amount of modulation of spring constant the polarizing voltage is able to perform. If we perform a Fourier transform of equation (3.13) and solve for displacement $x(t) = X(\Omega)exp(-j\Omega t)$, then we can write:

$$X = \frac{F}{(\Omega^2 - \Omega_{m0}^2 + \alpha V_{DC}^2)^2 + \Gamma_m^2\Omega^2} \tag{3.14}$$

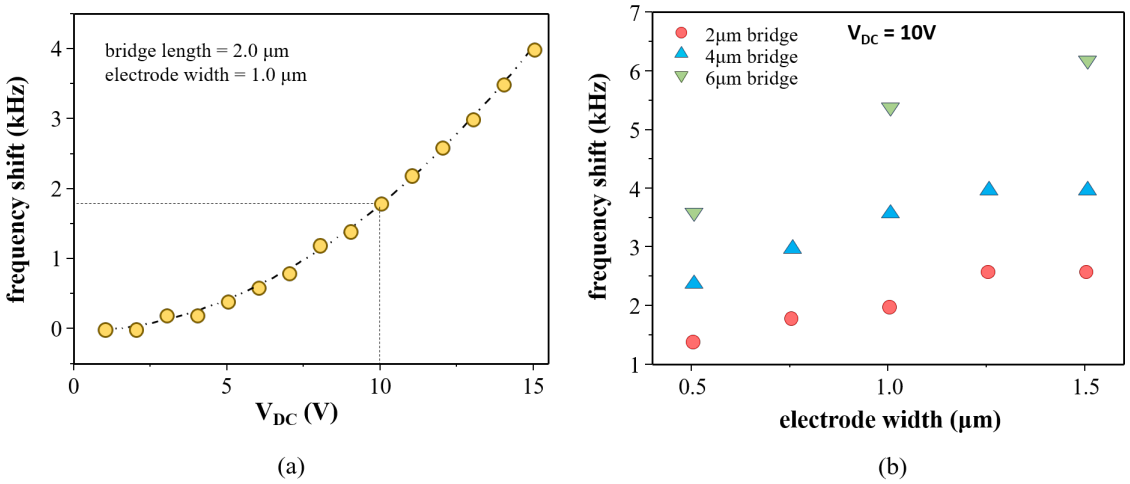


Figure 3.22: (a) Shift of eigenfrequency with $V_{DC}$ for a fixed geometry (b) Variation of eigenfrequency with the membrane and electrode geometry.

Resonance occurs when the denominator is minimum. Thus if we define the resonant frequency as $\Omega_m$, one can write:

$$\Omega_m = \Omega_{m0}(1 - \frac{\alpha V_{DC}^2}{\Omega_{m0}^2})^{1/2} \tag{3.15}$$

Under approximation that $\alpha V_{DC}^2 \ll \Omega_{m0}$ we can finally write:

$$\Omega_m = \Omega_{m0}(1 - \frac{\alpha V_{DC}^2}{2\Omega_{m0}^2}) \tag{3.16}$$

Thus the eigenfrequency is quadratically dependent on the applied $V_{DC}$, although the factor $\alpha$ finally determines how much shift in eigenfrequency is possible with $V_{DC}$. This $\alpha$ factor is dependent on material properties such as dielectric constant, stiffness matrix, membrane geometry as well as on the electrode designs. We have observed a considerable amount of dependence of the observed shift on the electrode width and period. To fully comprehend this effect we performed some FEM simulation via COMSOL Multiphysics on such a electrode-membrane platform. The simulation results are displayed in Figure 3.22. In the first simulation we fix the bridge length to $2\mu m$ and width of the electrode teeth to $1\mu m$ and then vary the applied $V_{DC}$ on the oscillator. As it can be observed from Figure 3.22(a) we are able to observe clearly an eigen-frequency shift of the oscillator and the dependence of this shift is parabolic as predicted by equation (3.16). Next we fix $V_{DC}$ at $10V$ and start playing with the membrane and the electrode geometry. Firstly we fix the bridge length to $2\mu m$ and then vary the electrode width from $0.5\mu m$ to $1.5\mu m$. Here we are able to clearly observe a shift in eigenfrequency of about $2kHz$ with electrode width. We repeat the same simulations for two other bridge lengths of $4\mu m$ and $6\mu m$. From the results (Figure 3.22(b)) we can conclude that there is an increase of frequency shift with bridge length. This is expected as

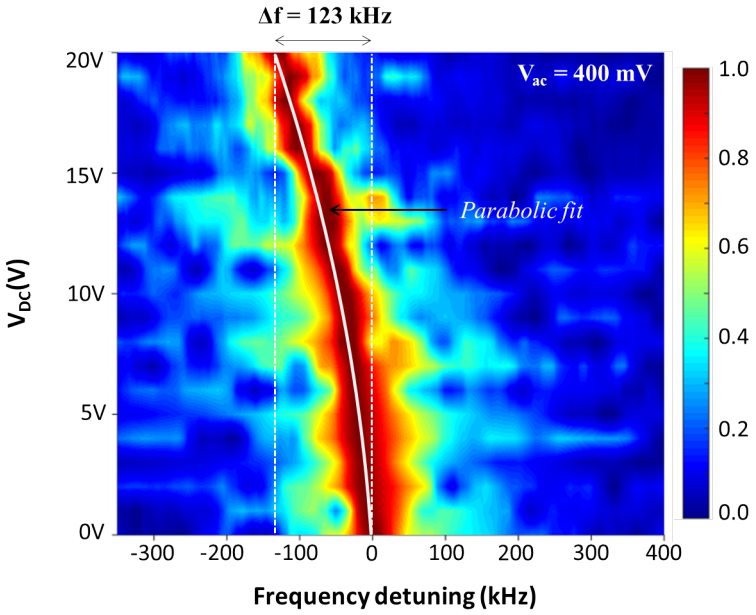


Figure 3.23: Tuning of eigenfrequency with $V_{DC}$ with corresponding parabolic fit (white line).

higher bridge length means lesser residual stress on the membrane and thus it is much easier to modulate the spring constant. But of course the bridge length as well as electrode width could not be increased indefinitely due to technical issues. However in conclusion we can say that the parameter $\alpha$ mentioned above is highly dependent on the membrane, electrode geometry.

Next, we move to the experimental realization of this principle. In the experiment first of all we fix the resonant drive at a constant value while making sure the system is far beyond nonlinear threshold, and then systematically vary $V_{DC}$. We fix $V_{ac}$ at $400mV$ and for each $V_{DC}$ we sweep the driving frequency $\Omega_{drive}$ around the mechanical resonance $\Omega_{m0}$ while recording the spectral response. Figure 3.23 shows the experimental results; here $V_{DC}$ is varied from $0V$ to $20V$ and a shift of about $125kHz$ is observed. However compared to the simulated result this shift is much higher (simulated shift was only about $2kHz$). The reason can be attributed to the overestimation of the residual stress in the simulations. The effect that is observed here is called spring softening effect as there is a decrease in the eigen-frequency of the system. More discussion on spring softening is done in Chapter 4. The shift as it can be seen from the figure is also parabolic as it was predicted by equation (3.16). This curve now can be fitted with this equation and from that fit one should be able to extract the parameter $\alpha$.

For the estimation of the parameter $\alpha$ we come back to equation (3.16) and rewrite the equation in the form:

$$|\Delta f| = |\frac{\Omega_{m0} - \Omega_m}{2\pi}| = \frac{\alpha V_{DC}^2}{4\pi} \tag{3.17}$$

When we fit the resulting frequency shift with this formula we are able to estimate value of $\alpha$ of about $4.31kHz/V^2$. The fit is shown by the white parabolic line in Figure 3.23.

## 3.5 Conclusion

This chapter was mainly focused on the implementation and preliminary investigation of the integrated electrode membrane platform. We started by introducing the basic principle of the membrane electrode structure: how it looks like, how the actuation works, how we optimize the electrode architecture via calculation of electromechanical coupling parameter. As a next step we move forward to the design and fabrication of these platforms. We discussed in details about the fabrication principles, conditions, challenges and finally how to overcome them. After that we discussed in brief about the first experiments on this NOEMS platforms especially actuation in the linear regime. We saw that with these integrated electrodes we were able to actuate the membranes much more efficiently compared to the piezo stack excitation. We saw that with BHD set up we are able to extract the amplitude as well as the phase response of the mechanical modes. This was followed by a discussion on the calibration of the membrane displacement when it is actuated by the electrical forces, from here we were able to calibrate the electromechanical coupling coefficient experimentally which supported the theoretical prediction quite closely. And finally we showed that keeping the system inside the linear regime it is possible to tune the eigen-frequency of the system by simply playing with the DC stress applied on the system.

A noteworthy mention is that in all of these discussions we kept the actuating voltage in a range such that the system remains inside the linear regime. Especially in Figure 3.18(a) we can see that the response keeps on growing with a symmetric spectral shape as we keep increasing the actuating voltage. However in next chapter we will see what happens when we cross a certain threshold voltage of actuation which pushes the system beyond the linear regime and inside the nonlinear regime. The following two chapters will focus on discussing some theoretical and experimental results while the system is deep inside the nonlinear regime. Phenomena like sub/super-harmonic resonance with parametric excitation/amplification will be discussed in chapter 4, while chapter 5 will focus on discussion of another nonlinear dynamical phenomenon called stochastic resonance.

# Chapter 4

# Actuation in Nonlinear regime

In this chapter we will concentrate on studying the behavior of our Nano Opto Electro Mechanical System in the nonlinear regime. NOEMS and NEMS devices [90][91][92][93][52] have witnessed huge advancement in the last decade in terms of advance in nano-technological applications like metrology or signal processing for instance. At the same time these devices have garnered attention for their effectiveness to study and explore nonlinear dynamical behavior. The study of nonlinear dynamics is of utmost importance in terms of application in different fields including signal/noise amplification, detection etc. Also nanoscale fabrication allows design of many coupled nanomechanical systems on a single chip, opening the way to study collective nonlinear dynamics effects of intermediate numbers of degrees of freedom.

For simplicity the discussion in this chapter will begin considering most simple kind of nonlinearity, called Duffing nonlinearity and then gradually move towards more complicated nonlinear dynamics. Both theoretical predictions and experimental response of a Duffing oscillator will be discussed in the first sections. The discussion will then move towards study of sub and super harmonics in forced oscillation regime, while discussing both theoretical and experimental aspects. This will be preceded by discussion on parametric amplification in weak actuation regime of the resonator. And finally the chapter will conclude with study on tuning the nonlinearity of the nano electro mechanical resonator by parametric excitation beyond the nonlinear threshold regime.

## 4.1 Duffing Nonlinearity

### 4.1.1 Origin of nonlinearity

Whenever a mechanical oscillator is considered, the first system that comes to the mind is a simple harmonic oscillator which follows Hooke's law of linear restoring force. The restoring force acting on such an oscillator is directly proportional to its displacement $x$. However this approximation does not hold true whenever a large deformation is involved. What makes micro and nano-mechanical systems very interesting candidates is that they can encounter nonlinear dynamics even before the intrinsic nonlinearity is imposed. The nonlinearity can arise in the system due to two main reasons:

(1) Firstly it can arise when the external force crosses a certain threshold and thereby induces high stress which generates nonlinearity in the system.

(2) Secondly this can happen due to effects induced by geometry even though the forces in play are linear.

The second factor is more interesting, where inherent geometrical effects causes nonlinearity to appear in the system. This situation is what is mostly encountered in NEMS/MEMS systems rather than the former one. In general these resonators are quite thin and when the amplitude of vibration exceeds the resonator width, nonlinearity is imposed in the system. Any system under such constraint can be described by Euler-Bernoulli equation. If we define the transverse displacement as $X(z,t)$, which is much smaller than the length of the doubly clamped beam $L$ we can write [**?** ]:

$$\rho S\frac{\partial^2 X(z,t)}{\partial t^2} = -EI\frac{\partial^4 X}{\partial z^4} + T\frac{\partial^2 X}{\partial z} \tag{4.1}$$

Here, $z$ is along the length of the beam, $S$ is the area of cross-section of the beam, $E$ is the Young modulus of the beam, $I$ is moment of inertia and $T$ is the tension arising from clamping on the beam. Now tension $T$ can be written as:

$$T = T_0 + \Delta T \tag{4.2}$$

where, $T_0$ is the inherent tension on the beam and $\Delta T$ is the tension induced from bending of the beam caused by external stress. Let us consider this additional tension causes beam length to be changed by an amount of $\Delta L$, this change can be either tensile or compressive. From the definition of Young's modulus the additional strain $\Delta T$ on the resonator can be written as:

$$\Delta T = ES\frac{\Delta L}{L} \tag{4.3}$$

For small displacement the total length of the beam can be expanded as:

$$L + \Delta L = \int_0^L dz\sqrt{1 + \left(\frac{\partial X}{\partial z}\right)^2} \simeq L + \frac{1}{2}\int_0^L dz\left(\frac{\partial X}{\partial z}\right)^2 \tag{4.4}$$

using the equation above, equation (4.1) can be transformed to:

$$\rho S\frac{\partial^2 X(z,t)}{\partial t^2} = -EI\frac{\partial^4 X}{\partial z^4} + \left[T_0 + \frac{ES}{2L}\int_0^L dz\left(\frac{\partial X}{\partial z}\right)^2\right]\frac{\partial^2 X}{\partial z^2} \tag{4.5}$$

In order to find a perturbative solution of the equation (4.5) we define solution of $X(z,t)$ as:

$$X_m(z,t) = x_m(t)\phi_m(z) \tag{4.6}$$

Here $\phi_m(z)$ is the spatially confined eigen-mode and we assume that the local maximum of the eigen-mode that is nearest to the center of the mechanical oscillator is scaled to 1. While $x_m(t)$ measures the actual displacement nearest to the center of the mechanical oscillator. Now if we multiply both sides of equation (4.5) by $\phi_m(z)$ and integrate over z, after some steps of integration by parts it can be shown that the equation of motion for the $m$-th order mode $x_m(t)$ is [**?** ]:

$$\ddot{x}_m(t) + \left[\frac{EI}{\rho S}\frac{\int \phi_m''^2 dz}{\phi_m^2 dz} + \frac{T_0}{\rho S}\frac{\int \phi_m'^2 dz}{\phi_m^2 dz}\right] x_m + \left[\frac{E}{2\rho L}\frac{\left(\int \phi_m'^2 dz\right)^2}{\int \phi_m^2 dz}\right] x_m^3 = 0 \tag{4.7}$$

Note that the coefficient of $x_m^3$ in equation (4.7) represents the amount of nonlinearity present in the system. Indeed if an oscillator is under nonlinear regime, then another component of the restoring force (along with the one obeying Hooke's law) acting on the system becomes proportional to the cube of oscillator displacement i.e. $F_{restoring} \sim x^3$. If we define the proportionality constant as $\beta_3$ we can define the restoring force to be $\beta_3 x^3$. This turns a simple harmonic oscillator with a linear restoring force into a Duffing oscillator. Thus using some approximations and dropping the suffix $m$, we can write equation (4.7) for the $m$-th order mode as:

$$\ddot{x}(t) + \Omega_m^2 x\left[1 + \beta_3 x^2\right] = 0 \tag{4.8}$$

Here we define $\Omega_m$ as the angular eigenfrequency of the $m$-th order eigen-mode and $\beta_3$ as the coefficient of Duffing nonlinearity.

Moreover, sign of the nonlinearity factor $\beta_3$ governs the nature of the induced nonlinearity. When sign of this $\beta_3$ factor is positive, this nonlinear restoring force works in such a way that it assists the linear restoring force thereby making the oscillator more difficult to excite and eventually increasing the natural resonance frequency. This effect for this very reason is known as spring hardening effect. The opposite situation of this is when the coefficient $\beta_3$ becomes negative. In such a situation the nonlinear restoring force works against the linear restoring force thereby making the oscillator easier to excite and shifting the natural resonance to a lower value. This is therefore known as the spring softening effect.

In other situations nonlinearities can be induced from nonlinearity in actuation or detection mechanisms that are interacting with the system. Other sources could include clamping of the mechanical oscillators with the surrounding medium.

Finally another source of nonlinearity can arise due to damping mechanisms that act on a mechanical oscillator. One can imagine that when a resonator is under a nonlinear restoring force (i.e. when the restoring force is proportional to $x^3$) then along with linear damping which is proportional directly to the velocity $\dot{x}$ there would another nonlinear damping term proportional to $\dot{x}x^2$. And this damping term should increase with increase in the amplitude of displacement $x$. Although in the following discussions to avoid complicacy we would neglect this nonlinear damping term.

### 4.1.2 The Duffing Oscillator

Typical behavior of a nanomechanical system in linear regime was discussed in the last chapter. It is well understood that behavior of a system in linear regime can be analyzed by considering it as a simple harmonic oscillator. The equation of motion of an oscillator in this regime can be described by equation (4.9).

$$\ddot{x} + \Gamma_m \dot{x} + \Omega_{m0}^2 x = \delta F \;\; where\, \delta F = F_0 \cos(\Omega_{drive} t) \tag{4.9}$$

Here, $\Gamma_m$ is the damping constant, $\Omega_{m0}$ is the linear natural frequency of the oscillator, $\delta F$ is the force acting on the oscillator at a drive frequency $\Omega_{drive}$. In the scenario when the system is in linear regime the response of the system follows simple Hooke's Law, which means the spring constant of the system is linearly proportional to the displacement i.e. the system has only a single stable point (indicated by figure 4.1(a)).

For ease of discussion a most common form of nonlinear equation is discussed, which was introduced in the previous section being famously known as the Duffing nonlinearity. In the Duffing model of nonlinearity only third order displacement term is taken into account and we would denote this nonlinear coefficient by $\beta_3$. The Duffing equation is a second order differential equation used to model damped and driven oscillator where the oscillator do not follow the simple Hooke's Law. This particular equation of motion is showed in equation (4.10).

$$\ddot{x} + \Gamma_m \dot{x} + \Omega_{m0}^2 x(1 + \beta_3 x^2) = \delta F \;\; where, \delta F = F_0 \cos(\Omega_{drive} t) \tag{4.10}$$

The restoring potential of such a system will not follow a simple linear rule i.e. restoring potential will not be a simple parabola (like in Fig. 4.1(a)). On the contrary it will have a rather complicated shape and the system will now have more than one stable states, in this particular case it will have two stable states and its potential will look like the one shown in Fig. 4.1(b), this is known as the bistability.

### 4.1.3 Bistability in amplitude and phase response

Solution of forced response of the system in Duffing regime is not straight forward as the linear superposition theory is no longer valid in this regime. The approximate Duffing response of the system can be derived by using secular perturbation theory [94] and the resulting equation is shown in equation (4.11).

$$|x|^2 = F_0^2 / [(1 + \beta_3 * x^2 - \frac{\Omega_{drive}^2}{\Omega_{m0}^2})^2 + \Gamma_m^2 / 4] \tag{4.11}$$

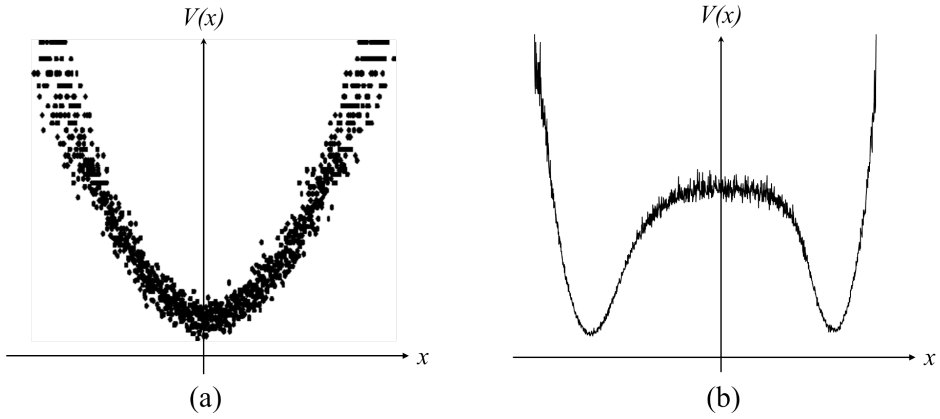


Figure 4.1: Potential of (a) linear oscillator with only a single stable state and of a (b) bistable system with two stable states.

Here $F_0$ is the amplitude of the external force, $\beta_3$ is the effective spring constant under Duffing approximation, $\Omega_{m0}$ is the undamped mechanical resonance frequency of the oscillator and $\Omega_{drive}$ is the driving frequency.

Also, the steady state response of the system does depend on the initial conditions, unlike the situation when the system is in linear regime. Interestingly the resonance of the system in this regime can also shift away from the natural resonant frequency attributed to the presence of nonlinearity in the system. Depending on several factors this shift in frequency can be either towards the red (or towards the blue side) of the frequency, this phenomena is known as the spring softening (or spring hardening) effect [**?** ][95], as it was discussed in the previous sections. This is mainly governed by the fact whether the system is under compressive or is under tensile stress [96]. Depending on the initial condition the nonlinear spring constant will either be positive or negative resulting in either decrease or increase (hardening or softening) in the natural resonance frequency when the system is in Duffing regime.

Solution of $x$ (equation (4.11)) can be found by using numerical programming. For our case MATLAB was used to derive the solution of this equation and the result is plotted in Figure 4.2. Both linear as well nonlinear response of the system is displayed in the figure. Figure 4.2(a) shows amplitude response of the system for three separate cases: firstly when the system is in linear regime (green curve); the response is simply a lorentzian. The response is linear as at each frequency of actuation there is only one accessible state i.e. an unique amplitude response of the oscillator. Secondly, when the excitation $F_0$ in equation (4.11) is high enough the response $x$ also goes towards the higher side. This means the nonlinearity factor $\beta_3$ is not negligible anymore and therefore the response becomes nonlinear. The nonlinear amplitude response while $\beta_3 > 0$ is shown by the blue curve in Figure 4.2(a). The blue shift of the resonant frequency means it's spring hardening effect. Under such a situation at some particular frequencies the system has access to two different amplitude states hence the bistability. This frequency range where the system exhibits such a bistable behavior is known

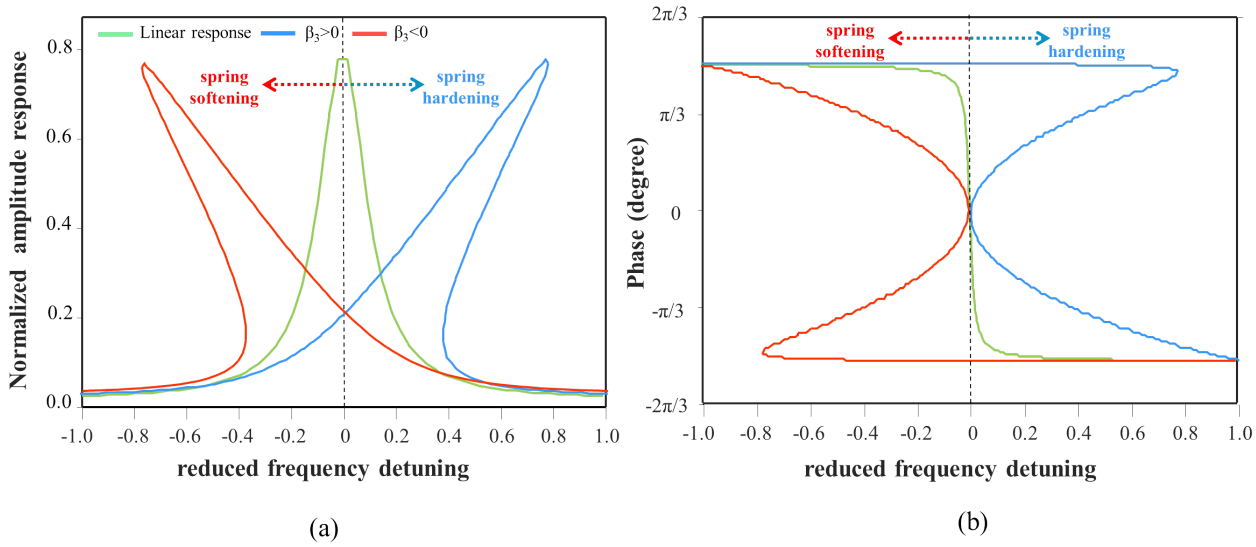


Figure 4.2: Oscillator response in (a) amplitude and in (b) phase for both linear and Duffing regime: In green it is the linear response of the oscillator, it is plotted by using standard lorentzian function; while in red and blue are the response of the system in spring softening ($\beta_3 < 0$) and spring hardening ($\beta_3 > 0$) configurations respectively.

as the hysteresis region. However when the parameter $\beta_3 < 0$ the eigenfrequency suffers a red-shift (Figure 4.2), thereby exhibiting the spring softening effect. Similar response can be observed also in phase response of the system; this situation is addressed in Figure 4.2(b), where like in the previous case we exhibit linear and spring softening as well as hardening phase response.

### 4.1.4 Phase space trajectory

Another interesting representation of the nonlinear systems can be shown through what is known as the phase space portrait of the system. A phase space of a dynamical system is a space where all possible states of the system are represented. Each state of the system is represented by an unique point in the phase space. For a mechanical system a phase space will consist of all the possible values of position and momentum of the system. Generally the displacement of the oscillator can be described as: $x(t) = R\exp(2\pi j\Omega_m t)$, where $R$ is the displacement amplitude of the membrane while the exponential term determines the phase of the mechanical oscillation. This term then can be expanded as $x(t) = R\cos(2\pi\Omega_m t) + jRsin(2\pi\Omega_m t)$ (here $\Omega_m$ is the frequency of mechanical oscillation). Now if one describes $X = R\cos(2\pi\Omega_m t)$ and $Y = Rsin(2\pi\Omega_m t)$, a polar plot with $R$ and $\Theta(= arctan(Y/X))$ as the coordinates will describe the phase portrait of the system. These phase portraits can be constructed by plotting the in-phase $X$ and out of phase component $Y$ of the displacement. The phase portrait of a system under study directly reveals several information about it; firstly it will exhibit clearly all the stable states of the system and at the same time might

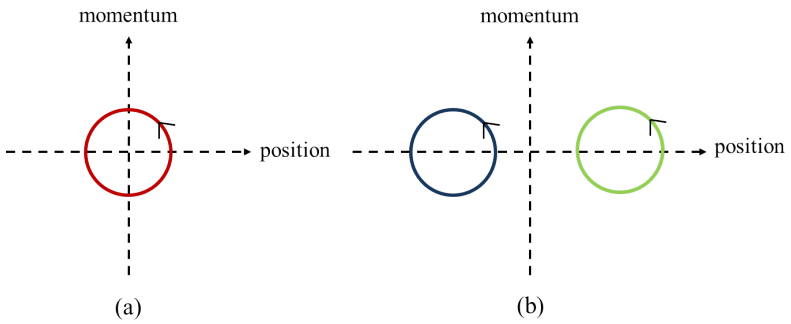


Figure 4.3: (a) Phase space trajectory of a resonator under linear regime with only a single phase state (b) in the bistable regime with two distinct phase states.

give indication about the existence of the unstable states of the system as well. For example in linear regime the phase space will give only a single state (Figure 4.3(a)), while in nonlinear regime the phase space can exhibit more than one stable state. This situation is displayed in Figure 4.3(b) where it is shown that two stable states of the system are observed in the bistable regime.

Such representations also allows to plot the phase space trajectory of a system under study. Observing how the system travels from its exited state to the rest state may reveal several information about the mechanical system under study. Firstly it gives a first hand estimation of the decay time of the system to the ground state which is directly related to the Q-factor of the system. The relation between the decay time $\tau_m$ and the Q-factor is defined as: Q $=\Omega_m \tau_m/2$, where $\Omega_m$ is the mechanical eigenfrequency. Also by observing how the system collapses to the rest state will give a direct indication of the nature of damping involved. If the system is undamped then it should keep on oscillating in the phase space even when the excitation is switched off. While system is overdamped if it returns to the rest state as quickly as possible without oscillating and finally the system is underdamped when the amplitude of oscillation gradually goes to zero with several oscillation before returning to the rest state.

## 4.2 Resonant excitation

In this section we will focus on the excitation of the NOEMS platform in the Duffing regime. We will investigate the bistable response in both amplitude and phase and finally focus on the response in phase trajectory of the system as well. Also we will see that how resonant excitation beyond nonlinear threshold generates several higher order harmonics at the same time.

### 4.2.1 Bistability of the fundamental mode: An hysteretic behavior

**Spring hardened oscillator:**

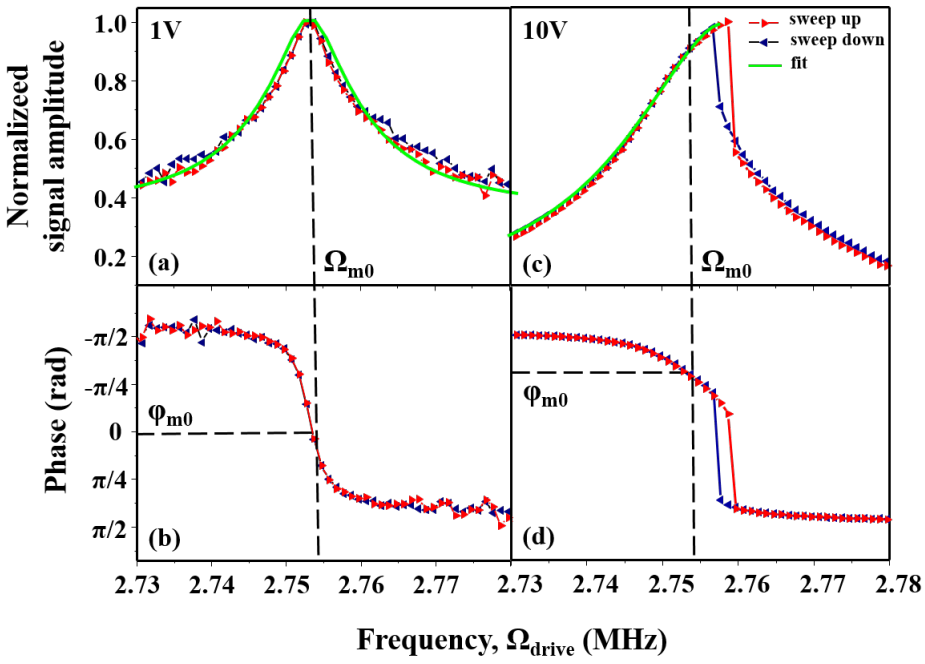


Figure 4.4: Normalized amplitude and phase response (at $V_{ac} = 1V$) of the system with the corresponding lorentzian fits shown in figure (a) & (b) displaying the response of the system when the system is in linear regime; (c) & (d) display the amplitude & phase response of the system with corresponding fits when the system is deep in the nonlinear regime ($V_{ac} = 10V$).

In this section the focus will shift towards the experimental results concerning Duffing nonlinearity under resonant excitation. The actuation in linear regime and the set up for characterizing the membrane displacement has been discussed in the earlier chapters. The force $\delta F$ acting on the system can be written as (provided the membrane is not pre-stressed by an external DC voltage):

$$\delta F = -\frac{1}{2}\frac{dC(x)}{dx}|_{x=x_0} V\delta V \ \ where,\ \delta V = V_{ac}cos(\Omega_{drive}t) \tag{4.12}$$

Where $V_{ac}$ is the amplitude of the AC voltage driving the system. In order to reach this nonlinear regime the PhC membrane is needed to be excited with an even higher AC bias $V_{ac}$. We start the actuation from a lower $V_{ac}$ $(1V)$ making sure that the system is far from the nonlinear threshold. The drive frequency $(\Omega_{drive})$ is swept in both upper and lower direction while the amplitude as well as the phase response of the oscillator is tracked simultaneously (Figure 4.4 (a,b)). The response in amplitude as well as in phase are found to be identical to each other giving no indication of existence of bistability in the system. However, when

the external actuation $V_{ac}$ exceeds some threshold of excitation ($V_{Th}$) the system starts to enter in the bistable regime. For our system this happens for $V_{ac} > 4.25V$. Response of the system when it is excited well above the threshold and deep into the nonlinear regime is shown in Figure 4.4(c,d), here the oscillator is resonantly excited at 10V and the frequency of excitation ($\Omega_{drive}$) is swept up and down consecutively. Different sweeps result in two different responses with two different resonant peaks and a hysteresis is being observed between these two sweeps. In this regime, the system is allowed to have two distinct stable and one unstable state at a particular frequency inside the hysteresis region. The width of this hysteresis region is around 4kHz at 10V. The amplitude response is fitted separately using two different fitting procedures. For the amplitude response in linear regime the response is simply fitted with a lorentzian function, while for the response in the bistable regime equation (4.11) is used. From this fit mechanical eigen-frequency of the drum mode ($\Omega_{m0}$= 2.73 MHz) and the FWHM ($\Gamma_{1st}$= 0.9 kHz) can be derived. Considering 3rd order nonlinearity (Duffing regime) the nonlinearity factor was computed using the fit and we obtain a value of $\beta_3 = 1.4 \times 10^{18} m^{-2}$.

**Spring softened oscillator:**

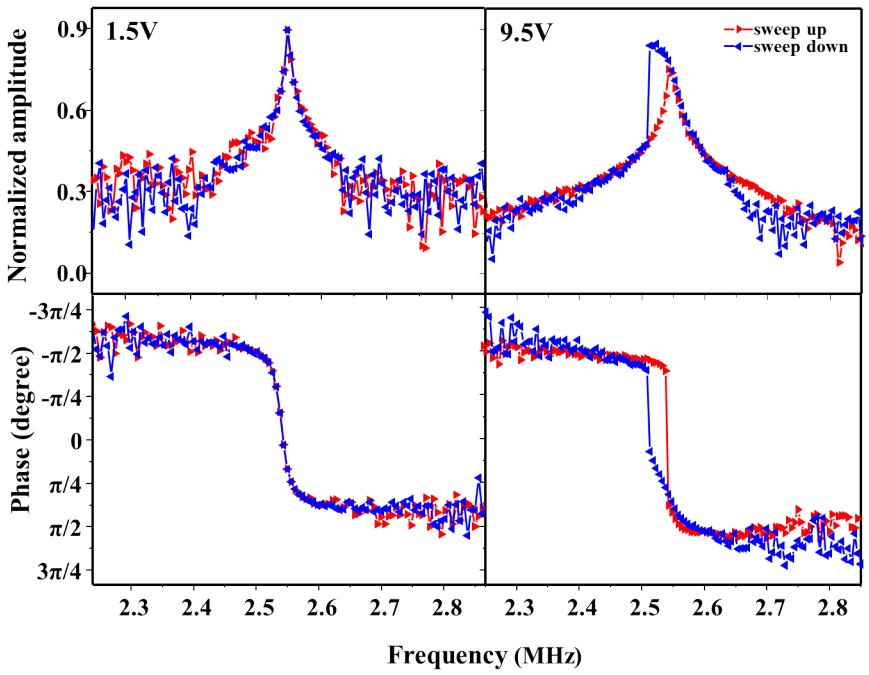


Figure 4.5: Normalized amplitude and phase response of the NOEMS oscillator in linear (1.5V) and bistable (9.5V) regime; the plots reveals existence of spring softening in this case unlike the previous case.

Previously the system that has been discussed exhibited only a particular kind of nonlinearity i.e. spring hardening. But it was seen in another similar membrane-electrode system on the same chip that it exhibited the opposite kind of behavior i.e. spring softening. The response

of this system in both linear and nonlinear regime is displayed in Figure 4.5. As it can be seen from the Figure 4.5, when the actuating voltage $V_{ac}$ is small ($V_{ac} = 1.5V$), the system resides in linear regime. While at sufficient excitation the system travels to the nonlinear regime and a hysteresis is observed. Although in this case the hysteresis is on the other side (i.e. red side) of natural resonance, similar effect can be seen in both amplitude and phase response of the system. The explanation of this difference in spring hardening or softening can be many fold; in general any oscillator can be viewed as a simple harmonic oscillator with the oscillation frequency $\Omega_0 = \frac{1}{2\pi}\sqrt{\frac{k_{eff}}{m}}$, where $k_{eff}$ is the effective spring constant. This effective spring constant $k_{eff}$ can be resolved into three different components; the first component is basically the term which defines the natural resonant frequency of the oscillator, the second term determines spring hardening and softening effect due to initial stress present in the system [96] and finally the last term is the capacitive softening term which induces spring softening effect in the oscillator [97][53]. Depending on how each term is modulated, the resonator would give rise to either spring hardening or softening effect. Now as mentioned before, in a more complicated nonlinear system, many nonlinear terms contribute to the nonlinearity. So the nonlinearity could be depicted more appropriately by replacing equation (4.10) with equation (4.13):

$$\ddot{x} + \Gamma_m \dot{x} + \Omega_m^2 x(1 + \beta_3 x^2 + \beta_4 x^3 + \beta_5 x^4 + ....) + \frac{1}{2}\frac{dC(x)}{dx}.V\delta V = 0 \;\; where, \delta V = V_{ac}\cos(\Omega_{drive} t) \tag{4.13}$$

Here, $\beta_n$ is the n-th order nonlinear coefficient of the system ($n$ = 3,4,5...). Now as predicted by Kozinsky et al. [53] nonlinear coefficients of different orders have different kind of impact on the response of the system: the cubic nonlinearity coefficient $\beta_3$ is mainly due to nonlinearity in elastic properties; effect of this nonlinearity can be increased by increasing the excitation on the system. Whereas the quadratic term $\beta_4$ is known as the symmetry breaking term, it appears when oscillator displacement from the central axis is broken by some means, for example capacitive attraction. Contribution of this quadratic nonlinearity $\beta_4$ can be increased either in an intrinsic or in an extrinsic manner. In case of intrinsic contribution to the quadratic nonlinearity, it can be increased by providing additional stress to the system [98]. On the other hand extrinsic modulation of the nonlinearity can be done by using DC bias for example. The influence of the DC bias can result in a reduction of the natural resonance frequency of the system which has been discussed in Chapter 3 [40][99]. Younis et al. [100] showed that it is possible to tune the nature of nonlinearity in the system by playing with the DC bias. For this particular system a very weak detuning of resonant frequency with bias has been observed which is discussed in section 4.4.4. In conclusion, we can say that as the system under study is not under any kind of bias, thus this spring softening effect is natural to the system. This can only mean that the intrinsic reasons hence inherent stress in the system are responsible for the existence of such nonlinearity. Although the width of the hysteresis region for this membrane was much higher than the previous case (40 kHz), unfortunately the sub and super-harmonic resonances discussed in the next section

were not observed for this particular electrode membrane system. So, from next section we will only focus on the membrane with spring hardening effect.

**Bistability tongue:**

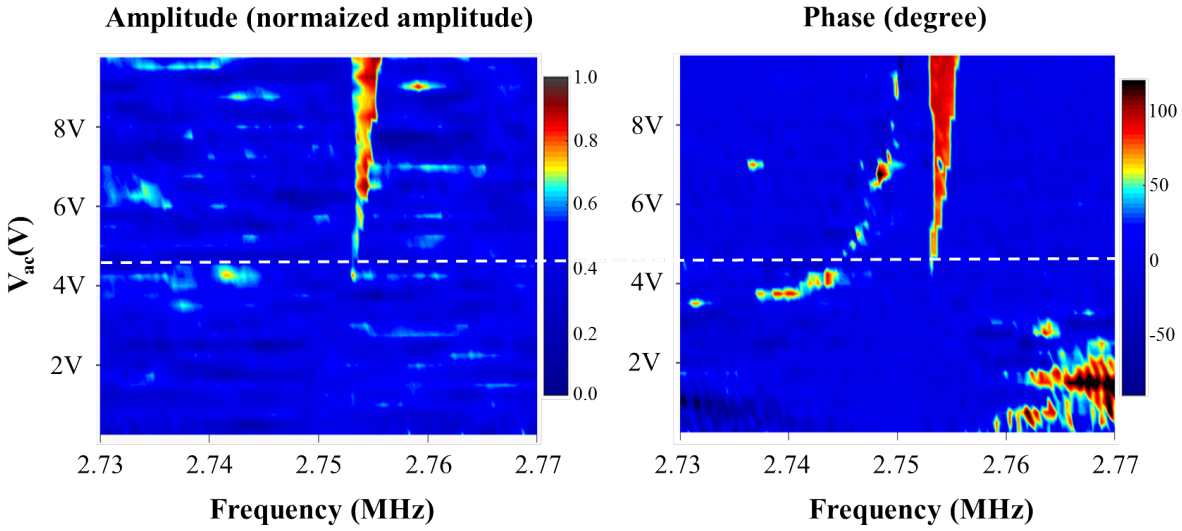


Figure 4.6: Bistability tongue for the system can be plotted for both amplitude and phase response; the regions in red and green are regions where the system has two stable states and one unstable state, while the region in blue is where the system is allowed to have only a single stable state.

An interesting representation of the bistable behavior can be done through the bistability tongue representation of the system. These tongues are constructed by plotting the difference spectra of sweep up and down in amplitude/phase as shown in Figure 4.6. Inside this bistablity tongue the system will have access to 3 different states; first two being the stable states and another being the unstable state which is inaccessible. As it can be seen, there are some regions of higher responses even outside the bistable regions, these can be attributed to the presence of noise in the response. A gradual increase of the hysteresis region width can be observed in both amplitude and phase response with applied voltage $V_{ac}$. The hysteresis region grows up to 4kHz of width at 10V of resonant excitation while the threshold of bistability being about 4.25V. The broadening of the hysteresis region can be attributed to the shift of resonance towards higher frequency induced directly by the nonlinearity. This gradual increase is also encountered by increase in the nonlinear damping acting on the resonator and after a certain threshold one should be able to observe a saturation in the hysteresis width. In this case presumably we are away from such a threshold and thus above-mentioned saturation is not observed. Another interesting observation is that the phase difference between the two stable states is identical across the hysteresis region, while as it will be seen later

individually each stable states goes through a 180 degree phase rotation across this hysteresis region.

**Phase space trajectories:**

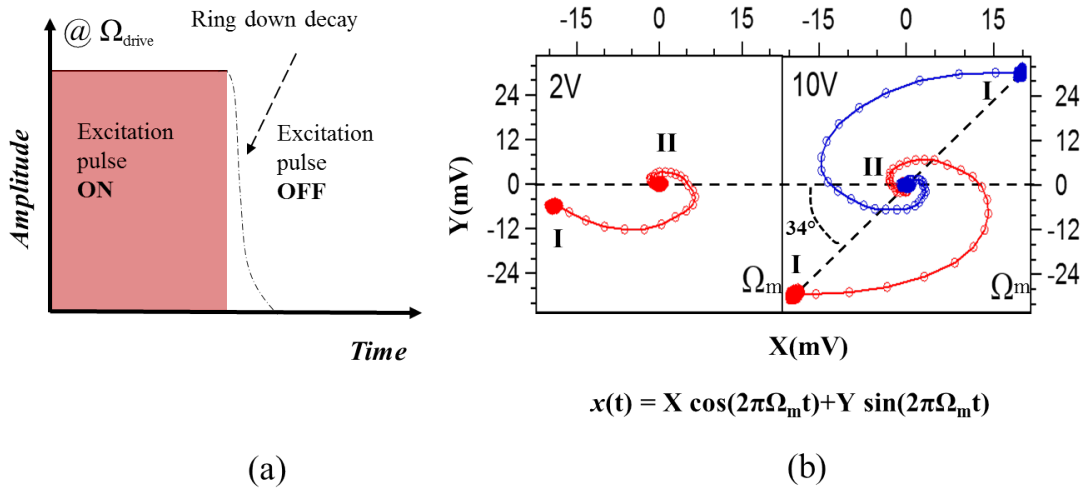


(a) (b)

Figure 4.7: (a) Ring down experiment in order to retrieve the phase trajectory of the system under study (b) Phase trajectory of the resonator under linear and nonlinear regime; exhibiting only a single state inside linear regime while two distinct states are observed when it is deep inside the nonlinear regime.

This bistable effect can be more readily observed while observing the phase space portrait of the system described in Figure 4.7. The phase dynamics of a mechanical system can be described as slowly varying quadratures X and Y. The phase trajectories of the system can be extracted by using a process called ring down (Figure 4.7(a)). The principal of these experiments is to resonantly excite the system i.e. $\Omega_{drive} = \Omega_m$ ; then when the drive is suddenly switched off the system slowly decays to its rest state. In each ring down measurement the in-phase (X) and out of phase (Y) quadrature data are recorded simultaneously and plots are constructed by taking approximately 300 points between the transition from excited to the rest state. In the experiment the system is prepared at one of its two stable states by either sweeping up or down the actuation frequency ($\Omega_{drive}$). Depending on this initialization procedure it should be possible to trace out the two distinct stable states.

Figure 4.7(b) explains how the phase trajectories works; the system when is resonantly excited displays a state in phase space shown by the point I. The radial distance of this point from origin gives the amplitude of oscillation while the angle this point makes with respect to the x-axis gives the phase of oscillation. However when the resonant drive is switched off the oscillator stops to oscillate and thus the amplitude of oscillation becomes zero. In the phase space a system in such a state will be represented by a circular point in origin (II). As it can be observed from Figure 4.7, in case of low excitation (2V) the system only

exhibits a single state, whereas when the excitation is high enough (10V) two distinct states in the phase space are observed with similar amplitudes; this is a clear indication of the existing bistability in the system. In order to extract two states with identical amplitudes we record the response at two different edges of the hysteresis which incidentally has a phase difference of 180°. Thus the spatial extension between these two points is directly related to the hysteresis width for a particular $V_{ac}$. Moreover the trajectory to the rest state reveals that the system is overdamped as it decays quite quickly to the rest state with almost no oscillation. One interesting phenomenon observed from these phase portraits is that the system undergoes a phase rotation when it travels from linear regime to nonlinear regime. This happens due to the detuning of natural resonance induced by the nonlinearity. As we keep the excitation still at $\Omega_{m0}$, which is not the frequency of maximum displacement under nonlinear regime we observe a shift in the detected phase $\theta$. In order to observe these two states distinctly the excitation is slightly detuned from the resonance, like this it is possible to extract this two states with similar amplitudes. At this point the measured phase offset is about 34° (Figure 4.7(b)). To avoid confusion in Figure 4.4 the natural resonant frequency is referred as $\Omega_{m0}$, while the mechanical resonance frequency in general will be referred as $\Omega_m$.

### 4.2.2 Excitation of higher order harmonics

**Origin of higher order harmonics:**

In this section we discuss when the system is still driven resonantly but beyond the nonlinear threshold and the response is probed at higher harmonics. A system under nonlinear forces can be represented by the equation:

$$\ddot{x} + \Gamma_m \dot{x} + \Omega_{m0}^2 x(1 + \sum_{i=3}^{\infty} \beta_i x^{i-1}) + \frac{1}{2}\frac{dC(x)}{dx}.V\delta V = 0, \quad where\ \delta V = V_{ac}\cos(\Omega_{drive}t) \quad (4.14)$$

Due to the presence of higher order nonlinear components denoted by $\beta_i's$ $(i = 3, 4, 5...)$ , responses at higher order harmonics can be observed when the amplitude of actuation $V_{ac}$ is beyond a certain threshold. It will be shown in this section that due to the presence of this nonlinear coefficients some equivalent forces at the higher harmonics are generated. For ease of discussion let us start from the nonlinear Duffing equation, thus we define the equation of motion of the system as:

$$\ddot{x} + \Gamma_m \dot{x} + \Omega_{m0}^2 x(1 + \beta_3 x^2) = \delta F_0 cos(\Omega_m t + \phi) \quad (4.15)$$

Here we assume that the force on the nanomechanical system is directly proportional to the applied sinusoidal voltage. Since there is no straight forward solution of this equation, we assume that when the parameter $\beta_3$ is weak the steady state solution somehow should be

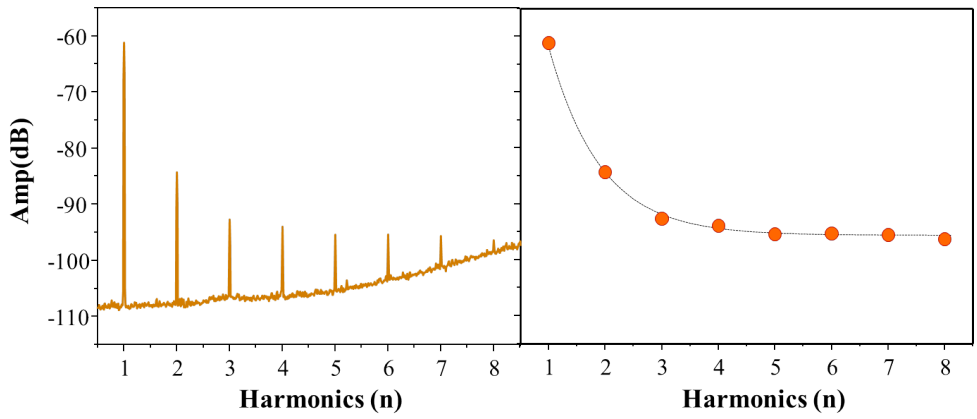


Figure 4.8: (a) Comb like frequency spectra with equally separated mechanical responses when the resonator is excited strongly ($V_{ac} = 10V$) at natural resonance, (b) plot of the peak amplitude of the response with the harmonics and the corresponding exponential fit.

related to the solution of the linear equation. For the time being let us denote the steady state solution as $x_0$ while the perturbation due to the present nonlinearity as $y$ i.e.

$$x = x_0 + y = Acos(\Omega_{m0}t + \phi) + y \tag{4.16}$$

Let us assume that $\phi = 0$, which is a safe assumption as value of $\phi$ in this case always keeps constant. Now if we eliminate the linear components from the equation above and only keep the terms concerning nonlinearity i.e. terms involving $y$ and $\beta_3$ the equation is reduced to:

$$\ddot{y} + \Gamma_m\dot{y} + \Omega_{m0}^2 y + \beta_3 y^3 + \beta_3 A^3 cos^3(\Omega_{m0}t) + 3\beta_3 y A^2 cos^2(\Omega_{m0}t) + 3y^2 Acos(\Omega_{m0}t) = 0 \tag{4.17}$$

It is possible now to replace the terms involving $cos^3(\Omega_{m0}t)$ and $cos^2(\Omega_{m0}t)$ with higher harmonic terms like $cos(3\Omega_{m0}t)$ and $cos(2\Omega_{m0}t)$ by using simple trigonometry. This means that the forcing side of the equation is not only influenced by the forcing component at $\Omega_{m0}$ but also at $2\Omega_{m0}$ and $3\Omega_{m0}$. This will give rise to responses around these frequencies, directly as a result of the existing nonlinearity in the system. Another interesting observation from the equation (4.16) is that the forcing at these harmonics is highly dependent on the value of the nonlinear coefficient $\beta_3$, which means that the effective response at these higher harmonics will be highly dependent on the corresponding nonlinear coefficients.

This idea can be extended for nonlinearity of $n$-th order and in conclusion we could say that these nonlinearities will produce response at the corresponding harmonics and the amplitude of the produced response will be completely dependent on the value of the corresponding nonlinear coefficients.

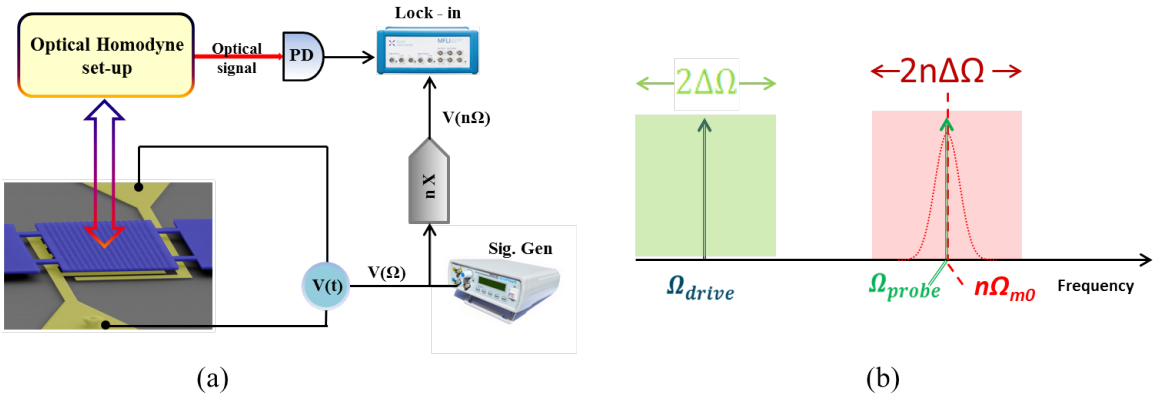


Figure 4.9: (a) Experimental set up for driving and probing the higher harmonics (b) Schematic of the probing scheme.

### A comb like spectrum:

Now we move to the discussion of the experiments that were performed linked with the discussion in the previous section. As a first set of experiment the actuation was fixed at the natural resonance $\Omega_{m0}$, and $V_{ac}$ was fixed at 10V. A spectrum extending up to 25 MHz was recorded and it revealed as much as 8 spectral peaks (Figure 4.8). Due to the increase of noise floor at higher frequency, we were not able to observe higher order peaks. The spectra has a comb like structure where each peaks are equally separated in the frequency spectra. This happens directly as a result of the existence of the higher order nonlinearity (up to 8th order comes into play in this case). The spectrum is displayed in Figure 4.8(a); the first peak with the highest intensity is the response of the system at the natural frequency $\Omega_{m0}$. A gradual decrease in the response of the higher harmonics can be observed (Figure 4.8(b)). The decay in the response is exponential and shows a gradual saturation in the response (in logarithmic scale), from which it can be concluded that the variation of nonlinear coefficients with harmonics will follow similar pattern as well. If the response in amplitude is denoted as $I$ and the harmonics are denoted as $n$, the behavior of the response with different harmonic orders can be defined as:

$$I = I_0 * exp(-n) + I_{NF} \tag{4.18}$$

where $I_0$ is the saturated amplitude and $I_{NF}$ defines the noise floor in the response. Fitting the response (dotted line in Figure 4.8(b)) with an exponent yields a value of $I_0 = -95dB$ and $I_{NF} = -105.6dB$. Possibly with an even higher excitation, even higher order harmonics could be excited.

### Spring hardening of the higher order harmonics

The actuation at the natural resonance transforms a response to the higher order harmonics due to presence of nonlinearity. To observe this effect in more details full response spectra

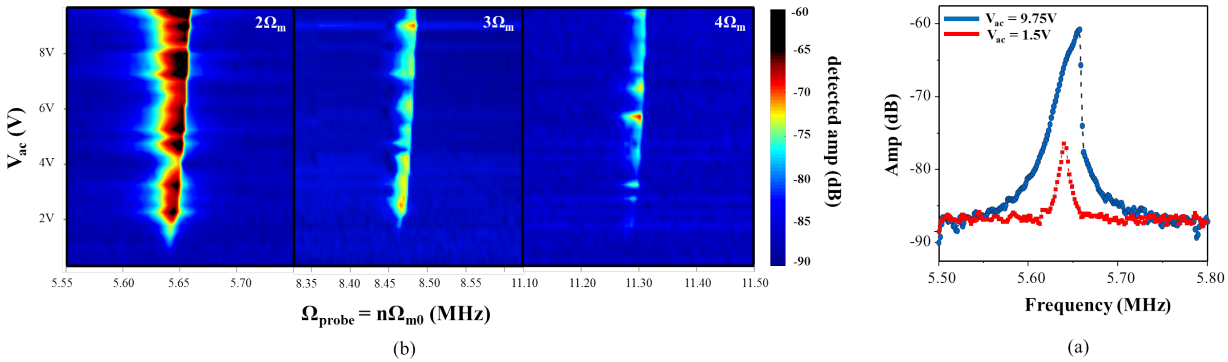


Figure 4.10: (a) 2D surface plot of response of the harmonics $n = 2, 3, 4$ while the drive frequency $\Omega_{drive}$ and the drive voltage $V_{ac}$ is swept (b) response of the 2nd harmonic, exhibiting a Duffing like response with spring hardening effect for higher excitation ($V_{ac} = 9.0V$) and linear response at $V_{ac} = 1.5V$.

around the higher order harmonics were recorded. The experimental procedure is displayed in the Figure 4.9(a) and the schematic is shown in Figure 4.9(b). The resonator is excited at the natural resonance ($\Omega_{m0}$) and the drive $V_{ac}$ is swept while the spectra is recorded around the higher harmonics ($n\Omega_{m0}$). In the experiment the resonator was driven at resonance by a signal generator which was at the same time fed into a frequency multiplier. The output of the frequency multiplier was fed to a lock-in amplifier, which demodulated the signal at that frequency. Depending on which harmonic was recorded ($n = 2, 3, 4...$) the order of the frequency multiplier was selected. The drive frequency ($\Omega_{drive}$) is swept across the natural resonance ($\Omega_{m0}$) by an amount $2\Delta\Omega$ while the response is probed withing an interval of $2n\Delta\Omega$ around $n\Omega_{m0}$.

As a next set of experiment the response of the resonator for harmonics up to $n = 4$ were recorded for various values of actuating drive $V_{ac}$ around the natural resonance ($\Omega_{m0}$). The resulting spectra is displayed in Figure 4.10(a). The resonator was actuated in each case for a window of $100kHz$ around the natural resonance and at the same time the response was probed for $n = 2, 3, 4$; while the actuation voltage $V_{ac}$ was varied from $0.25V$ to $9.75V$. The window of actuation is much larger than $\Gamma_m (= 0.9kHz)$ of the primary resonance. As it was discussed before the system exhibits spring hardening Duffing response in each case, the effect is most visible in the first case $\Omega_{probe} = 2\Omega_{m0}$. Although as the order of the harmonics are increased the response becomes weaker and also the threshold required for actuation increases. This can be attributed to the fact that higher order nonlinearities have lower coefficient. The higher order responses also show similar behaviors with a less pronounced response and higher threshold but they are not displayed here. A particular situation with $V_{ac} = 9.5V$ is shown in Figure 4.10(b), the 2nd harmonic ($2\Omega_{m0}$) is probed in this case while the resonator is driven around the natural resonance ($\Omega_{m0}$). The response in this case is a stark contrast to the results shown in the previous section. The response shows a clearly nonlinear spring hardening effect. This is merely an impression of the existing nonlinear response at resonance on the higher order harmonics due to presence of nonlinearities in the

system. For lower excitation $V_{ac} = 1.5V$, the response is quite small and it exhibits something closer to a Lorentzian response. Similar effects were observed for harmonics of higher orders as well, although the effect was not as pronounced as in this case with $\Omega_{probe} = 2\Omega_{m0}$. This can be attributed to the exponential decrease of nonlinear coefficients for higher orders (Figure 4.8(b)).

## 4.3 Sub and super harmonic resonance

In this section forced excitation of the NOEMS system in the sub and super harmonic regime will be discussed. Theoretical discussion of sub and super harmonic excitation has been greatly discussed by Mallow et al. [101] and A. Prosperetti [102]. As it was discussed before a nonlinear system can be described by equation (4.10), where several mechanical nonlinearity are present simultaneously in the system under study. The primary resonance is known when the system is driven at a frequency equal to the natural resonance frequency of the system i.e. $\Omega_{drive} = \Omega_m$. But the presence of higher order nonlinearities in the system means that several resonant overtones can exist for the system: (i) firstly what has been already introduced in this chapter i.e. when the drive frequency $\Omega_{drive}$ is near the natural frequency $\Omega_m$; it's called fundamental or primary resonance; (ii) when drive frequency $\Omega_{drive}$ is $n$ times the natural frequency i.e. $\Omega_{drive} = n\Omega_m$; then its called sub-harmonic resonance and (iii) when drive frequency $\Omega_{drive}$ is $1/n$ times the natural resonance frequency i.e. $\Omega_{drive} = \Omega_m/n$; it's called super-harmonic resonance.

### 4.3.1 Theoretical introduction to sub and super harmonic excitation

These kind of excitation are also referred as the parametric excitation as the system is excited on resonance but while being forced at some harmonic of the natural response. The modulation at the sub or higher harmonics of the natural resonance modulates the spring constant of the resonator and after a certain point when the excitation crosses a certain threshold the system is able to respond resonantly. The phenomenon is directly related to the nonlinearity of the system as the nonlinearity of $n$-th order helps the resonator to be excited at $n$-th super or sub-harmonic resonance. Thus the threshold of excitation is related to the order of nonlinearity in the system and the above-mentioned threshold increases for higher order nonlinearities.

#### Mathieu equation without damping

The equation of motion of the system under study is written as:

$$\ddot{x} + \Gamma_m \dot{x} + \Omega_{m0}^2 x + \beta_3 x^3 = F \;\; where, F = -\frac{1}{2}\frac{dC(x)}{dx}.V\delta V \tag{4.19}$$

The excitation of super and sub-harmonic resonance falls under parametric excitation, where somehow the spring constant of the resonator is modulated at some harmonic of the

natural resonance and a response is observed at the natural resonance. Since the physics of this kind of system is quite complicated, we will start without considering any damping and nonlinear terms, and slowly work towards more complicated situations. Thus for the time being let's begin with assuming that the system is under no damping as well as considering the system is excited far below from the nonlinear threshold. Which means for the time being we can consider $\beta_3 = 0$ and $\Gamma_m = 0$. Considering the fact that the harmonic driving causes the spring of the system to modulate at that frequency, we replace the term $F$ in equation (4.19) and add the harmonic drive to the spring constant term. Furthermore as discussed before when the system is excited at some harmonic other than the natural resonance it can directly affect the spring constant of the system, thus in short the spring constant will be modulated at the harmonic and when it exceeds a certain threshold it will produce a response at the natural resonance. Under such conditions considering a superharmonic resonance situation let's assume that the system is driven at a frequency $\Omega_{drive} = \Omega_{m0}/n$ with a modulation amplitude of the spring constant being $H$. The factor $H$ is related directly to the applied parametric force on the resonator. So the equation (4.19) can be rewritten as:

$$\ddot{x} + (\Omega_{m0}^2 + Hcos(\frac{\Omega_{m0}t}{n}))x = 0 \tag{4.20}$$

This form looks like an usual Mathieu equation which is used in order to comprehend the dynamics of a nonlinear system [59], the general form is written as:

$$\ddot{x} + (\delta + \epsilon cos(t))x = 0 \tag{4.21}$$

Thus we can draw a parallel between equation (4.20) and equation (4.21) by using the transformation $\tau = \frac{\Omega_{m0}}{n}t$, using $\epsilon = Hn^2/\Omega_{m0}^2$ as the external actuation and $\delta = \frac{\Omega_{m0}^2}{\Omega_{drive}^2} = n^2$ as the detuning from resonance. Under these conditions the transformed equation thereby can be written as:

$$\frac{d^2x}{d\tau^2} + (\delta + \epsilon cos(\tau))x = 0 \tag{4.22}$$

The solution of Mathieu equation can be derived using various techniques, for example: Lie transformation, perturbation theory, Floquet theory, Hill's equation, harmonic balance. The idea of all these processes above is actually to study the dependency of the parameters $\delta$ and $\epsilon$ on each other. The system under nonlinear regime can be solved by using harmonic balance theory with assumed solution of $x(t)$ to be (for detailed derivation please refer to Appendix (B)):

$$x(t) = \sum_{n=0}^{\infty} a_n cos\frac{nt}{2} + b_n sin\frac{nt}{2} \tag{4.23}$$

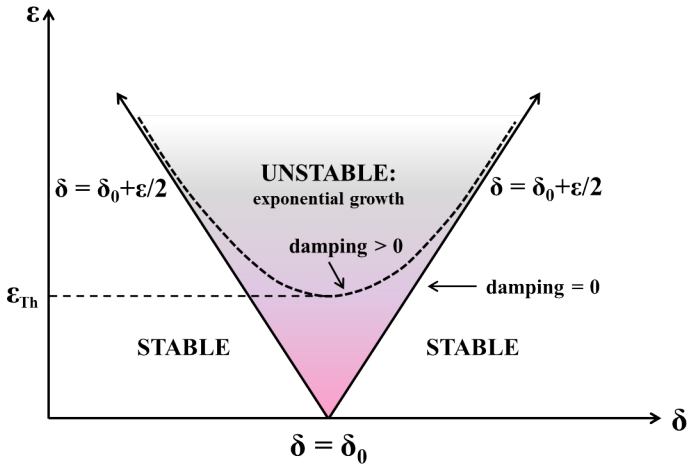


Figure 4.11: The instability tongue for parametric excitation of the system; the region of instability is bounded by $\delta$ which is dependent on the spring constants of the system. The tongue originates at $\delta = \delta_0$ and then enlarges with increase in excitation $\epsilon$. The smooth line indicates instability tongue in ideal case (damping = 0) while the dotted line indicates more pragmatic situation taking damping into consideration.

From here it can be shown that parametric excitation is possible for drive frequencies $\Omega_{drive} = \frac{2\Omega_{m0}}{n}$ (where, $n = 1, 2, 3....$). The dependance of detuning $\delta$ on the drive parameter $\epsilon$ can be written as:

$$\delta = \frac{n^2}{4} + \delta_1\epsilon + \delta_2\epsilon^2 + ... \tag{4.24}$$

The factors $\delta_1, \delta_2...$ are related to the detuning of the resonance due to higher power acting on the system. In our system this detuning arrives as a consequence of the existing nonlinearity in the system. Thus effect of an increase of $\epsilon$ results in a dispersion of $\delta$ i.e. increase in the excited frequency range for the superharmonic excitation. The resulting plot is shown in Figure 4.11, it displays a tongue like behavior with an increase in the tongue width with an increase in $\epsilon$. This kind of plot is known as the instability tongue. Thus we can conclude that parametric excitation is possible when the drive frequency satisfies the condition $\Omega_{drive} = \frac{2\Omega_{m0}}{n}$, where $n$ is an integer. In the next section experimental realization of this phenomenon will be discussed and it will be seen indeed it is possible to realize the up conversion of the excitation for various values of $n$.

### Mathieu equation with damping

The discussion up till now however has been a little pragmatic, as the damping coefficient has been completely neglected in the discussion which is very much present when a system

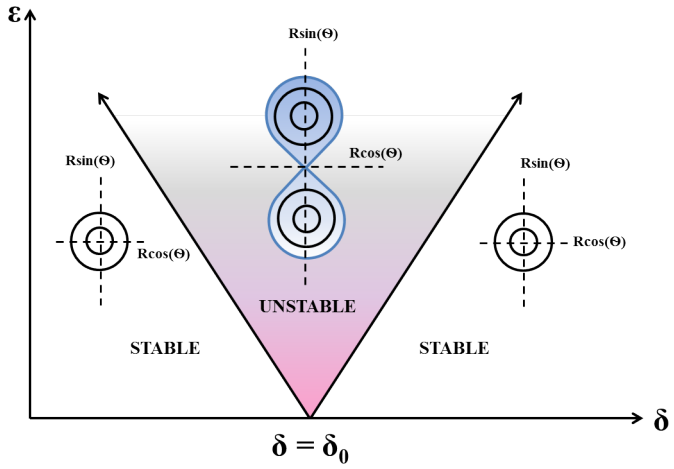


Figure 4.12: Instability tongue under nonlinear regime.

is studied under laboratory environment. Thus let us now consider the damped Mathieu equation and then observe how the transition curves are modified. For that let us consider what is known as the damped Mathieu equation:

$$\frac{d^2x}{d\tau^2} + c\frac{dx}{d\tau} + (\delta + \epsilon cos(\tau))x = 0 \tag{4.25}$$

Here, $c = \frac{n\Gamma_m}{\Omega_{m0}}$ is linearly related to the damping coefficient $\Gamma_m$. Like in the previous section using some assumed solutions dependence of $\delta$ on $\epsilon$ can be found and it can be shown that (detailed derivation in Appendix(B)):

$$\delta = \frac{p^2}{4} \pm \frac{\sqrt{\epsilon^2 - c^2}}{2} + O(\epsilon^2) \tag{4.26}$$

This clearly shows that for instability to occur for a given value of $c$, a minimum value of $\epsilon$ is required i.e. there exists a threshold in the external excitation from where output response will be observed. Also the minimum $\epsilon$ is slightly detached from the $\delta$ axis depending on the value of $c$. The dependence of $\delta$ on $\epsilon$ for low $\epsilon$ is a little parabolic which makes edges of the transition curves to be a little blunt rather than sharp compared to the case when there is no damping. Nonetheless when $\epsilon$ is sufficiently high, the dependence again becomes linear (ignoring higher order perturbations) which is shown by the dotted curve in Figure 4.11.

### Mathieu equation under nonlinear regime

In the previous sections it has been discussed how the unbounded states can exist inside the transition regions defined by the boundaries, but in real world a physical system does not demonstrate such unbounded behavior. The reason can be attributed to the existing

nonlinearity in the system. This phenomenon hasn't been examined in the discussion till now and it's due to the fact that up to now only a basic form of Mathieu equation has been considered in order to reduce complicacy. This is due to the fact that as the system enters into nonlinear regime due to the large motion in amplitude the eigen-frequency becomes detuned, as a result the amplitude in the response becomes smaller thereby not reaching the unbounded response. To study the parametric response of a system under nonlinear conditions we will need to consider the nonlinear Mathieu equation:

$$\frac{d^2x}{d\tau^2} + (\delta + \epsilon cos(\tau))x + \alpha x^3 = 0 \tag{4.27}$$

Here the coefficient $\alpha$ is related with the Duffing nonlinearity factor $\beta_3$ as: $\alpha = \frac{n^2\beta_3}{\Omega_{m0}^2}$. It can be shown that if we assume complex displacement $x(t) = Rexp(j\theta)$, where R is the amplitude of displacement and $\theta$ is the phase response, then under steady state approximation:

$$-\frac{R}{2}sin(2\theta) = 0 \tag{4.28}$$

$$and\ R = -\frac{4}{3\alpha}(\frac{cos(2\theta)}{2} + \delta_1) \tag{4.29}$$

From these solutions it can be shown that (Appendix(B)) for $R \neq 0$ i.e. inside the instability tongue a bifurcation exists for $\theta$. And solution will exist only for $\theta = \pi/2$ and $\theta = 3\pi/2$ i.e. there are two stable states which are separated by a phase difference of $\pi$ when the system is inside nonlinear regime. It will be shown in the next section that identical situation is achieved under experimental observations, where two separate states are observed under a parametric excitation (superharmonic resonance) being separated by a phase difference $\pi$.

### 4.3.2 Excitation of superharmonic resonance

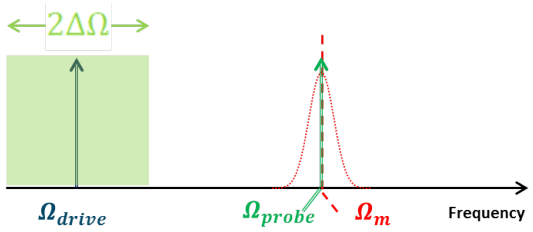


Figure 4.13: Schematic diagram of superharmonic resonance experiment: The drive frequency $\Omega_{drive}$ is swept around $\Omega_{m0}/n$ while at the same time the system is probed around the natural resonance of the system $\Omega_{m0}$.

The observation of sub/super-harmonic resonances requires high nonlinearity in the system. Due to some presence of damping in the system these kinds of excitation will be possible

only after the excitation exceeds a certain threshold ($V_{Th}$) as it was discussed in section 4.3.1. These experiments were performed by exciting the system far away from resonance i.e. at $\Omega_{m0}/n$ and at the same time probing the response of the system at $\Omega_{m0}$.

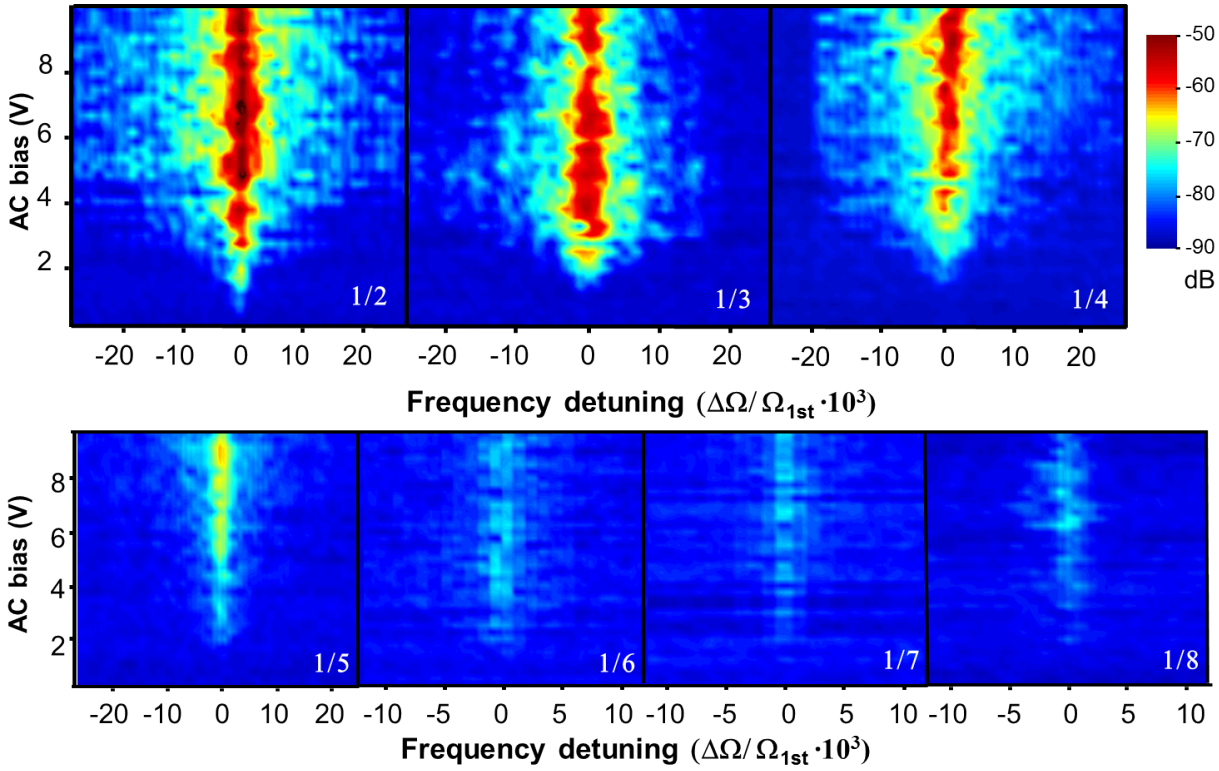


Figure 4.14: Superharmonic resonances for $\Omega_{drive} = \Omega_{m0}/n$; instability tongues are displayed for up to $n = 2$ to 8. Note the change of drive frequencies between different graphs. $\Delta\Omega$ denotes the frequency detuning $n\Omega_{drive} - \Omega_{m0}$.

Figure 4.13 shows a schematic diagram of how the experiments were performed. In order to perform the experiment the drive frequency $\Omega_{drive}$ was swept around $\Omega_{m0}/n$ ($n = 2, 3, 4...$) by an amount $2\Delta\Omega$ (Figure 4.13) and the system was always probed all the time at $\Omega_{m0}$. When the drive is not strong enough only a quasiperiodic motion of the oscillator is observed; while when the forcing amplitude is strong enough periodic oscillation at $\Omega_{m0}$ is observed. In the latter case, the locking of the oscillator frequency on the periodic force frequency occurs within the aforementioned instability tongues. Such regions for several superharmonic resonance configurations are plotted in Figure 4.14. In the experimental set up a point by point measurement was performed. Which means that the experiment was performed by recording the spectra at a fixed frequency while repeating the experiment step by step at a slightly shifted frequency and finally interpolating peaks from each plot to construct the final spectra. As a result the spectra unfortunately becomes a bit pixelited. Nonetheless, the instability tongue is clearly visible in every case. For the ease of discussion we will segregate this section into two subsections: in the first one we will discuss about the excited amplitude

evolution under superharmonic configuration, while in the later one we will shift our focus on the evolution of the phase space trajectories under superharmonic resonance.

### Amplitude evolution

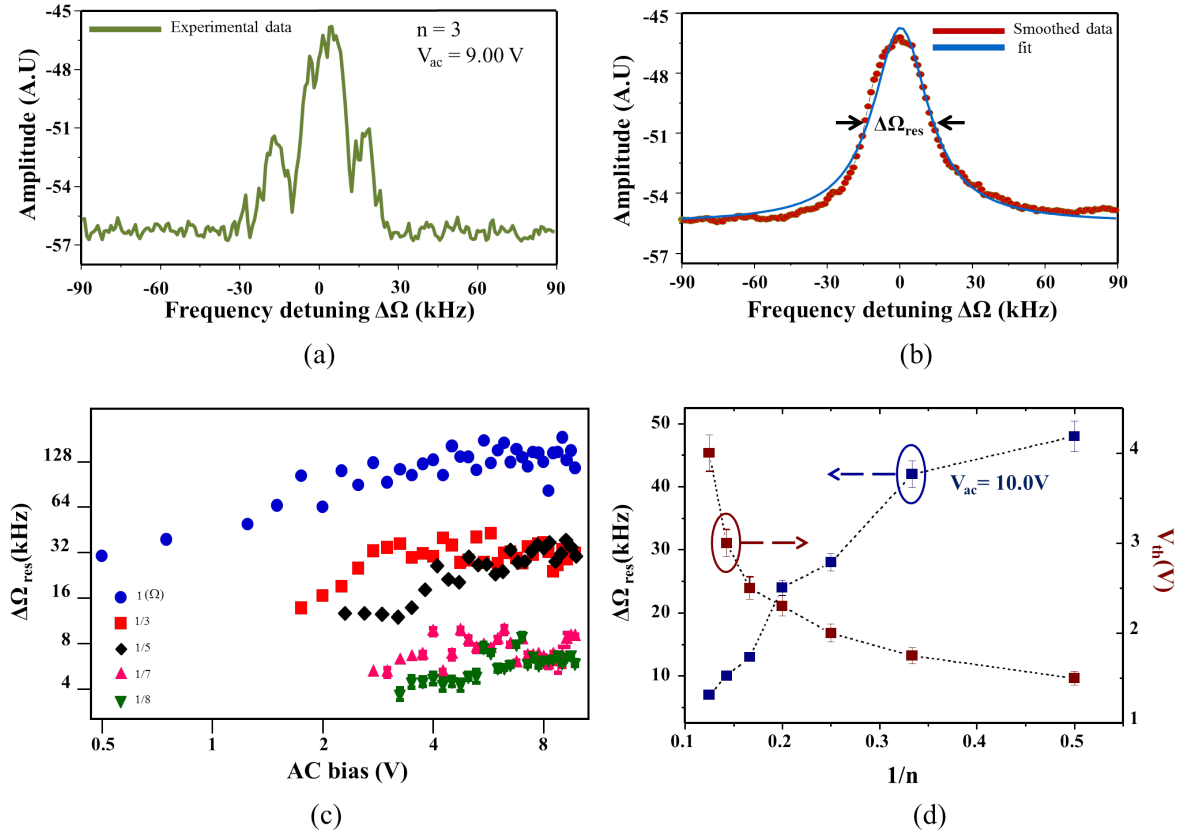


Figure 4.15: (a) Cross sectional picture of the 2D surface plot (b) noise spectra of superharmonic resonance after data smoothing (c) plot of FWHM against external excitation for different superharmonic resonances (d) plot of extracted $\Delta\Omega_{res}$(at $V_{ac} = 10.0V$) and $V_{Th}$ values with superharmonic resonance order $n$.

On the 2D surface plots of Figure 4.14 $x$-axis represents detuning of the frequency from the natural frequency of the system, on $y$-axis is the amount of AC voltage $V_{ac}$ applied to the oscillator, while the color axis represents the noise spectrum of the fundamental mechanical mode $\Omega_{m0}$. In relation with the theoretical discussion presented before thus $\epsilon$ resembles $V_{ac}$ while $\delta$ represents $\Omega_{drive}$. For $n = 2$ to $n = 5$ the tongue like behavior can be clearly observed while for $n > 5$ it becomes difficult to observe the tongue shape. The reason can be attributed due to the fact that the threshold required for the superharmonic resonance ($n > 5$) to be seen is directly related to the corresponding nonlinear coefficients, which decrease as $n$ increases. Several interesting parameters can be deduced from the response

spectra, one of them being how the FWHM ($\Delta\Omega_{res}$) of the spectra depends on the applied excitation as well as on $n$. The raw data however are quite noisy, this happens due to the point by point measuring procedure which was mentioned before. The raw experimental data for $n = 3$ and $V_{ac} = 9.0V$ is shown in Figure 4.15(a). In order to extract some useful information from these data some further data processing was needed to be performed. This was done by performing some data smoothing algorithm on the spectrum, a simple 4th-order average filter was used for the signal processing. The smoothed data is displayed in Figure 4.15(b), where it can be seen that we are able to reproduce data which looks much similar to a Lorentzian spectra. The data are successfully reproduced without much loss of information like amplitude and bandwidth of the spectra. Now it was possible to fit this spectra with a mechanical Lorentzian function and retrieve information. The Lorentzian function used to extract the data is displayed in the following equation:

$$x = x_0 + B * \frac{\Delta\Omega_{res}}{4(\Omega - \Omega_{m0})^2 + \Delta\Omega_{res}^2} \tag{4.30}$$

Where, $\Delta\Omega_{res}$ is the full width half maxima of the spectra. For the particular situation displayed in Figure 4.15(b) we were able to extract $\Delta\Omega_{res} = 30$kHz.

The extracted FWHM ($\Delta\Omega_{res}$) is plotted against the applied bias in Figure 4.15(c) for several superharmonic resonances ($n = 1, 3, 5, 7, 8$). The first noticeable result from the plots is the clear indication of the saturation of $\Delta\Omega_{res}$ at higher $V_{ac}$; this might be due to the higher orders of perturbation or dissipation due to temperature rise. The saturation effect is clear for $n = 1$ to 5, while from $n = 7$ this saturation effect is not particularly evident. Especially for $n = 8$ in Figure 4.15(c) the growth in $\Delta\Omega_{res}$ can still be seen even for higher $V_{ac}$ values. One more important information that can be extracted from the data is the variation of the excitation threshold referred as $V_{Th}$ before. The extracted $\Delta\Omega_{res}$ and threshold voltage $V_{Th}$ required for the superharmonic resonance to occur is plotted in Figure 4.15(d). All the $\Delta\Omega_{res}$ are extracted for $V_{ac} = 10V$ for different superharmonic resonances i.e. different $n$ values. It can be clearly seen from this plot that the FWHM ($\Delta\Omega_{res}$) gradually decreases with $n$, while threshold voltage $V_{Th}$ increases with $n$. This phenomenon can be attributed to the fact that lesser contribution from the higher order nonlinear terms, while the influence of these higher order terms can be enhanced by increasing the external excitation.

### Evolution of phase trajectories

The next study that was performed on the system was to understand the phase dynamics under superharmonic resonance. The method of study is similar to what was discussed in section 4.2.1 (Figure 4.7(b)). Using ring down technique, several trajectories for various superharmonic resonance were tracked and some of the results are plotted in Figure 4.16 ($n = 2, 4, 6$) for two values of excitation $V_{ac} = 2V$ & $V_{ac} = 10V$. The record of these phase trajectories are done by doing several ring down measurements while keeping the drive $V_{ac}$ and resonance order $n$ fixed. We start by observing the phase trajectory for $n = 2$; here we can observe that for a low level of excitation ($V_{ac} = 2V$) the system displays only

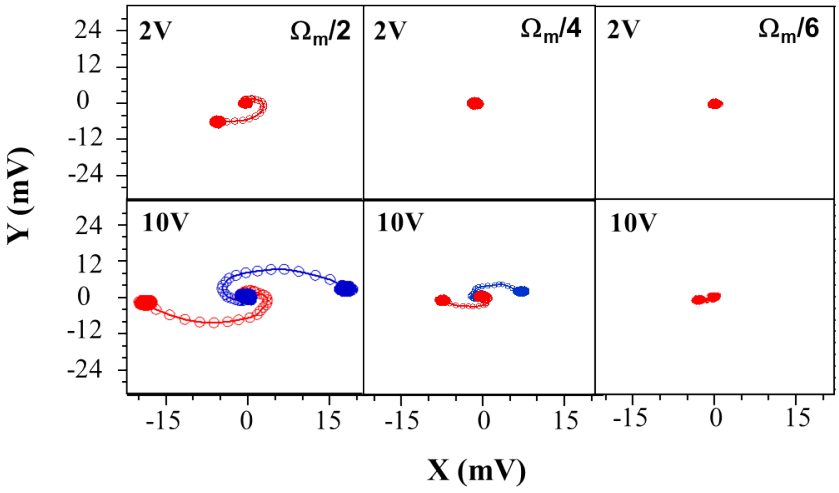


Figure 4.16: Phase trajectories of the system for $n = 2, 4, 6$. The phase trajectories show that after certain threshold the system displays in and anti-phase oscillation with respect to the drive. This effect is clearly seen for up to $n = 4$, after that this effect becomes less evident due to decrease in the corresponding nonlinear coefficient.

a single state which oscillates at a fixed phase difference with respect to the drive. The radial distance of the phase state from the center determines the amplitude of oscillation of this state. However, when the excitation is higher ($V_{ac} = 10V$) the system enters into the nonlinear regime and along with an enhancement in the oscillation amplitude it also starts to display a bifurcation in phase. This resembles the discussion we had on Mathieu equation under nonlinear regime (section 4.3.1), where it was shown that a system which is governed by Mathieu equation beyond nonlinear threshold, will display two bifurcated states separated by $\pi$. The system shows probability close to 50% to be in each state while different switching events are recorded. Similar situation is observed for 4th superharmonic resonance, near or below the threshold (around $V_{ac} = 2V$) the initial phase approaches the origin (Figure 4.16). When the drive strength is weak, the resonator occupies only a single state. But for $V_{ac} = 10V$, the phase potrait follows two spiral trajectories differed by $\pi$ phase shift. This effect as it was discussed in the previous section arises due to the presence of nonlinearity in the system (section 4.3.1), the phase difference between this two bifurcated points remaining $\pi$. Similar effects have been demonstrated by Mahboob et al. [38][39] and Chan et al. [103]. For higher order superharmonic resonances ($n > 5$), these in and anti-phase resonances are not observed due to the very narrow width of the instability tongue related to the lower value of the higher nonlinear coefficients.

The phase difference between the oscillator and the driving force is bounded and depends on the excitation frequency detuning. In the experiment we prepare the system at one of the two bifurcated states and then change the frequency detuning from one edge of the tongue to another. At each point of detuning we are able to extract the phase and amplitude of oscillation with respect to the external drive. In Figure 4.17(a) we show how the phase

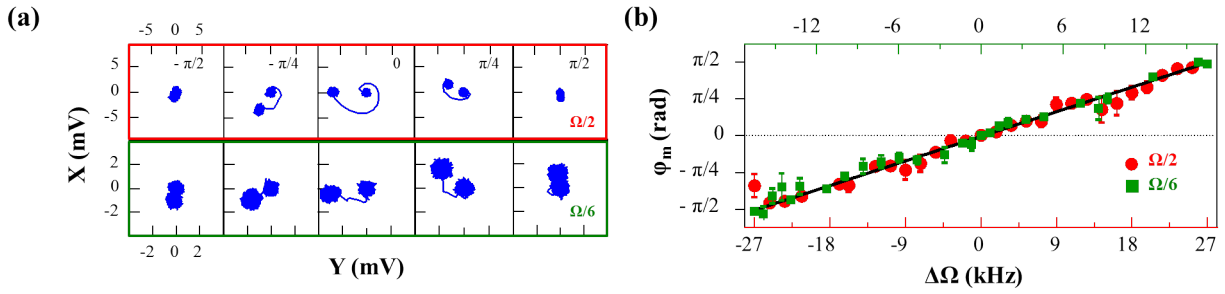


Figure 4.17: (a) Phase trajectories for $n$= 2 & 6 for discrete values of $\Delta\Omega$ for $V_{ac} = 10V$ (b) phase evolution of a single state with frequency detuning $\Delta\Omega$ for $n = 2$ & 6.

trajectory of one of the oscillator state is evolving for 5 different detuning values, identical behavior would be observed for the other state as well. We have observed that each states undergoes a $\pi$ phase shift with the detuning while maintaining a $\pi$ phase shift with the other state at each detuning point. We start from one edge of the hysteresis where the excited amplitude is quite small with a phase shift of $-\pi/2$ with respect to the external drive, and gradually this phase difference starts to increase towards 0 as the frequency detuning approaches 0. At 0 detuning the amplitude of oscillation is also the highest with zero degree of phase shift measured with 4% of uncertainity. From here as the detuning is increased the phase difference increases towards $\pi/2$ with a decrease in the oscillation amplitude. Similar effect is observed for both $n = 2$ and $n = 6$. While for obvious reason oscillation amplitude for $n = 2$ is being higher than for $n = 6$. Another representation of this phase shift is shown in Figure 4.17(b) where we can clearly observe the phase of individual states undergoing a $\pi$ phase shift while crossing the tongue for a constant drive $V_{ac}$. Two separate situations are displayed with $n = 2$ & 6; and in both cases we can observe that each state will under go a $\pi$ phase shift as the detuning is changed. Thus in conclusion one can say that the phase shift remains bounded within the width of the instability tongue, showing a linear behavior (varying by $\pi$ while 'crossing' the tongue).

## 4.4 Parametric amplification

Let us consider the situation where the spring constant of the system is modulated at twice the natural frequency, this leads to an amplification of a weak drive at resonance, this is known as parametric amplification. Parametric amplification is not only achieved while modulation is done at twice the natural frequency but also when modulation is done at a slower rate i.e. at $n$-th multiple of half a period of oscillation. The idea is that if a system resides within its instability tongue, any small perturbation could cause the response to grow exponentially, this happens when the amplitude of modulation is sufficiently strong enough to overcome any influence of damping. This phenomenon is known as the parametric amplification and it finds many interesting applications in the field of MEMS/NEMS resonators. This effect has been demonstrated in several nanomechanical systems; Unterreithmeier et al

[40] showed that parametric excitation is possible for a electromechanical system, Mahboob et al showed that parametrically coupled array could produce a network which can demonstrate binary operations [38], while Eichler et al [104] demonstrated parametric amplification for carbon nanotube microresonators. Other nano/micro-mechanical system have been also shown to exhibit the parametric amplification effect [54][105]. The threshold of this parametric amplification scales as $(Q^{-1})^n$ (where Q denotes the Q-factor of the resonator) [18] for the the $n$-th instability tongue; so the effect is strongest for the case when $n = 1/2$ i.e. when $\Omega_{drive} = 2 * \Omega_{m0}$. This is why it is customary to study the case of parametric amplification for this particular case. The idea is really similar to what has been done in the previous section but instead of using super-harmonic resonance we use sub-harmonic driving configuration. The resonator is driven at natural resonance ($\Omega_{drive} = \Omega_{m0}$) far away from the bistable threshold so that it remains well inside the linear regime and then at the same time another drive is added; generally referred as pump at a frequency $\Omega_{drive} = 2 * \Omega_{m0}$. This excitation however should be stronger than the drive. Most common case in micron scale is to use an external electrode to pump the system at twice the natural frequency. What happens in such a condition is basically the pump at this frequency modulates the spring constant and at the same time the seed at natural resonance helps this oscillation to build up provided the system is within the instability tongue. In such a condition it will be shown that it is possible to achieve either amplification or deamplification depending on the phase difference between the drive and pump.

The discussion here on parametric amplification will be divided into two sections: in the first section we will discuss the situation considering the system is far below the nonlinear regime. With this configuration it is possible to achieve the phenomenon of parametric amplification. However when the resonant excitation exceeds the threshold $V_{Th}$, the system enters in the nonlinear regime. Here it will be shown that it is possible to tune the nonlinearity of the oscillator.

### 4.4.1 Theoretical background: parametric amplification

We begin our discussion considering the equation of motion under resonant drive ($\delta V = V_{ac} cos(\Omega_{drive} t + \phi)$):

$$\ddot{x} + \Gamma_m \dot{x} + \Omega_{m0}^2 x = \delta F(t) \;\; where, \delta F(t) = -\frac{1}{2}\frac{dC}{dx}|_{x=x_0} V \delta V \tag{4.31}$$

As a reminder; the discussion will be done by considering the system is under the threshold and thus still in the linear regime. Knowing that spring constant per unit mass ($k_m$) related with the frequency as $k_m = \Omega_m^2$ and considering the modulated spring constant (by a parametric pump) being $k_p$, we can write:

$$k_m = k_{m0} + k_p(t) \tag{4.32}$$

where, $k_{m0}$ is the unperturbed spring constant/unit mass ($=\Omega_{m0}^2$) and $k_p(=\Omega_p^2)$ is the modulated spring constant/unit mass. This modulation of spring constant is done by applying some external parametric excitation. Under the condition of parametric amplification the forcing drive at natural resonance is $\delta F(t) = \frac{dC}{dx}|_{x=x_0} V\delta V$, while the parametric excitation on the system modulates the spring constant. Using the same excitation scheme the modulation on the spring constant can be defined as: $k_p = \Delta\delta F_p = \Delta(\frac{dC}{dx}|_{x=x_0} V\delta V_p)$. Here, the parametric voltage can be defined as $\delta V_p = V_p cos(2\Omega_{m0}t)$ which makes the parametric spring constant$k_p$ directly proportional to the applied parametric voltage i.e. $k_p = \Delta k cos(2\Omega_{m0}t)$, where $\Delta k = \frac{dC}{dx}|_{x=x_0} VV_p$.

Thus the modified equation of motion for the resonator becomes:

$$\ddot{x} + \Gamma_m\dot{x} + [k_{m0} + k_p(t)]x = \delta F(t) \tag{4.33}$$

The equation can be solved by using the normal mode approach described by Louisell for electrical parameters [106]. The transformation is defined as:

$$a = \frac{dx}{dt} + j\Omega_1^* x \;\&\; a^* = \frac{dx}{dt} - j\Omega_1 x \tag{4.34}$$

where, $j = \sqrt{-1}$ and $\Omega_1 = \Omega_{m0}[(1 - \Gamma_m^2/4)^{1/2} + j\Gamma_m/2]$.

The inverse transforms are:

$$x = \frac{a - a^*}{j(\Omega_1^* + \Omega_1)} \tag{4.35}$$

$$and,\ \frac{dx}{dt} = \frac{\Omega_1 a + \Omega_1^* a^*}{\Omega_1^* + \Omega_1} \tag{4.36}$$

From the equations derived above, it can be shown that:

$$\frac{da}{dt} = j\Omega_1 a + jk_p(t)\frac{a - a^*}{\Omega_1 + \Omega_1^*} + \delta F(t) \tag{4.37}$$

We assume the resonant force acting on the system is expressed as $\delta F = F_0 exp(j\Omega t + \phi)$, where $\phi$ is the phase difference between the resonant drive and the parametric pump. Now for steady state situation the solution of the equation (4.36) would take the form of: $a(t) = Aexp(j\Omega_{m0}t)$, where A is a complex constant.

Now, if we replace equation (4.36) with this term and by only taking the terms involving $\exp(j\Omega_{m0}t)$ one can show that:

$$[j(\Omega_1 - \Omega_{m0})A - \frac{\Delta k}{2(\Omega_1^* + \Omega_1)}A^* + F_0 exp(j\phi)]exp(j\Omega_{m0}t) = 0 \tag{4.38}$$

Under this condition that $\Gamma_m$ is negligible the first order approximation leads that: $\Omega_1^* + \Omega_1 \simeq \Omega_{m0}$ and $\Omega_1^* - \Omega_1 \simeq j2\Omega_{m0}\Gamma_m$. Using these approximations it can be shown that the amplitude of parametric amplification is:

$$|A| = (\frac{F_0\Omega_{m0}}{k_{m0}\Gamma_m})^{1/2}[\frac{cos^2\phi}{(1 + \Delta k/2k_{m0}\Gamma_m)^2} + \frac{sin^2\phi}{(1 - \Delta k/2k_{m0}\Gamma_m)^2}]^{1/2} \tag{4.39}$$

.

substituting the expression for $\Delta k$ in the equation above gives:

$$|A| = (\frac{F_0\Omega_{m0}}{\beta_{m0}\Gamma_m})^{1/2}[\frac{cos^2\phi}{(1 + V_p/V_t))^2} + \frac{sin^2\phi}{(1 - V_p/V_t)^2}]^{1/2} \;\; where, V_t = 2\beta_{m0}\Gamma_m/(V * \frac{dC}{dx}|_{x=x_0}) \tag{4.40}$$

From here one can compute the amount of parametric gain achieved under this configuration; which can be done by finding out the ratio of amplitude of response when parametric amplification takes place to the situation when there is no parametric amplification. The expression of response without parametric amplification can be found by putting $V_p = 0$; which is:

$$|A|_{pump-off} = (F_0\Omega_{m0}/\beta_{m0}\Gamma_m)^{1/2} \tag{4.41}$$

So finally we define the gain of parametric amplification as:

$$G(\phi) = \frac{|A_{pump-on}|}{|A_{pump-off}|} \tag{4.42}$$

Using equations defined above, we can finally express gain of parametric amplification as:

$$G(\phi) = [\frac{cos^2\phi}{(1 + V_p/V_t))^2} + \frac{sin^2\phi}{(1 - V_p/V_t)^2}]^{1/2} \tag{4.43}$$

The expression of this gain $G(\phi)$ is plotted against the reduced parametric drive $\bar{V}$ defined as $\bar{V} = V_p/V_t$ in Figure 4.18(a). As can be seen from the equation (4.42) when the phase difference $\phi$ is $\pi/2$ between the drive and the pump, there is an amplification which grows towards infinity with $V_p \to V_t$. While on the other hand there is a deamplification for the phase difference of $\phi = 0$ between the source and the pump, and it goes asymptotically towards 0.5 with an increase in the parametric pump. Figure 4.18(b) on the other hand plots the parametric gain of the resonator against the phase difference$\phi$ for a fixed $\bar{V} = 0.9$. The result is shows highest value at $\phi = \pi/2$, while asymptotically decreasing towards 0.5 as $\phi$ travels towards 0.

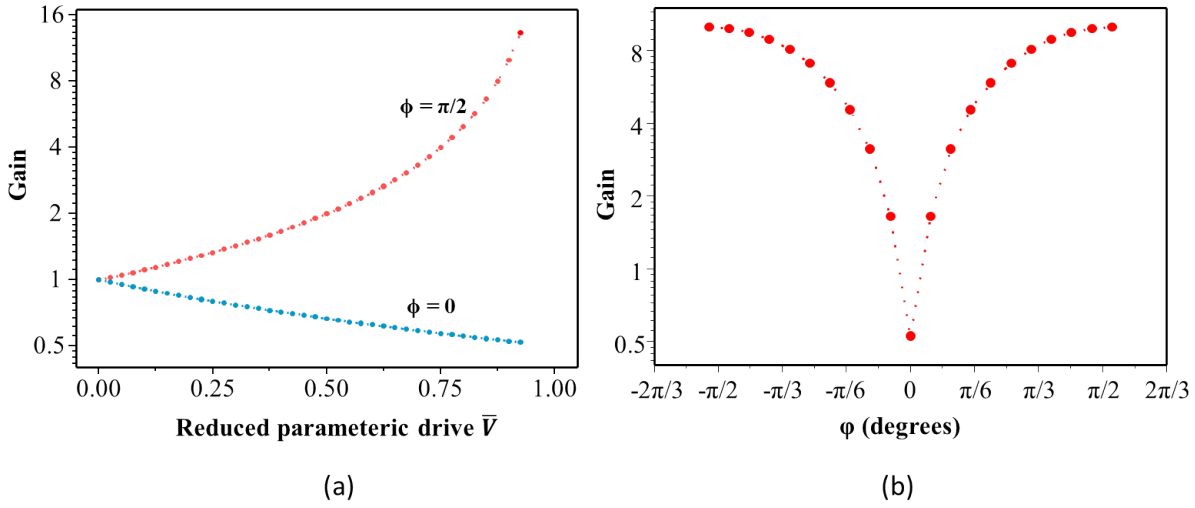


Figure 4.18: (a) Variation of parametric gain with the parametric drive under two separate phase differences $\phi = 0$ and $\phi = \pi/2$ (b) Variation of parametric gain with the phase difference between the resonant drive and parametric pump under a constant reduced parametric drive $\bar{V} = 0.9$.

### 4.4.2 Experiments: parametric amplification and deamplification

The experimental set up and the schematic of the experiment is shown in Figure 4.19. In the experiment two separate signal generators were used for driving the system in these two different frequencies. The first generator was used to drive the resonator weakly at the natural resonance ($\Omega_{m0}$) with a weak drive ($V_{ac} = 100mV$) well below nonlinear regime (Figure 4.6). A second generator then was used to pump the system at $2\Omega_{m0}$. At the beginning the second generator was used to generate a signal at $\Omega_{m0}$ with a higher amplitude (typically $4 - 10V$) being synchronized with the first generator. The output of the second generator was then fed to a frequency multiplier with a multiplication factor of 2 to finally produce a response at $2\Omega_{m0}$. In this way it was possible to keep a constant phase relationship between the drive and the pump. A phase shifter was connected at the output of the second signal generator in order to continuously vary the phase difference between the signal generators. Finally the response was recorded at the natural resonance by using a lock-in amplifier.

One important factor to note here is, as it will be seen later, that there is a gradual frequency shift with the parametric pump. This results in a detuning of the eigenfrequency of the oscillator, so every time when the pump voltage was increased the drive as well as the pump frequency was adjusted to counter this frequency shift effect. Another factor is the mixing of the drive and pump signals; since both the drive and the pump are applied to the membrane through the same electrodes the signal applied to the system suffers from a signal mixing problem. This mixing effect is really negligible when the drive and pump strength are similar, but increases when one of the amplitudes is much weaker than the other. So, the experimental results required some further calibrations which is discussed in Appendix C.

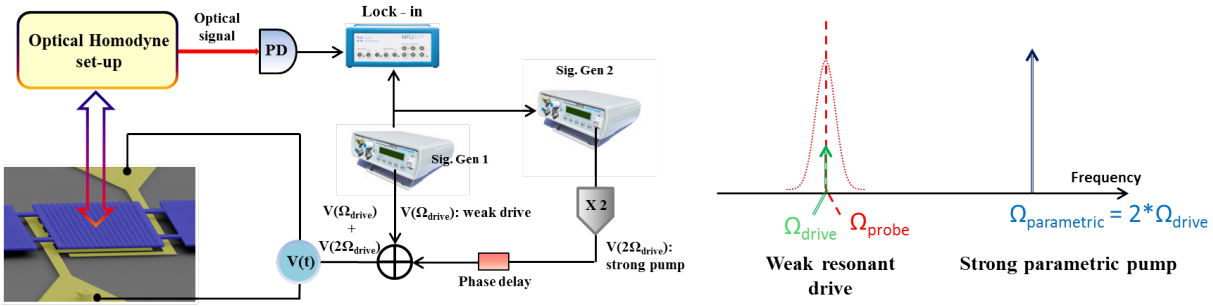


(a) (b)

Figure 4.19: (a) Experimental set-up for parametric amplification experiment, (b) scheme of experiment on parametric amplification: there is a strong pump at a frequency twice the natural resonance ($2\Omega_{m0}$) while there is weaker drive at the natural resonance ($\Omega_{m0}$). The system is also being probed at its natural resonance.

The experimental results are displayed in Figure 4.20, which shows variation of parametric gain with the phase difference between the resonant drive and the parametric pump. The parametric gain is defined as the ratio of the amplitude response of the system when parametric excitation is activated to response of the system when there is no parametric actuation. In every case the resonant drive was fixed below nonlinear threshold at 100mV, while the responses were recorded for several values of the parametric pump, from $V_p = 4V$ to $10V$. The phase difference between the resonant drive and parametric pump was also varied from 0° to 180° . In every case it can be noticed that the gain in the response varies from a region of amplification to a region of deamplification; the effect is strongest for a parametric pump of 10V. The height of amplification and depth of deamplification is really pronounced in this case, the difference between these two peaks (difference between highest value of amplification and lowest value of deamplification) however decreases as the parametric pump is reduced. For example, at 4V of parametric pump the response with respect to the phase difference is much more flatter compared to the case where parametric excitation was 10V.

Since the experiment is susceptible to several noise source (electrical fluctuations, fluctuations from detectors, lock-in to name a few) better estimation of the amplification and deamplification was extracted from fits rather than providing directly from the plots. These fits were performed by a modified version of the equation (4.42) and can be written as:

$$G(\phi) = \left[\frac{cos^2(\phi+\alpha)}{(1+\bar{V})^2} + \frac{sin^2(\phi+\alpha)}{(1-\bar{V})^2}\right]^{1/2} \tag{4.44}$$

A parameter $\alpha$ is introduced in equation (4.43) which acts as a constant phase offset. This is due to the fact that in practical conditions there is always a phase offset between the drive and the pump, which comes into play from various delays in electrical connections. This makes the maxima and minima of the gain to occur at different $\phi$ values (other than

classical $\pi/2$ and 0 degree), however the phase difference between the crest and base should always be $\pi/2$. It is the same reason for which these peaks and lows are observed to occur at different phase values for different pump voltage $V_p$. From the fits not only it's possible to extract the maxima and minima of the gain $G(\phi)$ but also it is possible to determine the critical parametric drive $\bar{V}$. The fits are also represented in Figure 4.20 by dotted black lines for each case of parametric amplification. The fit follows the response quite nicely, the phase value at which the lowest deamplification and highest amplification is observed is about 20 and 110 degrees respectively, which gives a expected phase difference of 90 degrees between them. From the fits it is possible to determine the maxima and minima for the gain in each case. The result is plotted in Figure 4.21(a), an increase of the amplification as well as a decrease of deamplification can be observed for two separate phase differences. For $V_p = 10V$ an amplification of about 4.5 and de-amplification close to 0.55 was observed. To compute the fit we use equation (4.43) with fixed phase differences (depending on if we are looking at gain maxima or minima) and the fits predict a critical voltage $V_t$ of around $14.0V$.

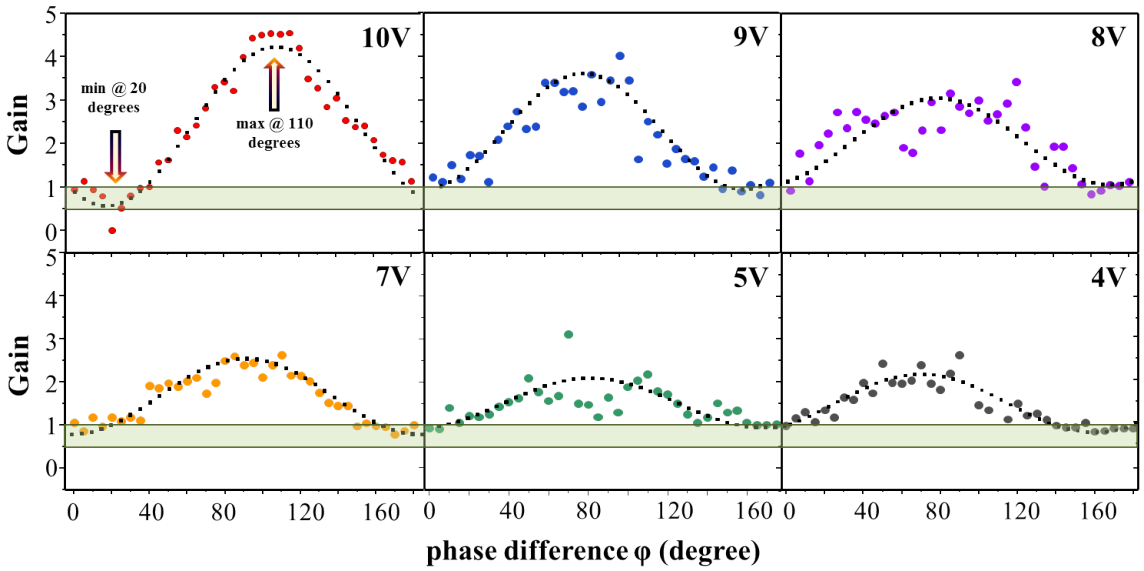


Figure 4.20: Parametric amplification of the nano-mechanical resonator for a fixed resonant excitation of 100mV and several parametric excitation ($V_p$ = 4-10V). While the Y-axis displays value of the parametric gain, the X-axis provides the variation of the phase difference between the resonant drive and parametric pump. The fits are shown by black dotted lines.

The critical drive $\bar{V}$ was also extracted for each case and are plotted in Figure 4.21(b). There is a monotonic increase in the critical drive with the increase in parametric excitation, although there is a bump in $\bar{V}$ around $6V$, which we believe is mainly due to some experimental noises rather than due to any other physical reasons. Value of the critical drive $\bar{V}$ at $V_p = 10V$ is about 0.7 as estimated from the fits (Figure 4.20). Now, since $\bar{V} = V_p/V_t = 0.7$,

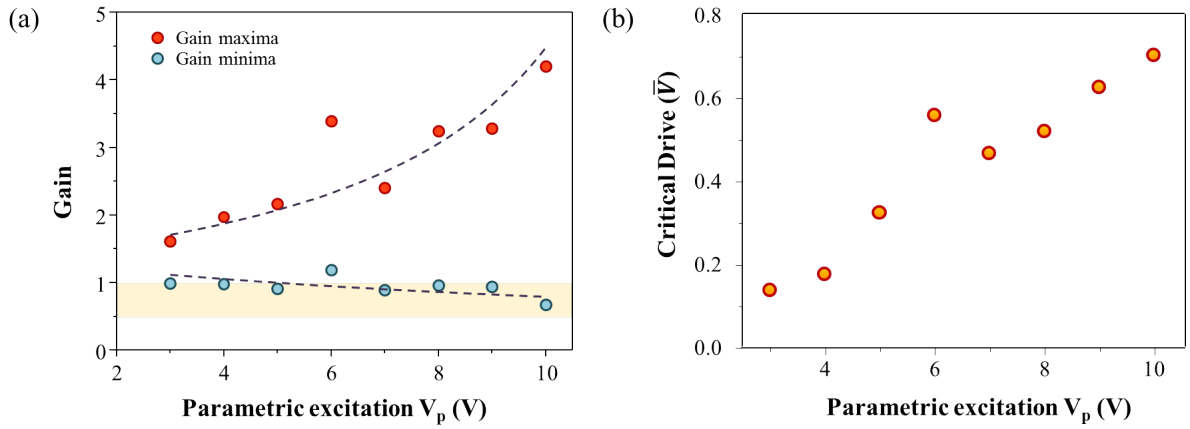


Figure 4.21: (a) Plot of extracted gain maxima and minima for various values of parametric pump with the fit (b) Plot of extracted critical drive $\bar{V}$ with parametric pump.

this gives a predicted value of $V_t$ of about $14.3V$, which is close to the value predicted by the fit from Figure 4.21(a). However this value is above the range of $V_p$ considered for the experiment. As expected for parametric amplifications with other $V_p$'s the same value of $V_t$ is extracted. Due to some technical reasons especially not to damage the membrane or the on chip electrical connectors, parametric excitation with higher drive were not explored. Such a high parametric excitation to observe this exponential enhancement in gain and hence self oscillation, can be attributed to the fact that the electromechanical coupling for this configuration is not high enough. This however can be increased by tuning the geometry of the system. The sample being used has a separation of $400nm$ between the bottom of the membrane and the top of the electrodes. This configuration gives a calculated electromechanical coupling of $3nm/V$, however this coupling increases exponentially with a decrease in the electrode membrane separation (section 3.2). With our recent optimization in the fabrication procedure we are able to go down to as small as $200nm$ of electrode membrane separation which in theory should result in approximately two time enhancement of the electromechanical coupling factor. With this high degree of coupling we can expect a lower$V_t$ and hence observation of self-oscillation at a much lower value of $V_p$.

### 4.4.3 Phase dependent amplification

In the next set of experiments we performed some phase dependent amplification schemes. The idea is to utilize a similar scheme as described before for parametric amplification, but instead of varying the phase continuously between the pump and drive we fix the phase difference at two discrete values. These discrete values being the phase differences where the gain is maximum and minimum respectively. In this configuration if we switch between these two phase differences we should be able to observe periodic amplification and deamplification effects. In the experiment we fixed the resonant drive at $V_{ac} = 100mV$ and the parametric pump at $V_p = 10V$. Both of these were kept on for the entire duration of the experiment.

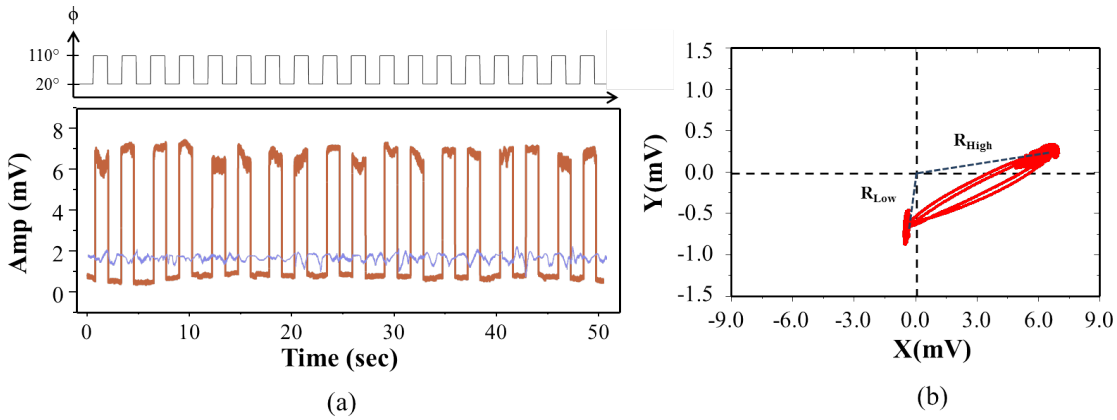


Figure 4.22: (a) Time domain response of the system as the phase difference between the resonant drive and the parametric pump is switched between 20° and 110° (b) same response when tracked in the phase space.

From Figure 4.20 we are able to identify the two phase difference being 20° and 110° for our configuration. After interfacing the computer with one of the signal generators and the lock-in using a python program we could switch discretely between these two phases at a period of $0.5Hz$. At the same time use of the lock-in amplifier helped us to perform acquisition of the in-phase (X) and out of phase quadrature (Y) at the same time. So, it was possible to observe the phase space trajectories of the oscillator during the entire process.

Figure 4.22(a) displays the time domain acquisition of the response as the phase difference is switched between these two discrete values. The signal without amplification is displayed by the blue line while the modulation signal (square phase modulation between 20° and 110°) at 0.5 Hz is displayed by the black line. We are able to observe switching at the output signal everytime there is a switch in the phase difference at the input. If we define the fidelity as the ratio of the number of switching observed at the output while there is a phase switching at the input then we can conclude that for all of our experiments a fidelity of 100% was observed. Another interesting representation can be given by tracking down how the system responds in the phase space as the switching is performed. We observe in Figure 4.22(b) that everytime there is a switch between amplification and deamplification a clear switch in phase space is always observed. The radial distance of the phase points from the origin denotes the amplitude of oscillation, therefore clearly indicating when the system is under amplification ($R_{High}$) and when it is under deamplification ($R_{Low}$). The advantage of a system exhibiting such separate states under parametric excitation is that it can be used to exhibit memory devices with binary like states as well as realizing complicated binary networks as exhibited by Mahboob et al. [39].

### 4.4.4 Eigenfrequency tuning with parametric excitation

Another very interesting effect under parametric excitation is the tuning the eigenfrequency of the resonator under study. It was mentioned earlier that when a system is well below the nonlinear threshold, the action of the parametric pump is to modulate the spring constant of the system at twice the natural resonance frequency. Thus the simplified equation of motion of a system under parametric excitation can be written as:

$$\ddot{x} + \Gamma_m \dot{x} + \Omega_{m0}^2 x * (1 - H_p cos(2\Omega_{m0} t)) = F \;\; where, F = F_0 cos(\Omega_{m0} t) \tag{4.45}$$

We define here $\Omega_{m0}$ as the unmodulated natural resonance frequency, similarly we define $\Gamma_m$ is the damping factor of the resonator, F is the force acting on the system at natural resonance frequency and $H = H_p cos(2\Omega_{m0} t)$ is the modulation of the spring constant of the system due to parametric excitation. The parameter H is directly related to the amount of parametric pump acting on the system. If we transform the equation (4.45) in frequency domain then it takes the form (considering displacement vector as $x(t) = X * exp(j\Omega t)$):

$$-\Omega^2 X + j\Omega\Gamma_m X + \Omega_{m0}^2 X * (1 - H_p)) = F \tag{4.46}$$

which if simplified takes the form:

$$|X| = F/\sqrt{[\{-\Omega^2 + \Omega_{m0}^2(1 - H_p)\}^2 + \Omega^2\Gamma_m^2]} \tag{4.47}$$

Now at resonance, ideally the displacement should diverge to infinity i.e. the denominator should approach minimum. Considering the modified resonance to be $\Omega_m$ one can write:

$$\{-\Omega_m^2 + \Omega_{m0}^2(1 - H_p)\}^2 = 0 \tag{4.48}$$

which can be reduced to:

$$\Omega_m^2 = \Omega_{m0}^2(1 - H_p) \tag{4.49}$$

$$i.e. \; \frac{\Omega_m^2}{\Omega_{m0}^2} = (1 - H_p) \tag{4.50}$$

So, as expressed by equation (4.50) the eigenfrequency has a parabolic dependence on the intensity of modulation of the spring constant $H_p$. As this intensity $H_p$ increases there is a decrease in the natural resonance i.e. the eigenfrequency of the system $\Omega_m$. As there is a decrease in the eigenfrequency with the applied parametric pump, it can be identified as a spring softening effect. Similar equations may be derived for other superharmonic frequencies as well, but as it was mentioned before the threshold required for parametric amplification is higher for those cases which will make the amplitude of spring modulation $H_p$ lower. Thereby making the observed frequency shift to be much smaller.

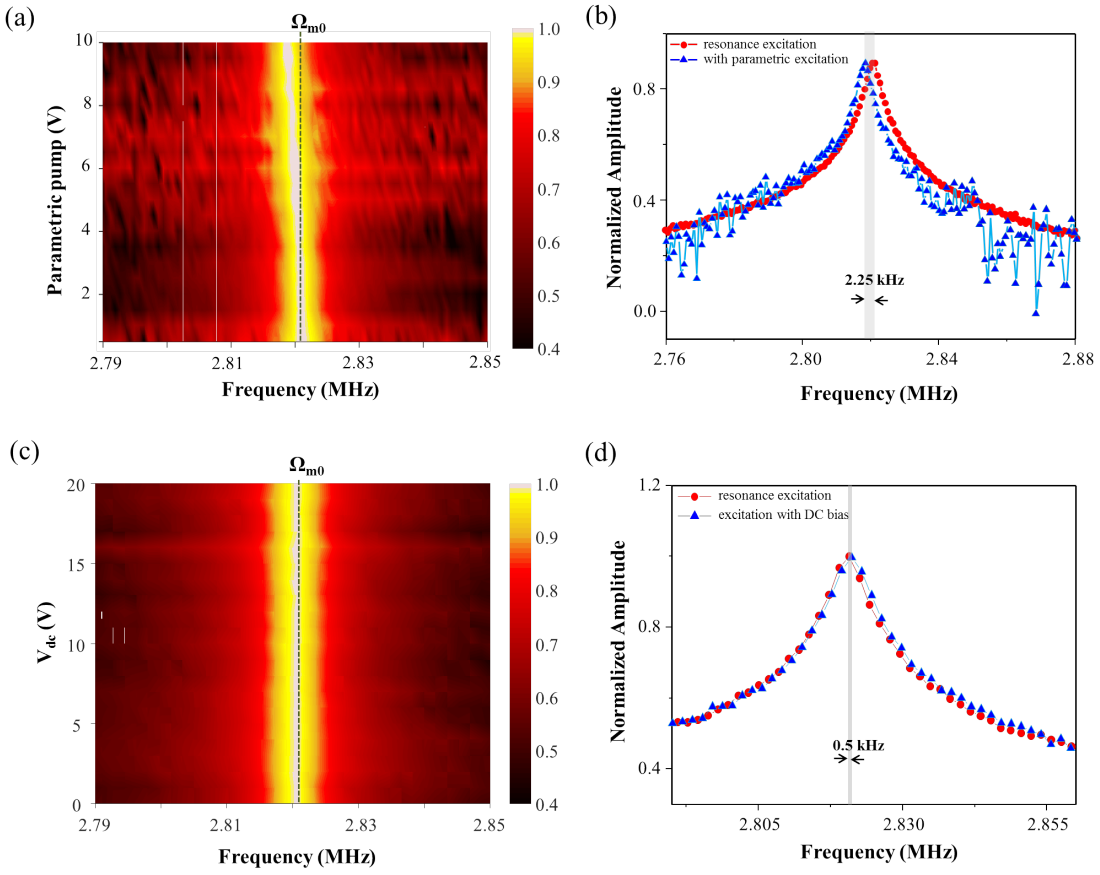


Figure 4.23: (a) Normalized spectra for eigenfrequency shift with an increase of the parametric pump (b) change in the response spectra as the parametric pump is activated, a clear spring softening shift in the frequency response can be observed when the parametric pump is activated ($V_p = 10V$) (c) Eigenfrequency shift with a DC pump on the same membrane electrode system (d) Shift in the response spectra as DC bias is activated, a small shift of only 0.5kHz is observed at $V_{DC} = 20V$.

The experiment was set up by first of all making sure that the system is under the nonlinear threshold, and then increasing the parametric excitation gradually while tracking down the resonant response at the same time. So the resonant excitation was fixed at 100mV

and the parametric excitation $V_p$ was increased from 0.25V gradually towards 10V. The resulting surface plot is shown in Figure 4.23(a), the spectra has been normalized to give a clear indication about the shift in the eigenfrequency. This supports strongly the equation where it clearly shows a gradual decrease in the eigenfrequency as the pump voltage is increased. To quantify the observed shift, we now focus on figure 4.23(b). Here we plot the response spectra of the system under two different conditions; the conditions have been chosen in such a way that the amplitude response is identical in both cases. The red graph shows the response of the system with only resonance excitation and no parametric excitation. The excitation voltage is fixed at $1V$ and the excitation frequency is swept around the natural resonance. Next, the pump was activated at twice the natural resonance frequency and at an excitation of $10V$ while the resonant excitation was fixed at $100mV$. Like before the excitation frequency was swept across the resonance and the response spectra was recorded around the natural resonance, this is shown by the blue curve. Clearly a shift in the eigenfrequency is observed, the shift is towards the red side of the spectra and thus this is a spring softening effect. To extract clearly the resonance, these graphs were fitted with lorentzian response and the resonance frequencies were extracted. A shift of $2.25kHz$ was observed at a parametric pump of $10V$. This phenomenon is what was discussed previously in equation (4.50) where we could observe a parabolic shift in the eigenfrequency with increase in parametric actuation which is identical with the experimental result.

This now brings us to the comparison between the case when a DC voltage is applied on the system instead of the parametric pump. This case was discussed in the previous chapter, but it was on a different membrane. In the case of this particular membrane however the effect was much less pronounced, the reason can be many fold. It may come from the fabrication imperfections, from variation in electrode designs or simply from the material properties. The surface plot of the response under this actuation scheme is shown in Figure 4.23(c), although it is very difficult any substantial shift in this graph. A little improvement is observed if we directly look at the spectra with no DC bias and with a DC bias of $20V$ (4.23(d)). The shift observed however is still very small and the Lorentzian fits produce a shift of only $0.5kHz$. With this we can conclude that for this sample frequency shift with parametric excitation seems to be more effective than usual DC bias which has been the norm used in many architectures [40][104]. The observed frequency shift with parametric excitation ($2.25kHz$) is more than the FWHM of the spectra which is about $0.9kHz$. This relative shift in frequency can be enhanced by playing with the geometry of the membrane. As mentioned above with a decrease in the electrode-membrane separation we expect to see an increase in the electromechanical coupling factor which in turn should increase the observed eigenfrequency shift.

### 4.4.5 Nonlinearity tuning by parametric excitation

In this section we will discuss on the situation where the system is still under parametric excitation but the resonant excitation crosses the nonlinear threshold ($V_{Th} = 4.25V$). This is basically an extension to the discussion done in the previous section. In the previous section it was observed that it was possible to tune the eigenfrequency by parametric excitation as

a direct result of spring constant modulation of the resonator. The result as it was observed is a spring softening effect which decreases the eigenfrequency of the system. When however the system is above the nonlinear threshold this softening should directly modulate the nonlinearity in the system. In order to understand the phenomenon better we comeback to the Duffing equation again but with an added quadratic nonlinear component along with the parametric excitation term.

$$\ddot{x} + \Gamma_m \dot{x} + \Omega_{m0}^2 x(1 - H_p cos(2\Omega_{m0} t) + \beta_2 x + \beta_3 x^2) = F cos(\Omega_{m0} t + \phi) \tag{4.51}$$

Where $\beta_2$ and $\beta_3$ are the quadratic and 3rd order nonlinear coefficients. As it was mentioned before, the odd nonlinear component is responsible for the spring hardening effect in the system, while the quadratic nonlinear term which is known as the symmetry breaking term in general like the DC term, responsible for the spring softening effect of the resonator. This gives us an unique opportunity to play with the quadratic nonlinearity and induce a spring softening effect on a already spring hardened resonator.

In the experiment the set up was kept same as in the case of parametric excitation, however with a resonant excitation above the nonlinear threshold. The experimental spectra is displayed in Figure 4.24(a), the resonant excitation is kept at $9V$ while firstly (in blue) the parametric excitation is turned off ($V_p = 0V$). The Duffing like response in the amplitude can be observed for this case exhibiting the nonlinearity in response. While when the parametric excitation is turned on with $V_p = 4V$ (in red) a clear change in the response is observed. A reduction in the hysteresis as a result of decrease in the nonlinearity is observed in this scenario. With an even higher parametric actuation of $V_p = 10V$ an even higher reduction in the hysteresis of the response is observed due to even more lowering in the nonlinearity (green).

The above experiments were performed for a fixed phase difference of 0 degree between the resonant drive and the parametric pump. An interesting factor was observed as the phase difference between the resonant drive and the parametric pump was varied. The detuning of nonlinearity seems to be present for any given phase differences, yet its magnitude of detuning happen to vary depending on the phase difference. Interestingly highest detuning was observed when the phase difference between the drive and the pump was 110 degrees and the least detuning was observed when the phase difference between the drive and the pump was about 20 degrees. This corresponds exactly to the phase difference values where highest parametric amplification and lowest parametric deamplification was observed. This we believe is in a direct consequence of the parametric amplification process which enhances and diminishes the effect of spring softening in the respective cases. Figure 4.24(b) explains how the system responds to situations when first of all there is no parametric excitation (in blue), then when there is a parametric pump of $10V$ at a phase difference of 20 degrees (orange) and finally for a parametric pump of $10V$ with a phase difference of 110 degrees (green). The same situation is observed while the pump voltage $V_p$ was varied from $10V$ to $5V$. If the resonant drive is weaker (for example $5V$) almost a pure linear response is been able to observe for the parametric pump of $10V$. The spectra with other pump voltages $V_p$ are not shown here although they will be used in the discussion below.

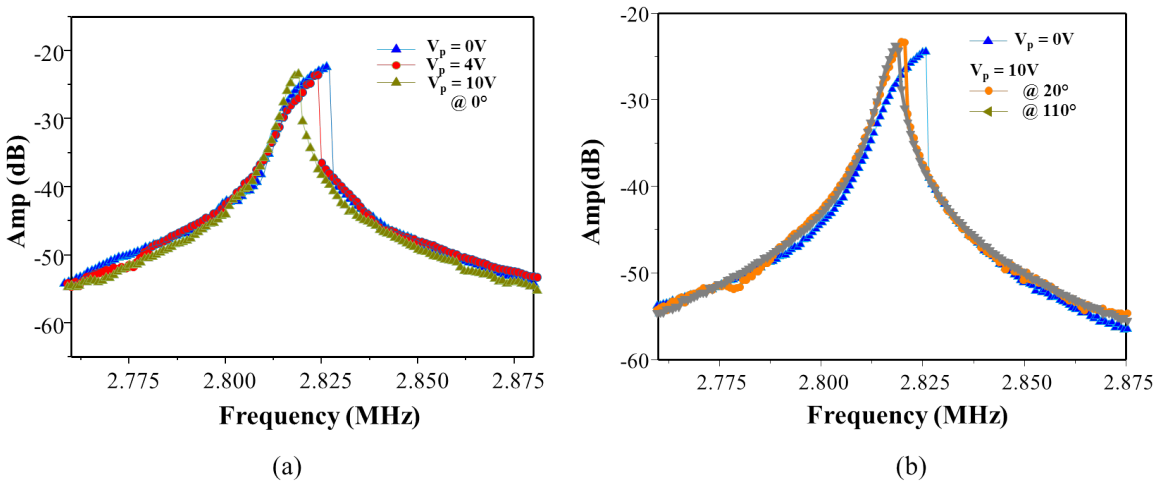


Figure 4.24: (a) Comparison between resonant excitation at $V_{ac} = 9V$ without any parametric excitation (blue) and with parametric excitation at $4V$ (red) & $10V$ (green) at a $0°$ phase difference between the resonant drive and the parametric pump (b) comparison between resonance excitation at $V_{ac} = 9V$ with no parametric excitation (blue) and with parametric excitation at $V_p = 10V$ with two different phase differences $20°$ (orange) and $110°$ (green) between the resonant drive and the parametric pump.

To properly comprehend the effect of this nonlinearity tuning it was then important to properly quantify the evolution of the nonlinear factor. The nonlinear coefficient could be extracted from the fitting with the Duffing equation described. We have changed the factor $\beta_3$ to $\beta_{eff}$ in order to include the influence of the quadratic nonlinear coefficient on the Duffing nonlinear factor $\beta_3$:

$$|x|^2 = F^2/[(1 + \beta_{eff} * x^2 - \frac{\Omega^2_{drive}}{\Omega^2_{m0}})^2 + \Gamma^2_m/4] \tag{4.52}$$

which is identical to equation (4.11). For the fitting we neglect the quadratic nonlinearity factor and only consider the 3rd order nonlinearity coefficient i.e. the Duffing coefficient. In this way we can quantify how the Duffing nonlinearity is modified by the parametric pump intensity and as well as by the phase difference between the resonant drive and the parametric pump.

Figure 4.25(a) describes how the nonlinearity coefficient is modified as a function of the phase difference between the resonant drive and the parametric pump. The resonant drive was fixed at $10V$ while the parametric pump was also kept at a value of $10V$ and then the phase difference between the drive and the pump was varied from 0 degree to 160 degrees. For each phase difference value the response spectra was fitted with equation (4.52) and then the Duffing nonlinearity parameter $\beta_{eff}$ was extracted. The resulting plot shows sinusoidal like variation of the nonlinear coefficient of the $\beta_{eff}$ factor with the phase difference. This

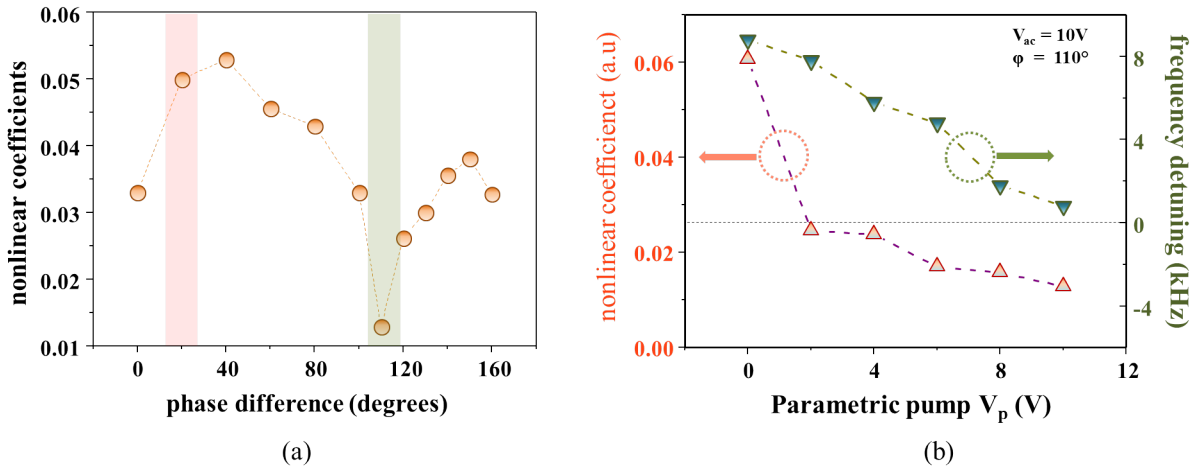


Figure 4.25: (a) Variation of nonlinear coefficient for a fixed resonant drive and parametric excitation with phase difference between the drive and the pump (b) Variation of nonlinear coefficient with a fixed resonant drive with parametric excitation (red) and variation of detuning with parametric pump for a fixed resonant drive (green).

behavior is related to the sinusoidal variation of parametric amplification in Figure 4.20 under the nonlinear threshold; these factors influence the nonlinear effects when the the pump is placed at different phase differences compared to the resonant drive. For example, when the phase difference between the drive and the pump is 20° there is a deamplification under the nonlinear threshold, however when the resonant drive is above nonlinear threshold this results in a lesser reduction of nonlinear coefficient $\beta_{eff}$ (Figure 4.25(b). While on the other side when this phase difference is 110° there is an amplification below the nonlinear threshold, however above the nonlinear threshold this results in a higher reduction in the factor $\beta_{eff}$. The highest value of the $\beta_{eff}$ was computed to be around 0.05 at 20 degrees while the lowest value of $\beta_{eff}$ was found to be around 0.025 at a phase difference of 120 degrees. These regions are highlighted by red and green color respectively.

Next, we tried to observe how this $\beta_{eff}$ factor varies with the parametric pump at a fixed resonant drive for a fixed phase difference $\phi$. In the experiment we keep the resonant excitation at $V_{ac} = 10V$ and fix a phase difference of 110° between the drive and the pump. At the beginning the pump remains switched off, however from here we start to increase the pump voltage $V_p$ in steps of $2V$. The detuning is measured by measuring the deviation of the hysteresis edge i.e. modulated eigenfrequency $\Omega_m$ with respect to the natural resonance frequency $\Omega_{m0}$. When the pump is switched off i.e. $V_p = 0V$, we observe no shift in the hysteresis edge as expected and thus the nonlinearity coefficient $\beta_{eff}$ remains on the higher side (around 0.06). While as we start to increase the parametric pump $V_p$ we observe a detuning of the resonance frequency $\Omega_m$ and at the same time a decrease in the nonlinearity. Initially the drop in nonlinearity is quite a lot, for $V_p = 2V$ the $\beta_{eff}$ factor drops to around 0.025 and after that slowly decays towards 0.013 at $V_p = 10V$. Finally we can conclude that with the parametric pump at $V_p = 10V$ we are able to achieve almost 75% decrease in

the nonlinearity factor $\beta_{eff}$ which occurs due to the spring softening effect discussed in the previous section. At the same time we also plot the detuning of eigenfrequency against the parametric pump $V_p$ for a fixed resonant drive of $10V$ and phase difference $\phi = 110°$. The highest detuning is about $8.8kHz$ for $V_{ac} = 10V$ with no parametric excitation. Whereas, as soon as the parametric excitation is activated a detuning is observed in the eigenfrequency. For $V_p = 10V$ at $\phi = 110°$, a detuning of $0.8kHz$ is achieved. For an even higher excitation it is possible to completely nullify the nonlinearity. But due to some technical reasons parametric excitation for higher $V_p's$ were not performed.

## 4.5 Conclusion

In this chapter we studied in depth the nonlinear behavior of our Nano-Opto-Electro-Mechanical system. We began the chapter by introducing a nonlinear Duffing system with spring hardening as well as softening effect and focused on extracting useful parameters about the nonlinearity. Then we shifted our attention to sub/super-harmonic excitation; this produced instability tongues for a damped resonator for up to 8th order. When the system is then excited in the nonlinear regime it is shown to exhibit bifurcation where it exhibits two distinct states separated by an angle of $\pi$ radians in the phase space. Existence of such bifurcations have been previously demonstrated for sub-harmonic excitation (i.e. frequency down conversion) [39] but not for super-harmonic excitation (frequency up conversion). Rigorous study of phase dynamics across the instability tongue was also carefully performed which gave a clear understanding on how the system evolves as one moves across the instability tongue. We were able to observe such effects up to 7th order and probably beyond if the excitation was increased. We then shifted our focus on parametric amplification experiments, where it was shown that it is possible to enhance the resonant response by modulating the spring constant of the resonator at twice the natural resonance provided the system is under nonlinear threshold. An amplification close to 5 was observed; by increasing the pump further it was theoretically possible to observe higher gain in response. We also demonstrate that tuning of the eigen-frequency is possible by playing with the excitation at twice the natural resonance frequency. As this resembles spring softening effect we decided to go further and explore what happens when the resonant excitation is beyond nonlinear threshold. As a result we were able to tune the nonlinearity of the resonator by directly playing with the parametric pump. The nonlinearity is not only tunable by the parametric pump but also more markedly by the phase difference between the drive and pump. This gives us a unique opportunity to continuously tune the nonlinearity of the system just by varying the phase difference from 0 to 180 degree.

Finally in this chapter we have seen that there exist a bistability in frequency for the NOEMS system. Bistability or hysteresis should also exist in amplitude as well as in phase. This gave us a platform to perform some experiments known as Stochastic Resonance, where it will be seen that it is possible to switch between the stable states (inside the bistable tongue) by using appropriate noise. These experiments followed by the results will be discussed in the next chapter.

# Chapter 5

# Stochastic Resonance

## 5.1 Introduction

The phenomenon of stochastic resonance corresponds to the amplification of a weak signal in a nonlinear system by application of external noise. The concept was actually put forward by Benzi and his collaborators [107] in order to explain the problem of periodically recurring ice ages; its modeling was put forward by Kramer in 1940 [108]. The role of stochastic resonance has become very important in recent years in fields of physics, chemistry, biology and engineering. The theory since then has been applied for many applications e.g. penning trap [109], superconducting loops with a Josephson junctions [110], atomic cloud in a magneto-optical trap [111] and in VCSEL lasers [112]. Recently this phenomenon has been extended to nanomechanical systems. These highly nonlinear systems include for example double clamped beams [113]-[114], cantilever structures [115] and torsional oscillators [116][63]. All of them display stochastic resonances by means of injected noise in the system. Most of them rely on injected amplitude noise. However it will be shown in the coming sections that another way to implement stochastic resonance can be by using phase of the driving signal.

In this chapter we start by introducing the externally induced bistability in amplitude and phase, and after that we show how this bistability can be utilized in order to jump between the bistable states. Later sections will focus on giving some idea about how switching between metastable states can be achieved by introducing noise in the system. Here we talk about switching rates and the threshold of switching. Moving to the next sections, we will realize stochastic resonance in amplitude and phase and will give a comparative study between the processes. In conclusion we will introduce a methodology by which the amplification of weak signal could be enhanced.

## 5.2 Basic concepts

### 5.2.1 The double well potential

In the previous chapter we talked about bistability of our NOEMS platform under strong excitation regime. We had shown that a hysteresis exists in frequency when a system is under this regime. When a system is inside such a regime, it has access to two stable and one unstable states, this is called bistability. This bistability can exist in amplitude, phase, polarization etc. A system in bistable regime can be represented by two different states in phase space (Chapter 4) which are commonly referred as the basins of attraction. An externally driven nonlinear system can be expressed by Duffing equation:

$$\ddot{x} + \Gamma_m \dot{x} + \Omega_{m0}^2 x(1 + \beta_3 x^2) = -\frac{1}{2}\frac{dC(x)}{dx}.V\delta V \tag{5.1}$$

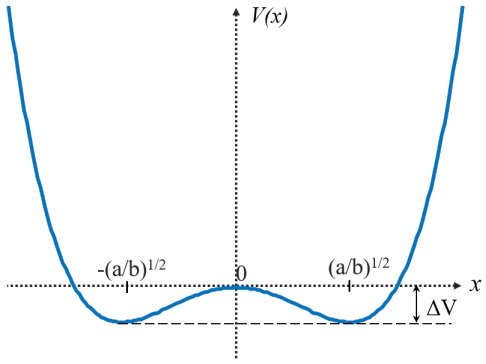


Figure 5.1: The normalized double well potential.

where, $\Gamma_m$ is the damping factor, $\Omega_{m0}$ is the natural eigen-frequency of the resonator, $\beta_3$ is the Duffing nonlinearity parameter and the right hand side consists of the driving term where $\delta V$ refers to the external voltage applied to the system (refer to Chapter 3 for detailed discussion on the forcing). From equation (5.1) the nonlinear forcing term therefore can be expressed as:

$$F = -\frac{dV}{dx} = -(\Omega_{m0}^2 x + \Omega_{m0}^2 \beta_3 x^3) \tag{5.2}$$

which gives us the potential function:

$$V(x) = -\frac{a}{2}x^2 + \frac{b}{4}x^4 \tag{5.3}$$

where, $a = \Omega_{m0}^2$ and $b = \Omega_{m0}^2 \beta_3$. Plot of the function described in equation (5.3) is shown in Figure 5.1; it gives a symmetric double-well potential with two minima located at $\pm x_m$ where $x_m = \left(\frac{a}{b}\right)^{1/2}$. The minima are separated by barrier of height $\Delta V = a^2/4b$. In absence of any external disturbance the system prefers to stay in one of the minima i.e. stable

states. However, if an external disturbance is used by means of modulation of the bistable potential by external modulation or noise, the stable states can become metastable. Under such circumstances the system can switch back and forth between these two states. When purely an external noise is used in order to facilitate this switching, the rate of these switching is defined by the so called Kramer's rate [108][117] and its normalized form is expressed as:

$$r = \frac{1}{\sqrt{2\pi}} exp(-\Delta V/\eta) \tag{5.4}$$

where, $r$ is the Kramer's rate and $\eta$ is the externally injected noise.

### 5.2.2 Stochastic resonance

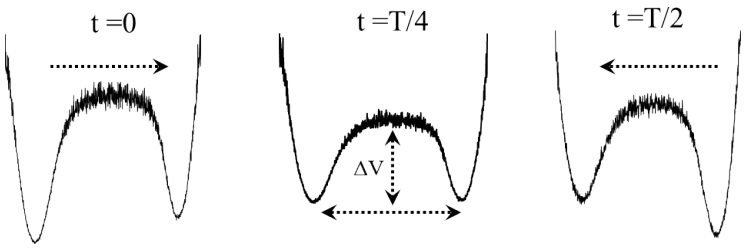


Figure 5.2: Evolution of the bistable potential well under modulation

Stochastic resonance is a phenomenon of amplification of a low amplitude low frequency signal by a bistable system under application of external noise. Let us consider our system with the bistable potential well (Figure 5.2), the bistability in this case is induced externally by driving the system within the hysteresis regime. In general if there is no modulation of the bistable potential, the jumps between the metastable states is random. Let us assume now that the bistable potential is modulated weakly by a external periodic drive with a time period of $T_{mod} = \frac{2\pi}{\Omega_{mod}}$. The modulation is small enough so that the system can not make jump from one state to another; in other words the system stays in one of the states always if not influenced externally. Under such conditions if some external noise is introduced, the system can jump between the metastable states. Under influence of external noise the jumps can be synchronized with the external modulation. In order to have a perfect synchronization therefore the system has to jump two times between the metastable states in a single period of driving. This yields fundamental stochastic resonance which will be realized provided $\Omega_{mod} < r(= 2\pi/T)$, the Kramer's rate. Thus one can write the optimal condition for stochastic resonance as:

$$T_{mod} = 2T = 2\nu exp(1/4\eta) \tag{5.5}$$

or the noise strength:

$$\eta = \eta_0 = \frac{1}{4} ln(\frac{T_{mod}}{2\nu}) \tag{5.6}$$

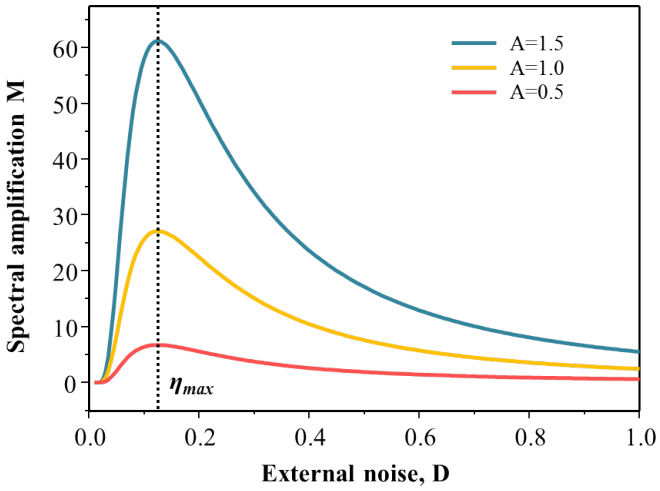


Figure 5.3: Spectral amplification by stochastic resonance for three different amplitude of modulations $A = 0.5, 1.0$ & $1.5$.

At this resonance the coherent contribution to the jump processes has maximum. This behavior can be thereby used to realize stochastic resonance where weak modulation can be amplified by synchronizing the jumps with the external modulation, with the use of some external noise. The amplification in such case thus will be defined as the ratio of the output spectral power and the power of the input modulation. Gammaitoni et al. [61] showed that the expression of the spectral amplification can be written as:

$$M(A, \eta) = \pi \left( \frac{A x_m}{\eta} \right)^2 r \tag{5.7}$$

Here $A$ is the amplitude of the external modulation. This modulation can be either in amplitude or in phase for our system. We will show later in this chapter that indeed modulation of the double well potential is possible either by modulation in amplitude or in phase.

In Figure 5.3 we plot the spectral amplification with applied external noise $\eta$ for a fixed modulation frequency $\Omega_{mod}$. We plot the same for different amplitude of modulations with $A = 0.5, 1.0$ and $1.5$. We observe that for a higher modulation there is an enhancement of the spectral amplification $M$. This happens as for higher modulation it becomes easier for the system to jump between the metastable states, hence there is an increase in the spectral amplification. If we define the optimized noise required for the maximum amplification to be $\eta = \eta_{max}$ (indicated by dashed line in Figure 5.3), then we observe a very weak to no dependence of $\eta_{max}$ on $A$. However it is shown by Jung et al. [118], that $\eta_{max}$ has a strong dependence on $\Omega_{mod}$. With an increase in the modulation frequency $\Omega_{mod}$ there is an increase in $\eta_{max}$ as well. This phenomenon is directly related to the Kramer's rate $r$ of the system; with an increase in $\Omega_{mod}$ one requires higher $r$ in order to achieve spectral amplification.

Realization of stochastic resonance hence requires combination of both external modulation and noise in the system. In this section we have introduced many parameters which

needs to be physically understood and optimized in order to realize stochastic resonance. These parameters are:

- Determination of the threshold of amplitude of modulation $A_{th}$: we define the threshold of amplitude of modulation $A = A_{th}$ beyond which jumps between the states takes place. Below $A_{th}$ modulation of the bistable potential is not enough to induce the switching, however when the modulation crosses this value system can jump between the states. This value is important in order to modulate the system well under this threshold under stochastic resonance configuration.
- Determination of the cut-off of $\Omega_{mod}$ (frequency of modulation): we need to find the cut-off to make sure the system is modulated always well under this frequency. Otherwise the system would not be able to follow the weak external modulation thereby producing no stochastic resonance.
- Determination of the Kramer's rate $r$: as it was shown by equation (5.5), in order to realize stochastic resonance, the system has to be modulated at a frequency lower than its Kramer's rate. Therefore before starting experiments with stochastic resonance it is imperative to determine Kramer's rate of the system, so that we can keep the external modulation below that frequency.

In the upcoming sections we will therefore at first systematically determine all the above-mentioned parameters and finally use them to realize stochastic resonance with both amplitude and phase. We start by reintroducing bistability in our NOEMS platform, however with a different perspective. In the previous chapter we showed that spectral bistability exists in our system, however here we will show that bistability also exist with the actuation voltage. This characterization is important in order find a proper operating point where we could set the system in the bistable regime and realize stochastic resonance.

## 5.3 Bistability: revisit

In this section we briefly revisit the externally induced bistability in our NOEMS platform. In the last chapter we showed that when the nanomechanical resonator is driven beyond a certain threshold ($V_{ac} > 4.5V$) nonlinearity is imposed in the system. This is what we call bistability induced by external excitation; in Figure 5.4(a) & (b) we exhibit such a bistability (with the induced hysteresis) against driving frequency $\Omega_{drive}$. This phenomenon and some of its applications were vastly discussed in the previous chapter, where we probed sub and super-harmonic resonances with excitation inside the hysteretic region. However bistability could also be observed while the driving power is swept at a fixed driving frequency; this is shown in Figure 5.4(c) & (d).

### 5.3.1 Power hysteresis

In order to retrieve the power hysteresis firstly we prepare the system in the upper branch of the hysteresis by sweeping the excitation frequency upwards; we start from a frequency

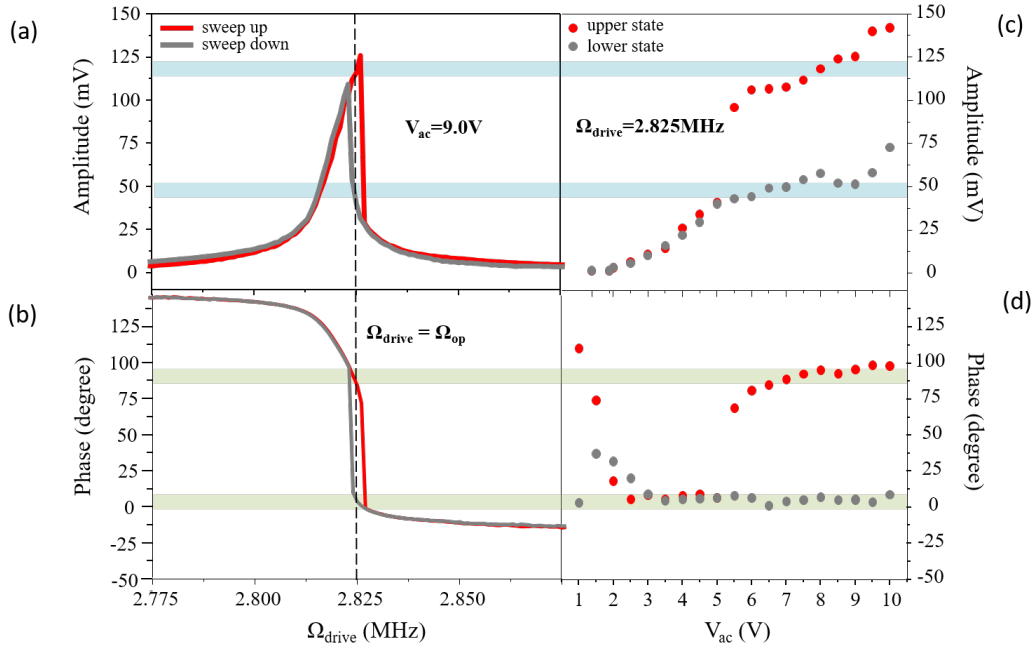


Figure 5.4: Existence of bistability in (a) amplitude and (b) phase response while the frequency of actuation is swept for an actuation voltage $V_{ac} = 9.0V$, bistability in (c) amplitude and (d) phase when the driving power is swept for a fixed drive frequency $\Omega_{drive} = 2.825MHz$.

of $2.80MHz$ for a $V_{ac} = 10V$, which is far from the hysteresis regime. We scan the drive frequency up to $\Omega_{drive} = 2.825MHz$ and fix it to this particular value shown by the dashed line in Figure 5.4(a) & (b). From here we start to decrease the excitation slowly. From now on we will select this frequency (i.e. $\Omega_{drive} = 2.825MHz$) as the operating point and will refer to this frequency as $\Omega_{op}$ (Figure 5.4(a) & (b)) for convenience. Choice of this frequency is related to the shape of the bistable potential, which will be described in details in section 5.5.1. As we keep decreasing $V_{ac}$ we observe now a gradual decrease in amplitude and phase response. When the drive crosses a certain threshold ($V_{ac} \sim 5V$) the system goes out of the bistable regime and we observe a sudden shift in the amplitude and phase (Figure 5.4(c) & (d)). This sudden shift in response occurs due to the change in the eigen-frequency induced by the nonlinearity in the system. For this very reason the phase response below the threshold (for $V_{ac} < 5.0V$) is a little random. The red dots in the concerning figure however only describes evolution of only one of the states of the two stable states. To find the evolution of the other branch we need to prepare the system in the other state; this can be done by sweeping the actuation frequency downward. Like before we begin at a frequency far away from the hysteresis regime ($\Omega_{drive} = 2.850MHz$) and sweep the actuation frequency down to $\Omega_{op}$. We fix the $\Omega_{drive}$ at this point and start to decrease $V_{ac}$ gradually; like before we observe a gradual decrease of the response accompanied with a jump at around $V_{ac} = 5.0V$. This is represented by the gray dotted line in Figure 5.4(c) & (d).

These two branches now represent evolution of the two stable states with $V_{ac}$. However

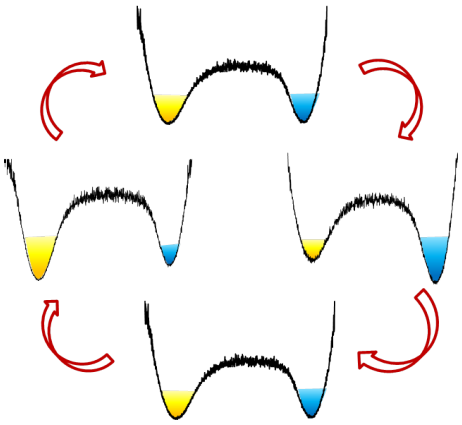

Figure 5.5: Periodic modulation of the bistable potential.

in the Figure 5.4 we do not observe closure of the hysteresis region as one needs to be at a higher value of $V_{ac}$ in order to observe this effect. Regions with higher $V_{ac}$ were not explored due to some technical reasons. Here if we fix $\Omega_{drive}$ and $V_{ac}$ at certain values so that system have access to two stable states at once, then depending on the initial conditions the system has equal probabilities to stay at each one of these states.

After we have established the bistable regime for our nanomechanical system, the next step was to switch between these states via external periodic modulation. From there we will quantify values of the threshold of amplitude modulation and cut-off frequency.

## 5.4 Switching via external modulation

In this section we will discuss about the periodic modulation of the double well potential. The basic concepts is reintroduced in Figure 5.5; under ideal situation the bistable potential is perfectly symmetric with equally probable states. However if the potential is modulated by a periodic force, the probability of being in one state becomes higher than the other. On one half cycle of the modulation if the left sided well gains higher probability, then in the other half cycle the right handed well gains the same. Then governed by the modulation strength the system can switch between different states.

### 5.4.1 Periodic driving of the bistable potential by phase modulation

Switching between the states with such periodic modulation has been demonstrated in a doubly clamped nanomechanical beam by Badzey et al. [57] with amplitude and Guerra et al. [119] with phase. Although it was possible to perform either kind of modulation in our system, we decided to proceed with only one kind of modulation i.e. phase modulation. Since the main reason to perform these modulations were to extract some system parameters, therefore we decided to proceed with only one kind of modulation for the time being. For such a modulation the externally applied voltage can be written as:

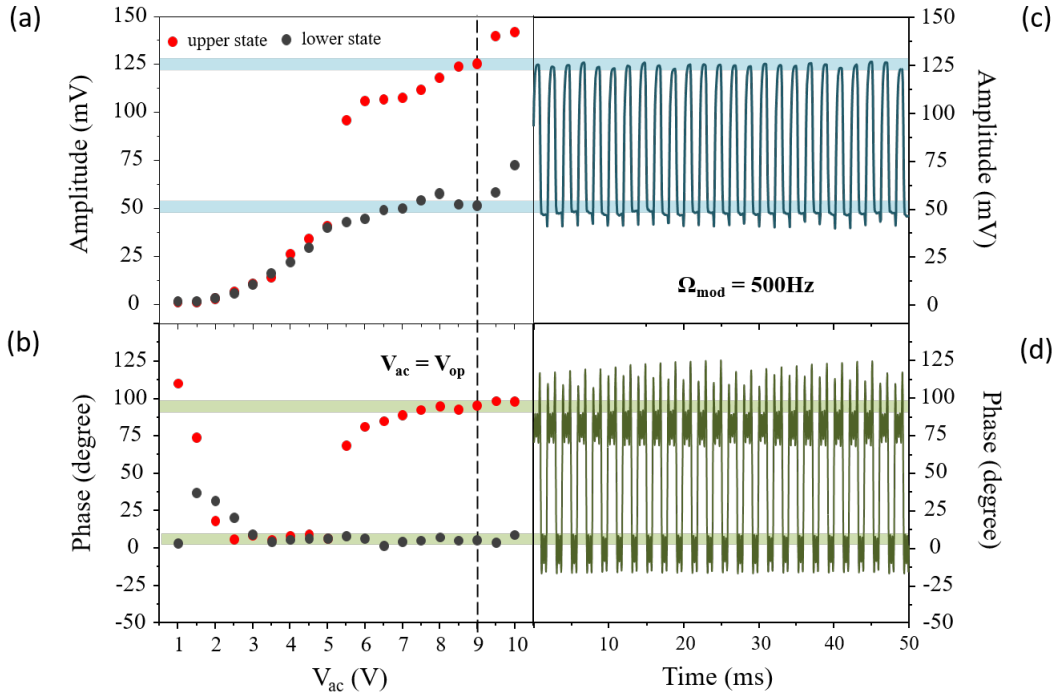


Figure 5.6: (a) Bistability in amplitude & (b) phase response with the actuation power at a drive frequency $\Omega_{drive} = \Omega_{op}$; switching between bistable states in (c) amplitude & (b) phase response for a modulation frequency $\Omega_{mod} = 500Hz$ and phase deviation $\Delta\phi = 140°$.

$$\delta V = V_{ac} cos(\Omega_{drive} t + \Delta\phi sgn(\Omega_{mod} t) + \phi_0) \tag{5.8}$$

here $V_{ac}$ is the carrier excitation, $\Omega_{mod}$ is the frequency of modulation, $\Delta\phi$ is the amplitude of phase modulation, $\phi_0$ is a phase offset of the drive and the drive frequency is $\Omega_{drive}$, which we fix at $\Omega_{op}$. The $sgn$ function actually refers to a square wave signal which is used for modulation instead of a sinusoidal wave. In order to experimentally obtain the spectra we needed to fix the drive at a $V_{ac}$ value such that the system lies in the hysteresis region. For all the experiments we decided to fix the excitation at $V_{ac} = 9.0V$, shown by the dashed line in Figure 5.6(a) & (b). From now on we refer this voltage as $V_{op}$ (Figure 5.6(a)), thus the operating point is at $(\Omega_{op}, V_{op})$. Now keeping the system at this operating point, we start to modulate the phase of the drive between the two phases highlighted by the green lines at 5 and 95 (Figure 5.6). The system then starts tp switch back and forth between its two stable states.

The switching in the detected output signal is synchronized with the switching in the input phase modulation (Figure 5.6(c) & (d)). Since the amplitude and the phase response are correlated, every time we observe a switching in output amplitude it is accompanied with a switching in output phase. In Figure 5.6 we observe that the switching in amplitude and in phase always happens between two discrete values, from here we are able to identify two separate states in phase space and we refer to them as state $\{x_U\}$ and $\{x_L\}$. The

abbreviation stands as *'Upper'* for *'U'* and *'Lower'* for *'L'*. The state parameters are given as follows; for the upper state: $\{x_U\} \sim \{x, \theta\} \sim \{125mV, 95°\}$ and for the lower state: $\{x_L\} \sim \{x, \theta\} \sim \{50mV, 5°\}$. These values are rounded approximations of the mean of the experimentally observed data. In the following sections we will see that everytime the system switches, it's always between these two specific states. Thus the modulation has two free parameters; namely the amplitude of modulation $\Delta\phi$ and the frequency of modulation $\Omega_{mod}$. We will see in the next sections how these factors influence the jumps between the metastable states.

**Amplitude of phase modulation: Switching fraction**

After we are able to observe jumps between the metastable states, the next step was to quantify some of the system parameters. The first system quantification was the amplitude of phase modulation required to observe jumps. For this purpose we use the drive in equation (5.8), here we fix the operating point at $(\Omega_{op}, V_{op})$ and $\Omega_{mod}$ at $500Hz$. To obtain the statistics of switching we had to calculate a parameter known as the switching fraction; defined as the number of times there is jump in the output (between the metastable states) divided by the number of times there is a switching in the input phase. In order to perform these calculations we needed to first of all mark a threshold which we define to be around $85mV$ for the output amplitude (dotted line in Figure 5.7(a)). The choice is done simply by averaging the response amplitudes of the two states. Now we calculate the switching by calculating every time the system crosses the threshold in the output. We vary $\Delta\phi$ i.e. the amplitude of phase modulation in order to observe how the input of phase modulation is synchronized with the modulated output. The resulting plots are displayed in Figure 5.7; we start from $\Delta\phi$=0 with no phase modulation and increase the modulation by a step of 5° and for each case we record the time response for a relatively longer time (around $60s$) in order to obtain a higher amount of statistics. In Figure 5.7(b) we observe the evolution of switching fraction with the amplitude of phase modulation $\Delta\phi$; when $\Delta\phi < 100°$ we are not able to observe any switching, this is shown in the top most figure in Figure 5.7(a). Instead we see is a small modulation of the output signal around $\{x_U\}$, although it does not jump to the other state $\{x_L\}$. This is known as the intra-well modulation of the system, where the system is modulated inside one of the potential wells. However when the modulation is around 110° the system occasionally jumps from state $\{x_U\}$ to $\{x_L\}$ by crossing the threshold. This situation is represented by the response at 110° modulation in Figure 5.7(a). The reason of such a behavior can be attributed to the phase hysteresis width at $(\Omega_{op}, V_{op})$. It was previously mentioned that the hysteresis width in phase is about 90°, thus in order to switch from one state to the other the phase modulation in the input has to be higher than this value. Therefore beyond 110° we are able to observe a perfect synchronization between the input and the output. This situation is represented by the 160° modulation scenario in Figure 5.7(a), where we see a perfectly periodic signal at $500Hz$ between the states $\{x_U\}$ and $\{x_L\}$. In the figures although we only show the amplitude response, but it's needless to say that it's correlated with the phase response.

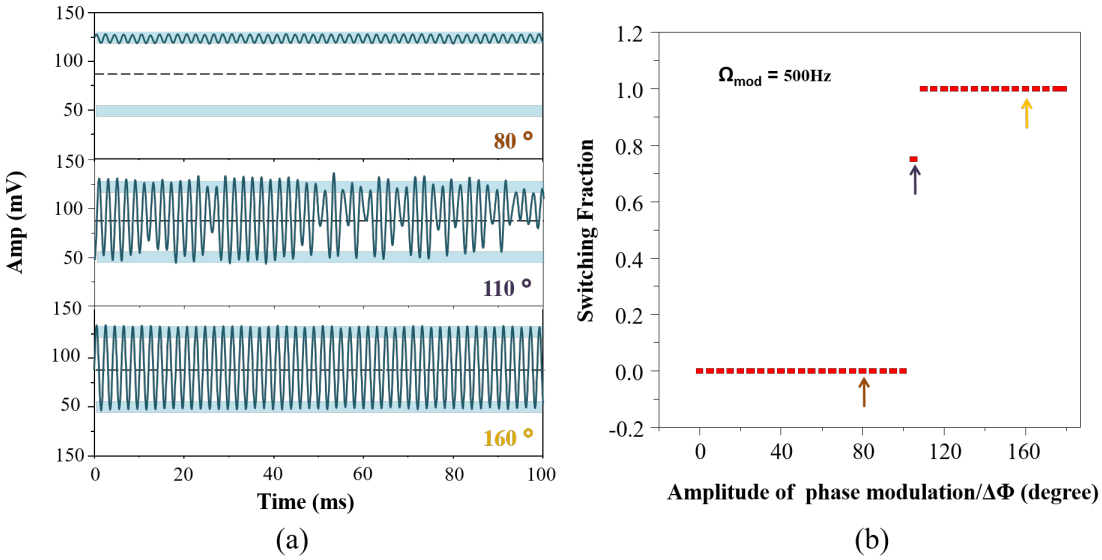


Figure 5.7: Dependence of switching fraction on the amplitude of phase modulation; (a) time traces of switching as the amplitude of phase modulation is swept for a fixed $\Omega_{mod} = 500Hz$ (b) dependence of switching fraction on the amplitude of phase modulation.

### Frequency of phase modulation: Cut-off frequency

It was shown by P.Jung [118] that the output modulation scales inversely to the square of the modulation frequency i.e. when the modulation frequency goes beyond a certain threshold the system is not able to follow the modulation anymore and the escape rate decreases rapidly. For realization of this experiment we go back to equation (5.8) but instead of varying $\Delta\phi$, we vary $\Omega_{mod}$. In order to have a switching fraction of 100% we fix $\Delta\phi$ to a value of 135°. Like in the previous case we make long measurements in order to have high statistics and in each case we calculate what we call the normalized amplitude of deviation; this is defined as the ratio of amplitude of deviation (in degrees) in the output at a certain frequency with amplitude of deviation (in phase) at the lowest modulation frequency which is $10Hz$. In order to calculate this ratio we needed to define a threshold like before and is represented by the dotted line in Figure 5.8. The threshold is defined at 40° by taking an average of the upper and lower phase values. We start from a low $\Omega_{mod}(= 10Hz)$ and slowly increase it towards a higher value. In Figure 5.8(b) we show how the normalized amplitude of modulation varies with the modulation frequency $\Omega_{mod}$, with a relatively low $\Omega_{mod}(= 100Hz)$, we see that the system switches efficiently back and forth between the metastable states. As we start to increase $\Omega_{mod}$ we then observe that the switching between these states increases (see response at $1kHz$ in Figure 5.8(a)) and as $\Omega_{mod}$ increases beyond this point the system has trouble following the modulation. At each case we have kept same time scales in order to be able to compare different scenarios. For $\Omega_{mod} = 3kHz$ we see from Figure 5.8(a) the system is no more able to switch between the metastable states. If we observe the evolution of the normalized amplitude modulation with $\Omega_{mod}$ we observe a sharp decrease as we go in the

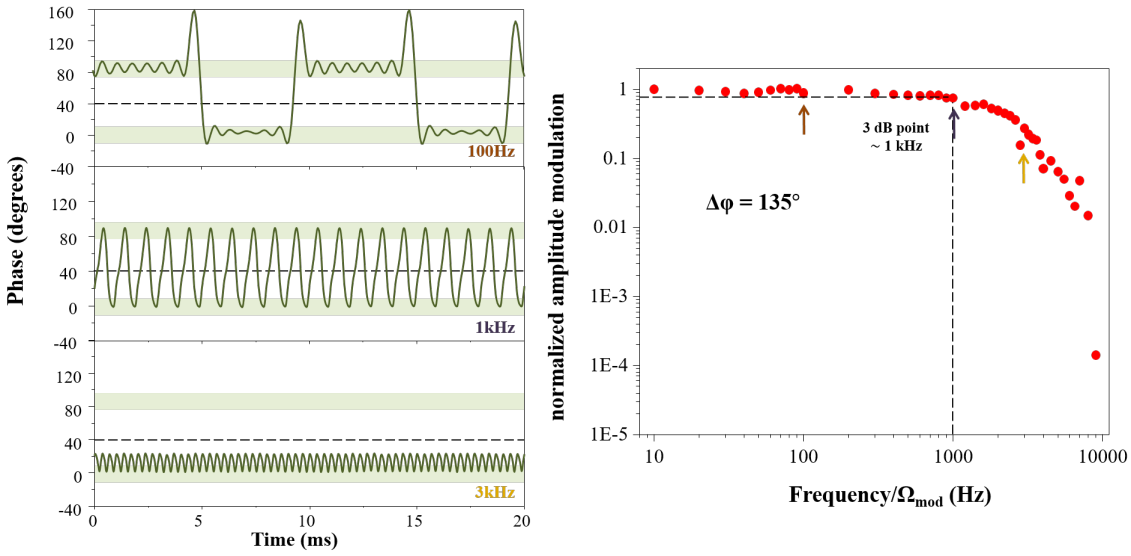


(a) (b)

Figure 5.8: (a) Evolution of time traces of the phase responses with the modulation frequency $\Omega_{mod}$ for a phase deviation $\Delta\phi = 135°$, (b) dependence of the normalized amplitude of deviation with the modulation frequency $\Omega_{mod}$.

$kHz$ regime. From the response then we calculate the 3-dB response frequency, which we find to be at around $1kHz$. In conclusion thus we say that the system is not able to follow the modulation when $\Omega_{mod}$ goes beyond $1kHz$, thus for all the future experiments we keep the $\Omega_{mod}$ value below this regime.

After we established the system behavior via external modulation, in the next sections we will modulate the bistable potential via both phase and amplitude noise. From there we will establish Kramer's rate of the system with both phase and amplitude noise.

## 5.5 Switching by phase noise

In the new set of experiments, we replace the modulation by noise in order to realize a stochastic modulation of the double well potential. In presence of noise $\eta(t)$ the system jumps from one state to the other, however in a stochastic manner governed by the Kramer's rate. The phase noise is introduced in the system by phase modulating the drive with an external noise. The noise has a Gaussian shape with zero mean. The drive acting on the system hence looks like:

$$\delta V(t) = V_{ac} cos(\Omega_{drive} t + \eta_\phi(t)) \tag{5.9}$$

$$\langle \eta_\phi(t)\eta_\phi(t')\rangle = 2D_\phi \delta(t-t'),\ \langle \eta_\phi(t)\rangle = 0 \tag{5.10}$$

where, $\eta_\phi$ is the injected phase noise in the system. This is an uncorrelated noise with Gaussian distribution and zero mean. As the noise is introduced in terms of phase, the range of $\eta_\phi$is $0^\circ \rightarrow 360^\circ$. Calibration of the noise is discussed in details in Appendix (D).

### 5.5.1 Determination of the operating point

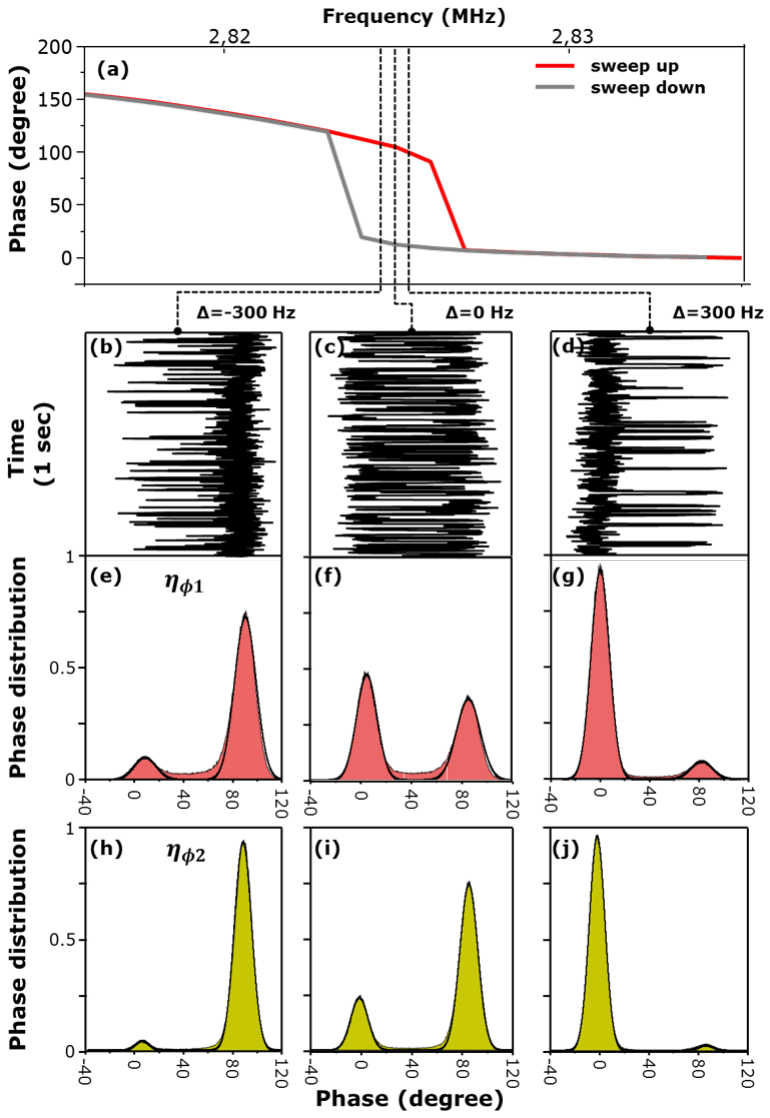


Figure 5.9: (a) Phase response for sweeping frequency up (red) and down (gray). Time traces of the phase response (for three different $\Omega_{drive}$) (b-d) for a phase noise of $\eta_{\phi 1} = 30^\circ$, the corresponding histograms (e-g). Histograms of the responses at the same $\Omega_{drive}$ but for a different noise of $\eta_{\phi 2} = 35^\circ$.

In the previous sections we discussed about the selection of the operating point $(\Omega_{op}, V_{op})$. Choice of $V_{op}$ is obvious, with just making sure that the system lies inside the bistable regime. However the choice of $\Omega_{op}$ is not straightforward. For a system in bistable regime, depending on the value of $\Omega_{drive}$ the system can prefer to stay in either of the states. In absence of any noise the residence time for each of the states can be relatively longer, thus to have a better statistics we decided to inject some phase noise in the system which follows equation (5.9). From here we start to vary $\Omega_{drive}$ and for each $\Omega_{drive}$ we record the time trace for different values of $\eta_\phi$. Although we had to perform several measurements to retrieve the correct operating point, here we show only a few striking results.

Firstly we fix $\Omega_{drive}$ at $\Omega_{op} - 300Hz$ and we record the time trace (Figure 5.9(b)) and obtain the histogram of the metastable states for different values of $\eta_\phi$. Figure 5.9(e) & (h) shows histograms for $\eta_{\phi 1} = 30°$ and $\eta_{\phi 2} = 35°$ respectively. Here we can see that at this value of $\Omega_{drive}$ the system prefers to stay at $\{x_U\}$ and with an increase in noise the system starts to have a higher probability to stay at $\{x_U\}$. Same thing is observed for the other state (i.e. $\{x_L\}$), for $\Omega_{drive} = \Omega_{op} + 300Hz$. Here with an increase in noise the system becomes more trapped in the state $\{x_L\}$ with the bistable potential becoming more distorted. However, for $\Omega_{drive} = \Omega_{op}$ we see that the bistable potential is almost symmetric for $\eta_\phi = \eta_{\phi 1}$ (Figure 5.9(c) & (f)) and for a higher noise the bistable potential changes shape and becomes asymmetric. This phenomenon can be explained by considering the effect of multiplicative noise instead of an additive noise which appears due to the injection of phase noise in the system [120][121].

In Figure 5.9(i) we also observe that with noise even at $\Omega_{drive} = \Omega_{op}$ the symmetry between the states are lost. We see that with higher noise $\eta_{\phi 2}$, the state $\{x_U\}$ becomes more probable than $\{x_L\}$. Thus not only the drive frequency $\Omega_{drive}$ but the injected noise is also crucial in order to have a symmetry in the bistable potential. In the next section we talk about the optimization of the injected phase noise $\eta_\phi$ in order to have a symmetrical potential.

### 5.5.2 Residence time and Kramer's rate distribution

The Kramer's rate is defined as the switching rate between the metastable states. The Kramer's rate was introduced in the previous section and is defined as:

$$r = \frac{1}{\sqrt{2\pi}} exp(-\Delta V_\phi / \eta_\phi) \tag{5.11}$$

Where $\eta_\phi$ is the externally injected phase noise in degrees and $\Delta V_\phi$ is the activation barrier for phase noise in degrees.

If one takes logarithm on both sides of the equation then by considering non-normalized form of Kramer's rate one can write:

$$ln(r) = C - \frac{\Delta V_\phi}{\eta_\phi} \tag{5.12}$$

$C$ being a proportionality constant. The logarithm of the Kramer's rate $r$ thereby has a linear dependence on the inverse of the applied noise $\eta_\phi$. Moreover, from the slope of the plot it should be also possible to calculate the depth of the double well barrier $\Delta V_\phi$.

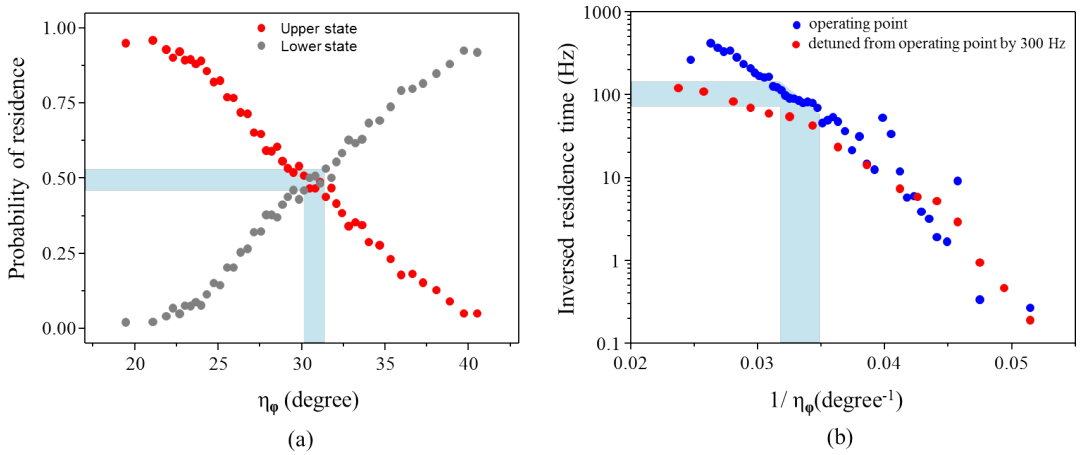


Figure 5.10: (a) Variation of probability of residence with phase noise at $\eta_\phi$, (a) evolution of Kramer's rate with $\eta_\phi$ for $\Omega_{drive} = \Omega_{op}$ (blue) and $\Omega_{drive} = \Omega_{op} - 300Hz$ (red).

We start by preparing the system at the upper state $\{x_U\}$ and at the operating point $(\Omega_{op}, V_{op})$; from here we start to increase the phase noise in steps and record the time domain amplitude as well as phase response of the system. For each value of phase noise $\eta_\phi$ we record the response for a duration of about $60sec$. It was now possible to extract various information from these data including evolution of the probability of residence and Kramer's rate with applied phase noise $\eta_\phi$.

We started injecting phase noise from a low value of $\eta_\phi = 18°$ and start increasing in steps. At a low noise the system stays mostly in $\{x_U\}$, however with an enhancement in the applied noise the stable states start to become metastable and the system starts to jump back and forth between these states. At first we extracted distribution of probability of residence for various applied phase noise $\eta_\phi$ which is shown in Figure 5.10(a). The red dots represents state $\{x_U\}$ while the gray dots represents state $\{x_L\}$. In order to properly define the two states discretely we defined the threshold at around 40°, which is the average of the upper and lower values of the phase. Since the amplitude and phase response are correlated we could use any of the values in order to perform calculation. For this case and later as well we will use the phase response in order to perform the data extractions. The calculations were performed by simply calculating the amount of time the system spends on one of the states divided by the total acquisition time ($60sec$). The system is seen to have equal probabilities to reside in any one of the states for $\eta_\phi \sim 30$, this is highlighted in Figure 5.10(a). Thereby this is the value of the noise $\eta_\phi$ required in order to have a symmetric potential well.

The next step was to calculate the Kramer's rate $r$ for the phase noise. The threshold is still at 40° and we calculate the flux of jumps between $\{x_U\}$ and $\{x_L\}$. This calculated flux then had to be divided by the average time the system spends in the corresponding states in order to finally calculate the Kramer's rate. The plot of the Kramer's rate with the injected phase noise is displayed in Figure 5.10(b) for two different operating points i.e. for $\Omega_{drive} = \Omega_{op}$ and for $\Omega_{drive} = \Omega_{op} - 300Hz$. As expected from the previous discussions

the later had a lesser value for the Kramer's rate compared to the former for the same phase noise $\eta_\phi$. From the plot for $\Omega_{drive} = \Omega_{op}$ we observe that $r = 100Hz$ for $\eta_\phi \sim 30°$, where the bistable potential well is symmetric. This symmetry of the potential will be used in order to realize stochastic resonance with phase noise in the following sections as stochastic resonance is most effective when the bistable potential is symmetric.

### 5.5.3 Evolution of phase trajectory with phase noise

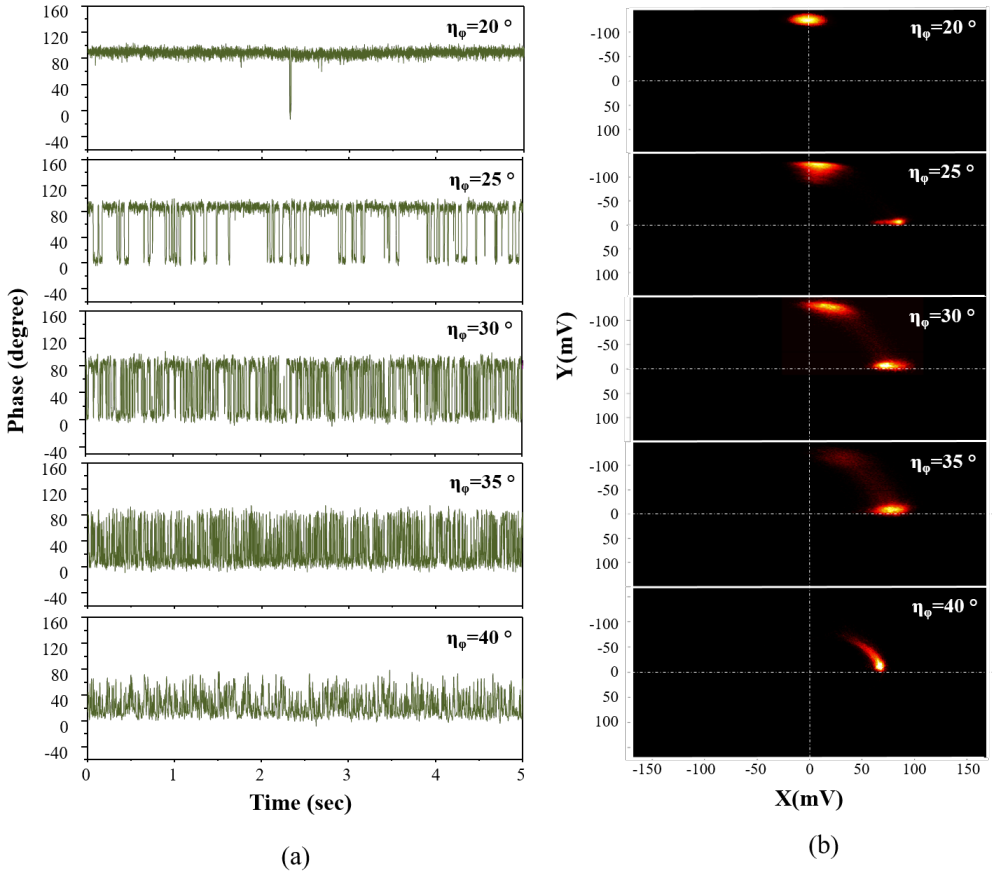


Figure 5.11: (a) Time trace of jumps between the metastable states with phase noise, (b) evolution of the same in terms of phase trajectories for $\eta_\phi = 20°$ to $40°$.

In this section we will show how the system evolves in the time domain as well as in the phase space. Five different situations are displayed in Figure 5.11; on the left hand side (Figure 5.11(a)) we have the time traces of the phase response of the system. While on the right hand side (Figure 5.11(b)) we show the constructed phase portrait for the corresponding time domain responses. The phase space is constructed from the recorded amplitude and phase response of the system using the method described in section (4.2.1). Selection of the

bandwidth of the applied noise is also quite important, we were able to observe most frequent jumps around $10kHz$ of noise bandwidth.

When $\eta_\phi$ is relatively low ($\eta_\phi = 20°$) the system prefers to stay mostly at $\{x_U\}$ with some scarce jumps to the state $\{x_L\}$. In the phase space space we observe only a single circular state as the system stays mostly in state $\{x_U\}$. As we start to increase $\eta_\phi(=25°)$ more frequent jumps between $\{x_U\}$ and $\{x_L\}$ are observed. This is also observed in the phase space configuration, where another weak state starts to appear with the increased noise close to the $x$-axis. This is basically the state $\{x_L\}$, the radial distance of these states from the origin gives the corresponding amplitude of oscillation $R$, and the angle that the line individual state and the origin makes to the $x$-axis, gives away the oscillation phase $\theta$. From the phase space thus evidently we are able to observe the states $\{x_U\}$ and $\{x_L\}$ very distinctly. When we keep on increasing $\eta_\phi(30°)$, the state $\{x_L\}$ becomes more and more prominent as the jumps between the states becomes more frequent. For phase noise injection here we computed the bistable potential to be most symmetric (Figure 5.11(b)). As we start increasing the injected noise, the bistable potential starts to become more and more asymmetric, however the jumps keeps on increasing due to the increase in the noise in the system. This asymmetry in the bistable well is what was predicted by Jia et al [120], where the multiplicative noise is introduced in the system along with the additive noise component which deforms the bistable potential. Hasegawa et al [121] also predicted similar effect. When $\eta_\phi$ is around 40° the lower state $x_L$ becomes much more brighter in the phase space and we can observe a deformation of the bistable potential well.

### 5.5.4 Activation barrier scaling with frequency detuning

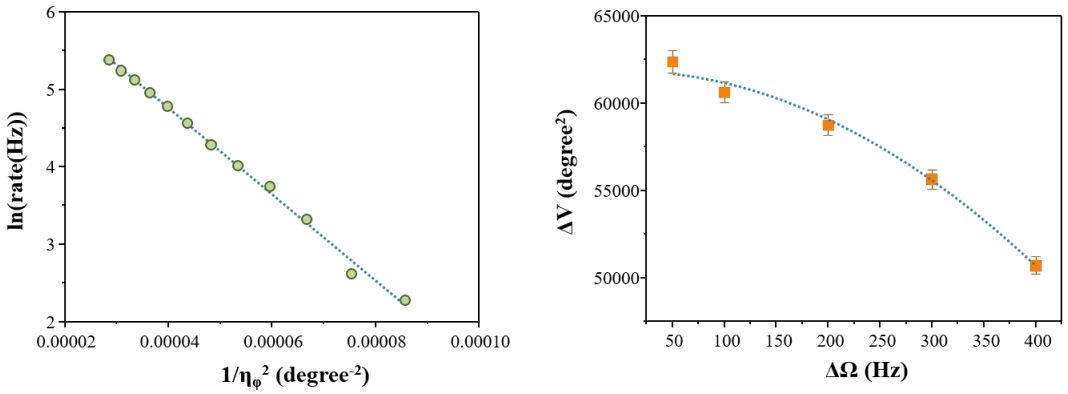


Figure 5.12: (a) Variation of the switching rate with inverse of the applied phase noise (b) variation of the calculated barrier height (from the switch rate vs noise plot) with frequency detuning.

It was shown in equation (5.12), that the switching rate has a dependence on the activation barrier governed by the relation:

$$ln(r) = C - \frac{\Delta V}{\eta} \tag{5.13}$$

Thereby the slope of $ln(r)$ with applied noise $\eta$ will give an indication of the activation barrier $\Delta V$. However close to the bifurcation point where one of the states disappears, the activation energy should have a scaling governed by the following relation [27,28]:

$$\Delta V \propto (\Delta\Omega)^{\nu} \tag{5.14}$$

where $\Delta\Omega = |\Omega_{drive} - \Omega_{bif}|$, is the detuning of the drive frequency from the frequency of bifurcation $\Omega_{bif}$ i.e at the point where one of the stable states completely vanishes. For our case we choose $\Omega_{bif} = 2.8245MHz$ where we are able to observe only the upper state $\{x_U\}$ i.e. the lower state $\{x_L\}$ completely vanishes. $\nu$ is the exponent which governs the variation of the activation energy with $\Delta\Omega$. As it is proposed by Aldridge et al. [112] the activation barrier $\Delta V$ should have a quadratic dependence on the frequency detuning $\Delta\Omega$ which makes $\nu \sim 2$.

In order to determine how the activation barrier scales with the frequency detuning, we decided to use phase noise experiments in order to determine the activation barriers for different frequency detuning $\Delta\Omega$. The experimental scheme is identical to what was done in the previous sections, however we repeat the experiments for several values of frequency detuning $\Delta\Omega$. Since the logarithm of the Kramer rate should have a linear dependence on the applied noise, we found that the Kramer's rate actually scales linearly with inverse of the square of applied phase noise $\eta_\phi$. In each case we calculate the Kramer's rate for various phase noise $\eta_\phi$(with a bandwidth of $10kHz$) and we plot the logarithm of $r$ with square of the phase noise $\eta_\phi^2$. In each case we fit a linear slope in the graph in order to retrieve $\Delta V$. Firstly we prepare the system in the state $\{x_U\}$ by sweeping the actuation frequency upwards identical to the previous section. Then at this point we calculate the Kramer's rate $r$ by varying the applied phase-noise $\eta_\phi$ to the system. A particular example is given here in Figure 5.12(a) for $\Delta\Omega = 100Hz$, here we are able to retrieve a $\Delta V$ value of $55640\,degree^2$. We do the same experiments for $\Delta\Omega = 50, 200, 300$ & $400Hz$. The calculated activation barrier $\Delta V$ for various $\Delta\Omega$ values are shown in Figure 5.12(b). $\Delta V$ is seen to have a quadratic dependence on $\Delta\Omega$ (i.e. $\nu = 2$) as predicted by Aldridge et al. [112]. While the switching rate $r$ is seen to decrease as one moves further away from the operating point and towards the bifurcation point.

## 5.6 Switching by amplitude noise

In the next set of experiment we changed the phase noise to amplitude noise in order to play on the other quadrature and retrieve the evolution of the bistable potential with amplitude noise. The use of amplitude noise is quite straight forward where we just add the noise with the applied drive. Therefore the expression of the drive for injection of amplitude noise is:

$$\delta V(t) = V_{ac} cos(\Omega_{drive} t + \phi) + \eta_R \tag{5.15}$$

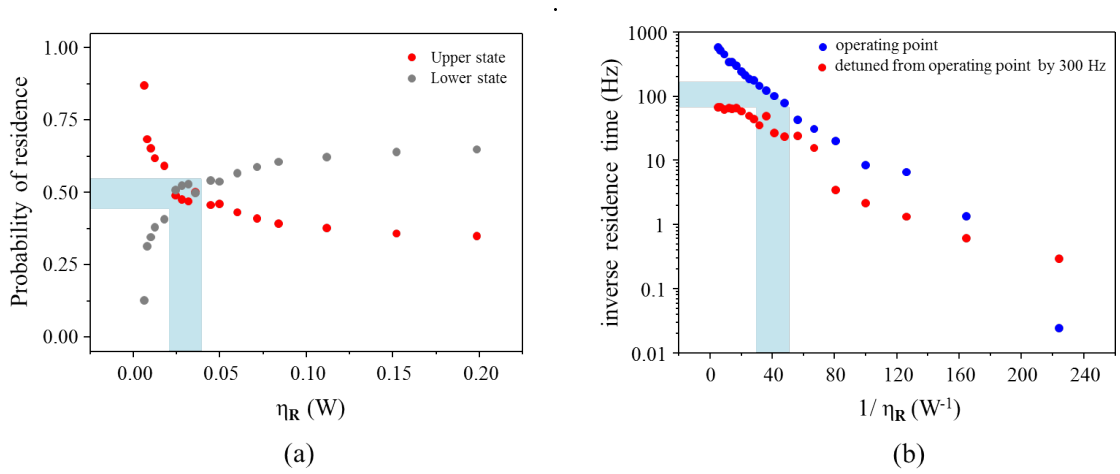


Figure 5.13: (a) Variation of probability of residence with amplitude noise at $\eta_R$, (a) evolution of Kramer's rate with $\eta_R$ for $\Omega_{drive} = \Omega_{op}$ (blue) and $\Omega_{drive} = \Omega_{op} - 300Hz$ (red)

$$\langle \eta_R(t)\eta_R(t')\rangle = 2D_R\delta(t-t'),\ \langle \eta_R(t)\rangle = 0 \tag{5.16}$$

Here $\eta_R$ refers to the amplitude noise power injected in the system, the noise is a zero mean Gaussian spectra. Here we also quantify the amplitude noise power in terms of the standard deviation of the injected noise and thus we define the amplitude noise $\eta_R = (225V_{pp}^2)/50\,(mW)$ (for noise calibration refer to Appendix (D)). The optimized bandwidth for amplitude noise $\eta_R$ was $10kHz$, identical to the previous section. The rest of the experiment resembles the one with the phase noise in the section before. We could calculate the same parameters like residence time, Kramer's rate and retrieve phase portrait of the system under study from the recorded data.

### 5.6.1 Residence time and Kramer's rate distribution

The method of calculation of the parameters are identical to the phase noise scheme. Here also we record both the amplitude and phase response for a duration of $60s$. We use the phase response in order to calculate the relevant parameters, while we define threshold like before at $40°$ identical to the previous section. We calculate the probability of residence for each of the states ($\{x_U\}$ and $\{x_L\}$); the resulting plot is shown in Figure 5.13(a). The states show equal probability for a amplitude noise of around $\eta_R = 30mW$ where the bistable potential is symmetric.

Here like in the section before we calculate the Kramer's rate for two different $\Omega_{drive}$. One is for $\Omega_{drive} = \Omega_{op}$ and another one for $\Omega_{drive} = \Omega_{op} - 300Hz$ and we calculate the Kramer's rate for each scenario. The resulting plot is shown in 5.13(b); expectedly like the situation before the later has a Kramer's rate which is lower than the former for each $\eta_R$. We retrieve a Kramer's rate of about $100Hz$ for a phase noise $\eta_R = 30mW$ where the bistable potential is symmetric. This value is very important in order to realize stochastic resonance

with amplitude noise as the best results could be achieved when the bistable potential is symmetric.

### 5.6.2 Evolution of the phase trajectory with amplitude noise

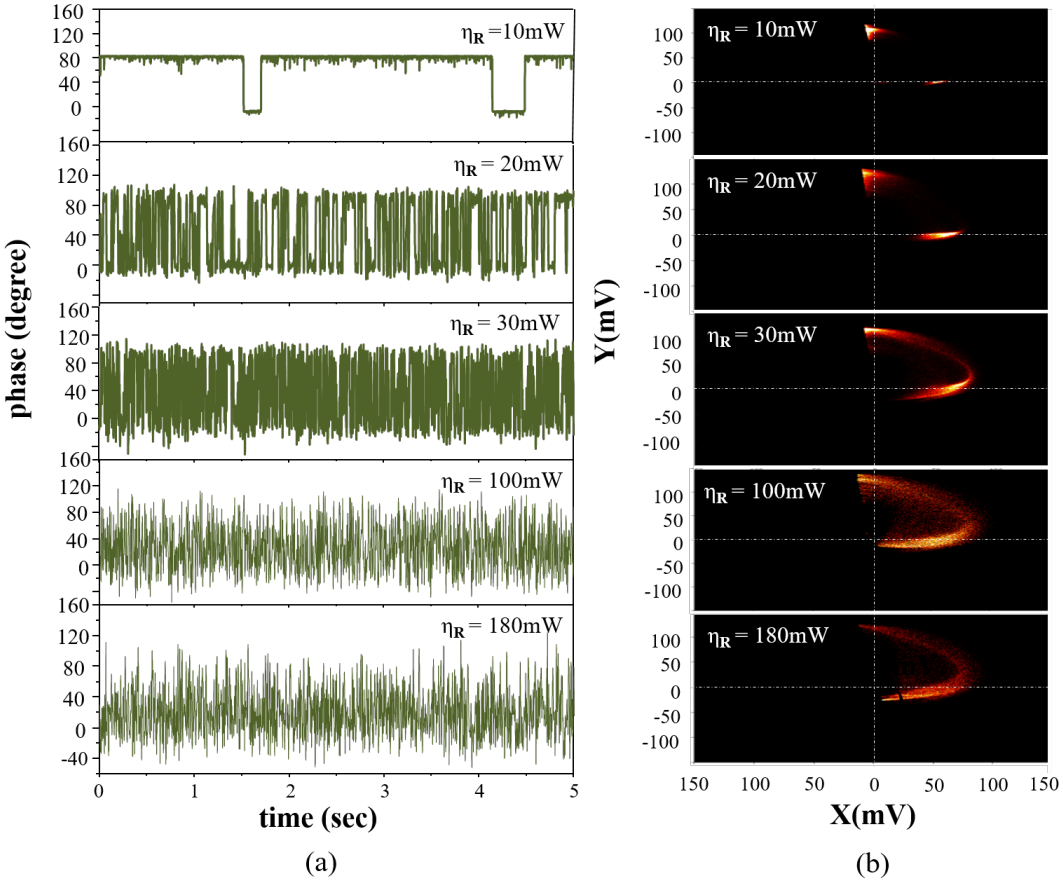


Figure 5.14: (a) Time trace of the jumps between the metastable states with amplitude noise, (b) evolution of phase trajectories as the amplitude noise is changed for $\eta_R = 10mW$ to $80mW$.

Here again we reconstruct the phase portrait of the system under study from the recorded amplitude and phase response. On the left hand side of Figure 5.14 we show the time traces of the recorded phase response (Figure 5.14(a)) and on the other side we show the constructed phase space response of the system. Firstly we prepare the system in the upper branch by sweeping the frequency up to the operating point $(\Omega_{op}, V_{op})$. When the excitation is low $(\eta_R = 10mW)$ the system prefers to stay in the upper state $\{x_U\}$. That is what is seen from the time traces of phase response and the phase trajectories. When value of the noise is increased to $\eta_R = 20mW$, the jumps between $\{x_U\}$ and $\{x_L\}$ start to increase and the lower state $\{x_L\}$ in phase space starts to become more and more prominent. We encounter

highest number of jumps for a $\eta_R$ of $30mW$ and both states at this stage seem to appear with equal probabilities. Finally with a high enough power the bistable potential becomes asymmetric and the shape becomes deformed. The potential well becomes deformed although the switching rate keep on increasing because of the enhancement of injected noise in the system.

### 5.6.3 Hysteretic quenching

Following the discussion in the previous section on how the injected noise deforms the bistable potential, one can ask whether the noise has any effect on the bistable/hysteretic regime. Venstra et al. [115] showed that they observed some kind of quenching of the hysteretic regime when noise was injected in the system. Therefore we decided to observe if similar kind of behavior was observed for our system under comparable conditions.

P. Jung [118] showed that when the modulation of the bistable potential is weak, two separate metastable states are observed and the system can switch back and forth between the states. However when the modulation is too strong this behavior does not exist any more, in turn system starts to exhibit a single state under such a high amount of modulation. From there we can draw a similar conclusion for noise as well as the effect of noise on the system should be somehow similar to the periodic modulation. The only difference is that with noise the modulation of the bistable potential is not periodic but rather stochastic. However with noise of higher intensity we should be able to observe similar effects.

In order to do that we decided to reconstruct the hysteretic/bistable regime against external excitation for different noise powers. The construction of these bistable regimes can be done by doing subtraction of the sweep up and sweep down system responses. We start from zero noise power and then go to some intermediate value and finally to relatively high amount of noise. When operating with phase noise due to some technical reasons we are limited in the upper cut-off of the applied noise, while for amplitude noise we are not limited by such issues. This is why we use amplitude noise in order to construct the hysteresis responses in various scenarios.

The generated hysteretic regimes are displayed in Figure 5.15; firstly we start by constructing the hysteretic regime without introducing any noise in the system (Figure 5.15(a)). The threshold of $V_{ac}$ for which bistability is observed in this case is found to be about $4.25V$, while the width of the bistable region is about $40kHz$ for a $V_{ac}$ of $10.0V$. Next we start injecting amplitude noise $\eta_R$ in the system with the method described by equation (5.15); firstly we inject a noise at an intermediate level of $\eta_R = 180mW$ and with a bandwidth of $10kHz$. Under such condition we start to vary the drive $V_{ac}$ from $0V$ to $10V$. As a result of noise injection we observe that the threshold of $V_{ac}$ required to induce bistability is increased; for this particular case it's around $5.5V$. A consequence of that is quenching of the hysteretic regime, the hysteretic width becomes significantly smaller in this case with a width of around $20kHz$ for $V_{ac} = 10.0V$. Furthermore we increase $\eta_R$ to even higher values (Figure 5.15(c)). For $\eta_R = 725mW$ we observe a drastic change in the hysteretic region. The hysteresis region almost vanishes and we see a very faint hysteresis regime starting from $V_{ac} \sim 7.0V$ with a hysteresis width of only about $0.5kHz$ for $V_{ac} = 10.0V$. Effectively thereby we can conclude

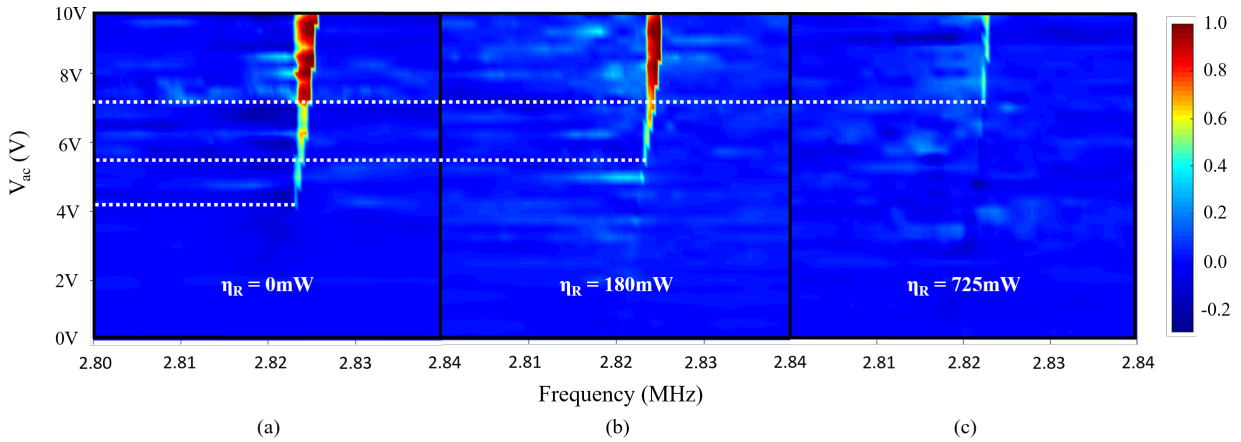


.

Figure 5.15: Quenching of the hysteretic/ bistable region with amplitude noise: (a) without any amplitude noise (b) with $\eta_R = 180mW$, there is a small quenching of the hysteresis region (c) with $\eta_R = 725mW$ there is almost no hysteresis region i.e. somehow the bistability in the system is lost due to modulation of the spring constant by means of the added noise.

that the injection of noise changes the effective spring constant of the resonator and thereby modulates the double well potential. This therefore results in quenching of the hysteretic regime and loss in the bistability.

### 5.6.4 Comparison between these two noise schemes

In this section we will give a comparative study between the two types of noise induced switching processes i.e. amplitude and phase shown previously. In order to find a better comparison between these switching processes the phase portrait with amplitude and phase noise are plotted side by side in Figure 5.16(a) & (b). The plots represent more or less identical scenarios in the respective cases. The advantage of using phase space representation of the system dynamics is that from these plots it is possible to retrieve evolution of the individual states with applied noise. We can retrieve the trajectory between the attractors but not only that we can also observe how the phase angle between individual states evolve with noise and also how noise influence individual states.

#### Trajectory between the basins of attraction

We start from a situation when the system is prepared in the state $\{x_U\}$ preceded to when noise is injected in the system. Under injection of noise the system starts to exhibit the other state $\{x_L\}$ and jumps back and forth between this state and state $\{x_U\}$. The transitions between the basins of attraction can not follow an arbitrary path in the phase; the system always should and does have preferred paths in which it makes the transition. With phase noise we see that the system prefers a path which is almost a straight line between the two states; while for amplitude noise the system prefers strongly curved path between the states.

Interestingly another observation from the phase portrait is the collapsing of one of the states at a high noise. However, the effect of noise has different consequences for the different states e.g. for phase noise if one looks closely to Figure 5.16(a) the state $\{x_U\}$ appears to move with injection of noise. In the beginning the state has a phase angle $\theta$ which is close to 90°, however with increase in the phase noise the phase angle decreases and apparently the state $\{x_U\}$ moves closer to state $\{x_L\}$.On the other hand, for amplitude noise it's the opposite; in this case the lower state $\{x_L\}$ starts to move away from the upper state $\{x_U\}$.

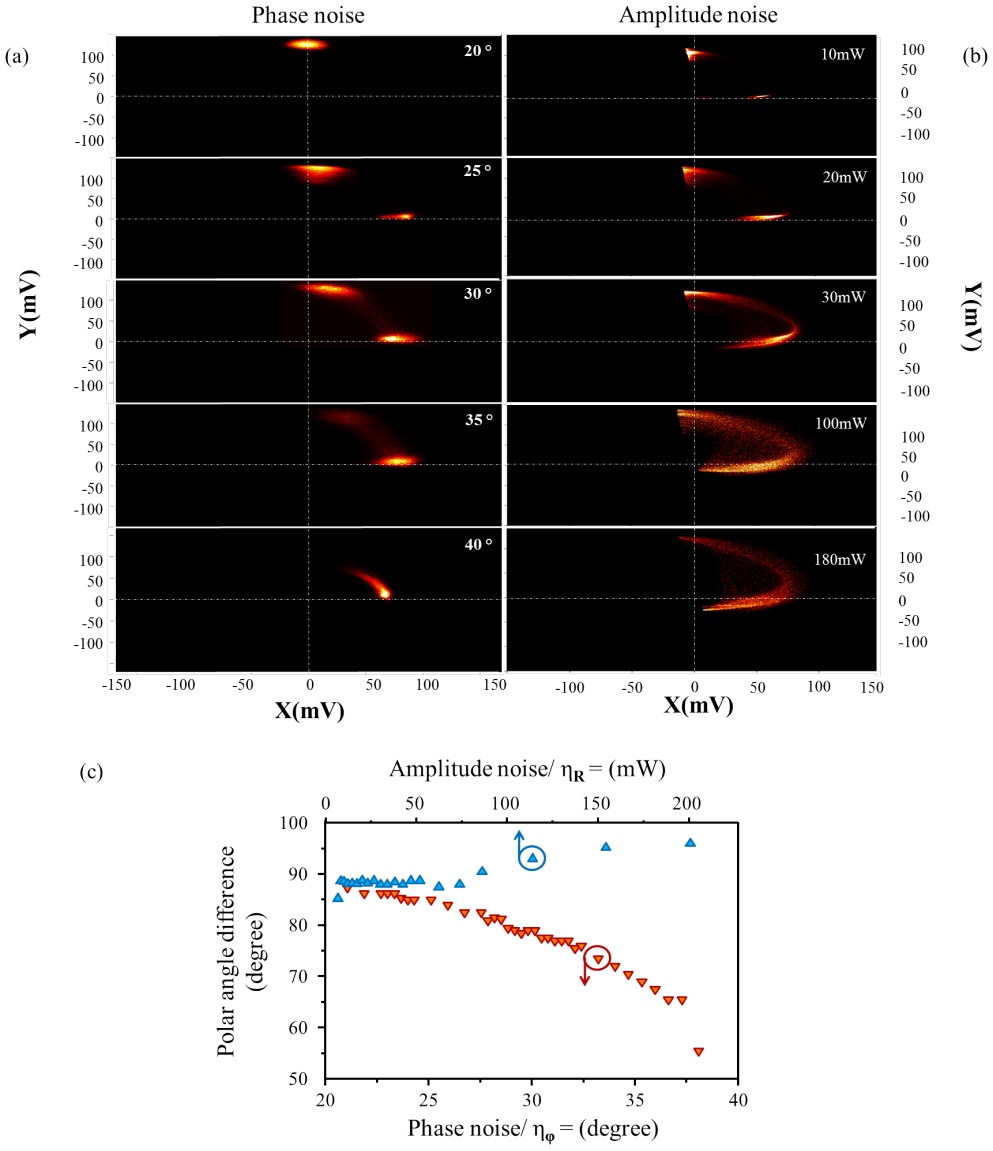


Figure 5.16: (a) Comparison of the phase trajectory evolution with phase and amplitude noise (b) change of phase angle between the two states as the phase and amplitude noise is changed.

### Phase angle between the basins of attraction

In order to formulate this behavior we decided to quantify this shift of the states for each scenario. The idea was to find how the phase angle difference between the states deviate as more noise is injected in the system. Each state as it was shown in Figure 5.9 has a Gaussian distribution, thus it was possible for us to fit each distribution with a Gaussian function and extract the mean and standard deviation for noise value. The difference between the mean of each states $\{x_U\}$ and $\{x_L\}$ gave us the phase angle difference and it is plotted for amplitude and phase noise in Figure 5.16(c). The blue triangles are indicator of evolution of the phase angle with amplitude noise while the red triangles give how the phase angle evolves with injected phase noise. For amplitude noise the phase angle difference between $\{x_U\}$ and $\{x_L\}$ was around 89° for low noise injection. However, with an increase in the injected noise the phase angle difference increases and finally for a noise of $\eta_R = 200mW$ this value becomes around 96°. On the other hand, for phase noise the change in the phase angle difference is much more rapid. As soon as we start to introduce some phase noise $\eta_\phi$ in the system the phase angle difference starts to decrease rapidly and for $\eta_\phi = 38°$, the phase angle difference becomes as small as 55°. This could be a direct consequence of the effect of multiplicative noise introduced in the system by means of phase noise $\eta_\phi$. Whereas the amplitude noise $\eta_R$ being additive has a smaller effect on the same.

### Distortion of the individual states

The mean of the fits gave us the phase angle, while the standard deviation of the fits in principle are correlated with the injected noise in the system. Increase of the injected noise in the system is accompanied with broadening of the individual states. The resulting standard deviations of states $\{x_U\}$ and $\{x_L\}$ are plotted against the injected phase noise in Figure 5.17(a) and for injected amplitude noise in Figure 5.17(b). Although the manner in which the individual states are influenced with injected amplitude and phase noise are different in the respective cases. Firstly let's start with Figure 5.17(a) where we show the evolution of standard deviation for state $\{x_U\}$ (in red) and $\{x_L\}$ (gray) with injected phase noise. We see that somehow the broadening of $\{x_U\}$ is more than that of $\{x_L\}$ starting from $\eta_\phi \sim 30°$ highlighted in Figure 5.17(a) (symmetric potential for phase noise), incidentally this is the same state which shifts in the phase space under influence of the injected phase noise (Figure 5.17(a)). Similar effect is observed for amplitude noise $\eta_R$ as well, where the state $\{x_L\}$ is seemingly more influenced by the noise than $\{x_U\}$ starting from $\eta_R \sim 30mW$ (symmetric potential for amplitude noise) highlighted in Figure 5.17(b). Again, the state which shifted under the influence of the injected amplitude noise was $\{x_L\}$. This leads us to believe that broadening of the states are in direct correlation to the shifting of the same. The amplitude and phase noise while influencing the switching rate also selectively influences individual states causing one of the states to move in the phase space.

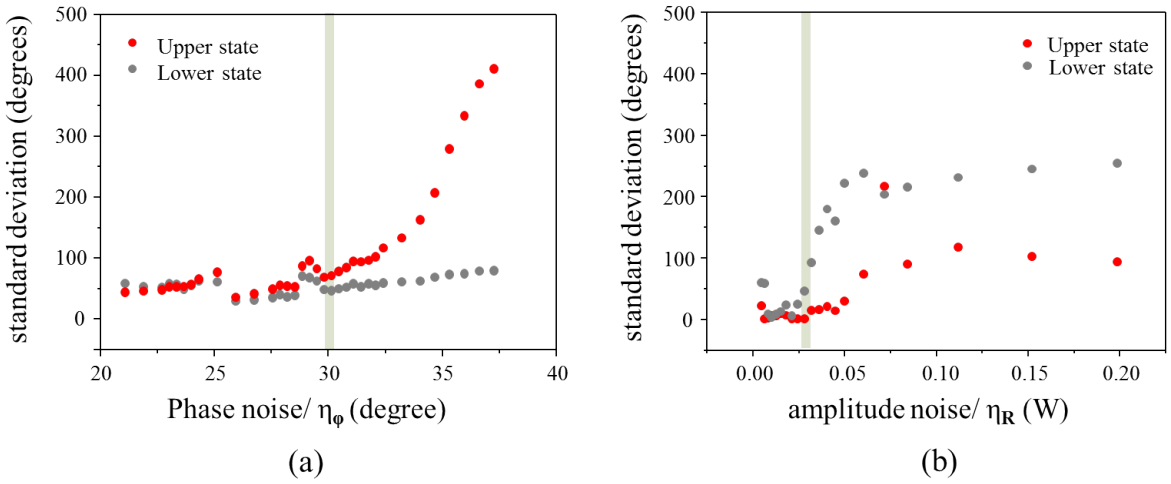


Figure 5.17: Evolution of standard deviation for each bistable states ($\{x_U\}$ in red, $\{x_L\}$ in blue) with (a) phase and (b) amplitude noise.

Therefore at this point we are able to calculate all the important parameters in order to realize stochastic resonance. It involves the threshold of amplitude of modulation, the cut-off frequency, Kramer's rate for both amplitude and phase noise and last but not the least, operating point inside the bistable regime.

## 5.7 Stochastic resonance with phase

In order to realize stochastic resonance in phase we require to modulate the phase of the drive with two signal; first one is with the low amplitude low frequency signal and secondly with noise. The operating point is kept at $\{\Omega_{op}, V_{op}\}$, the drive can be written as:

$$\delta V(t) = V_{ac} cos(\Omega_{drive} t + \Delta\phi sgn(\Omega_{mod} t) + \phi_0 + \eta_\phi(t)) \tag{5.17}$$

$$\langle \eta_\phi(t)\eta_\phi(t')\rangle = D_\phi \delta(t-t') \ , \langle \eta_\phi(t)\rangle = 0 \tag{5.18}$$

Here, $\Delta\phi$ is the amplitude of phase modulation and the modulation is a square like wave. The frequency of modulation is $\Omega_{mod}$ and $\phi_0$ is a phase offset, while $\eta_\phi$ is the external phase noise injected in the system. The noise like in previous sections is Gaussian like with zero mean and has a bandwidth of $1kHz$.

From the discussions in the previous measurements with pure phase noise and pure phase modulation, we can impose some values for the parameters:

- We choose an operating point at $\{\Omega_{op}, V_{op}\}$ in order to have a bistable potential which is symmetric in order to achieve highest efficiency for stochastic resonance.

- In order to realize stochastic resonance it is imperative that the natural Kramer's rate of the system is higher than the modulation frequency i.e. $r > \Omega_{mod}$. Since for a symmetric bistable potential the value of $r$ was found to be around $100Hz$, we choose $\Omega_{mod} = 50Hz$. This is done in order to make sure that the system can jump twice between the metastable states in one period of modulation.

- It was shown in the previous section (Figure 5.7) that the threshold for amplitude of phase deviation $\Delta\phi$ in order to observe jumps between the metastable states was about 110°. Thereby in this set of experiments the modulation was kept significantly below this level.

Based on these preconditions for the experiments we choose mainly two values of phase deviation: $\Delta\phi = 5°$ & $10°$, with $\Omega_{mod} = 50Hz$. Thereafter, we start to inject noise in the system and observe the system response as a function of the injected noise.

### 5.7.1 Time and frequency domain response

Before starting the experiment, we needed to bring the system in the operating point $\{\Omega_{op}, V_{op}\}$. To do that the drive frequency $\Omega_{drive}$ is swept in upward direction to be in state $\{x_U\}$. From here we start by doing a small phase modulation of $\Delta\phi = 10°$, the evolution of time and frequency domain response is shown in Figure 5.18(a) & (b). We start by pure modulation i.e. $\eta_\phi = 0°$ and the time domain response is shown in the Figure. We perform Fast Fourier Transform (FFT) on the acquired signal for a duration of $t = 60s$. The FFT response is shown in Figure 5.18(b), we see that for $\eta_\phi = 0°$ there is a small peak at $50Hz$. This peak appears a direct consequence of the intra-well modulation of the system by the external phase modulation. It is important to note here that the system in such a situation still does not start to jump between the metastable states; in order to achieve that more noise has to be inserted into the system. It is worth reminding that we define jumps in the system when it crosses the threshold defined at a phase of 40°.

Thereby from here we start to inject noise in the system, and record amplitude and phase response in time domain. For each recording we calculate FFT in order to observe how the peak at $\Omega_{mod}$ evolves with noise. When the noise is relatively small ($\eta_\phi = 22.0°$) we immediately observe an enhancement in the intra-well dynamics thereby resulting in an amplification of the injected signal, however the jumps between the metastable states are still scarce. With an even higher noise introduced in the system ($\eta_\phi = 25.0°$ & $27.5°$) we start to observe jumps between the metastable states more often and as it can be observed from the time domain responses, some of the jumps are well synchronized with the external modulation. This results in an even higher FFT response at $\Omega_{mod}$. With even higher noise injection ($\eta_\phi = 30.0°$) the jumps become more random and the synchronization is lost. This results in a decrease in the FFT peak (Figure 5.18(b)), however a small peak is still observed due to the inter-well dynamics discussed before. However it was very difficult to find a perfect synchronization between the external modulation and the jumps between the metastable states $\{x_U\}$ and $\{x_L\}$. The reason for the loss of synchronization is related to the loss of the symmetry of the bistable potential well discussed in section 5.5.1. As the potential well

becomes asymmetric due to the multiplicative noise, the two states merge into almost to a single state and thereby the jumps are lost.

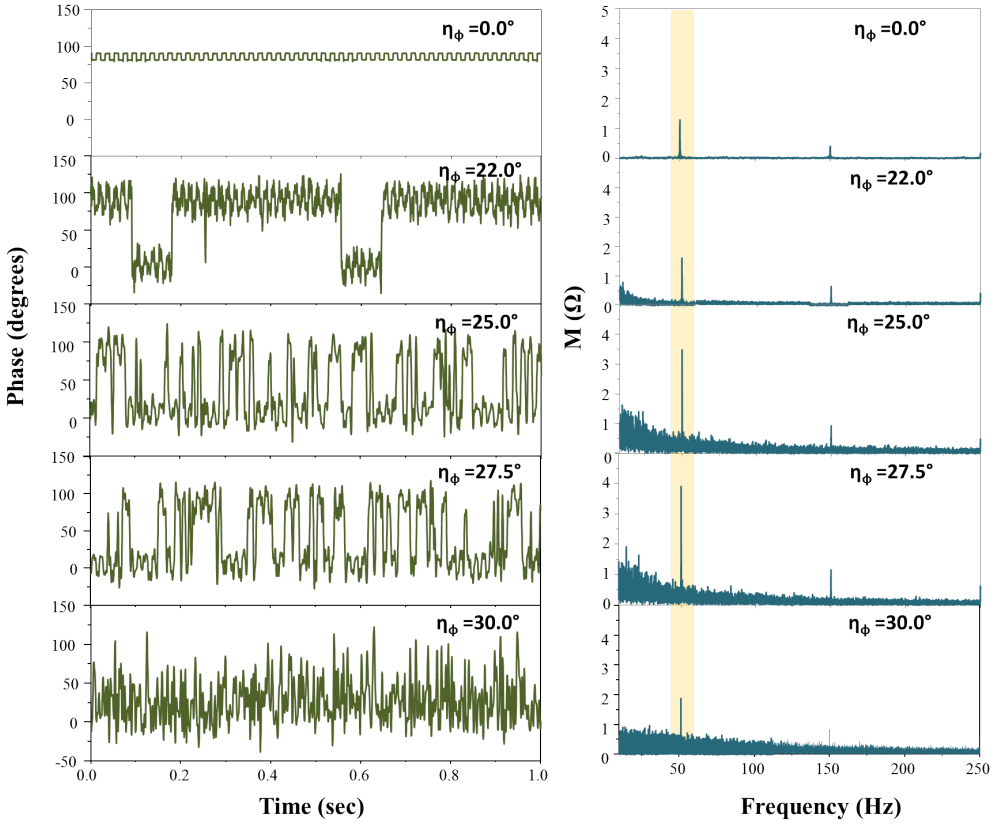


Figure 5.18: (a) Resonance in time domain for different phase noise values (b) FFT spectra of stochastic resonance for different phase noise values with $\Delta\phi = 10°$.

If we observe the FFT response carefully, we would be able to see presence of some odd harmonics on the spectra. This is attributed to the modulation scheme, as we use square wave instead of a sinusoidal one, along with the main spectral component odd harmonics also arrive with the drive. The same experiment was then repeated for a $\Delta\phi = 5$, and we measure the time domain amplitude and phase response of the system like before and after calculate the FFT response for each $\eta_\phi$. The time and frequency domain response are not shown here as it essentially shows the same behavior, important aspects of the results are discussed in the next section.

### 5.7.2 Gain due to stochastic resonance

From the FFT spectrum shown previously we can extract the evolution of amplification at $\Omega_{mod}$ as a function of applied phase noise $\eta_\phi$. This evolution of the FFT at $\Omega_{mod} = 50Hz$

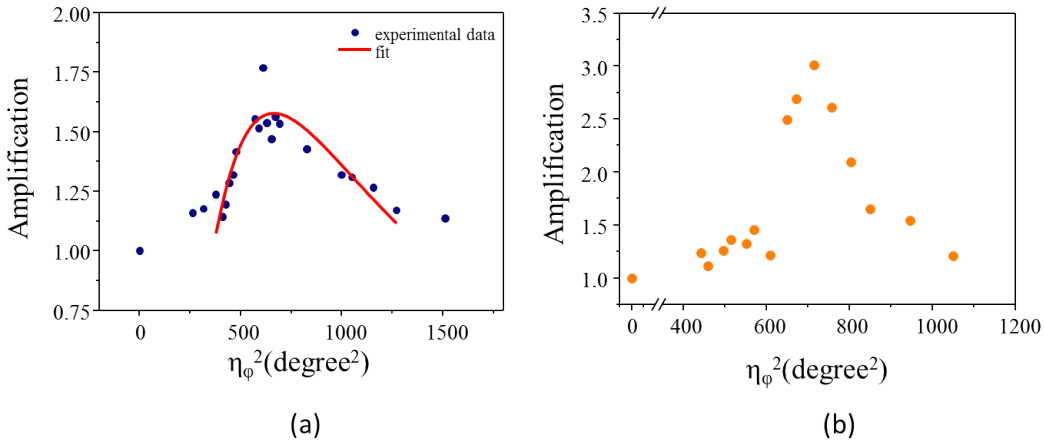


Figure 5.19: Amplification by stochastic resonance with phase modulation and noise for a modulation frequency of $\Omega_{mod} = 50Hz$ and for a phase modulation of (a) 5° and (b) 10°.

against square of the applied phase noise $\eta_\phi$ is plotted in Figure 5.19(a) for a modulation of 5°. The evolution is fitted with the expression of spectral amplification in equation (5.7), and it follows the behavior quite well. The amplification for a certain $\eta_\phi$ is normalized with respect to the one without any noise i.e. $\eta_\phi = 0°$. We observe that the amplification increases as more noise is applied to the system, we achieve highest amplification of about 1.75 for a $\eta_\phi \sim 25°$. Interestingly this is around the same value at where the same system under similar conditions (without the external modulation) had a Kramer's rate of about $100Hz$ (Figure 5.10). This is expected since the modulation frequency $\Omega_{mod}$ is $50Hz$, thereby we require $r \sim 100Hz$ in order to realize amplification. This scenario is explained in Figure 5.19(b); here we plot the resulting FFT for stochastic resonance with $\Delta\phi = 10°$ and with identical conditions as before. In this case we observe an increase in the amplification as higher phase modulation makes the system easier to synchronize with respect to the drive. Here we are able to observe a amplification of about 3.25 for a $\eta_\phi \sim 28°$. The behavior of enhancement in spectral amplification with increase in the amplitude of modulation was described in Figure 5.3, where we observed similar effect with increase in amplitude of modulation. Also the optimized $\eta_\phi$ required to achieve amplification is identical in the both cases, this is also reminiscent of the effect described in Figure 5.3.

### 5.7.3 Phase trajectories

In order to have a deeper understanding we constructed the phase trajectories of the system under stochastic resonance. The resulting trajectories are shown in Figure 5.20 with two separate situations; Figure 5.20(a) shows stochastic resonance for a phase modulation $\Delta\phi = 5°$ and Figure 5.20(b) shows for a modulation of $\Delta\phi = 10°$ for a phase noise $\eta_\phi = 30°$. In both cases we observe that there is a small modulation around the metastable states (due to the intra-well modulation) as a consequence of the small phase modulation. With an increase in the modulation (Figure 5.20(b)) we observe higher modulation in the phase space. The

transitions takes place along a fixed path in the phase space similar to the case in Figure 5.11. Interestingly the modulation in the phase space is perpendicular to the trajectory between the states $\{x_U\}$ and $\{x_L\}$. According to us this is the reason why it was difficult to synchronize perfectly the drive and the response.

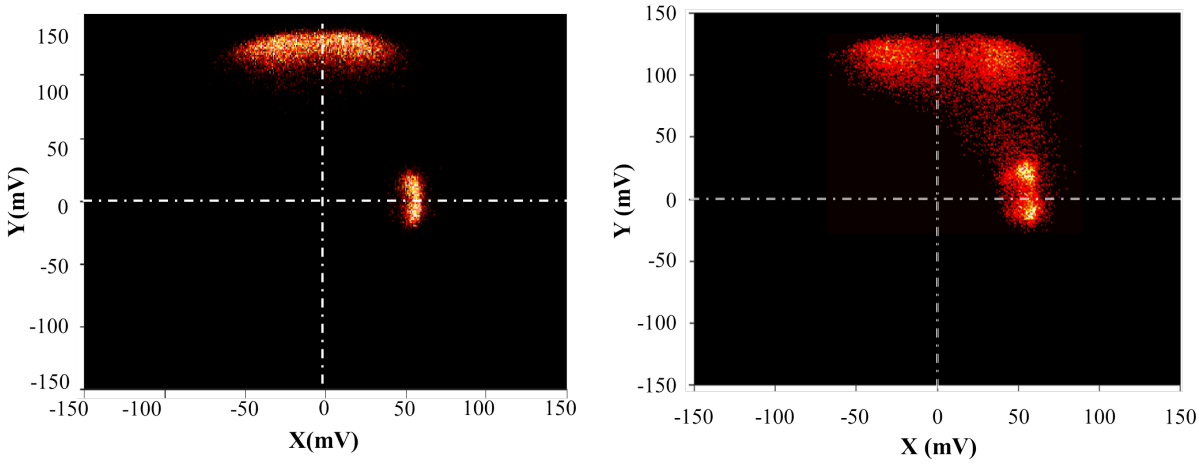


Figure 5.20: (a) Phase trajectory of stochastic resonance with a phase modulation of 5°, (b) phase trajectory of stochastic resonance with a phase modulation of 10° for a phase noise $\eta_\phi = 30°$.

## 5.8 Stochastic resonance with amplitude

In this section we switch to the stochastic resonance by amplitude modulation. The idea like before is to weakly amplitude modulate the drive around the operating point $V_{op}$, while injecting some noise with the drive into the system. However, in this case instead of plugging the noise inside the modulation we directly add a noise signal $\eta_R$ to the drive. The noise is Gaussian like with zero mean and uncorrelated. The drive acting on the NOEMS resonator thus can be written as:

$$V(t) = V_{ac}(1 + mcos(\Omega_{mod}t))cos(\Omega_{drive}t + \phi_0) + \eta_R(t) \tag{5.19}$$

$$\langle \eta_R(t)\eta_R(t')\rangle = D\delta(t - t') \ , \langle \eta_R(t)\rangle = 0 \tag{5.20}$$

where $V_{ac}$ is the excitation voltage, $\Omega_{drive}$ is the frequency of the drive, $m$ is the modulation index, $\phi_0$ is the phase offset of the drive and $\eta_R$ is the amplitude noise applied to the system. As it was mentioned before like previous section the drive is at the operating point $\{\Omega_{op}, V_{op}\}$ while $\eta_R$ has a bandwidth of $10kHz$. The process of selecting $\Omega_{mod}$ is similar compared to the case with phase stochastic resonance where it is dependent on the Kramer's rate $(r)$ of the system. Since the Kramer's rate $r$ for equally probable metastable states was found to

be $100Hz$ (Figure 5.13), for amplitude as in phase we keep the modulation frequency $\Omega_{mod}$ at the same value i.e. $50Hz$.

### 5.8.1 Time and frequency domain response

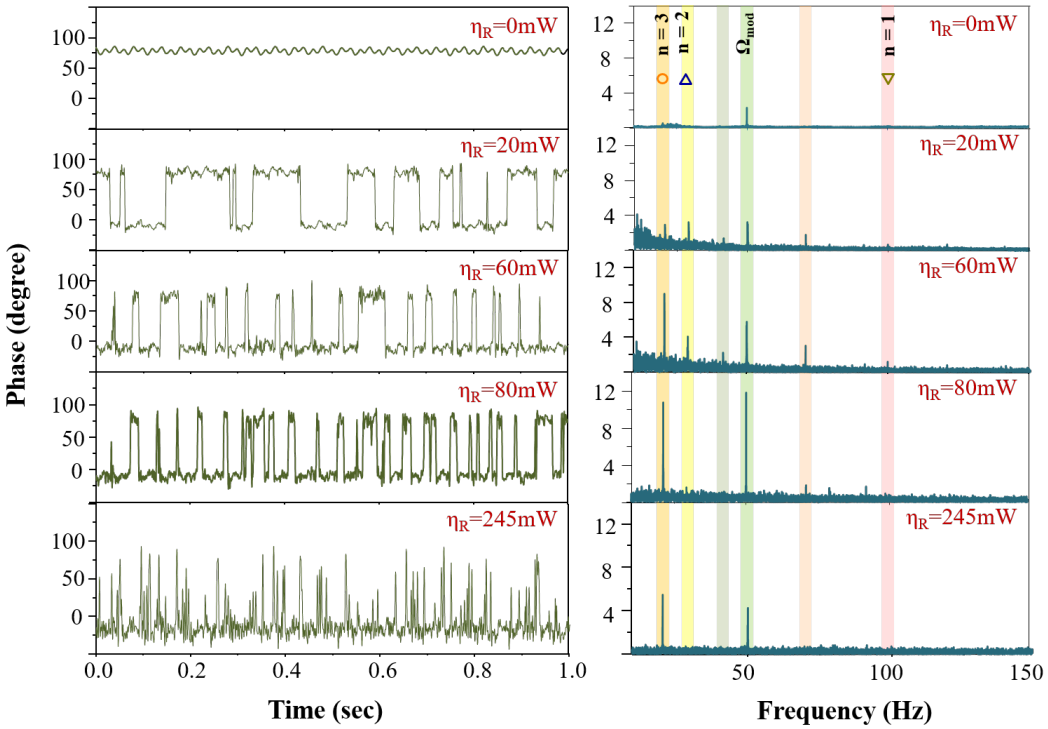


Figure 5.21: (a) Time evolution of phase switching with increase in the amplitude noise (at $50Hz$ of modulation frequency); we observe the best situation of synchronization for a amplitude noise of $80mW$, (b) evolution of the corresponding FFT spectra; we observe several harmonics along with the main resonance peak at $50Hz$.

From here we start a weak amplitude modulation of the drive ($m = 0.1$) with $\eta_R = 0mW$ and we record the time domain response in amplitude and phase. We reconstruct the FFT using the phase response although FFT with similar components could be constructed with the amplitude response as well. Figure 5.21(a) shows the time domain response while Figure 5.21(b) shows the reconstructed FFT from the acquired signal.

Like before the system needs to be prepared at state $\{x_U\}$ by sweeping the actuation frequency up to the operating point $\Omega_{drive} = \Omega_{op}$. When there is only a pure modulation of the amplitude, a weak intra-well modulation in phase response is observed for $\eta_R = 0mW$. This is observed in the reconstructed FFT as a weak peak at $\Omega_{mod}$. As we start increasing the injected noise power $\eta_R$ ($= 20mW$) from here we start observing jumps between the metastable states, as a reminder we define jumps whenever the system crosses the predefined threshold. This is reflected in a small enhancement of resonance at FFT spectra. However, as

we start increasing the injected amplitude noise in the system for $\eta_R = 60mW$ and $80mW$ the jumps become more frequent and most of them become synchronized with the modulation. This results in significant enhancement of the FFT peak. From here as we start increasing the noise $\eta_R$ even further, for $\eta_R = 245mW$ the jumps loose the synchronization completely and the FFT peak starts to decrease considerably. This is again related to the change in the bistable potential like for phase noise, as the bistable potential starts to become more unistable.

From here we repeat the experiment with an amplitude modulation of $m = 0.2$ and repeat the experiment for several values of $\eta_R$. Each case we record the amplitude and phase response of the system in time and construct FFT spectra from the time domain measurements.

### 5.8.2 Amplification of stochastic resonance

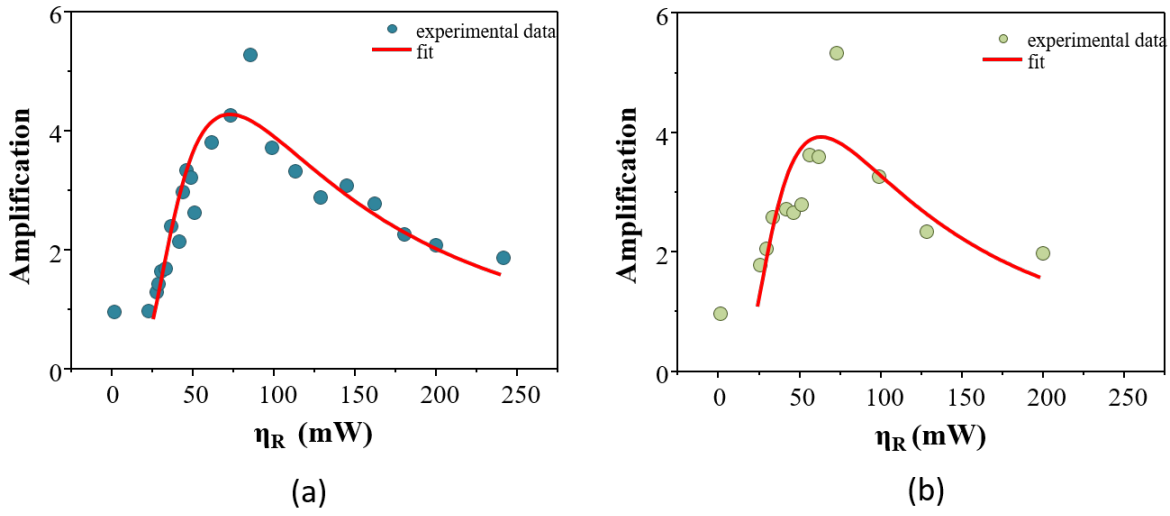


Figure 5.22: Amplification by stochastic resonance with amplitude modulation and noise for a modulation frequency of $50Hz$ and for a modulation depth $m$ of (a) 10% and (b) 20%.

In this section we study the amplification from stochastic resonance with amplitude modulation and noise. In Figure 5.22 we plot the amplification due to stochastic resonance in amplitude with applied amplitude noise $\eta_R$. Firstly in Figure 5.22(a) we plot the amplification versus noise for $m = 0.1$; we define the amplification like before i.e. with respect to the one with zero noise i.e. $\eta_R = 0mW$. We were able to fit the experimental data with equation (5.7), which shows to follow the data points satisfactorily. For these particular conditions we were able to achieve an amplification of 5.5, this is higher than the amplification achieved for stochastic resonance with phase noise. For $m = 0.2$, the amplification versus amplitude noise $\eta_R$ is plotted in Figure 5.22(b). Similar to the situation before we are able to observe amplification for a certain range of the applied noise $\eta_R$. The highest amplification observed in this particular case was about 5.75. Slightly higher value can be attributed to the fact

that higher modulation makes the system easier to switch between the metastable states. In this case the experimental data seems to fit the theoretical equation quite well as seen in Figure 5.22(b) by the red line.

### 5.8.3 Behavior of the subharmonics

Apart from the fundamental resonance at $\Omega_{mod}$, one can also observe sub-harmonic or super-harmonic resonances. Instead of following the modulation directly (two escape periods in one period of driving) it can wait for the next cycle in both wells. This means the system can perform two escapes in one driving period, thereby leading to sub-harmonic resonances. Also instead of waiting, the system can instead jump two times more between the wells leading to exhibit super-harmonic resonances. Thereby extending this concept if the system waits for $n$ periods in both the wells, we can write [61]:

$$T_{sub} = (n - \frac{1}{2})T_{mod} \tag{5.21}$$

$$i.e.\ \ \Omega_{sub} = \frac{\Omega_{mod}}{(n - \frac{1}{2})}\ for\, n = 1, 2.... \tag{5.22}$$

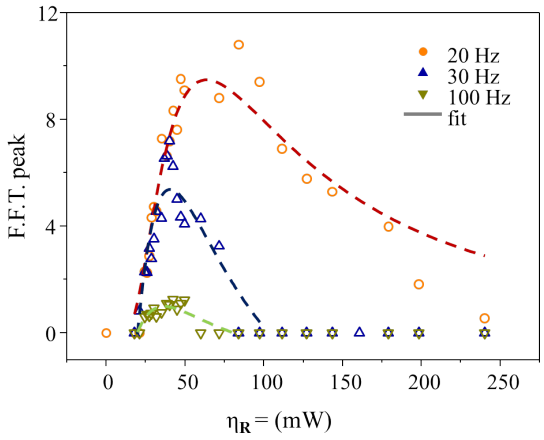


Figure 5.23: Stochastic resonance for the subharmonics $n = 1, 2$ & 3

This particular situation is shown in Figure 5.21(b), where we highlight the existence of such subharmonics in the spectra. Considering the modulation $\Omega_{mod} = 50Hz$, we should be able to observe harmonics at around $20Hz, 33Hz$ and $100Hz$ for $n = 1, 2$ and 3 respectively. This is exactly what we observe in our case, as highlighted in Figure 5.21(b). As the next step we plot the evolution of the FFT peaks of the harmonics with applied noise. The resulting plot is displayed in Figure 5.23, we observe the harmonics at $\Omega = 20, 30$ & $100Hz$ show stochastic resonance like behavior and fit quite well with the expression for spectral amplification in equation (5.7). Highest response is obtained for $20Hz$ at a noise of about

$75mW$, while for the other the response becomes relatively smaller and they occur at a lower value of $\eta_R$ compared to the former. For the FFT responses in these cases normalization was not possible as for $\eta_R = 0mW$ no FFT peak appear. Thereby unlike Figure 5.22, instead of plotting amplification here we plot only the FFT amplitudes with applied noise.

### 5.8.4 Phase trajectories

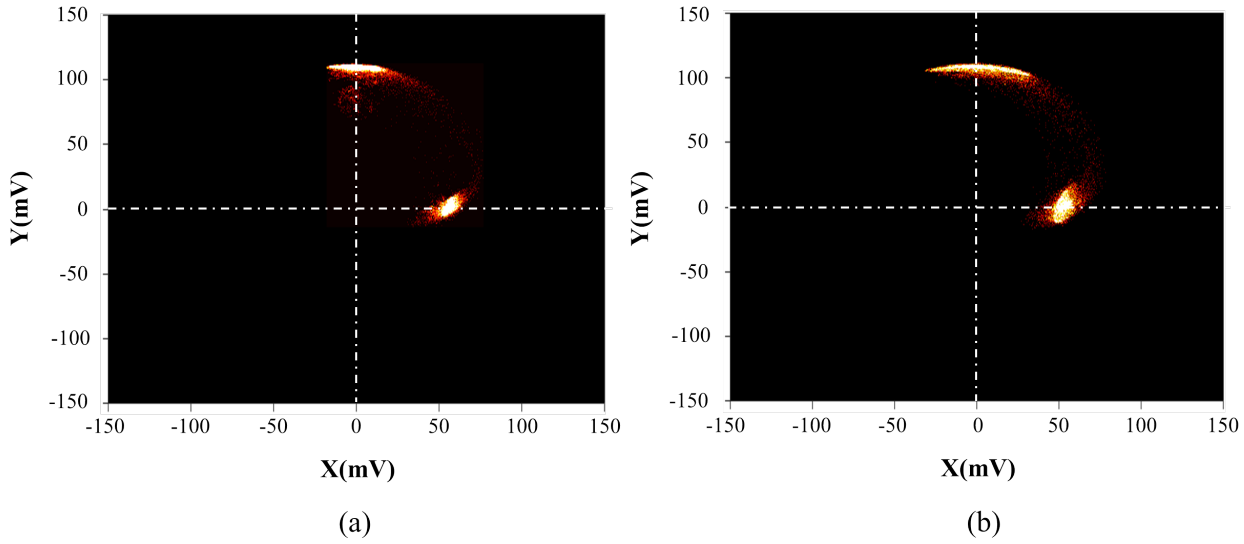


Figure 5.24: (a) Phase trajectory for stochastic resonance for an amplitude modulation of 10% (b) phase trajectory for stochastic resonance at an amplitude of modulation of 20%; with expectedly higher dispersion of the states are observed for higher modulation in amplitude.

Here again we plot the phase trajectory of the system under stochastic resonance with amplitude modulation and noise. The resulting plots for $m = 0.1$ and $m = 0.2$ are shown in Figure 5.24(a) & (b). We can observe that for $m = 0.1$ the modulation of the states $\{x_U\}$ and $\{x_L\}$ are small around the mean value while for $m = 0.2$ the modulation is relatively larger. The reason of such behavior is that when the system is modulated in amplitude, the intra-well modulation is parallel to the $x$-axis and thereby making the system easier to transit between the metastable states (Figure 5.24). This enhances the spectral amplification for amplitude noise and amplitude modulation. While on the other hand for amplitude modulation the modulation of the system is along the $y$-axis which is not the preferred transition path for phase noise (Figure 5.20). This makes overall spectral amplification lower for stochastic resonance with phase noise and modulation.

## 5.9 Conclusion and perspectives

In conclusion we can say that in this chapter we demonstrated the implementation of stochastic resonance with pure amplitude noise and pure phase noise. In order to realize stochastic resonance, we had to first of all optimize many parameters. First of all we had to determine how the bistable potential well behaves as a function of the drive frequency $\Omega_{drive}$, in order to realize stochastic resonance it is imperative that both the metastable states are equiprobable. Next we needed to determine the frequency range of operation for the double well system, we found a cut-off frequency of about $1kHz$ for the NOEMS system. We also had to find out the Kramer's rate of the system for various externally applied noise (both in amplitude as well as in phase), this step was necessary in order to find a suitable modulation frequency of operation for the system. And finally we gave a overall understanding experimental point of view for the stochastic resonance. Interestingly we found that somehow the amplitude stochastic resonance seemed to have a higher spectral amplification compared to the one with phase stochastic resonance. The phase trajectory was quite revealing in order to explain this behavior, we saw that the transitions between the metastable states happen along different paths for injected phase and amplitude noise. Finally this factor governs the difference in achieved amplification in the system for different kind of noise schemes.

In order to improve the amplification due to phase stochastic resonance thereby we propose an idea where we can combine the two modulation schemes (i.e. amplitude and phase) at the same time in order to tilt the intra-well modulation along the transition path in order to improve the spectral amplification. Thus under such conditions the applied voltage signal to the system can be written as:

$$V(t) = V_{ac}(1 + mcos(\Omega_{mod}t))cos(\Omega_{drive}t + \Delta\phi sgn(\Omega_{mod}t) + \phi_0) \tag{5.23}$$

The amplitude modulation index $m$ needs to very small and also has to be optimized in order to reach optimized amplification.

The next set of experiments were a natural extension to the stochastic resonance, called vibrational resonance. Vibrational resonance is defined as the amplification of the low amplitude, low frequency signal applied to a bistable system by using an externally injected high frequency signal instead of noise. Detailed discussion of this phenomenon is out of the scope of this report. With vibrational resonance it is not only possible to amplify the low frequency signal but at the same time second harmonic generation of this low frequency signal is possible [122][58].

# Chapter 6

# Conclusion and perspectives

## 6.1 General conclusion

Main objective of this work is aimed at investigating the nonlinear dynamics in a fully integrated NOEMS platform, combining the mechanical and optical resonators as well as actuation tools. Such integrability is essential in view of potential applications in metrology or signal processing for instance. The platform under study consists of a two dimensional photonic crystal mirror. Actuation was realized by integrating underneath the interdigitated electrodes, implementing capacitive transduction. Compared to external actuators such integrated actuation scheme allows for high electromechanical coupling and hence higher transduction, opening a way to reach the high excitation regime. Such high excitation pushes the system into nonlinear regime where the system is described by Duffing equation instead of linear one. A system under such a regime has two different stable points instead of just one, this is known as the bistability. We used this existing nonlinearity to perform what is known as sub/super-harmonic resonance on the nonlinear system. We showed that with the excitation, these resonances generate tongue like response known as the instability tongues. We were able to show such behavior for up to 8th order. At the same time we also probed the evolution of the system in the phase space, as the detuning of excitation is changed. The system goes under a 180° of phase rotation with the drive as the frequency is detuned from one edge of the tongue to the other. Such platform exhibits phase dependent amplification of a weak resonant drive under application of a strong modulation at a frequency twice the natural resonance, this is known as parametric amplification. We extended this scheme further in order to show that it can be utilized to tune the eigen-frequency and nonlinearity of the system.

Noise in any nonlinear system is usually considered as prejudicial, it can however sometimes provide a signal processing benefit. This is the case when implementing stochastic resonance, corresponding to the resonant amplification of a weak coherent signal by introducing noise in a nonlinear system. In order to implement such resonance, we had to optimize some parameters; including the drive frequency, the amplitude and frequency of modulation of the weak coherent signal. Once we could determine these parameters, first of all we had to find how the system responds to the injected noise. We studied the behavior of the system

with both amplitude and phase noise injected externally. From these data we were able to estimate what is known as the Kramer's rate, the characteristic switching rate of the system between the bistable states. We showed that for optimized conditions this value was about $100Hz$ for both amplitude and phase noise. We therefore could use this value to finally perform stochastic resonance on our NOEMS platform at a frequency of $50Hz$. We performed stochastic resonance with both amplitude and phase modulation. Stochastic resonance with phase noise revealed to be less effective than the one with amplitude noise. The explanation was found when looking at the phase portrait with both situations. It was seen that with amplitude noise the intra-well modulation is in similar direction with the inter-well transitions, unlike that with the phase noise. This causes amplitude stochastic resonance gain to be higher compared to the one with phase. Finally we proposed a scheme which combines these two schemes in order to enhance the gain attained by phase stochastic resonance.

## 6.2 Perspectives

### 6.2.1 Electro-opto-mechanical platforms

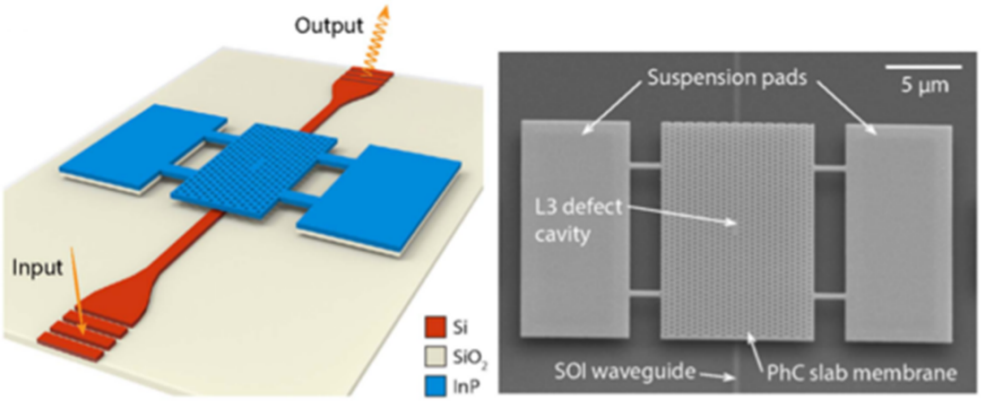


Figure 6.1: (a) Schematic of the PhC membrane and waveguide system; light is injected through one end of the waveguide and it interacts with the PhC cavity and the modified field is collected at the other end of the waveguide, (b) An scanning electron micrograph of the fabricated membrane-waveguide structure where the membrane is suspended about $230nm$ above the Si waveguide.

Previous to present work, a first step towards integration aimed at combining an optical and mechanical system on the same chip, as well as optical functionalities to inject light into the resonator. One example of such integrated device was implemented in the lab by Tsvirkun et al. [123], where heterogeneous integration of a III-V material Indium Phosphide (InP) with Silicon on insulator waveguide was performed. The fabricated device and the

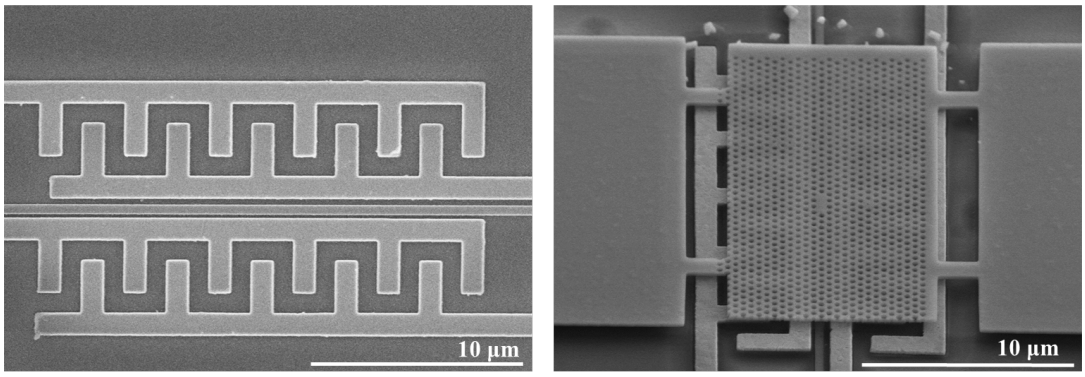


(a) (b)

Figure 6.2: (a) The modified interdigitated electrodes along with the waveguide, (b) the suspended photonic crystal membrane with a L3 cavity on top of the interdigitated electrodes and the waveguide.

light coupling mechanism are shown in Figure 6.1(a); light is injected through one side of the tapered waveguide and is coupled to the PhC cavity (L3 cavity) residing above it. The injected light after interacting with the PhC cavity is modified via optomechanical coupling and is collected at the other end of the waveguide. This enables detection of the Brownian motion of the membrane. Figure 6.1(b) shows the fabricated scanning electron micrograph of the PhC-waveguide system, the PhC having a dimension of $10 \times 20\mu m^2$ is suspended about $230nm$ above a Si waveguide.

During the course of this thesis, we extended such approach to integrate a suspended PhC membrane having both electrical and optical properties and integrated actuation tools on the same chip. The next step is therefore to integrate these two schemes in order to implement a system with a true electro-opto-mechanical coupling. This required a new design of the electrodes as shown in Figure 6.2(a). The pair of interdigitated electrodes are separated by a waveguide with thickness varying from 250 to $550nm$. Optimization of the electrode-waveguide separation was important in order to minimize plasmonic effects observed in FDTD simulations. A separation of $1\mu m$ between the electrodes and the waveguide center was chosen to minimize this effect. Also we required to spatially separate the electrodes and membrane on the chip; this required use of 'via' to connect the electrodes from outside world on to the chip. The fabricated suspended membrane, electrode and the waveguide system is shown in Figure 6.2(b). The membrane also embeds a L3 cavity used to couple the light from the waveguide. Such platforms shall thus realize an electro-opto-mechanical coupling.

### 6.2.2 Towards phase locking of coupled oscillators

Phase locking is a branch of synchronization where one harmonic oscillator is disturbed by another harmonic oscillator operating at a nearby frequency. When the coupling is strong enough and the frequencies are close enough, the second oscillator could capture the first oscillator and finally having identical frequencies. Due to this reason it is also referred as

injection locking. When the second oscillator follows the first oscillator but do not capture it, it is called injection pulling. Observing the phase dynamics of the coupled oscillators is an usual way in general to observe this behavior. Synchronization can be observed between from two oscillators to $N$ number of oscillator provided $N \geq 2$. Synchronization is of great importance in view of enhancing the performance of electro-opto-mechanically driven sensors or in implementation of high spectral purity RF oscillators exploiting photon-phonon interaction.

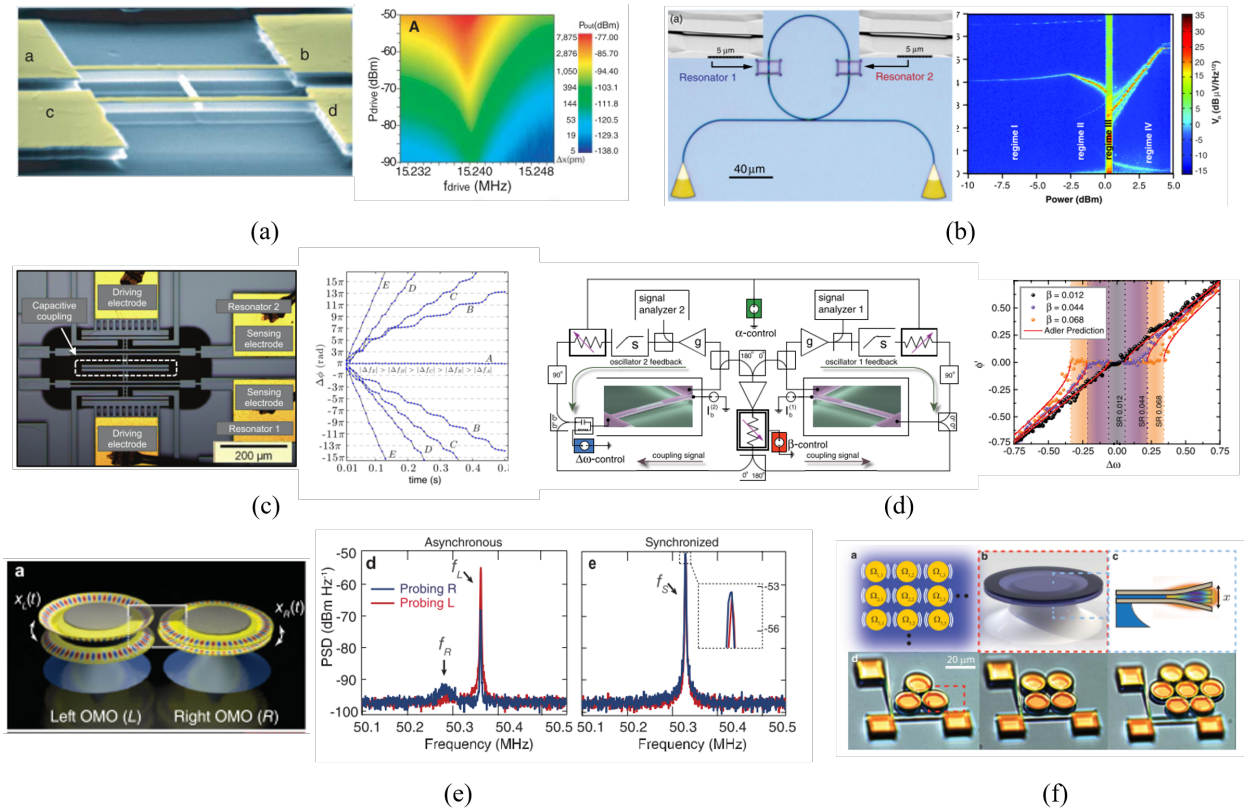


Figure 6.3: (a) Synchrnoization between mechanically coupled oscillators in sub-harmonic excitaion regime [60], (b) synchronization between oscillators via a photonic resonator [124], (c) synchronization by reactive coupling force [125], (d) phase locking between two anharmonic oscillators [55], (e) synchronization of two oscillators by common optical noise [126], (f) synchronization between oscillator array by common optical noise [127].

In past few years nanomechanical/optomechanical systems have exhibited such synchronization effect and have grown a tremendous interest in the field of NEMS/NOEMS. For nanomechanical devices, it was shown by the group of P.Mohanty [60] that two mechanically coupled oscillator were able to display synchronization behavior under sub-harmonic excitation regime. They exhibited what is famously known as the Arnold's tongue like behavior, a signature of phase locking (Figure 6.3(a)). Bagheri et al. [124] demonstrated synchronization between two spatially separated nanomechanical oscillator via a photonic resonator (Figure

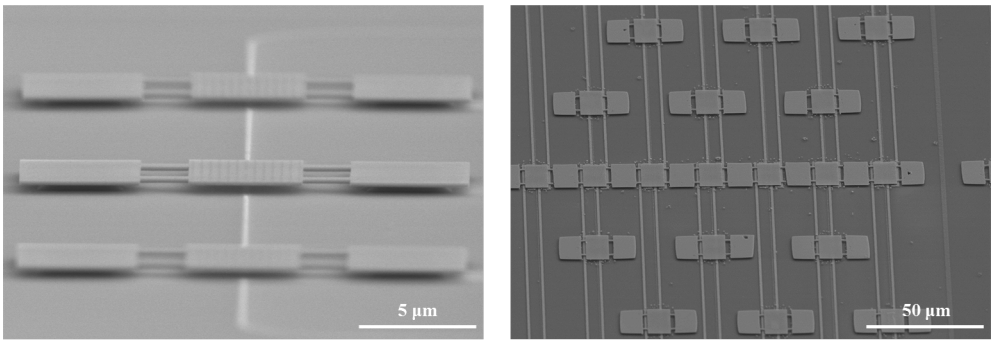


Figure 6.4: (a) Synchronization possible by placing several PhC membrane nanomechanical oscillators on same waveguide, (b) a control over eigen-frequencies and coupling strength of these membranes are possible by using integrated electrodes along with the waveguide membrane systems on the same chip.

6.3(b)). They showed the evolution of the power spectrum in four different regimes; thermal state regime, regenerative oscillation regime, chaotic regime and finally the synchronized regime. Agarwal et al. [125] showed synchronization in silicon micromachined resonators by reactive coupling force between the oscillators (Figure 6.3(c)). While the group of Roukes studied theoretically and experimentally, coupling between two reactively coupled Duffing oscillators with saturated feedback gain [55] (Figure 6.3(d)). They were able to show phase locking between these two anharmonic oscillators by controlled feedback loop. The feedback reduced significant amount of phase noise of the oscillators which can be important for sensor and clock applications. The group of Lipson were able to demonstrate synchronization between two oscillators by means of common optical noise [126] (Figure 6.3(e)), a concept they later extended for oscillator arrays [127] (Figure 6.3(f)).

Therefore the next step of experiments on the NOEMS platform shown in Figure 6.2 is to realize such synchronization phenomenon between two or more oscillators via common optical noise. Placing several oscillators over same waveguide allows oscillator coupling via a common optical noise (Figure 6.4(a)) However, due to fabrication imperfections these devices might have eigen-frequencies far away from each others. This eigen-frequency then could be tuned by using a DC bias on the electrodes fabricated on the same chip (Figure 6.4(b)) (following the method described in section 3.4.4). The electrodes could also be used to amplify the resonant (or sub/super-harmonic) oscillation of the membranes and drive them in the self-oscillation regime, in order to increase the coupling strength between the oscillators.

### 6.2.3 Nonlinearity with electro-opto-mechanical systems

Potential future experiments on nonlinear dynamics involve what is known as the vibrational resonance [58]. The concept of vibrational resonance is somewhat similar to that of stochastic resonance, with the noise being replaced by a high frequency signal. The bistable potential is

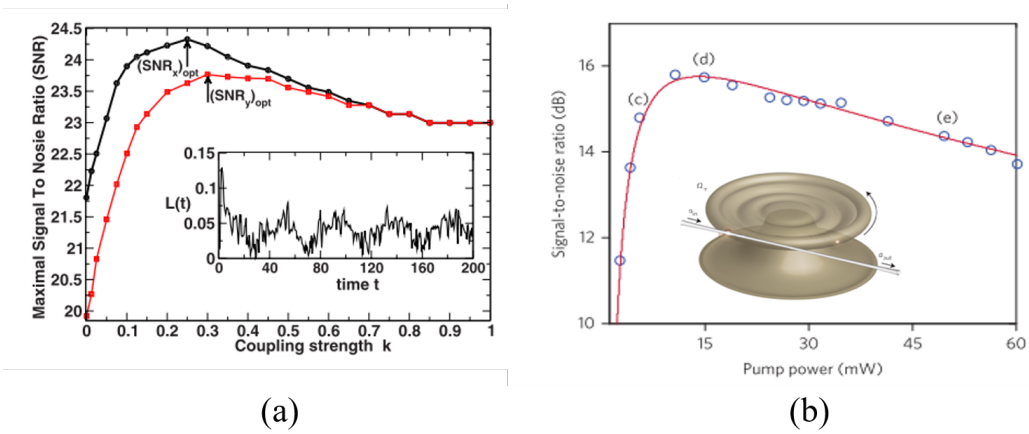


(a) (b)

Figure 6.5: (a) Stochastic resonance coupled underdamped bistable systems [129], (b) optomechanically induced stochastic resonance [130].

modulated by a weak low frequency signal and a strong high frequency signal. At a certain strength of the high frequency signal, the system is able to jump twice between the two stable points at a single period of the low frequency signal. This results in amplification of the low frequency signal at the output. Vibrational resonance like stochastic resonance should be also applicable for amplitude as well as phase. Another extension of such experiments concerns with vibrational resonance in Duffing oscillators using time delayed feedback [128]. Such time delayed feedback gives rise to a periodic or quasiperiodic pattern of vibrational resonance profile with respect to the time delayed parameter. It was shown, that with such a scheme it is possible to achieve resonance in an overdamped single well system with an optimized time delay.

However, systems with electro-opto-mechanical coupling can possibly open new doors to realize other experiments involving nonlinear dynamics. This involves for example, stochastic resonance in coupled underdamped bistable systems [129]. Consider two driven bistable systems, coupled and subject to independent noises. When a coupling between these two systems is turned on, stochastic resonance although is not affected, however under strong coupling regime SNR of the subsystems match (Figure 6.5(a)). It was also shown that for a certain value of the coupling strength the stochastic resonance is optimum. Monifi et al. [130] recently demonstrated chaos mediated stochastic resonance in optomechanical systems (Figure 6.5(b)), this not only essential for fundamental understanding of nonlinear dynamics induced by optomechanical coupling, but also interesting for implementation of stochastic resonance in optomechanical systems in order to enhance signal processing capabilities; to detect, amplify or manipulate weak signals.

# Appendix A

# Characterization of GaN/AlN and diamond PhC membranes

It was mentioned in Chapter 2 that due to the small residual stress in InP membrane, it was difficult to fabricate suspended membranes with higher bridge lengths. However this can be countered by using substrates with higher stress. Highly stressed membranes could be generated either by using sandwich of two different substrates with lattice mismatch (for example GaN/AlN) or by using bulks having higher inherent Young's modulus (for example diamond), which was fabricated in collaboration with X.Checoury of IEF (Paris-sud University). Such devices were fabricated and their mechanical properties are discussed in this section.

## A.1 Characterization of GaN/AlN PhC membrane

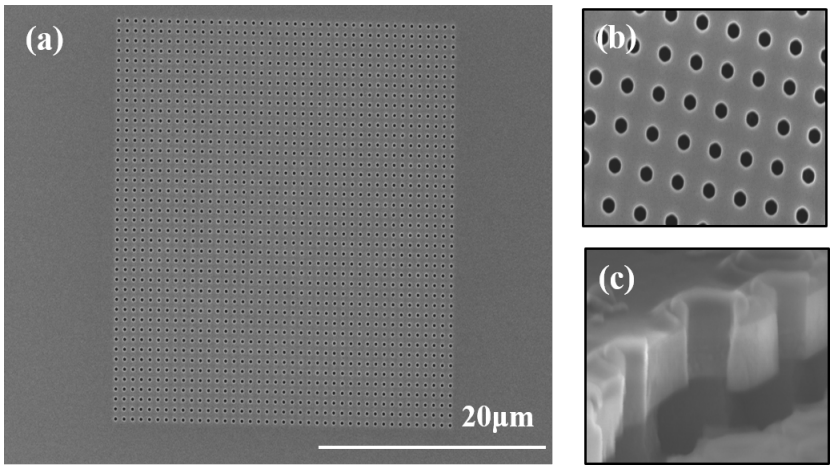


Figure A.1: (a) Fully clamped GaN/AlN membrane of dimension $30\mu m \times 30\mu m$, (b) closer view of the etched cylindrical photonic crystal holes, (c) cross-sectional view of the photonic crystal membrane.

Apart from working with InP membranes we characterized GaN/AlN fully clamped membranes as well. The membrane consists of AlN layer of thickness $200nm$ and GaN layer of thickness $160nm$ on silicon substrate. The double layer is required in order to reach a thickness of around $400nm$. This can be attributed to the lattice mismatch between the GaN layer and silicon. This is the reason we require to use AlN layer as an intermediate layer to reach this thickness. Another advantage is that such structure results in a high stress membrane resulting in higher mechanical Q-factors. The GaN/AlN membrane results in a highly stressed membrane which produces mechanical response with higher quality factor and higher eigen-frequencies. The fabricated fully clamped GaN/AlN membrane is shown in Figure A.1(a), the membrane is $30\mu m \times 30\mu m$ of size. The membrane is patterned with cylindrical holes of diameter varying from $175nm$ to $215nm$ (however these values are unoptimized for this design). The etched cylindrical holes and their cross-sectional profile is shown in Figure A.1(b) & (c). The sample is then placed inside the vacuum chamber where it is mounted on top of the piezo stack. The detection of the mechanical modes were performed optically with the help of the Balanced Homodyne Detector (BHD).

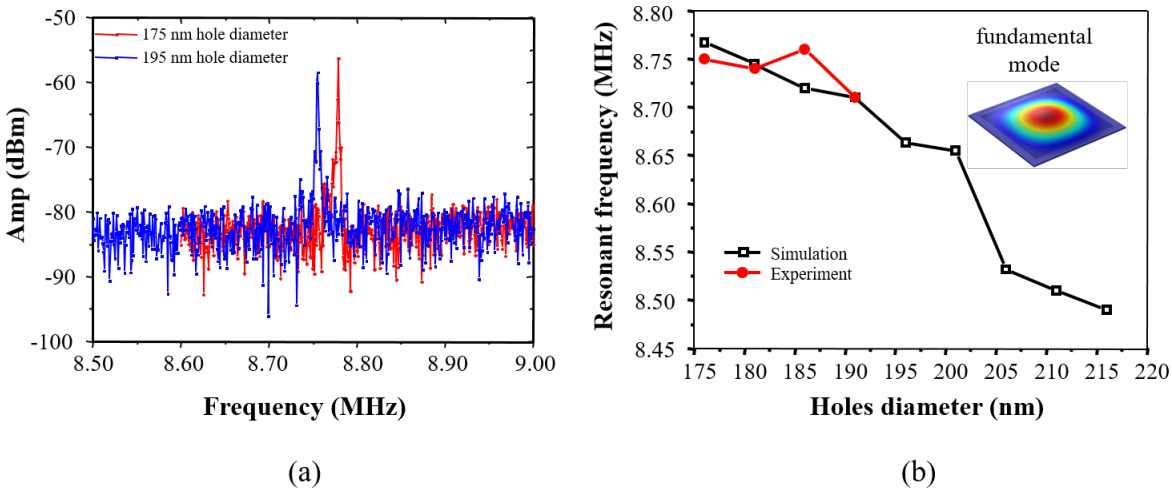


Figure A.2: (a) Experimentally detected fundamental mode of the GaN/AlN rectangular membrane for two different hole diameters: $175nm$ and $185nm$, (b) experimental results and simulation fit for the eigen-frequencies of GaN/AlN membrane, the inset shows FEM simulation of the fundamental mechanical mode of the fully clamped membrane.

The piezo was driven by an external signal generator at an excitation voltage of about $5V$. The actuation frequency is swept in order to find the mechanical modes. The retrieved fundamental mechanical mode for a membrane with a dimension of $30\mu m \times 30\mu m$ is shown in Figure A.2(a). In Figure A.2(a) we show the mechanical modes for membranes with hole diameters $175nm$ and $185nm$. The fundamental eigen-frequency was found to be around $8.75MHz$ and at around $8.78MHz$ for membrane with hole diameter $195nm$ and $175nm$ respectively. The values of the obtained eigen-frequencies are significantly higher than that of the InP membranes. This happens due to the high stress induced because of AlN/GaN

structure. We recorded the mechanical spectra for membranes with same size (i.e. $30\mu m \times 30\mu m$) but with different hole diameters. The result is shown by the red line in Figure A.2(b). We were able to simulate the mechanical modes for identical design and structures for various hole diameters. The simulated results are plotted in Figure A.2(b) and shown by the black line. The simulated results support the experimental results quite well, an effective Young's modulus of $1860MPa$ for AlN and $1116MPa$ for GaN was used in order to achieve comparable eigen-frequency with the experimental result. This required use of an effective Young's modulus which was almost 6 times higher than that of the bulk for either cases, rise in the Young's modulus occurs due to the existing strain in the structure. The FEM simulation of the fundamental mode is shown in the inset of Figure A.2(b). Detection of higher order modes were not possible as the next visible mode predicted by FEM simulations were around $30MHz$ which is far beyond $10MHz$, the limit of piezo stack actuation. The Q-factors of these membranes were detected via ring-down technique and were found to be between 500 and 1000. This value is similar to the one found for InP but with optimized mechanical geometry.

The sample also contained membranes with dimension of $10 \times 10\mu m^2$ and $20 \times 20\mu m^2$, although we couldn't retrieve any mechanical modes for these membranes. The reason can be attributed to the fact that intuitively one can say that these membranes have fundamental eigen-frequency which is higher than that of the one discussed previously (due to the reduced dimension). Thereby the fundamental eigen-frequency have a value more than $10MHz$, which is beyond the frequency range of operation.

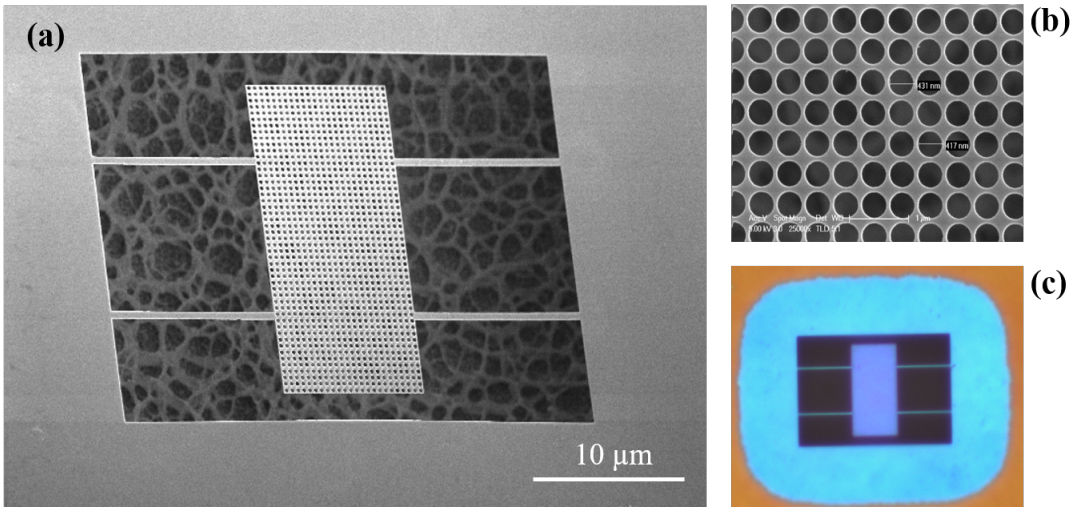


Figure A.3: (a) The fabricated diamond photonic crystal membrane suspended by four bridges (fabricated in collab. with X.Checoury (IEF)) (b) closer view on the etched cylindrical PhC holes in the membranes, (c) image of the suspended PhC membrane in an optical microscope.

## A.2 Characterization of the diamond PhC membrane

Diamond photonic crystals were fabricated in collaboration with X.Checoury of IEF, Paris-sud University. The membranes contain cylindrical holes etched inside of diameter of $145nm$ with a period of $425nm$. The dimension of the membranes are $10 \times 20\mu m^2$ having a thickness of $140nm$. Unlike the fully clamped GaN/AlN and fully clamped InP membranes these diamond membranes are suspended by four bridges on both side of the rectangular membrane (Figure A.3). The width of the bridges are between $0.5\mu m$ and $1.0\mu m$ while having bridge lengths varying between $2\mu m$ to $12\mu m$ with a step of $2\mu m$. These factors finally define the mechanical properties of these membranes. The FEM simulations show the mechanical modes to lie around the MHz frequency regime. These membranes are also highly reflective for the He/Ne laser wavelength at around $633nm$. The SEM pictures of the fabricated diamond photonic crystal membranes are shown in Figure A.3. Unlike the InP membranes the diamond photonic crystal membranes exhibited suspended structures even with high bridge lengths ($12\mu m$) as shown in Figure A.3(a). This can be attributed to the high existing high stress in the membranes. The high stress also makes the diamond PhC membranes to be very interesting candidate for optomechanics as this ensures high mechanical quality factor for these membranes.

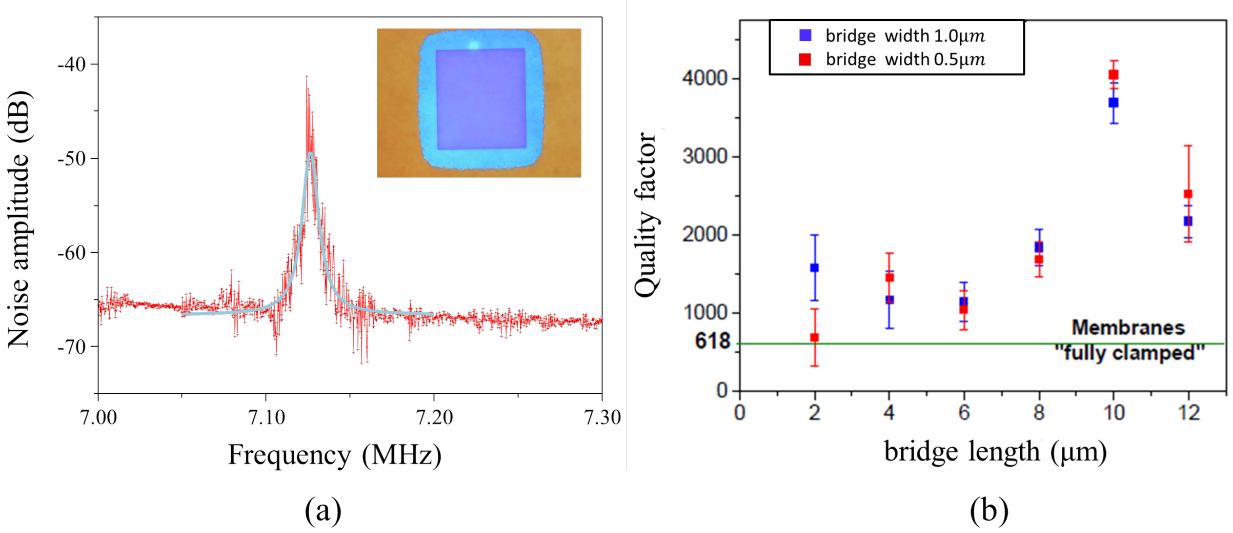


Figure A.4: Experimentally detected fundamental mechanical mode of

The experimentally detected fundamental mechanical mode with a lorentzian fit is shown in Figure A.4(a). The method of detection is identical to the one described in the previous section; the membrane mounted on a piezo stack placed inside the vacuum chamber and is driven externally by a signal generator. The excitation voltage was set to $5V$, as the actuation frequency is changed when this frequency is close one of the mechanical mode of the membrane, the membrane starts to oscillate and the mode then is detected by the BHD. The mechanical mode retrieved is for a fully clamped diamond photonic crystal membrane (shown

in the inset) of dimension $20 \times 20\mu m^2$ having a fundamental mechanical eigen-frequency around $7.125MHz$. Higher order modes were not detected possibly due to the upper cut-off frequency of the piezo stack in use, which was $10MHz$. A ring-down measurement gave a Q-factor of about $591 \pm 20$ for this particular membrane. We were able to characterize the bridged membranes of different bridge lengths as well. Evolution of this quality factor with bridge lengths is shown in Figure A.4(b); we observe a monotonous increase of the quality factors with the bridge length. However the drop of the quality factor for the bridge length of $12\mu m$ can be attributed to the shift in eigen-frequency due to increase in bridge length. Thus the probed mode is probably the second order one rather than the first order one.

# Appendix B

# Derivation of Mathieu equation for a nonlinear system

Excitation of super and sub-harmonic resonance falls under the situation of parametric excitation, where somehow the spring constant of the resonator is modulated at some harmonic of the natural resonance and a response is observed at the natural resonance. Since the physics of this kind of system is quite complicated, we will start from the basic Mathieu equation and slowly work towards more complicated situations. The phenomenon is directly related to the nonlinearity of the system as the nonlinearity of $n$-th order helps the resonator to be excited at $n$-th super or sub-harmonic resonance. Thus the threshold of excitation is related to the order of nonlinearity in the system and the above-mentioned threshold increases for higher order nonlinearities.

## B.1 Mathieu equation without damping

A nonlinear system under study can be described by using a special differential equation which is known as the Mathieu equation [59]. The general form of Mathieu equation can be described as:

$$\ddot{x} + (\delta + \epsilon cos(t))x = 0 \tag{B.1}$$

The idea of Mathieu equation is that the dynamics of a system under study could be described by using equation of this form. To understand how this actually works let us consider the equation under study with Duffing nonlinearity:

$$\ddot{x} + \Gamma_m \dot{x} + \Omega_m^2 x + \beta x^3 = F \tag{B.2}$$

Thus for the time being lets start with assuming the system is under no damping as well considering the system is excited far below from the nonlinear threshold. Which means for

the time being we can consider $\beta = 0$ and $\Gamma_m = 0$. Considering the fact that the harmonic driving causes the spring of the system to modulate at that frequency, we replace the term $F$ in equation (B.2) and add the harmonic drive to the spring constant term. Furthermore as discussed before when the system is exited at some harmonic other than the natural resonance it can directly affect the spring constant of the system, thus in short the spring constant will be modulated at the harmonic and when it exceeds a certain threshold it will produce a response at the natural resonance. Under such conditions considering a super-harmonic resonance let's assume that the system is driven at a frequency $\Omega_{drive} = \Omega_m/n$ with a modulation amplitude of the spring constant being $H$. So the equation (B.2) can be transformed to:

$$\ddot{x} + (\Omega_m^2 + Hcos(\frac{\Omega_m t}{n}))x = 0 \tag{B.3}$$

using the transformation $\tau = \frac{\Omega_m}{n}t$ the equation reduces to:

$$\frac{d^2x}{d\tau^2} + (\delta + \epsilon cos(\tau))x = 0 \tag{B.4}$$

Where $\epsilon = Hn^2/\Omega_m^2$ and $\delta = n^2$, this equation now completely resembles Mathieu equation and we can now proceed to find a solution of the equation. The solution of Mathieu equation can be derived using various techniques, for example: Lie transformation, perturbation theory, Floquet theory, Hill's equation, harmonic balance. The idea of all these processes above is actually to study the dependency of the parameters $\delta$ and $\epsilon$ on each other. Since the system under study is shown to have a nonlinear behavior thus we decided to use harmonic balance theory in order to find the response of the system. So for the time being let us assume the solution of $x(t)$ in terms of Fourier series:

$$x(t) = \sum_{n=0}^{\infty} a_n cos\frac{nt}{2} + b_n sin\frac{nt}{2} \tag{B.5}$$

We now can substitute equation (B.5) into equation (B.4) and using some trigonometric simplifications and collection of harmonic terms (harmonic balance) we are able to generate four sets of algebraic equations involving coefficients $a_n$ and $b_n$(for details please refer to [59]). These four sets being for coefficients $a_{even}$, $b_{even}$, $a_{odd}$ and $b_{odd}$. All the four sets are homogeneous and of infinite order, in order to find a nontrivial solution determinants for each set must vanish. Which leads us to the four determinants:

$$a_{even}: \begin{vmatrix} \delta & \epsilon/2 & 0 & 0 & \\ \epsilon & \delta - 1 & \epsilon/2 & 0 & ... \\ 0 & \epsilon/2 & \delta - 4 & \epsilon/2 & \\ & & ... & & \end{vmatrix} = 0 \tag{B.6}$$

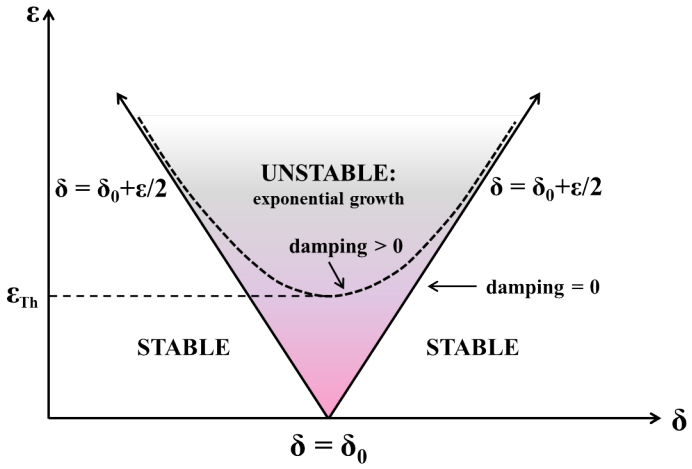


Figure B.1: The instability tongue for parametric excitation of the system; the region of instability is bounded by $\delta$ which is dependent on the spring constants of the system. The tongue originates at $\delta = \delta_0$ and then diverges with increase in excitation $\epsilon$. The smooth line indicates instability tongue in ideal case (damping = 0) while the dotted line indicates more pragmatic situation taking damping into consideration.

$$b_{even}: \begin{vmatrix} \delta-1 & \epsilon/2 & 0 & 0 & \\ \epsilon/2 & \delta-4 & \epsilon/2 & 0 & \dots \\ 0 & \epsilon/2 & \delta-9 & \epsilon/2 & \\ & & \dots & & \end{vmatrix} = 0 \tag{B.7}$$

$$a_{odd}: \begin{vmatrix} \delta-1/4+\epsilon/2 & \epsilon/2 & 0 & 0 & \\ \epsilon/2 & \delta-9/4 & \epsilon/2 & 0 & \dots \\ 0 & \epsilon/2 & \delta-25/4 & \epsilon/2 & \\ & & \dots & & \end{vmatrix} = 0 \tag{B.8}$$

$$b_{odd} = \begin{vmatrix} \delta-1/4-\epsilon/2 & \epsilon/2 & 0 & 0 & \\ \epsilon/2 & \delta-9/4 & \epsilon/2 & 0 & \dots \\ 0 & \epsilon/2 & \delta-25/4 & \epsilon/2 & \\ & & \dots & & \end{vmatrix} = 0 \tag{B.9}$$

In all the determinants a typical row is of the form (except for the first one or two rows):

$$\dots \quad 0 \quad \epsilon/2 \quad \delta - p^2/2 \quad \epsilon/2 \quad 0 \quad \dots \tag{B.10}$$

Each of these four determinants now give a particular dependence of $\delta$ on $\epsilon$ which will produce some unique transition curves in the $\delta, \epsilon$ plane. By setting $\epsilon = 0$ in the above determinants it is easy to obtain the intersection with the $\delta$ axis. The transition curves for

$a_{even}$ and $b_{even}$ intersects the $\delta$ axis at $\delta = p^2 (p = 1, 2, 3...)$. While transition curves for $a_{odd}$ and $b_{odd}$ intersects $\delta$ axis for $\delta = \frac{(2p+1)^2}{4}$ $(p = 1, 2, 3..)$. Thus for $\epsilon > 0$, each point on $\delta$ axis will give rise to two transition curves, first one is generated from the associated transition curve originating from $a$ determinant while the other one associated with the parameter $b$ determinant. Thus there is a tongue originating from the $\delta$ axis provided:

$$\delta = \frac{p^2}{4},\ p = 1, 2, 3.... \tag{B.11}$$

Now knowing that $\delta = n^2$, we can write $n = p/2$. Which means the parametric excitation would be observed for drive frequencies $\Omega_{drive} = \frac{\Omega_m}{n} = \frac{2\Omega_m}{p}$ $(p = 1, 2, 3....)$. Equation (B.10) however merely gives the originating point of the transition curve from the $\delta$ axis, but to properly understand the nature of these transition curves in $\delta, \epsilon$ plane one needs to take into account the influence of $\epsilon$ in the above determinants. Considering effect of the drive parameter $\epsilon$ the dependence between $\delta$ and $\epsilon$ can be written as (for detailed derivation please refer to [59]):

$$\delta = \frac{p^2}{4} + \delta_1 \epsilon + \delta_2 \epsilon^2 + ... \tag{B.12}$$

Thus effect of an increase of $\epsilon$ (external excitation) is a dispersion of $\delta$ i.e. increase in the excited frequency range for the super-harmonic excitation. The resulting plot is shown in Figure B.1. Thus we can conclude that parametric excitation is possible when the drive frequency satisfies the condition $\Omega_{drive} = \frac{2\Omega_m}{n}$, where n is an integer.

## B.2 Mathieu equation with damping

The discussion up till now however has not been very practical, as the damping coefficient has been completely neglected in the discussion. Thus let us now consider the damped Mathieu equation and then observe how the transition curves are modified. For that let us consider what is known as the damped Mathieu equation:

$$\frac{d^2x}{d\tau^2} + c\frac{dx}{d\tau} + (\delta + \epsilon cos(\tau))x = 0 \tag{B.13}$$

Using the procedure of harmonic balance to find a solution of these equations can become quite complicated. So in order to make this discussion a little easier we will try another technique called the perturbation method in order to derive the transition curves. For that case we will use a special situation for which $\delta = 1/4$ which could be extended for all of the other cases. In order to facilitate the perturbation we will assume:

$$c = \epsilon\mu \tag{B.14}$$

Along with that in order to use this perturbation methods let us use some more transformations:

$$\zeta = \tau \; and \; \eta = \epsilon\tau \tag{B.15}$$

Using this transformations the equation (B.13) can be written as:

$$\frac{\partial^2 x}{\partial\zeta^2} + 2\epsilon\frac{\partial^2 x}{\partial\zeta\partial\eta} + \epsilon^2\frac{\partial^2 x}{\partial\eta^2} + \epsilon\mu(\frac{\partial x}{\partial\zeta} + \epsilon\frac{\partial x}{\partial\eta}) + (\delta + \epsilon cos(\zeta))x = 0 \tag{B.16}$$

let us assume the solution of $x(\zeta, \eta)$ to be of the form:

$$x(\zeta, \eta) = x_0(\zeta, \eta) + \epsilon x_1(\zeta, \eta) + ..... \tag{B.17}$$

Substituting this into equation (B.16) and equating coefficients of '1' and $\epsilon$ (while neglecting higher orders $O(\epsilon^2)$) we can write:

$$\frac{\partial^2 x_0}{\partial\zeta^2} + \delta x_0 = 0 \tag{B.18}$$

$$\frac{\partial^2 x_1}{\partial\zeta^2} + \frac{1}{4}x_1 = -2\frac{\partial^2 x_0}{\partial\zeta\partial\eta} - x_0 cos(\zeta) - \mu\frac{\partial x_0}{\partial\zeta} + \delta x_1 + x_0 cos(\zeta) \tag{B.19}$$

Solution of equation (B.18) is just a superposition of sinusoidal signals and can be written as:

$$x_0(\zeta, \eta) = A(\eta)cos(\sqrt{\delta}\zeta) + B(\eta)sin(\sqrt{\delta}\zeta) \tag{B.20}$$

At this stage to simplify the equations in hand let us consider a particular situation where:

$$\delta = \frac{1}{4} + \delta_1\epsilon \tag{B.21}$$

Using equation (B.20) and (B.21) into equation (B.19) and using some trigonometrical identities we derive the following equation:

$$\begin{aligned}\frac{\partial^2 x_1}{\partial\zeta^2} + \frac{1}{4}x_1 \;\; = \;\; & -\{-\frac{dA}{d\eta}sin(\frac{\zeta}{2}) + \frac{dB}{d\eta}cos(\frac{\zeta}{2})\} - \frac{1}{2}\{Acos(\frac{3}{2}\zeta) + Acos(\frac{1}{2}\zeta) + Bsin(\frac{3\zeta}{2}) \\ & + Bcos(\frac{\zeta}{2})\} - \frac{\mu}{2}\{-Asin(\frac{\zeta}{2}) + Bcos(\frac{\zeta}{2})\} - \delta_1\{Acos(\frac{\zeta}{2}) + Bsin(\frac{\zeta}{2})\}\end{aligned}$$

Removal of resonance terms gives:

$$\frac{dA}{d\eta} = -\frac{\mu A}{2} + (\delta_1 - \frac{1}{2})B \tag{B.22}$$

$$\frac{dB}{d\eta} = -\frac{\mu B}{2} - (\delta_1 + \frac{1}{2})A \tag{B.23}$$

Intuitively we can assume the solution of parameters $A(\eta)$ and $B(\eta)$ as $A(\eta) = A_0 exp(\lambda\eta)$ and $B(\eta) = B_0 exp(\lambda\eta)$. Using these trial solutions in equation (B.23) & (B.24), we can say a trivial solution could exist only when:

$$\begin{vmatrix} -\mu/2 - \lambda & -1/2 + \delta_1 \\ -1/2 - \delta_1 & -\mu/2 - \lambda \end{vmatrix} = 0 \tag{B.24}$$

Which gives the allowed values of $\delta_1$for $\lambda = 0$ (for transition between stable and unstable regime):

$$\delta_1 = \pm\frac{\sqrt{1-\mu^2}}{2} \tag{B.25}$$

This gives values of $\delta$ as:

$$\delta = \frac{1}{4} \pm \epsilon\frac{\sqrt{1-\mu^2}}{2} + O(\epsilon^2) = \frac{1}{4} \pm \frac{\sqrt{\epsilon^2 - c^2}}{2} + O(\epsilon^2) \tag{B.26}$$

This clearly shows us for instability to occur for a given value of $c$, a minimum value of $\epsilon$ is required. Also the minimum$\epsilon$ is slightly detached from the $\delta$ axis depending on the value of $c$. The dependence of $\delta$ on $\epsilon$ for low $\epsilon$ is a little parabolic which makes edges of the transition curves to be a little blunt rather than sharp compared to the case when there is no damping. Nonetheless when $\epsilon$ is sufficiently high the dependence again becomes linear (ignoring higher order perturbations) which is shown by the dotted curve in Figure B.1.

## B.3 Mathieu equation under nonlinear regime

In the previous sections it has been discussed how the unbounded states can exist inside the transition regions defined by the boundaries, but in real world a physical system does not demonstrate unbounded behavior. The reason can be attributed to the existing nonlinearity in the system. This phenomenon hasn't been examined in the discussion till now and its due to the fact that up to now only linear Mathieu equation has been considered. This is due to the fact that as the system enters into nonlinear regime due to the large motion in amplitude the eigen-frequency becomes detuned. As a result the amplitude in the response becomes smaller. To study the parametric response of a system under nonlinear conditions we will need to consider the nonlinear Mathieu equation:

$$\frac{d^2x}{d\tau^2} + (\delta + \epsilon cos(\tau))x + \epsilon\alpha x^3 = 0 \tag{B.27}$$

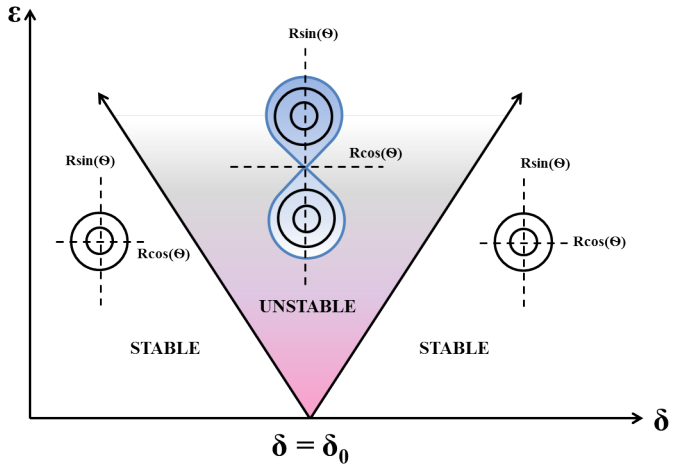


Figure B.2: Instability tongue under nonlinear regime.

Here we use the nonlinear coefficient as $\epsilon\alpha$, considering the fact that the nonlinearity is directly related to the external excitation. We assume this as more excitation means higher amplitude of motion which in turn means higher tuning of resonance. Here we use the similar transformations and assumptions as in the last section and finally for the coefficients of $\epsilon$ we can write:

$$\frac{\partial^2 x}{\partial \zeta^2} + 2\epsilon \frac{\partial^2 x_0}{\partial \zeta \partial \eta} + \epsilon^2 \frac{\partial^2 x}{\partial \eta^2} + (\delta + \epsilon cos(\zeta))x + \epsilon \alpha x^3 = 0 \tag{B.28}$$

Again in order to avoid complicacy we can use approximated value of $\delta$ as: $\delta = \frac{1}{4} + \delta_1 \epsilon$, which transforms equation above to:

$$\frac{\partial^2 x_1}{\partial \zeta^2} + \frac{1}{4} x_1 = -2\epsilon \frac{\partial^2 x_0}{\partial \zeta \partial \eta} - \delta_1 x_0 - x_0 cos(\zeta) - \alpha x_0^3 \tag{B.29}$$

Now using the approximate solution of $x_0(\zeta, \eta) = A(\eta)cos(\frac{\zeta}{2}) + B(\eta)sin(\frac{\zeta}{2})$ with removal of resonant terms and neglecting some additional cubic terms we are able to write:

$$\frac{dA}{d\eta} = (\delta_1 - \frac{1}{2})B + \frac{3\alpha}{4} B(A^2 + B^2) \tag{B.30}$$

$$\frac{dB}{d\eta} = -(\delta_1 + \frac{1}{2})A - \frac{3\alpha}{4} A(A^2 + B^2) \tag{B.31}$$

Simplifying these equations by using polar coordinates $A = Rcos\theta$ and $B = Rsin\theta$ in the above equations, it can be transformed and we can show that for nontrivial solution to exist the following conditions must hold (for details refer to [59]):

$$-\frac{R}{2} sin(2\theta) = 0 \tag{B.32}$$

$$-\delta_1 - \frac{cos(2\theta)}{2} - \frac{3\alpha}{4}R^2 = 0 \;\; or \;\; R^2 = -\frac{4}{3\alpha}(\frac{cos(2\theta)}{2} + \delta_1) \tag{B.33}$$

Solution of equation (B.33) for $R \neq 0$ requires $\theta = 0, \frac{\pi}{2}, \pi \, or \, \frac{3\pi}{2}$. For a nontrivial real solution of equation (B.34) we must have $R^2 > 0$. With $\alpha > 0$ we have two possible states with $\theta = 0$ or $\theta = \pi$ and in that case a nontrivial solution would exist only when $\delta < -\frac{1}{2}$. On the other hand for $\theta = \frac{\pi}{2}$ or $\theta = \frac{3\pi}{2}$ a nontrivial solution would exist when $\delta_1 < \frac{1}{2}$. This shows existence of a bifurcation as one traverses across the transition region. As the bifurcation is bounded by $\delta > \pm\frac{1}{2}$ a bifurcation between $\theta = \frac{\pi}{2}$ and $\frac{3\pi}{2}$ is observed as $\delta$ is detuned from the transition curve at the right side (Figure B.2) for a fixed $\epsilon$. The amplitude also grows as $\delta$ is detuned and a second bifurcation is observed on the left side transition curve, this bifurcation happens between $\theta = 0$ and $\pi$. Although this effect is not observed in our system as it will be seen later, this can be attributed to the fact that in this region the system simply just do not respond as $R = 0$ for this regime. A special case of parametric excitation called parametric amplification will be discussed in later sections with both theoretical and experimental viewpoint.

# Appendix C

# Calibration for parametric resonance

In this section we discuss about how the resonant excitation ($V_{ac}$) is influenced by the parametric excitation ($V_p$). As we use the same electrodes in order to inject both the drives to the NOEMS system, the weak resonant drive is somewhat influenced by the strong parametric drive. In order to retrieve how the resonant excitation evolves with the parametric excitation we fix the resonant excitation at $V_{ac} = 0.20V$ and vary the parametric excitation from $0V$ to $10V$ while recording the evolution of the resonant excitation in an oscilloscope. We observe that the weak resonant drive $V_{ac}$ has little to almost no influence on the high parametric drive $V_p$. However the opposite is not true, how $V_p$ influences $V_{ac}$ is shown in Figure C.1. When $V_p = 0V$ peak to peak voltage retrieved in the oscilloscope is about $0.181V$. The discrepancy in the detected voltage comes from presence of some noise in the electrical paths. We observe an exponential dependence expressed as:

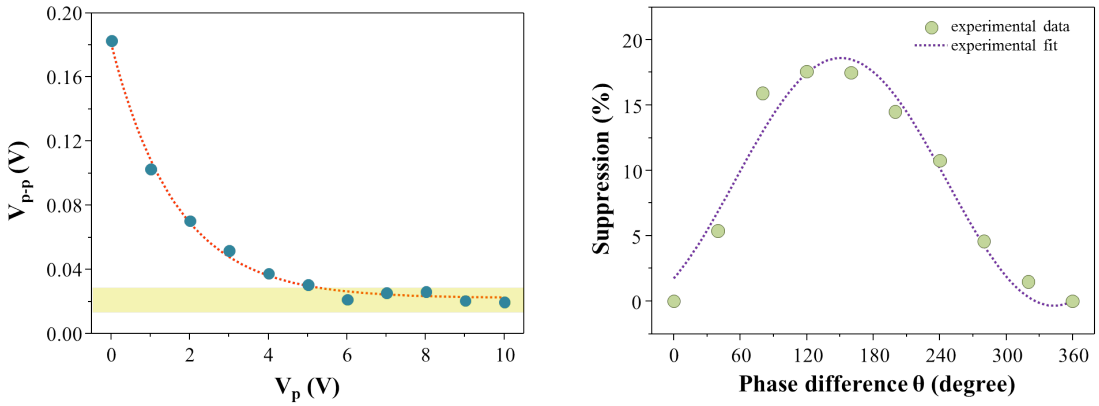


Figure C.1: (a) Suppression of resonant drive at $V_{ac} = 0.2V$ due to parametric excitation ranging from $V_p = 0V$ to $10V$.

$$V_{peak-peak} = 0.022 + 0.159exp\left(-\frac{V_p}{1.65}\right) \tag{C.1}$$

$V_{peak-peak}$ is the detected peak to peak $V_{ac}$ in the oscilloscope. If one observe closely at Figure C.1(b) a saturation of the detected voltage for a high $V_p$ around $0.022V$ is seen.

Moreover, the resonant drive $V_{ac}$ also has a dependence on the phase of the parametric drive $V_p$. In order to retrieve how this is influenced we use similar scheme like before i.e. we fix the drive the resonant drive at $V_{ac} = 0.2V$ and the parametric drive at $V_p = 1.0V$ while changing the phase of the parametric drive $V_p$. From there we calculate the influence of the parametric drive $V_p$ on the resonant drive $V_{ac}$ for phase difference $\theta$ ranging from 0° to 360°. The result is plotted in Figure C.1(b), we calculate the above-mentioned influence in terms of percentage. We see that $V_p$ has a sinusoidal influence over the resonant drive $V_{ac}$. Fitting with a sinusoidal function we can write:

$$\delta V_{peak-peak} = 9.1 + 9.5 sin\left[\frac{\pi(\theta - 54.7)}{192.15}\right] \tag{C.2}$$

where $\delta V_{peak-peak}$ is defined as the percentage of error in the applied and the detected voltage i.e. $\delta V_{peak-peak} = \left|\frac{V_{ac} - Vpeak-peak}{V_{ac}}\right| (\%)$.

Knowing now the full mapping i.e. how the amplitude as well as the phase $\theta$ of the parametric drive $V_p$ influences the resonant drive $V_{ac}$, we could calculate the effective resonant drive for each parametric drive amplitude $V_p$ and its phase.

# Appendix D

# Calibration of phase and amplitude noise

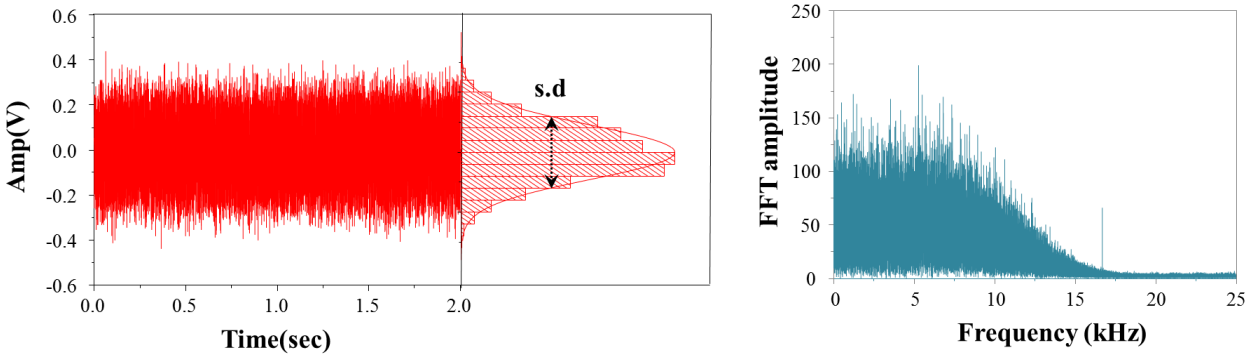


Figure D.1: (a) Time trace of the noise and its distribution with zero mean, (b) FFT of the acquired signal of bandwidth $10kHz$.

In this section we discuss about the calibration of the injected phase noise in the system, we needed this calibration in order to quantify the injected noise. We decided to calibrate the phase noise in terms of the standard deviation. To do this, first of all we generated a noise signal by the signal generator under consideration with peak to peak noise amplitude of $V_{pp} = 1V$ and a bandwidth of $10kHz$. The time domain signal is shown in Figure D.1(a), with an acquisition time of $2sec$. The histogram of the acquired signal is shown in the same figure, the histogram with the Gaussian fit shows clearly that the noise has zero mean with a finite value of standard deviation. The standard deviation is defined as:

$$S.D = \sqrt{mean(signal^2) - \{mean(signal)\}^2} \tag{D.1}$$

Figure D.1(b) on the other hand shows the frequency domain representation of the same signal, this is constructed by performing Fast Fourier Transform (FFT) of the time domain signal. We observe that the noise has almost a pink noise like feature, however it is more or less white in nature in the $10kHz$ bandwidth.

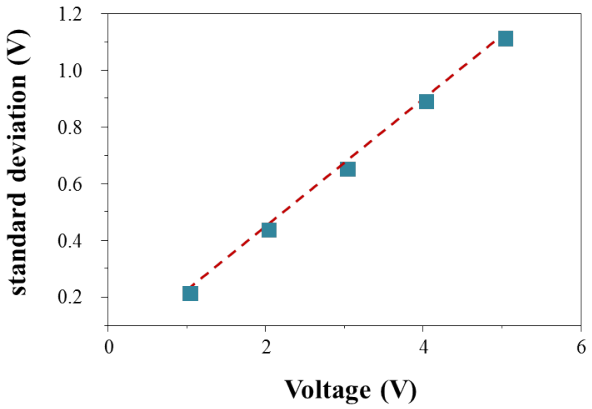


Figure D.2: Variation of the standard deviation of the acquired signal with the peak to peak amplitude.

To obtain a relation between the standard deviation and the peak to peak to amplitude we calculate this value for different values of the noise amplitude. The resulting plot is shown in Figure D.2, from there we are able to find a relationship: $S.D = 0.225V_{pp}$. Knowing the specified conversion (in the signal generator manual) between the external electrical signal and the output phase to be 36°/V, we can finally write the conversion between the standard deviation of the phase noise $\eta_\phi$ and the input voltage as: $\eta_\phi = 8.1V_{pp}$.

The amplitude noise however is represented in Watts, the relation between power and voltage is written as: $P = V^2/R$. Knowing the termination resistance to be 50Ω, the amplitude noise is quantified as $\eta_R = (0.225V_{pp})^2/50$.

# Appendix E

# Résumé en Français

Cette thèse est basée sur l'observation des dynamiques non linéaires d'un système mécanique commandé de l'extérieur par les électrodes. Le plan du travail est tout d'abord concevoir le système, puis le fabriquer et finalement valider par des expériences sur le système développé. Le système développé pendant cette thèse est une membrane de cristal photonique suspendu par quatre ponts au-dessus des électrodes interdigitales. Le système est représenté dans la Figure E.1.

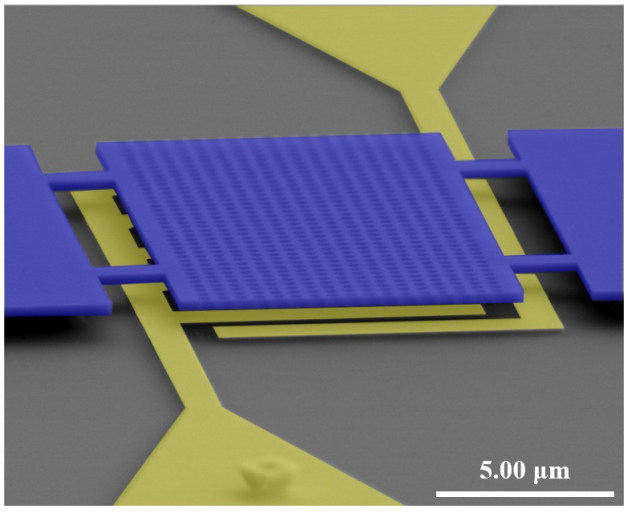


Figure E.1: Faux couleur SEM du système. En bleu, il est la membrane cristaux photonique suspendu sur électrodes intégrée. La lumière est incidente verticalement sur la membrane. Mode mécaniques sont détectes par interférométrie optique.

La conception du système a été suivie d'une étude des simulations numérique sur un système identique. La membrane de cristal photonique est un structure rectangle des dimensions $10 \times 20\mu m^2$ avec des trous cylindriques fabriqué sur elle. Cela rend la structure opaque à la lumière incidente. D'autre côté, la structure est suspendue par quatre ponts de dimensions $1 \times 2\mu m^2$ qui génère des modes mécaniques dans le régime MHz. La membrane de

cristal photonique est suspendue à 400 nm au-dessus des électrodes interdigitales. L'efficacité d'excitation des modes mécanique est contrôlée par cette séparation. Un détecteur homodyne équilibré optiquement a été utilisé pour mesurer ces modes mécaniques. Dans la section suivante, nous décrirons en bref sur l'actionnement en régime linéaire et en suite nous allons décrire brièvement l'étude de la dynamique non linéaire sur le même système.

## E.1 Actionnement dans le régime linéaire

L'actionnement en régime linéaire a été fait en gardant la tension d'actionnement en dessous d'un certain seuil tout en balayant la fréquence d'actionnement $\Omega_{drive}$. Avec cette configuration plusieurs modes mécaniques ont été identifiés. Toutes ces mesures ont été effectuées à la température ambiante et sous vide. Les spectres pour les modes mécaniques mesuré expérimentalement ont représenté sur la Figure E.2 avec les profiles des modes mécaniques correspondants. Ces profiles ont été calculé par une simulation MEF (COMSOL). Toutes les expériences réalisées à partir de ce point a été porté sur le premier mode mécanique autour de $2.75MHz$. Désormais, nous pouvons augmenter la tension d'actionnement pour mettre le système dans le régime non linéaire.

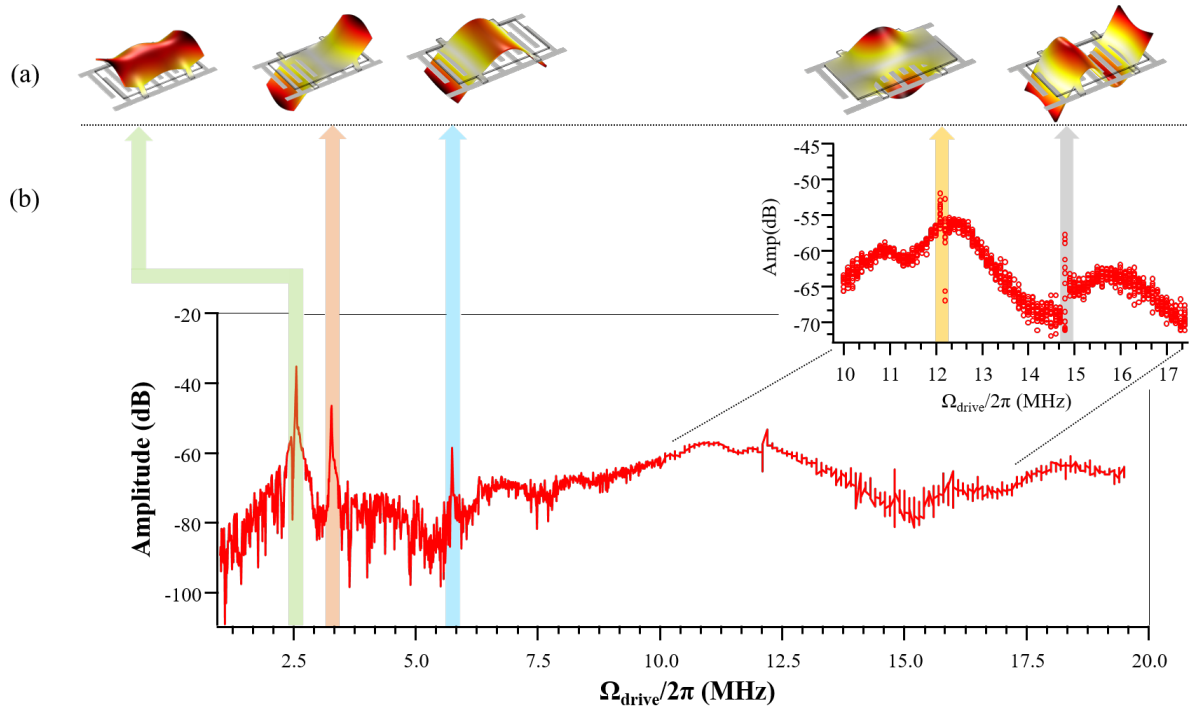


Figure E.2: (a) Simulation MEF de mode mécanique (b) mode mécanique observées avec balayage de fréquence, la tension d'actionnement est maintenu constante.

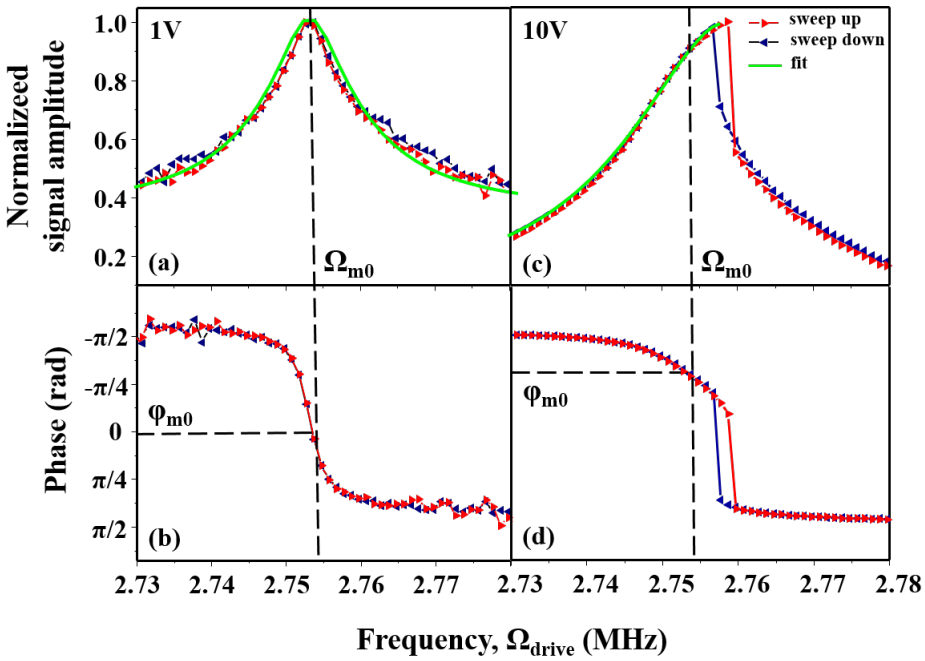


Figure E.3: (a) & (b) Réponse du système en amplitude et phase dans le régime linéaire, (c) & (d) Réponse du système en amplitude et phase dans le régime non-linéaire. La réponse pressentant une hystérésis avec balayage 'up' et 'down'.

## E.2 Actionnement dans le régime non linéaire

Il est possible de mettre le même système dans le régime non linéaire en utilisant la tension d'actionnement au-delà d'un certain seuil. Cette situation apparait dans la Figure E.3. Lorsque la tension d'actionnement est maintenu petit à $\sim$ 1V la réponse est linéaire en amplitude et également en phase. Cependant, comme la tension d'actionnement est augmentée à $\sim$ 10V nous avons observé une bistabilité en amplitude et en phase. Ceci est une indication claire de la non-linéarité induite dans le système. Avec le système en régime non linéaire, plusieurs expériences intéressantes ont été réalisées comme le résonance harmonique (sub/super), excitation paramétrique et résonance stochastique. Dans les sections suivantes, nous allons décrire brièvement les résultats expérimentaux concernant la dynamique non linéaire.

### E.2.1 Résonance super-harmonique

Résonances (sub/super) harmoniques peuvent être utilisés pour génère une réponse résonnante, même en conduisant le système loin de la résonance, grâce à la non-linéarité dans le système. Réalisation de résonance super-harmonique peut être effectuée en excitant le système dans le sous-harmonique de la fréquence propre, tout en générant la réponse de résonance. La réponse est généré seulement après un certain seuil de la tension d'actionnement

et au-delà de ce seuil, la fréquence de la réponse se règle a la fréquence d'entrainement par l'excitation extérieure. Cet ajustement se traduit par une réponse qui ressemble une 'tongue', connue par la 'tongue' de Mathieu. De telles réponses sont observées pour notre système pour une non-linéarité jusqu'à 8eme ordre.

Cependant, au-delà le 8eme ordre, il devient difficile d'observer cette réponse en raison de la moindre contribution des composants non linéaires d'ordre supérieur. Nous avons également été en mesure de voir la rotation de la phase de la réponse par rapport à la fréquence d'entrainement lorsque'il est balayé sur la 'tongue' de l'instabilité.

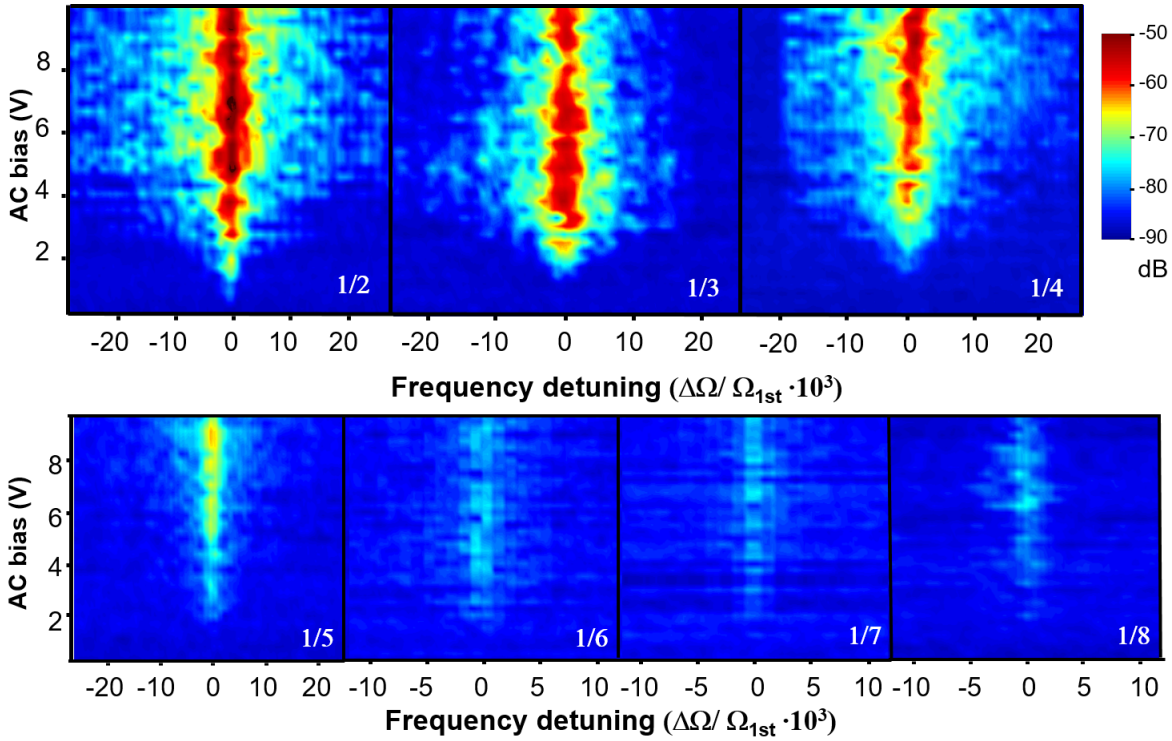


Figure E.4: Super-harmonique réponse généré jusqu'à huitième ordre, il y a réponses comme 'tongue' est observes avec tension d'actionnement.

### E.2.2 Résonance stochastique

Résonance stochastique fait référence de l'amplification d'un signal périodique faible par l'introduction de bruit dans un système non linéaire. La première démonstration d'une telle résonance a été faite pour prédire l'occurrence des âges de glace. Depuis lors, ces résonances ont été démontrées dans de nombreux systèmes, y compris optique, électrique et mécanique. En raison de l'avance en nano fabrication, il y a eu récemment une certaine démonstration de résonance stochastique dans les systèmes nano mécaniques. Cependant, la plupart de ces manifestations a porté principalement sur la résonance stochastique de l'amplitude. Au cours de ma thèse, nous avons été en mesure d'effectuer la résonance stochastique de la phase. Les mesures expérimentales sont montrées sur la Figure E.5.

Stochastique résonance avec une modulation de phase et bruit de phase avec un gain de 1.75 a été montrée avec notre système. Avec la résonance de l'amplitude on a obtenu un gain de 4.5. La raison a été attribuée simplement à la façon dont le système évolue dans l'espace de phase sous l'influence de la phase ou l'amplitude du bruit. Et aussi une nouvelle technique a été proposée dans laquelle une très faible modulation d'amplitude peut avoir été ajouté à la résonance stochastique de phase, afin d'augmenter le gain en phase de résonance stochastique.

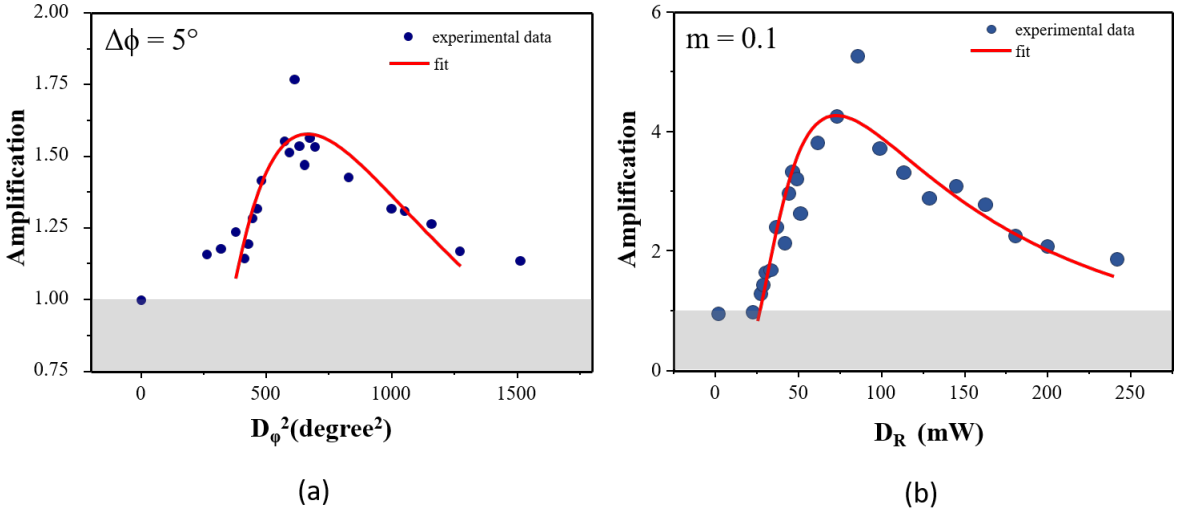


Figure E.5: (a) Résonance stochastique avec bruit de phase (b) résonance stochastique avec bruit de amplitude.

## E.3 Conclusion

En conclusion, au cours de la thèse plusieurs expériences en ce qui concerne la dynamique non linéaire ont été réalisées sur le système. Les expérience sur la dynamique non linéaire impliquées la résonance (sub/super) harmonique, amplification paramétrique et la résonance stochastique (avec une amplitude ainsi que la phase). Aussi une compréhension profonde de cette plate-forme électromécanique a été faite au cours de cette thèse. L'étape suivante consiste à inclure des fonctionnalités optiques du système pour réaliser ce qui est une plate-forme complet d'opto-électro-mécanique. Ceci implique l'intégration des guides d'ondes, des électrodes et résonateur mécanique sur la même puce. Première réalisation d'un tel système est représenté sur la Figure E.6. Avec un tel système, il est possible de mettre plusieurs oscillateurs sur la même puce et les coupler via un bruit optique commun. Cela pourrait conduire à des expériences sur la synchronisation.

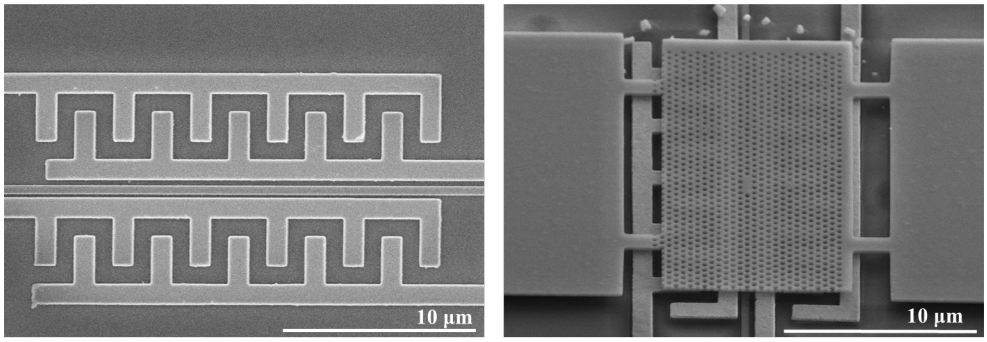


(a) (b)

Figure E.6: (a) Électrodes 'integerdigitated' avec guide d'ondes sur la mémé puce (b) la système avec la membrane cristaux photonique suspendu sur électrodes intégrée et guide d'ondes. La membrane contient une cavité L3.

# Bibliography


[1] Navid Yazdi, Farrokh Ayazi, and Khalil Najafi. Micromachined inertial sensors. *Proceedings of the IEEE*, 86(8):1640–1658, 1998.

[2] T. Tajima, T. Nishiguchi, S. Chiba, A. Morita, M. Abe, K. Tanioka, N. Saito, and M. Esashi. High-performance ultra-small single crystalline silicon microphone of an integrated structure. *Microelectronic Engineering*, 67-68:508–519, 2003.

[3] J H Smith W P Elaton. Micromachined pressure sensors : review and recent developments. *Smart Materials and Structures*, 6:530–539, 1997.

[4] M S Hanay, S Kelber, a K Naik, D Chi, S Hentz, E C Bullard, E Colinet, L Duraffourg, and M L Roukes. Single-protein nanomechanical mass spectrometry in real time. *Nature nanotechnology*, 7(9):602–8, 2012.

[5] K a Cook-Chennault, N Thambi, and a M Sastry. Powering MEMS portable devices, a review of non-regenerative and regenerative power supply systems with special emphasis on piezoelectric energy harvesting systems. *Smart Materials and Structures*, 17(4):043001, 2008.

[6] Dhiman Mallick, Andreas Amann, and Saibal Roy. Interplay between electrical and mechanical domains in a high performance nonlinear energy harvester. *Smart Materials and Structures*, 24(12):122001, 2015.

[7] Andreas Manz, H Michael Widmers, and N Graber. Miniaturized total chemical analysis systems: A novel concept for chemical sensing. *Sensors and Actuators B: Chemical*, 1(1-6):244–248, 1990.

[8] S. S. Narine. Use of the quartz crystal microbalance to measure the mass of submonolayer deposits: Measuring the stoichiometry of surface oxides. *Journal of Vacuum Science & Technology A: Vacuum, Surfaces, and Films*, 16(3):1857, 1998.

[9] T. Thundat, E. a. Wachter, S. L. Sharp, and R. J. Warmack. Detection of mercury vapor using resonating microcantilevers. *Applied Physics Letters*, 66(13):1695, 1995.

[10] B. Ilic, D. Czaplewski, H. G. Craighead, P. Neuzil, C. Campagnolo, and C. Batt. Mechanical resonant immunospecific biological detector. *Applied Physics Letters*, 77(3):450–452, 2000.

[11] Takahito Ono, Xinxin Li, Hidetoshi Miyashita, and Masayoshi Esashi. Mass sensing of adsorbed molecules in sub-picogram sample with ultrathin silicon resonator. *Review of Scientific Instruments*, 74(3 I):1240–1243, 2003.

[12] Nickolay V. Lavrik and Panos G. Datskos. Femtogram mass detection using photothermally actuated nanomechanical resonators. *Applied Physics Letters*, 82(16):2697–2699, 2003.

[13] a. N Cleland and M L Roukes. A nanometre-scale mechanical electrometer. *Nature*, 392(6672):160–162, 1998.

[14] K. L. Ekinci, X. M H Huang, and M. L. Roukes. Ultrasensitive nanoelectromechanical mass detection. *Applied Physics Letters*, 84(22):4469–4471, 2004.

[15] Quirin P Unterreithmeier, Eva M Weig, and Jörg P Kotthaus. Universal transduction scheme for nanomechanical systems based on dielectric forces. *Nature*, 458(April):1001–4, 2009.

[16] T. Bagci, a Simonsen, S Schmid, L G Villanueva, E Zeuthen, J. Appel, J M Taylor, a Sørensen, K Usami, a Schliesser, and E. S. Polzik. Optical detection of radio waves through a nanomechanical transducer. *Nature*, 507(7490):81–5, 2014.

[17] Silvan Schmid, Tolga Bagci, Emil Zeuthen, Jacob M. Taylor, Patrick K. Herring, Maja C. Cassidy, Charles M. Marcus, Luis Guillermo Villanueva, Bartolo Amato, Anja Boisen, Yong Cheol Shin, Jing Kong, Anders S. S??rensen, Koji Usami, and Eugene S. Polzik. Single-layer graphene on silicon nitride micromembrane resonators. *Journal of Applied Physics*, 115(5), 2014.

[18] Y. T. Yang, K. L. Ekinci, X. M H Huang, L. M. Schiavone, M. L. Roukes, C. A. Zorman, and M. Mehregany. Monocrystalline silicon carbide nanoelectromechanical systems. *Applied Physics Letters*, 78(2):162–164, 2001.

[19] Xue Ming, Henry Huang, Christian A Zorman, and Michael L Roukes. Nanodevice motion at microwave frequencies. 421(January):496–497, 2003.

[20] Clark T C Nguyen, Linda P B Katehi, and Gabriel M Rebeiz. Micromachined devices for wireless communications. *Proceedings of the IEEE*, 86(8):1756–1767, 1998.

[21] K J Bruland, J L Garbini, W M Dougherty, and J A Sidles. Optimal control of force microscope cantilevers. I. Controller design. *Journal of Applied Physics*, 80(1996):1951–1958, 1996.

[22] K J Bruland, J L Garbini, W M Dougherty, and Sidles. Optimal control of ultrasoft cantilevers for force microscopy. *Journal Of Applied Physics*, 83(8):3972–3977, 1998.

[23] a. N. Cleland and M. L. Roukes. Fabrication of high frequency nanometer scale mechanical resonators from bulk Si crystals. *Applied Physics Letters*, 69(18):2653–2655, 1996.

[24] Rob Legtenberg and Harrie A C Tilmans. Electrostatically driven vacuum-encapsulated polysilicon resonators Part I. Design and fabrication. *Sensors and Actuators: A. Physical*, 45(1):57–66, 1994.

[25] Michael J. Burek, Daniel Ramos, Parth Patel, Ian W. Frank, and Marko Lon??ar. Nanomechanical resonant structures in single-crystal diamond. *Applied Physics Letters*, 103(13):21–24, 2013.

[26] Krishna C. Balram, Marcelo Davanco, Jin Dong Song, and Kartik Srinivasan. Coherent coupling between radio frequency, optical, and acoustic waves in piezo-optomechanical circuits. pages 1–20, 2015.

[27] D. S. Greywall, B. Yurke, P. A. Busch, A. N. Pargellis, and R. L. Willett. Evading amplifier noise in nonlinear oscillators. *Physical Review Letters*, 72(19):2992–2995, 1994.

[28] R. G. Beck, M. A. Eriksson, M. A. Topinka, R. M. Westervelt, K. D. Maranowski, and A. C. Gossard. GaAs/AlGaAs self-sensing cantilevers for low temperature scanning probe microscopy. *Applied Physics Letters*, 73(8):1149–1151, 1998.

[29] R. Knobel and A. N. Cleland. Piezoelectric displacement sensing with a single-electron transistor. *Applied Physics Letters*, 81(12):2258–2260, 2002.

[30] Markus Aspelmeyer, Tobias J. Kippenberg, and Florian Marquardt. Cavity optomechanics. *Reviews of Modern Physics*, 86(4):1391–1452, 2014.

[31] I Yeo, P-L de Assis, a Gloppe, E Dupont-Ferrier, P Verlot, N S Malik, E Dupuy, J Claudon, J-M Gérard, a Auffèves, G Nogues, S Seidelin, J-ph Poizat, O Arcizet, and M Richard. Strain-mediated coupling in a quantum dot-mechanical oscillator hybrid system. *Nature Nanotechnology*, 9(2):106–10, 2014.

[32] Matt Eichenfield, Ryan Camacho, Jasper Chan, Kerry J Vahala, and Oskar Painter. LETTERS optomechanical cavity. *Nature*, 459(7246):550–555, 2009.

[33] Justin D Cohen, Seán M Meenehan, and Oskar Painter. Optical coupling to nanoscale optomechanical cavities for near quantum-limited motion transduction. *Optics Express*, 21(9):11227–11236, 2013.

[34] G. Anetsberger, P. Verlot, E. Gavartin, O. Arcizet, Q. P. Unterreithmeier, E. M. Weig, M. L. Gorodetsky, J. P. Kotthaus, and T. J. Kippenberg. Measuring nanomechanical motion with an imprecision below that at the standard quantum limit. *2011 Conference on Lasers and Electro-Optics Europe and 12th European Quantum Electronics Conference, CLEO EUROPE/EQEC 2011*, 061804:1–4, 2011.

[35] Jasper Chan, T. P. Mayer Alegre, Amir H. Safavi-Naeini, Jeff T. Hill, Alex Krause, Simon Groeblacher, Markus Aspelmeyer, and Oskar Painter. Laser cooling of a nanomechanical oscillator into its quantum ground state. *Nature*, 478:18, 2011.

[36] Joerg Bochmann, Amit Vainsencher, David D. Awschalom, and Andrew N. Cleland. Nanomechanical coupling between microwave and optical photons. *Nature Physics*, 9(11):712–716, sep 2013.

[37] Krishna C. Balram, Marcelo Davanco, Jin Dong Song, and Kartik Srinivasan. Coherent coupling between radio frequency, optical, and acoustic waves in piezo-optomechanical circuits. *Nature Photonics*, 10(5):1–20, 2015.

[38] I Mahboob and H Yamaguchi. Bit storage and bit flip operations in an electromechanical oscillator. *Nature nanotechnology*, 6:275–279, 2008.

[39] I Mahboob, M Mounaix, K Nishiguchi, a Fujiwara, and H Yamaguchi. A multimode electromechanical parametric resonator array. *Scientific reports*, 4:4448, 2014.

[40] Quirin P Unterreithmeier, Eva M Weig, and Jörg P Kotthaus. Universal transduction scheme for nanomechanical systems based on dielectric forces. *Nature*, 458(April):1001–4, 2009.

[41] Leonardo Midolo and Andrea Fiore. Design and Optical Properties of Electromechanical Double-Membrane Photonic Crystal Cavities. *Quantum Electronics, IEEE Journal of*, 50(6):404–414, 2014.

[42] Grutter Karen and Srinivasan K Avanco Marcelo. Slot-mode optomechanical crystals : a versatile platform for multimode optomechanics. 2(11), 2015.

[43] J. Gomis-Bresco, D. Navarro-Urrios, M. Oudich, S. El-Jallal, a. Griol, D. Puerto, E. Chavez, Y. Pennec, B. Djafari-Rouhani, F. Alzina, a. Martínez, and C. M. Sotomayor Torres. A 1D Optomechanical crystal with a complete phononic band gap. *arXiv*, page 1401.1691, 2014.

[44] E. Gavartin, R. Braive, I. Sagnes, O. Arcizet, a. Beveratos, T. J. Kippenberg, and I. Robert-Philip. Optomechanical Coupling in a Two-Dimensional Photonic Crystal Defect Cavity. *Physical Review Letters*, 106(20):203902, may 2011.

[45] A H Safavi-Naeini and O Painter. Design of optomechanical cavities and waveguides on a simultaneous bandgap phononic-photonic crystal slab. *Opt Express*, 18(14):14926–14943, 2010.

[46] Jasper Chan, Matt Eichenfield, Ryan Camacho, and Oskar Painter. Optical and mechanical design of a zipper photonic crystal optomechanical cavity. 17(5):555–560, 2009.

[47] Kevin Makles, T Antoni, A G Kuhn, Samuel Deléglise, T. Briant, P.-F. Cohadon, R Braive, G Beaudoin, L Pinard, C Michel, V Dolique, R Flaminio, G Cagnoli, I Robert-Philip, and A. Heidmann. 2D photonic-crystal optomechanical nanoresonator. *Opt. Lett.*, 40(2):174–177, 2015.

[48] Corey Stambaugh, Haitan Xu, Utku Kemiktarak, Jacob Taylor, and John Lawall. From membrane-in-the-middle to mirror-in-the-middle with a high-reflectivity subwavelength grating. *Annalen der Physik*, 527(1-2):81–88, 2015.

[49] A Kraus and R H Blick. Mechanical mixing in nonlinear nanomechanical resonators. *Applied Physics Letters*, 77(19):3102–3104, 2000.

[50] Dominik V. Scheible, Artur Erbe, Robert H. Blick, and Gilberto Corso. Evidence of a nanomechanical resonator being driven into chaotic response via the Ruelle-Takens route. *Applied Physics Letters*, 81(10):1884–1886, 2002.

[51] R H Blick, a Erbe, L Pescini, a Kraus, D V Scheible, F W Beil, E Hoehberger, a Hoerner, J Kirschbaum, H Lorenz, and J P Kotthaus. Nanostructured silicon for studying fundamental aspects of nanomechanics. *Journal of Physics: Condensed Matter*, 14(34):R905–R945, 2002.

[52] K. L. Ekinci and M. L. Roukes. Nanoelectromechanical systems. *Review of Scientific Instruments*, 76(6):061101, 2005.

[53] I. Kozinsky, H. W Ch Postma, I. Bargatin, and M. L. Roukes. Tuning nonlinearity, dynamic range, and frequency of nanomechanical resonators. *Applied Physics Letters*, 88(25):1–4, 2006.

[54] R. B. Karabalin, S. C. Masmanidis, and M. L. Roukes. Efficient parametric amplification in high and very high frequency piezoelectric nanoelectromechanical systems. *Applied Physics Letters*, 97(18):14–17, 2010.

[55] Matthew H. Matheny, Matt Grau, Luis G. Villanueva, Rassul B. Karabalin, M. C. Cross, and Michael L. Roukes. Phase synchronization of two anharmonic nanomechanical oscillators. *Physical Review Letters*, 112(January):1–5, 2014.

[56] Georg Heinrich, Max Ludwig, Jiang Qian, Björn Kubala, and Florian Marquardt. Collective dynamics in optomechanical arrays. *Physical Review Letters*, 107(4):8–11, 2011.

[57] Robert L. Badzey and Pritiraj Mohanty. Coherent signal amplification in a nanomechanical oscillator via stochastic resonance. *Nature*, 850(October):1675–1676, 2006.

[58] Shyamolina Ghosh and Deb Shankar Ray. Nonlinear vibrational resonance. *Physical Review E*, 88(4):042904, 2013.

[59] R. S. Zounes and H. R. Rand. Subharmonic resonance in the non-linear Mathieu equation. *International Journal of Non-Linear Mechanics*, 37(1):43–73, 2002.

[60] Seung-Bo Shim, Matthias Imboden, and Pritiraj Mohanty. Synchronized oscillation in coupled nanomechanical oscillators. *Science (New York, N.Y.)*, 316(5821):95–9, apr 2007.

[61] Luca Gammaitoni, Peter Hänggi, Peter Jung, and Fabio Marchesoni. Stochastic resonance. *Review of Modern Physics*, 70(1):223–287, 1998.

[62] Sylvain Barbay, Giovanni Giacomelli, and Francesco Marin. Stochastic resonance in vertical cavity surface emitting lasers. *Physical Review E*, 61(1):157–166, 2000.

[63] F. Mueller, S. Heugel, and L. J. Wang. Optomechanical stochastic resonance in a macroscopic torsion oscillator. *Physical Review A - Atomic, Molecular, and Optical Physics*, 79(3):3–6, 2009.

[64] D. Rugar and P. Gr??tter. Mechanical parametric amplification and thermomechanical noise squeezing. *Physical Review Letters*, 67(6):699–702, 1991.

[65] T Faust, P Krenn, S Manus, J P Kotthaus, and E M Weig. Microwave cavity-enhanced transduction for plug and play nanomechanics at room temperature. *Nature communications*, 3:728, 2012.

[66] Sotiris C Masmanidis, Rassul B Karabalin, Iwijn De Vlaminck, Gustaaf Borghs, Mark R Freeman, and Michael L Roukes. Multifunctional nanomechanical systems via tunably coupled piezoelectric actuation. *Science (New York, N.Y.)*, 317(5839):780–3, aug 2007.

[67] M. Tortonese, R. C. Barrett, and C. F. Quate. Atomic resolution with an atomic force microscope using piezoresistive detection. *Applied Physics Letters*, 62(8):834–836, 1993.

[68] RE Mihailovich and JM Parpia. Low temperature mechanical properties of boron-doped silicon. *Physical review letters*, 68(20):3052–3055, 1992.

[69] William C. Tang, Tu Cuong H Nguyen, Michael W. Judy, and Roger T. Howe. Electrostatic-comb drive of lateral polysilicon resonators. *Sensors and Actuators: A. Physical*, 21(1-3):328–331, 1990.

[70] Qing Zhu, Wan Y. Shih, and Wei Heng Shih. Enhanced detection resonance frequency shift of a piezoelectric microcantilever sensor by a DC bias electric field in humidity detection. *Sensors and Actuators, B: Chemical*, 138(1):1–4, 2009.

[71] Quirin P. Unterreithmeier, Stephan Manus, and Jörg P. Kotthaus. Coherent detection of nonlinear nanomechanical motion using a stroboscopic downconversion technique. *Applied Physics Letters*, 94(26):3–5, 2009.

[72] H P Yuen and V W Chan. Noise in homodyne and heterodyne detection: errata. *Optics letters*, 8(6):345, jun 1983.

[73] G L Abbas, V W Chan, and T K Yee. Local-oscillator excess-noise suppression for homodyne and heterodyne detection. *Optics letters*, 8(8):419–421, 1983.

[74] Yuameng Chi. High speed homodyne detector for gaussian-modulated coherent-state quantum key distribution. page 96, 2009.

[75] Thomas Antoni, Aurélien G Kuhn, Tristan Briant, Pierre-François Cohadon, Antoine Heidmann, Rémy Braive, Alexios Beveratos, Izo Abram, Luc Le Gratiet, Isabelle Sagnes, and Isabelle Robert-Philip. Deformable two-dimensional photonic crystal slab for cavity optomechanics. *Optics letters*, 36(17):3434–3436, 2011.

[76] Viktor Tsvirkun, Isabelle Robert-philip, Université Pierre, and Curie Cnrs. Optomechanics in hybrid fully-integrated two-dimensional photonic crystal resonators Viktor Tsvirkun Viktor Tsvirkun Optomechanics in hybrid fully-integrated two-dimensional photonic crystal resonators. 2015.

[77] Thomas Antoni, Kevin Makles, Remy Braive, Tristan Briant, Pierre-Francois Cohadon, Isabelle Sagnes, Isabelle Robert-Philip, and Antoine Heidmann. Nonlinear mechanics with suspended nanomembranes. *EPL (Europhysics Letters)*, 100(6):68005, 2012.

[78] a Eichler, J Moser, J Chaste, M Zdrojek, I Wilson-Rae, and a Bachtold. Nonlinear damping in mechanical resonators made from carbon nanotubes and graphene. *Nature nanotechnology*, 6(6):339–42, jun 2011.

[79] R G Knobel and A N Cleland. Nanometre-scale displacement sensing using a single electron transistor. *Nature*, 424(6946):291–293, 2003.

[80] I. Bargatin, I. Kozinsky, and M. L. Roukes. Efficient electrothermal actuation of multiple modes of high-frequency nanoelectromechanical resonators. *Applied Physics Letters*, 90(9):56–59, 2007.

[81] H. X. Tang, X. M H Huang, M. L. Roukes, M. Bichler, and W. Wegscheider. Two-dimensional electron-gas actuation and transduction for GaAs nanoelectromechanical systems. *Applied Physics Letters*, 81(20):3879–3881, 2002.

[82] Tin Komljenovic, Michael Davenport, Jared Hulme, Alan Liu, Christos Santis, Alexander Spott, Sudharsanan Srinivasan, Eric Stanton, Chong Zhang, and John Bowers. Heterogeneous Silicon Photonic Integrated Circuits. *Journal of Lightwave Technology*, 34(1):1–1, 2015.

[83] H. Namatsu, T. Yamaguchi, M. Nagase, K. Yamazaki, and K. Kurihara. Nanopatterning of a hydrogen silsesquioxane resist with reduced linewidth fluctuations. *Microelectronic Engineering*, 41-42:331–334, 1998.

[84] Maik Wiemer, Chenping Jia, Michael Toepper, and Karin Hauck. Wafer bonding with BCB and SU-8 for MEMS packaging. *ESTC 2006 - 1st Electronics Systemintegration Technology Conference*, 2:1401–1405, 2007.

[85] RF Wolffenbuttel. Low-temperature intermediate Au-Si wafer bonding; eutectic or silicide bond. *Sensors and Actuators A: Physical*, 62(1-3):680–686, 1997.

[86] F. Niklaus, H. Andersson, P. Enoksson, and G. Stemme. Low temperature full wafer adhesive bonding of structured wafers. *Sensors and Actuators, A: Physical*, 92(1-3):235–241, 2001.

[87] Alexandre Bazin. III-V Semiconductor Nanocavitieson Silicon-On-Insulator Waveguide : Laser Emission, Switching and Optical Memory. 2013.

[88] D. L. Olynick, B. Cord, a. Schipotinin, D. F. Ogletree, and P. J. Schuck. Electron-beam exposure mechanisms in hydrogen silsesquioxane investigated by vibrational spectroscopy and in situ electron-beam-induced desorption. *Journal of Vacuum Science & Technology B: Microelectronics and Nanometer Structures*, 28(3):581, 2010.

[89] Ruwin Pandithage. Brief Introduction to Critical Point Drying. pages 2–5, 2012.

[90] Roukes. Plenty of room indeed. *Scientific American Reports*, 1:4–11, 2007.

[91] William Mclellan. Features : February 2001 Nanoelectromechanical systems face the future Features : February 2001 Feynman ' s challenge. *World Magazine*, 14(2), 2001.

[92] H G Craighead. Nanoelectromechanical systems. *Science (New York, N.Y.)*, 290(5496):1532–6, 2000.

[93] Andrew Cleland. Foundation of nanomechanics.

[94] Strogatz. nonlinear dynamics and chaos_strogatz.pdf.

[95] Amro M. Elshurafa, Kareem Khirallah, Hani H. Tawfik, Ahmed Emira, A. K S Abdel Aziz, and Sherif M. Sedky. Nonlinear dynamics of spring softening and hardening in folded-mems comb drive resonators. *Journal of Microelectromechanical Systems*, 20(4):943–958, 2011.

[96] Hanna Cho, Bongwon Jeong, Min-Feng Yu, Alexander F. Vakakis, D. Michael McFarland, and Lawrence a. Bergman. Nonlinear hardening and softening resonances in micromechanical cantilever-nanotube systems originated from nanoscale geometric nonlinearities. *International Journal of Solids and Structures*, 49(15-16):2059–2065, aug 2012.

[97] Changyao Chen and James Hone. Graphene nanoelectromechanical systems. *Proceedings of the IEEE*, 101(7):1766–1779, 2013.

[98] Fen Guan, Piranavan Kumaravadivel, Dmitri V. Averin, and Xu Du. Tuning strain in flexible graphene nanoelectromechanical resonators. *Applied Physics Letters*, 107(19):193102, 2015.

[99] Wayne Y. Fung, Eric N. Dattoli, and Wei Lu. Radio frequency nanowire resonators and in situ frequency tuning. *Applied Physics Letters*, 94(20):14–17, 2009.

[100] Mohammad Ibrahim Younis. A Study of the Nonlinear Response of a Resonant Microbeam to an Electric Actuation. *Nonlinear Dynamics · December 2002*, pages 91–117, 2002.

[101] J. V. Mallow and R. J. Lucas. Multiple resonances in the double-flash effect. *Journal of the Optical Society of America A*, 9(12):2105, dec 1992.

[102] Andrea Prosperetti. Subharmonics and ultraharmonics in the forced oscillations of weakly nonlinear systems. *American Journal of Physics*, 44:548, 1976.

[103] H. B. Chan and C. Stambaugh. Activation barrier scaling and crossover for noise-induced switching in micromechanical parametric oscillators. *Physical Review Letters*, 99(6):3–6, 2007.

[104] Daniel Midtvedt, Yury Tarakanov, and Jari Kinaret. Parametric resonance in nano-electromechanical single electron transistors. *Nano Letters*, 11(4):1439–1442, 2011.

[105] E. Collin, T. Moutonet, J. S. Heron, O. Bourgeois, Yu M. Bunkov, and H. Godfrin. Nonlinear parametric amplification in a triport nanoelectromechanical device. *Physical Review B - Condensed Matter and Materials Physics*, 84(5):1–16, 2011.

[106] W.H. Louisell. Coupled mode and parametric electronics. 2011.

[107] Roberto Benzit$, Alfonso Sutera, and Angelo Vulpiani. The mechanism of stochastic resonance. *J. Phys. A: Math. Gen*, 14:453–457, 1981.

[108] H A Kramers. Brownian motion in a field of force and the diffusion model of chemical reactions. *Physica (Utrecht)*, 7(4):284–304, 1940.

[109] L. J. Lapidus, D. Enzer, and G. Gabrielse. Stochastic Phase Switching of a Parametrically Driven Electron in a Penning Trap. *Physical Review Letters*, 83(5):899, 1999.

[110] A. D. Hibbs, A. L. Singsaas, E. W. Jacobs, A. R. Bulsara, J. J. Bekkedahl, and F. Moss. Stochastic resonance in a superconducting loop with a Josephson junction. *Journal of Applied Physics*, 77(6):2582–2590, 1995.

[111] David Wilkowski, Jean Ringot, Daniel Hennequin, and Jean Garreau. Instabilities in a Magneto-optical Trap: Noise-Induced Dynamics in an Atomic System. *Physical Review Letters*, 85(9):1839–1842, 2000.

[112] J. S. Aldridge and A. N. Cleland. Noise-enabled precision measurements of a duffing nanomechanical resonator. *Physical Review Letters*, 94(15):5–8, 2005.

[113] Ronen Almog, Stav Zaitsev, Oleg Shtempluck, and Eyal Buks. Signal amplification in a nanomechanical Duffing resonator via stochastic resonance. *Applied Physics Letters*, 90(1):12–15, 2007.

[114] Quirin P. Unterreithmeier, Thomas Faust, and Jörg P. Kotthaus. Nonlinear switching dynamics in a nanomechanical resonator. *Physical Review B - Condensed Matter and Materials Physics*, 81(24):1–4, 2010.

[115] Warner J Venstra, Hidde J R Westra, and Herre S J van der Zant. Stochastic switching of cantilever motion. *Nature communications*, 4:2624, jan 2013.

[116] H. B. Chan and C. Stambaugh. Fluctuation-enhanced frequency mixing in a nonlinear micromechanical oscillator. *Physical Review B - Condensed Matter and Materials Physics*, 73(22):1–4, 2006.

[117] Farkas. Mid-Term Review Meeting ITN Cavity Quantum Optomechanics. *Z Phys. Chem*, 125:236, 1927.

[118] Peter Jung. PERIODICALLY D R I V E N STOCHASTIC Periodically driven stochastic systems.

[119] Diego N. Guerra, Matthias Imboden, and Pritiraj Mohanty. Electrostatically actuated silicon-based nanomechanical switch at room temperature. *Applied Physics Letters*, 93(3):2006–2009, 2008.

[120] Y. Jia and J. R. Li. Steady-state analysis of a bistable system with additive and multiplicative noises. *Physical Review E*, 53(6):5786–5792, 1996.

[121] Hideo Hasegawa. Stochastic resonance in bistable systems with nonlinear dissipation and multiplicative noise: A microscopic approach. *Physica A: Statistical Mechanics and its Applications*, 392(10):2532–2546, 2013.

[122] C. Stambaugh and H. B. Chan. Noise-activated switching in a driven nonlinear micromechanical oscillator. *Physical Review B - Condensed Matter and Materials Physics*, 73(17):1–4, 2006.

[123] Vi. Tsvirkun, A. Surrente, F. Raineri, G. Beaudoin, R. Raj, I. Sagnes, I. Robert-Philip, and R. Braive. Integrated III-V Photonic Crystal Si waveguide platform with tailored optomechanical coupling. *Scientific Reports*, 5:16526, 2015.

[124] Mahmood Bagheri, Menno Poot, Linran Fan, Florian Marquardt, and Hong X. Tang. Photonic cavity synchronization of nanomechanical oscillators. *Physical Review Letters*, 111(November):1–5, 2013.

[125] Deepak K. Agrawal, Jim Woodhouse, and Ashwin a. Seshia. Observation of locked phase dynamics and enhanced frequency stability in synchronized micromechanical oscillators. *Physical Review Letters*, 111(8):1–5, 2013.

[126] Mian Zhang, Gustavo S. Wiederhecker, Sasikanth Manipatruni, Arthur Barnard, Paul McEuen, and Michal Lipson. Synchronization of micromechanical oscillators using light. *Physical Review Letters*, 109(23):1–5, 2012.

[127] Mian Zhang, Shreyas Shah, Jaime Cardenas, and Michal Lipson. Synchronization and Phase Noise Reduction in Micromechanical Oscillators Arrays Coupled through Light. pages 1–9, 2015.

[128] C. Jeevarathinam, S. Rajasekar, and M. A F Sanjuán. Theory and numerics of vibrational resonance in Duffing oscillators with time-delayed feedback. *Physical Review E - Statistical, Nonlinear, and Soft Matter Physics*, 83(6):1–12, 2011.

[129] A. Kenfack and Kamal P. Singh. Stochastic resonance in coupled underdamped bistable systems. *Physical Review E - Statistical, Nonlinear, and Soft Matter Physics*, 82(4):1–5, 2010.

[130] Faraz Monifi, Jing Zhang, Sahin Kaya Ozdemir, Bo Peng, Yu-xi Liu, Fang Bo, Franco Nori, and Lan Yang. Optomechanically induced stochastic resonance and chaos transfer between optical fields. *Nature Photonics*, 10(May):1–7, 2016.